SLAC-434
SLAC/SSRL-0065
UC-404
(SSRL-M)

ANOMALOUS SMALL ANGLE X-RAY SCATTERING STUDIES OF AMORPHOUS METAL-GERMANIUM ALLOYS

Marybeth Rice

Stanford Linear Accelerator Center
Stanford Synchrotron Radiation Laboratory
Stanford University, Stanford, California 94309

December 1993

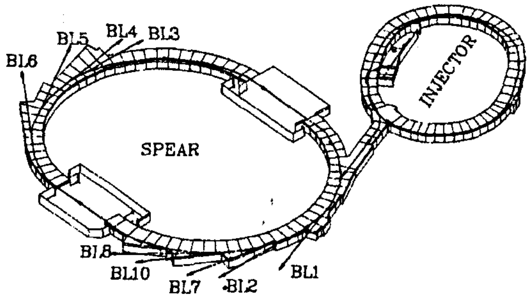

Prepared for the Department of Energy under contract number DE-AC03-76SF00515
Printed in the United States of America. Available from the National Technical
Information Service, U.S. Department of Commerce, 5285 Port Royal Road, Springfield,
Virginia 22161

---

*Ph.D. thesis

ABSTRACT

This dissertation addresses the issue of composition modulation in sputtered amorphous metal-germanium thin films with the aim of understanding the intermediate range structure of these films as a function of composition. The investigative tool used in this work is anomalous small-angle X-ray scattering (ASAXS).

The primary focus of this investigation is the amorphous iron-germanium (a-Fe$_x$Ge$_{100-x}$) system with particular emphasis on the semiconductor-rich regime. Brief excursions are made into the amorphous tungsten-germanium (a-W$_x$Ge$_{100-x}$) and the amorphous molybdenum-germanium (a-Mo$_x$Ge$_{100-x}$) systems. All three systems exhibit an amorphous structure over a broad composition range extending from pure amorphous germanium to approximately 70 atomic percent metal when prepared as sputtered films. Across this composition range the structures change from the open, covalently bonded, tetrahedral network of pure a-Ge to densely packed metals. The structural changes are accompanied by a semiconductor-metal transition in all three systems as well as a ferromagnetic transition in the a-Fe$_x$Ge$_{100-x}$ system and a superconducting transition in the a-Mo$_x$Ge$_{100-x}$ system.

A long standing question, particularly in the a-Fe$_x$Ge$_{100-x}$ and the a-Mo$_x$Ge$_{100-x}$ systems, has been whether the structural changes (and therefore the accompanying electrical and magnetic transitions) are accomplished by homogeneous alloy formation or phase separation. Several structural analysis tools have already been applied to this question with limited, and in some cases contradictory, results.

The application of ASAXS to this problem proves unambiguously that fine scale composition modulations, as distinct from the simple density fluctuations that arise from cracks and voids, are present in the a-Fe$_x$Ge$_{100-x}$, a-W$_x$Ge$_{100-x}$, and a-Mo$_x$Ge$_{100-x}$ systems in the semiconductor-metal transition region. Furthermore, ASAXS shows that germanium is distributed uniformly throughout each sample in the $x<25$ regime of all three systems. ASAXS results show further that the a-Fe_xGe_{100-x} system is also phase separated for $x>33$ while the a-Mo_xGe_{100-x} system is not. The ASAXS results are compared with two and three phase models.

ACKNOWLEDGMENTS

This work benefited enormously from the contributions of many people. I would like to thank my thesis advisor, Artie Bienenstock, for his intellectual and financial support and for the scientific training he provided.

This project would not have been possible with out the very careful and beautiful structural analyses of the *a*-Mo_xGe_{100-x} and *a*-Fe_xGe_{100-x} systems by my predecessors, Jeff Kortright and Denny Lorentz. I thank them also for the loan of their samples. Mike Regan's complementary work on these samples is also noted. This work was enhanced greatly by discussions with Mike.

I learned the experimental ins and outs of anomalous small angle X-ray scattering from Soichi Wakatsuki who also collaborated with us on the first publications and who was my co-author on *A User's Guide to the Small-Angle X-Ray Scattering/Diffraction Data Acquisition System at SSRL*. I thank Steve Hubbard and his thesis advisors Keith Hodgson and Seb Doniach for allowing me to steal some of his beam time to perform the first failed feasibility experiments. In spite of the first null result, Wakatsuki, Hodgson and Doniach donated their time to a second successful feasibility study at a different camera length which launched this project.

Keith Hodgson and Seb Doniach helped to arrange the trip to beam line X14A at NSLS, Brookhaven. The beam line crew on X14A, Gene Ice, Paul Zshack, and Mark Egbretson were fabulous. They were accommodating beyond belief, fixing water cooling trips at 4 a.m. (Paul Zshack), realigning the beam line optics at odd hours (Gene Ice), reconfiguring the computer (Mark Egbretson) and cheerfully tolerating the complete devastation of their beam line by these crazy kids from Stanford.

I have especially fond regard for my companions in the trenches who shared the Brookhaven adventure with me and helped with camera alignment and data collection:

Soichi Wakatsuki, David Eliezer, Mike Regan, Pat Frank, and especially Nanna Gillis who also kept me sane.

David McKay allowed us to take over his X-ray lab in Cell Biology to test our new quadrant detector which broke two days before the trip to Brookhaven. Andre Gabriel fixed our quadrant detector on no notice and Michel Koch lent us his linear detector for the SSRL experiments (we were always facing beam time with a broken detector).

Pierre Capeder, Robert Mayer, Tad Slowikowski, and George Husek contributed to the design and constructuction of our experimental apparatus. Our data acquisition and analysis systems are largely the product of Tony Cox and Ethan Merritt.

The X-ray staff at SSRL provided a lot of assistance on the beam line, particularly J. R. Troxel, Tom Hostetler, Tony Tiscareno, Dave Day, and Alan Swithenbank as did the SSRL duty operators. Thanks go to my experimental companions on the beam line at SSRL: Mike Regan, David Eliezer, Hiro Tsuruta, and Caroline Stahle.

I learned the black art of sputtering from Doug Keith and Bill Holmes. Help with preliminary sample characterization came from Chris Zercher, Julie Paque, Helen Kirby and Waldo Winterburn. David Silverberg helped with the grunt work of data crunching.

I thank Ruth and Fred Waldhauer, Tony Cox, and George Husek for their friendship and encouragement. And finally, I thank my boyfriend, Ron Sid, for his generous non-scientific support during the agonizing last few months of thesis writing.

TABLE OF CONTENTS

CHAPTER I

INTRODUCTION

CHAPTER II

SAMPLES

CHAPTER III

ACQUISITION OF ANOMALOUS SMALL ANGLE X-RAY SCATTERING DATA

CHAPTER IV

REDUCTION OF ANOMALOUS SMALL ANGLE X-RAY SCATTERING DATA

CHAPTER V

ASAXS RESULTS: SAMPLES WITH x<25

CHAPTER VI

ASAXS RESULTS: SAMPLES WITH $x>25$

CHAPTER VII

CONCLUSIONS

LIST OF TABLES

LIST OF FIGURES

CHAPTER I
INTRODUCTION

This dissertation describes efforts to detect and characterize composition modulations in sputtered amorphous metal-germanium (a-M_xGe_{100-x}) thin films as a function of metal concentration. Three systems are discussed here: amorphous iron-germanium (a-Fe_xGe_{100-x}), amorphous tungsten-germanium (a-W_xGe_{100-x}), and amorphous molybdenum-germanium (a-Mo_xGe_{100-x}). These three systems of sputtered thin films exist in the amorphous state over a composition range extending from pure germanium to approximately 70 atomic percent metal. Across this composition range the structures of these films change from an open, covalently bonded, tetrahedrally coördinated semiconductor to densely packed metals. The structural changes are accompanied by electronic and magnetic transitions. Each of these systems undergoes a semiconductor-metal transition near 15 atomic percent metal while the a-Fe_xGe_{100-x} system also exhibits a ferromagnetic transition and the a-Mo_xGe_{100-x} system exhibits a superconducting transition.

1.1 THE CONTINUOUS RANDOM NETWORK

The structure of the compositional endpoints, pure a-Ge and a-$M_{70}Ge_{30}$, can be described in terms of the two most successful models for amorphous materials. The first model, proposed by Zachariasen (1932) and later developed by Polk (1971) for a-Ge and a-Si, is that of the continuous random network (CRN). In the Ge CRN, as in crystalline Ge (c-Ge), each Ge atom is covalently bonded by sp^3 bonds to four other Ge atoms located at the vertices of a tetrahedron. Hence, the c-Ge coordination distance of 2.45 Å and coordination number of 4 are preserved in the amorphous state. In the crystalline state the tetrahedral bond angles are all optimized at 109° while in the CRN model they vary by ± 10° about this value.

This variation in the bond angles gives rise to the crucial difference between the amorphous and crystalline structures: the arrangement of the tetrahedra. In *c*-Ge the tetrahedra are fixed in orientation with respect to each other such that the dihedral angle between each pair of tetrahedra is 60°. The Ge atoms are thus arranged in the crystalline diamond cubic structure with each atom belonging to 12 different six-membered rings. In *a*-Ge the tetrahedra are randomly oriented with respect to each other. The dihedral angle can take on any value between 0 and 60 ° such that Ge atoms form five-, six-, and seven-membered rings. The presence of odd numbered rings stabilizes the amorphous structure by preventing long range translational symmetry and by preventing homogeneous phase transformation to the crystalline structure since significant topological rearrangement is required to attain the six-membered ring configuration. The five-membered rings also decrease the frequency of atomic separations at the crystalline third neighbor distance (Turnbull & Polk, 1972). The lack of atoms at such a distance is the signature of *a*-Si and *a*-Ge. The CRN model is the only model that successfully reproduces this feature of *a*-Ge and seems to successfully describe the structure of *a*-Ge.

1.2 DENSE RANDOM PACKING OF HARD SPHERES

The other model that successfully describes amorphous structures is the dense random packing of hard spheres (DRPHS) which is relevant to the most metal rich *a*-M_xGe_{100-x} films. Metallic structures, both crystalline and amorphous, are characterized by dense local packing of atoms with isotropic bonds. In two dimensions the densest packing of equal sized circles is a hexagonal arrangement where each circle is in direct contact with six others. In three space, the densest arrangement of equal sized spheres is a stacking of sheets of six-fold coordinated spheres. The sheets can be stacked in innumerable ways. A stacking of the sheets in an ABAB format yields the hexagonal close packed (hcp) structure while a stacking of the sheets in an ABCABC format yields the face centered cubic (fcc) structure.

In crystalline close packed systems, such as fcc and hcp metals, each sphere (atom) is twelve-fold coordinated. The spaces between spheres are either formed by four spheres in hard contact or six spheres in hard contact. These two types of spaces are called tetrahedral and octahedral sites, respectively. In the tetrahedral site four atoms are found at the vertices of a tetrahedron whereas the octahedral sites have six atoms at the vertices of an octahedron. A tetrahedron of spheres is the densest simple packing of spheres. Clusters of tetrahedra including spiral chains, pentagonal bipyramids, and icosahedra are locally denser than fcc and hcp structures but as the clusters increase in size and extent the tetrahedral sites occlude one another and large holes are formed in the structure. It is impossible to tile space with tetrahedra alone and the densest packing of spheres is an ordered array of tetrahedra and octahedra.

The theory of dense random packing of hard spheres (DRPHS) was first formulated by Bernal (1959, 1960, 1964) in an attempt to use geometrical analysis to understand the structure of monatomic liquids. His analysis is actually most relevant to metallic glasses. By assuming homogeneous irregular assemblages of atoms with no crystalline regions and no holes large enough to admit another atom and realizing that atoms cannot come closer than the sum of their radii without raising their mutual potential enormously, he developed the DRPHS model for non-crystalline systems. The model was realized by kneading ball-bearings in balloons to prevent nucleation of crystalline stacking by planar surfaces. The most important results of the model building experiments were that the coordination number varied and that there were five types of polyhedral holes: the tetrahedral and octahedral holes of crystalline close packing plus trigonal prisms, Archimedean anti-prisms, and tetragonal dodecahedra. The presence of the latter three prevent long range order. Seventy-three percent by number, or 48 percent by volume, of the holes are tetrahedra. The DRPHS fills 63.7 percent of the volume whereas crystalline close packing fills 74.05 percent of the volume. Bernal also observed a preponderance of colineations in the DRPHS with three, four, and five atoms in a line.

Finney (1970), expanding on Bernal's idea, created a 7994 sphere model, entered the coordinates of each sphere center into a computer program, and generated radial distribution functions. A radial distribution function (rdf) represents the average number of atom (sphere) centers at a distance *r* from an average atom (sphere). His rdf, plotted as a function of distance expressed in sphere diameters, has its first maximum at 1.00 sphere diameter. This obviously represents the nearest-neighbor distance. The second peak is split with a sub-peak at 1.99 sphere diameters that arises from three-membered colineations, and a sub-peak at 1.73 sphere diameters that arises from the distance between the apices of coplanar tetrahedra. Finney's model also shows a shoulder at 1.65 sphere diameters which corresponds to the distance between the apices of two tetrahedra with a common base. These geometries were illustrated by Bennett in 1971.

The splitting of the second peak in the rdf is one of the signatures of DRPHS structures. The split second peak appears not only in the rdf but also in the structure factor, $I(s)$, which is a measure of the intensity of the scattered radiation as a function of scattering vector, s. The split second peak in the scattering factor is another signature of the DRPHS structure.

Leung and Wright (1974) made films of monatomic amorphous metals by evaporation onto substrates held at liquid helium temperatures. They obtained structure factors for amorphous manganese, iron, chromium and cobalt. These structure factors are typical of those from DRPHS models. Although the crystal structures for these four metals are different, the amorphous structures appear to be similar. The structure factors all exhibit a sharp first peak and a broader second peak that is split. In microcrystalline models for amorphous metals, all peaks of the structure factor are equally broadened. Only the DRPHS model reproduces the sharp first peak and broadened second and third peaks.

Another class of metallic glasses is the melt-quenched metal-metalloid glasses that typically contain 20 atomic percent metalloid. These glasses also display the split second peak in the structure factor and in the rdf that is characteristic of the pure amorphous metals. Cargill (1970) compared data from *a*-$Ni_{76}P_{24}$ to Finney's computer generated rdf's from the DRPHS model. Cargill assumed that the nickel and phosphorous atoms are the same size, since their twelve-fold coordinated Goldschmidt radii are almost identical, and assumed that they are randomly distributed in the DRPHS. Cargill compared his reduced radial distribution function to Finney's model. While the fit is generally quite good there is a density deficit produced by fitting to the DRPHS model and the position of the first peak, R_1, corresponds to a distance that is greater than the hard sphere diameter, D_{HS}.

Polk (1970, 1972) tried to resolve the difficulties with Cargill's fit by proposing modifications to the DRPHS model. Polk observed that in many metal-metalloid crystals (*c*-M-Me) the metal-metalloid distance is often less than the sum of the Goldschmidt radii. He postulated that the Me atoms fit into the larger holes in the metal DRPHS and "jam" the structure, preventing crystallization. Polk calculated the center-to-vertex distance for the larger Bernal holes and, using the Me size deduced from *c*-M_3Me structures, concluded that the Me atoms fit into the interstices of the metal DRPHS. While this model solves the density deficit problem it doesn't help the R_1 greater than D_{HS} problem.

Cargill (1974, 1975) later showed that Polk's calculation for the size of the Bernal holes was wrong. Cargill showed that the metal skeleton of the DRPHS is disturbed by the metalloid atoms (using the Me size calculated from *c*-M_3Me structures) which are a little too large to fit into the interstices. Cargill & Cochrane (1974) noticed that the metal-metal distance in M-Me glasses increases with increasing metalloid content, showing that the Me atoms do not simply fit into the interstices of the metal DRPHS as proposed by Polk. The Me atoms cause the M atoms to pack more loosely yielding R_1 greater than D_{HS}.

The qualitative aspects of Polk's model, however, are borne out in many systems. In many M-Me glasses the Me atoms are surrounded exclusively by M atoms as they would be if they fit into the interstices of a metal DRPHS. Also the Me-M distance is typically shorter than the sum of the Goldschmidt radii and the Me coordination is less than the M coordination. Table I.1 shows data compiled by Spaepen (1978) on M-Me glasses and M_3Me crystals which support the qualitative aspects of Polk's model.

TABLE I.1

Nearest neighbor structural data for amorphous and crystalline M-Me alloys.

(from Spaepen 1978)

Composition M_xMe_{1-x}	Me Coordination Number	M Coordination Number	Average Distance M-Me (Å)	Average Distance M-M (Å)	Metal Goldschmidt Diameter (Å)
Amorphous					
a-$Co_{81}P_{19}$	8.9	12.2	2.32	2.54	2.50
a-$Ni_{80}P_{20}$	8.5	12.9	2.35	2.55	2.49
a-$Pd_{84}Si_{16}$	9.0	12.8	2.40	2.76	2.75
a-$Pd_{78}Ge_{22}$	8.6		2.486		2.75
Crystalline					
c-Mn_3P	9	13.7	2.37	2.76	2.61
c-Fe_3P	9	13.7	2.34	2.71	2.55
c-Ni_3P	9	13.7	2.29	2.68	2.49
c-Pd_3Si	8	12.7	2.44	2.90	2.75

A computer model that a priori includes two sizes of spheres was generated by Sadoc, Dixmier & Guinier in 1973. In their model, the small spheres were constrained to have only large spheres as neighbors. The results showed that the small spheres tended to be nine-fold coordinated. Five-fold symmetry was common. The computer generated structure factor, *I*(*s*), has the characteristic split second peak and fits well to experimental data from *a*-$Ni_{84}P_{16}$.

Another important contribution to the theory of M-Me glasses came from Gaskell in 1978 and 1979. Gaskell observed the preponderance of trigonal prismatic coordination in *c*-M_3Me compounds and remarked that it would be "exceptional if this type of polyhedron does not represent the dominant motif in the glassy state" given that "well defined local coordination in the crystalline and glassy states is an almost universal feature of inorganic oxides, chalcogenides, halides, etc." Gaskell went on to postulate that M-Me glasses are random packings of trigonal prisms with the prisms stacked such that each Me atom is surrounded by nine M atoms. The Me atom is in the center of a Bernal hole: the trigonal prism capped with three half octahedra. Gaskell plotted an rdf generated from a computer model of his randomly stacked trigonal prisms against neutron scattering data from *a*-$Pd_{80}Si_{20}$. The fit is quite good. In Gaskell's model, all of the Me atoms are in trigonal prismatic cavities. In Bernal's DRPHS model, the trigonal prismatic cavities make up an appreciably smaller fraction of the available holes.

All these models from Polk onward indicate that M-Me glasses have a preferred local order with metalloid atoms preferentially surrounded by metal atoms. The preferred environments are probably not solely the result of size effects. Geny, Marchal, Mangin, Janot & Piecuch (1982) studied amorphous alloys of tin (Sn) with iron, cobalt (Co), and nickel (Ni). The Sn Goldschmidt radius is 1.62 Å while those of Fe, Co, and Ni are 1.27 Å, 1.25 Å, and 1.25 Å, respectively. These three transition metal-tin systems exhibit very different amorphous composition ranges and stabilities which obviously are not due to size effects. Thus chemistry appears to play an important role in the local structure of both the CRN and the DRPHS models of amorphous solids.

The melt-quenched M-Me glasses that are described well by Cargill's and Gaskell's improvements on Polk's model have a deep eutectic in their phase diagrams at the glass forming composition, which is typically near 80 atomic percent metal. The sputtered thin films discussed here exist in the amorphous state independent of eutectics in their phase diagrams and cannot be made amorphous at the melt-quenched M-Me composition of 80 atomic percent. Additionally, these films are created by a vapor deposition process that builds up the film atomic layer by atomic layer while the melt-quenched glasses are produced by rapid solidification of a bulk liquid. Furthermore, in the Fe-Ge system the metalloid (Ge) atom is bigger than the metal (Fe) atom. Still, the DRPHS is the only reasonable model that has been developed so far to describe the structure of amorphous metals and, if nothing else, is a good starting point for understanding these structures. As will be discussed later, the structure factors from the a-$M_{70}Ge_{30}$ films display the characteristic shape of structure factors from melt-quenched glasses.

1.3 AMORPHOUS STRUCTURE IN THE INTERMEDIATE COMPOSITION RANGE

While there are strong models for the compositional end points of the a-M_xGe_{100-x} systems, there is no definitive model for amorphous structures in the composition range intermediate to pure a-Ge and 70 atomic percent metal. How the structure changes from a CRN to a DRPHS is not well understood. Many attempts have been made to understand this intermediate composition range.

Massenet, Daver & Geneste (1974) studied evaporated a-Fe_xGe_{100-x} films with electron diffraction and suggested that Fe initially enters the a-Ge network substitutionally but begins to progressively break up the tetrahedral structure at higher concentrations. Chopra, Nath & Rastogi (1975) studied evaporated a-Fe_xGe_{100-x} films with transmission electron microscopy and electron diffraction and concluded that the Fe, for x less than 20, was uniformly distributed and did not bond with Ge. Thermal cycling indicated that the Fe diffuses and bonds with other Fe atoms creating small segregated regions of Fe at higher temperatures. Further work by Randhawa, Nath, Malhotra & Chopra (1976) indicated that the short range order of a-Fe$_x$Ge$_{100-x}$ evaporated films is identical to that of pure a-Ge for x less than 20 and that Fe is tetrahedrally coordinated.

More work by Daver & Massenet in 1977 suggested that Fe creates a disordered metal matrix upon alloying with a-Ge. They suggested that Fe forms bonds with Ge with hybridization between Fe 3d and Ge sp electrons. Sawicki & Sawicka (1977) used Mössbauer spectroscopy to study ^{57}Fe implanted in Ge and concluded that Fe lies in the interstitial sites of the a-Ge network. Popescu (1980) computer modeled the hole structure of a-Ge and saw that Fe atoms could fit in the a-Ge holes up to a concentration of 16 atomic percent Fe. Further computer modeling by Popescu (1983) showed that Fe is not substitutional in the a-Ge network but fits an interstitial model with a weak Fe-Ge interaction. His coordination numbers were similar to those of c-FeGe$_2$. Uemura, Suzuki & Satow (1977) tried to fit a microcrystalline model to electron diffraction data from evaporated a-Fe$_x$Ge$_{100-x}$ without success. They obtained a reasonable fit to experimental data by modeling a-Fe$_{40}$Ge$_{60}$ as a severely distorted c-FeGe$_2$ structure. Their studies convinced them that no more tetrahedra of a-Ge were present at Fe concentrations exceeding 25 atomic percent.

In magnetic and structural studies of evaporated a-Fe$_x$Si$_{100-x}$, Mangin & Marchal concluded that the structure, for all x greater than 30, could be described as a DRPHS with the Si and Fe atoms randomly distributed. They took the broad hyper-fine field distributions as an indication that Fe exists in a variety of surroundings in the amorphous structure. They concluded that the changes in magnetic properties with composition were due to changing chemical environments rather than gross structural rearrangements. Further structural studies on the same system by Mangin, Marchal, Rodmacq & Janot (1977) showed that the structure of a-Fe$_x$Si$_{100-x}$ is essentially unvarying and DRPHS-like for all x between 75 and 30. They took as a structural unit for the DRPHS model a thirteen atom icosahedron and showed how the Si CRN can be progressively transformed into the DRPHS by the addition of atoms to the centers of five-membered rings.

The diversity of structural models offered to explain the intermediate composition range is indicative of the difficulty of the problem. There is no clear understanding of the structure of these systems taken individually or more importantly as a class of materials. No obvious model suggests itself as in the cases of the CRN and DRPHS glasses.

All of the models described above assume a homogeneous solid solution. In the analogous crystalline systems, Fe forms a solid solution in Ge or Si only in minute amounts. The addition of Fe, in atomic concentrations exceeding 10^{-4} percent, to c-Ge leads to the precipitation of c-FeGe$_2$. In fact, the equilibrium Fe-Ge system is phase separated at all compositions except those corresponding to stoichiometric compounds and to the extremely limited range of primary solid solutions.

Crystalline systems exhibit three distinct types of structure: a) solid solutions, b) intermetallic compounds, and c) phase mixtures. An obvious question is whether there are analogs in the amorphous systems. The work described above on the a-Fe$_x$Ge$_{100-x}$ and a-Fe$_x$Si$_{100-x}$ systems is based on the premise of a homogeneous solid solution. Given that chemical bonding constraints play such an important role in the CRN glasses and seem to be important even in the binary DRPHS metallic glasses, it is reasonable to expect the possibility of preferred atomic structures in the intermediate composition range of amorphous materials. In analogy to crystalline systems, preferred amorphous structures could be present in varying proportions as the overall composition changes.

Just such preferred amorphous structures have been seen in studies of the evaporated a-Au$_x$Si$_{100-x}$ system by Mangin, Marchal, Mourey & C. Janot (1980) and Audier, Guyot, Simon & Valignat (1983). Mangin, et al. saw that for x values between 10 and 70, a-Au$_x$Si$_{100-x}$ is separated into an amorphous gold rich phase with a composition near Au$_3$Si and an a-Si phase with Au atoms in the interstices. Below x=10 only the amorphous Si-Au solid solution exists and above x=70 only the amorphous gold rich phase is found. Crystallization occurs in samples with x greater than 80. In contrast, Audier et al. saw clear phase separation in a-Au$_{17}$Si$_{83}$ and a-Au$_{27}$Si$_{73}$ but not in a-Au$_{46}$Si$_{54}$. They did not identify the composition of the Au-rich phase, but concluded that the Si-rich phase is close to pure *a*-Si.

Another example of phase separation in an amorphous intermetallic system is given by the work on *a*-Fe_xSn_{100-x} alloys by Janot (1983). Within x limits of 25 and 67, the samples are a mixture of an *a*-$Fe_{25}Sn_{75}$ structure and an *a*-Fe_2Sn structure. At higher Fe concentrations, the samples contain *a*-Fe clusters embedded in *a*-Fe_2Sn. For x between 10 and 25, the structure can be described as an amorphous solid solution of Fe in Sn. The *a*-Fe_2Sn structure is a variation on Gaskell's trigonal prisms. This was first noticed by Geny, Marchal, Mangin, Janot & Piecuch (1982) in studies of the Fe-rich *a*-Fe_xSn_{100-x} system.

The possibility of phase separation in the *a*-Fe_xGe_{100-x} system has been explored by Lorentz (1986) and Lorentz, Bienenstock & Morrison (1994). Lorentz's work builds on the analysis of the *a*-Mo_xGe_{100-x} system by Kortright (1984) and Kortright & Bienenstock (1988) which included investigations of phase separation in the intermediate composition range.

1.4 PREVIOUS WORK ON SPUTTERED *a*-MO_xGE_{100-x} THIN FILMS

Kortright investigated the structures of *a*-Mo_xGe_{100-x} films as a function of metal concentration with the combined tools of extended X-ray absorption fine structure (EXAFS), anomalous wide-angle X-ray scattering (AXS), and conventional small-angle X-ray scattering (SAXS). He drew the following conclusions from his work.

1) Samples with 4, 8, 14, and 21 atomic percent Mo consist of a Mo modified material very finely dispersed in *a*-Ge. The Mo modified material has a local structure similar to those of the crystalline Ge-rich intermetallic compounds and is present on a size scale of only tens of Ångströms. Kortright called this concentration regime "structural region I" and assigned it boundaries of 0 and 23 atomic percent Mo.

2) Samples with 25 and 42 atomic percent Mo are apparently homogeneous with a structure that resembles those of the Ge-rich intermetallic compounds. This structure changes little with metal concentration. Kortright called this concentration regime "structural region II" and assumed that it extends from about 23 atomic percent Mo to roughly 50 atomic percent Mo.

3) Samples with 65 and 70 atomic percent Mo have the structure of a typical metal-metalloid glass and are apparently homogeneous. These samples are representative of "structural region III" to which Kortright assigned boundaries of approximately 50 and 70 atomic percent Mo.

Kortright's conclusion that the samples in structural region I are compositionally modulated is based partly on his EXAFS data which are reproduced in Figures I.1 and I.2. EXAFS is the oscillation of the X-ray absorption coefficient above an absorption edge. This oscillation is caused by interference between the ejected photoelectron wave traveling away from the absorbing atom and backscattering of the wave from the surrounding atoms. EXAFS is therefore sensitive to the number and location of the backscattering atoms surrounding an absorbing atom.

These figures present the normalized absorption coefficient, $k^3\chi(k)$, as a function of the scattering vector, k. The scattering vector, k, is defined by the relation

$$E-E_0 = \hbar^2k^2/2m \qquad (1.1)$$

where E is the incident photon energy, E_0 is the threshold energy for the absorption edge, m is the electron mass, and $\hbar$ is Planck's constant divided by 2π.

The Mo edge EXAFS data look almost identical for all samples with Mo concentrations between 4 and 42 atomic percent. The only change in the EXAFS signal across this concentration range is a slight decrease in amplitude with increasing Mo content. In going from the 42 atomic percent Mo sample to the 65 atomic percent Mo sample, the Mo edge EXAFS changes dramatically. The EXAFS signal is again identical for the 65 and 70 atomic percent Mo samples. This implies that Mo exists in essentially the same

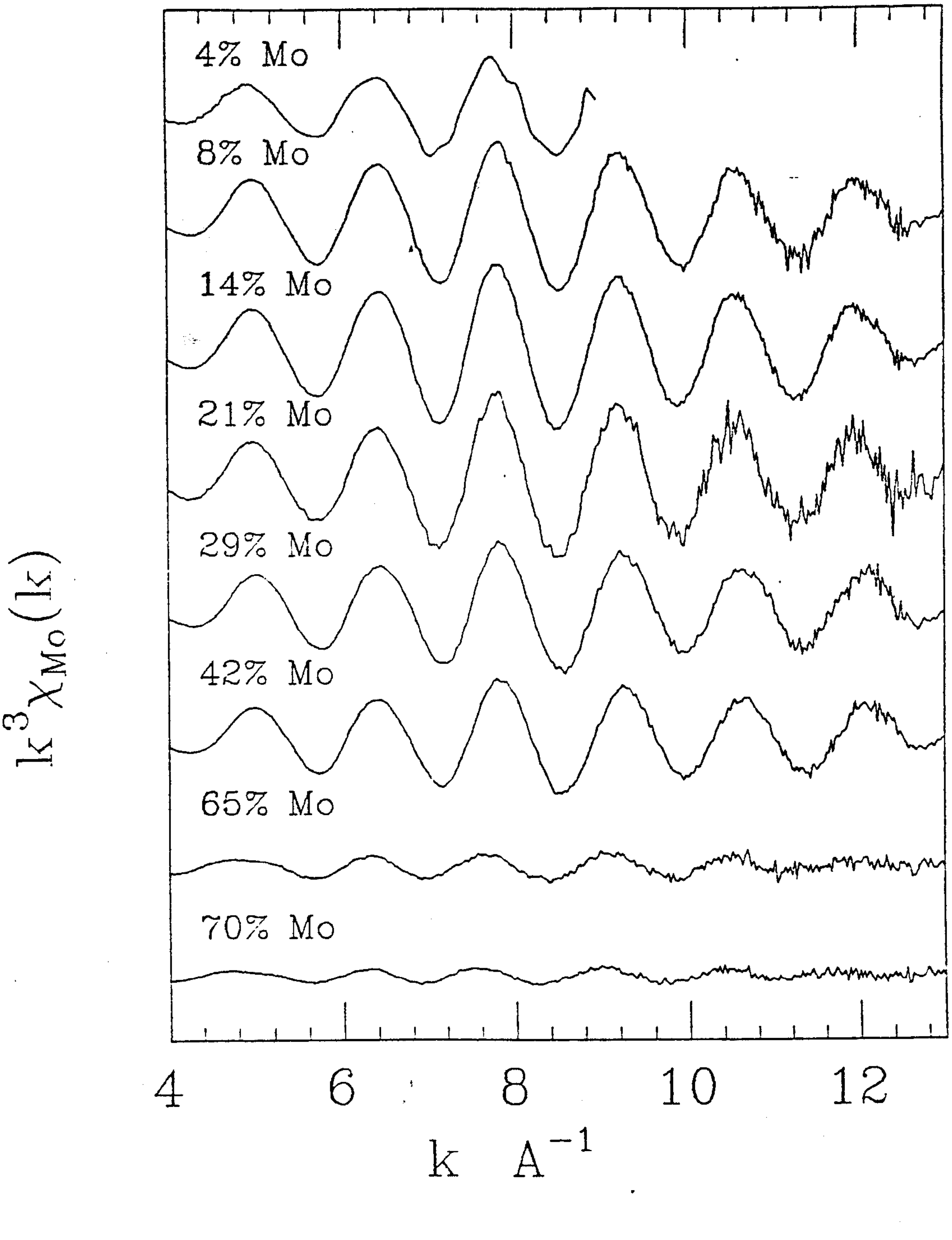

FIGURE I.1 Kortright's (1984) EXAFS data at the Mo *K* absorption edge. Mo edge $k^3\chi(k)$ are plotted as a function of *k* for samples with 4 to 70 atomic percent Mo.

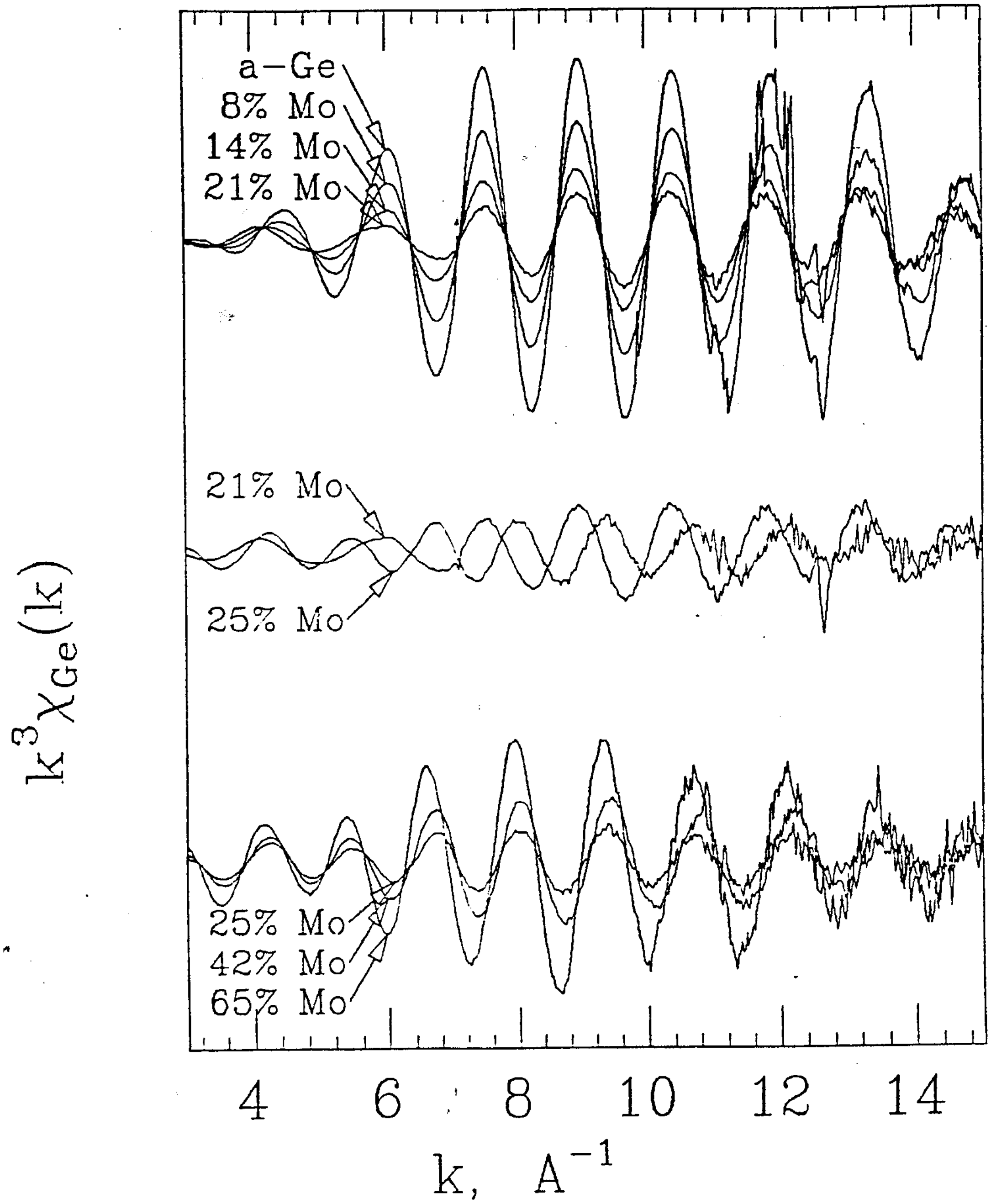

FIGURE I.2 Kortright's (1984) EXAFS data at the Ge *K* absorption edge. Ge edge $k^3\chi(k)$ are plotted as a function of *k* for samples with 0 to 65 atomic percent Mo.

environment in all samples within structural regions I and II. The Mo environment changes between structural regions II and III but is also essentially identical for all samples within structural region III.

Similarly, the Ge edge EXAFS has the same phase (coordination distance) for all the samples with 21 atomic percent Mo or less, including pure amorphous Ge. Across this concentration regime the amplitude (coordination number) decreases with increasing Mo content. The sample with 25 atomic percent Mo has a completely different phase from the samples in structural region I. The 42 atomic percent Mo and the 65 atomic percent Mo samples have the same phase as the 25 atomic percent Mo sample with successively increasing amplitudes.

Kortright interpreted these data as an indication that pure *a*-Ge coexists with a Mo modified material in all samples within structural region I. He further concluded that *a*-Ge is absent from all samples with Mo concentrations exceeding approximately 23 atomic percent. In structural regions II and III, all the Ge atoms are apparently consumed by the Mo modified material and no excess Ge atoms are left to form clusters of pure *a*-Ge.

Kortright's conclusions are also supported by his scattering data which are reproduced in Figure I.3. These data are presented as the normalized scattering intensity, $S(k)$, versus the magnitude of the scattering vector, k. Here k is equal to $4\pi \sin(\theta)/\lambda$, where λ is the X-ray wavelength, and 2θ is the scattering angle.

The abrupt changes seen in the EXAFS data between structural regions I and II at the Ge edge and between structural regions II and III at the Mo edge are paralleled in the scattering data. For samples in structural region I, the data are roughly superpositions of the scattering from the 25 atomic percent Mo sample and *a*-Ge as shown in Figure I.4. Kortright interpreted the deviation of the data from the combined scattering of *a*-Ge and *a*-$Mo_{25}Ge_{75}$ as a result of interference between the compositionally different regions.

The data in structural region I can also be modeled as superpositions of the scattering from *a*-Ge and *a*-$Mo_{42}Ge_{58}$, since the scattering factors from *a*-$Mo_{25}Ge_{75}$ and

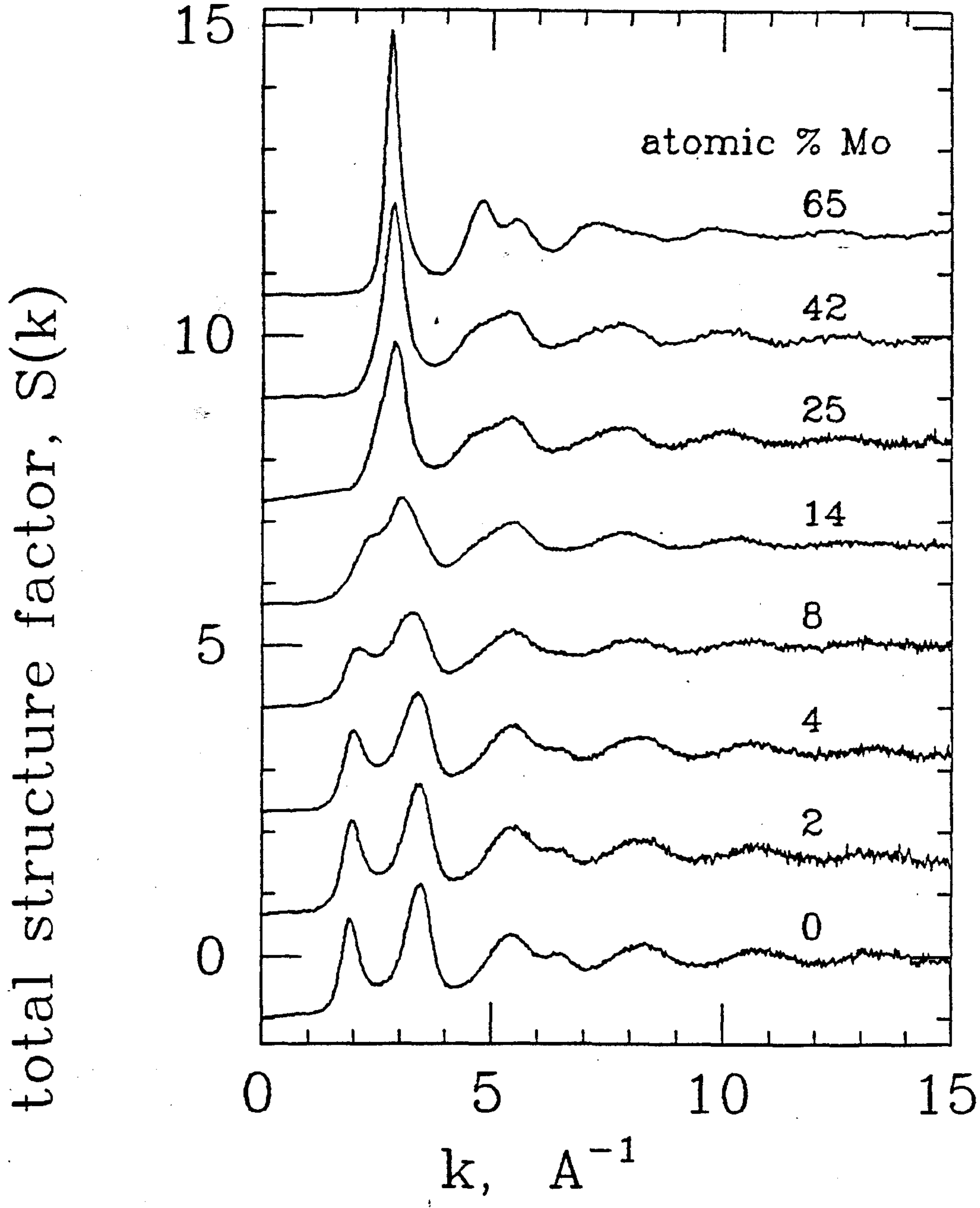

FIGURE I.3 Kortright's (1984) structure factors, $S(k)$, as a function of k for a-Mo$_x$Ge$_{100-x}$ samples with x ranging from 0 to 65. Amorphous Ge appears to be present in all samples with less than 25 atomic percent Mo and absent from samples with 25 or more atomic percent Mo. The 25 and 42 atomic percent Mo samples have almost identical structure factors. The shape of the structure factor for the 65 atomic percent Mo sample is similar to those of DRPHS glasses.

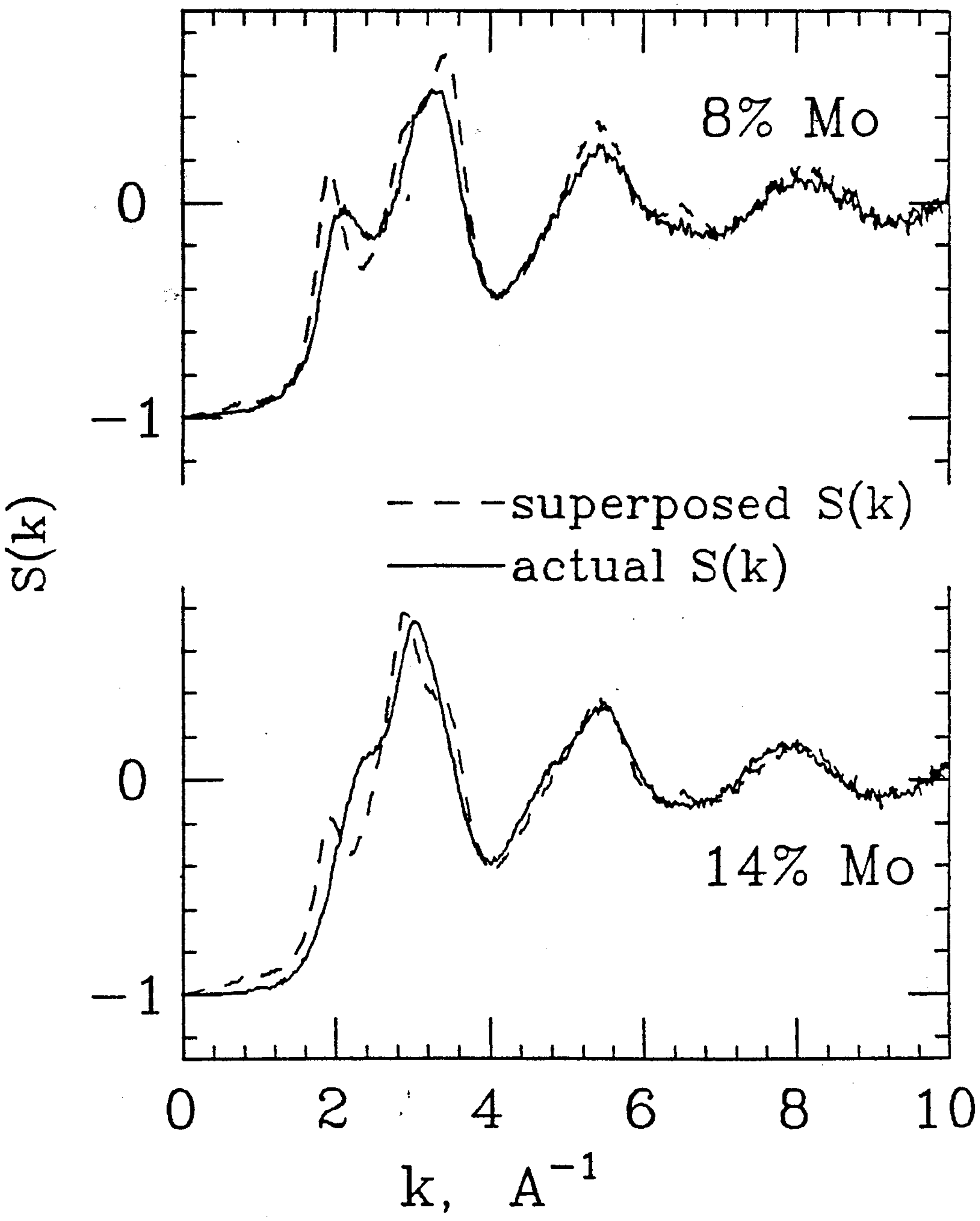

FIGURE I.4 Kortright's (1984) plot of the actual structure factors for the 8 and 14 atomic percent samples against the superpositions of the structure factors from the *a*-Ge sample and the 25 atomic percent Mo samples.

a-$Mo_{42}Ge_{58}$ are nearly identical. These two samples with nearly identical scattering factors lie in structural region II. Together the EXAFS data and the scattering data indicate that structural region I is composed of pure a-Ge coexisting with the Mo modified material from structural region II.

Structural region III contains the samples with 65 and 70 atomic percent Mo. The scattering from these samples is clearly different from the scattering from samples with 42 atomic percent Mo and less. This abrupt change in the scattering data coincides with the abrupt change observed in the Mo edge EXAFS data. The scattering from these very Mo-rich samples looks like the scattering from typical melt-quenched transition metal-metalloid glasses.

To further investigate the question of phase separation in these materials Kortright collected SAXS data. SAXS is sensitive to electron density fluctuations on a scale of tens to thousands of Ångströms. Kortright collected data between k=0.004 and k=0.15 Å^{-1}, with k equal to $4\pi\sin(\theta)/\lambda$. This corresponds to a real space sensitivity ranging from 42 Å to 1570 Å.

For all the a-Mo_xGe_{100-x} samples Kortright's data show a rapid, monotonic decrease in intensity with increasing k, for k values less than 0.05 Å^{-1}. At k values greater than 0.05 Å^{-1} there is a diffuse intensity that is constant across the entire measured k range. Kortright suspected that the monotonically decreasing intensity in his SAXS data at low k was caused by cracks and voids. To test this hypothesis he crumpled one of his samples and observed a hundred fold increase in the intensity at low k as a result. He thus attributed the low k intensity to the presence of cracks and voids.

In contrast, the diffuse background intensity was not affected by crumpling the samples and it varies smoothly as a function of Mo content. The diffuse background is zero for pure a-Ge and increases with increasing Mo content, peaking at 8 atomic percent Mo. It then decreases rapidly for samples with Mo concentrations exceeding 8 atomic percent.

Kortright was able to reproduce the magnitude of the diffuse intensity of the 8 atomic percent Mo sample (but not quite the shape) with a Guinier model of 5 Å radius spheres of a-$Mo_{25}Ge_{75}$ in pure a-Ge, with each phase occupying 50 percent of the volume. He attributed the poorness of the fit to the inadequacy of the Guinier model in high volume concentration regimes. Kortright interpreted the maximum in the diffuse intensity at 8 atomic percent Mo as evidence that the inhomogeneity is a maximum at this composition. This interpretation is consistent not only with his SAXS data but with his EXAFS and AXS data as well.

In summary, Kortright concluded that a-Mo_xGe_{100-x} samples are compositionally modulated on a size scale of the order of 10 Å for all x less than 23 and are homogeneous at all higher concentrations. Kortright concluded that the samples in structural regions II and III are homogeneous although his EXAFS data, in particular, do not exclude the possibility of composition modulation in these regimes. Work that supports Kortright's conclusions was performed by Ding & Anderson (1987). In molecular dynamics computer simulations of a-Mo_xGe_{100-x}, they saw that Mo atoms tend to cluster in samples with low Mo concentration. The Mo atoms form chains, branched chains, and rings in an a-Ge matrix. It is interesting to note that the first intermetallic compound in the equilibrium Mo-Ge system, c-$MoGe_2$, has no Mo-Mo distances of less than 3.5 Å.

1.5 PREVIOUS WORK ON SPUTTERED a-FE_xGE_{100-x} THIN FILMS

Lorentz used X-ray absorption near edge structure (XANES), conventional SAXS, AXS, and EXAFS, to study the structure of sputtered a-Fe_xGe_{100-x} thin films as a function of composition. He concluded that:

1) For samples with less than 33 atomic percent Fe, either the techniques he used are insensitive to very fine scale composition modulation or the samples are homogeneous.

2) For samples with compositions between 33 atomic percent Fe and 72 atomic percent Fe, the data indicate phase separation into a-$Fe_{33}Ge_{67}$ and a-$Fe_{72}Ge_{27}$ on a size scale of 150 to 200 Å.

Lorentz's conclusions are based on his SAXS and XANES data. His SAXS data for some representative samples are reproduced in Figure I.5. They are plotted as normalized intensity, $I(k)$, versus the magnitude of the scattering vector, k. Here k is equal to $4\pi\sin(\theta)/\lambda$ and extends from 0.015 $Å^{-1}$ to 0.185 A^{-1}. This corresponds to a real space sensitivity ranging from 34 Å to 419 Å.

For all samples with Fe concentrations between 0 and 33 atomic percent and for the 72 atomic percent Fe sample, the SAXS intensity falls off sharply at low k and is small but constant at high k. These results are similar to Kortright's SAXS results across the entire composition range of a-Mo_xGe_{100-x}. The steep fall off in the a-Fe_xGe_{100-x} samples can be fit by a model of voids in an amorphous matrix.

A model of phase separation into a-Ge and an amorphous $FeGe_2$-like compound is inconclusive for these data. The model produces a flat scattering across the entire k range. Lorentz's data show a constant diffuse background but since they were collected at an energy above the Fe absorption edge, they contain Fe fluorescence. It is thus impossible to tell whether the diffuse background arises from fluorescence alone or from a combination of fluorescence and a finely dispersed second phase. This ambiguity.makes it impossible to draw the conclusions about fine scale phase separation that Kortright was able to draw.

For the samples with Fe concentrations between 37 and 65 atomic percent, the monotonic decrease at low k is gradual and for some samples there is a shoulder or even a resolved peak. These data could not be fit with a model of voids in an amorphous matrix. Except for the 37 atomic percent Fe sample, all these samples fit a model of phase separation into an amorphous $FeGe_2$-like compound and an amorphous Fe_3Ge-like compound. The intensity for the model of the 37 atomic percent Fe sample was five times larger than the data. This may be due to normalization problems with the data.

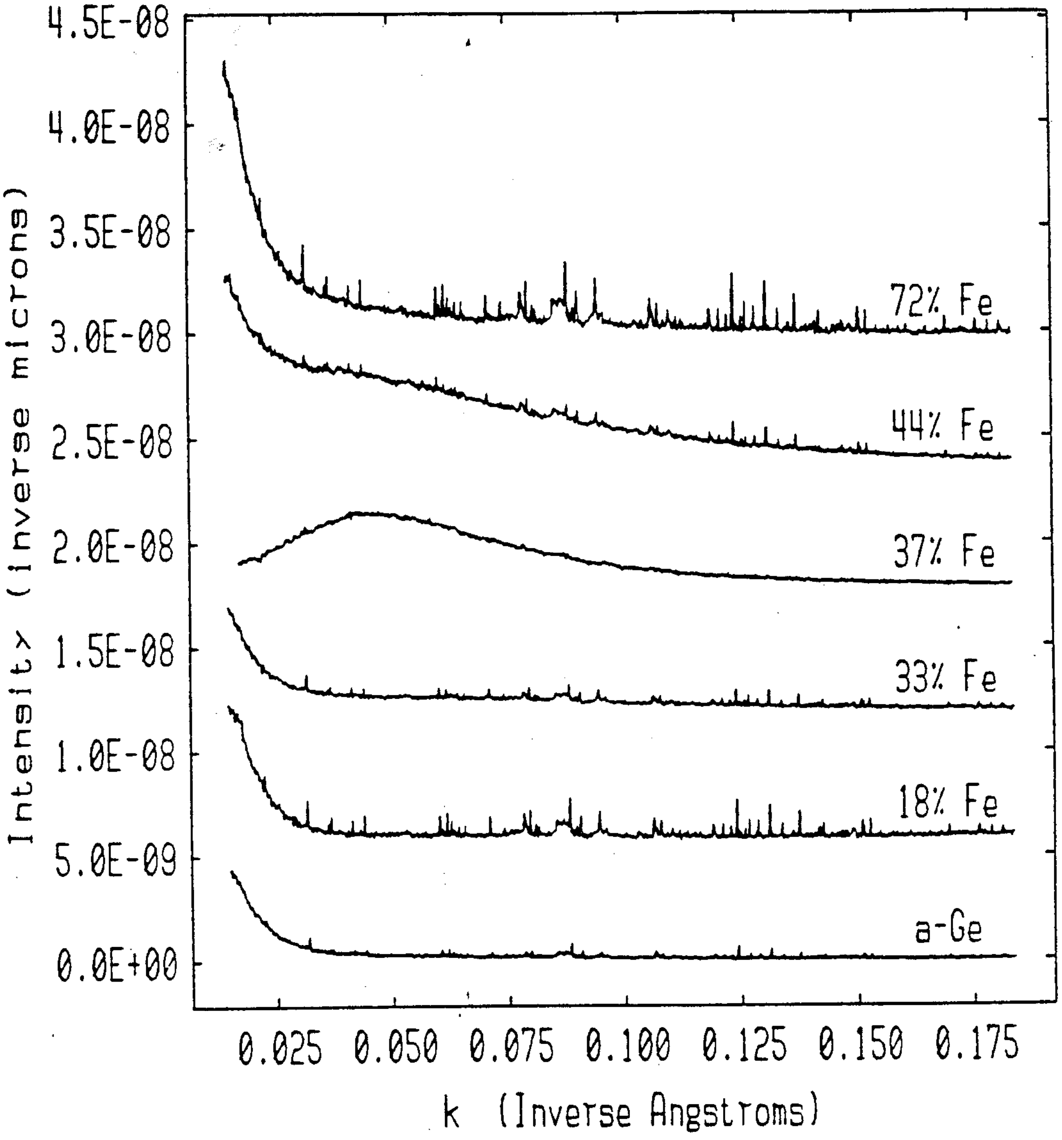

FIGURE I.5 Lorentz's (1986) SAXS patterns plotted as scattered intensity versus scattering vector, *k*, for *a*-Fe_xGe_{100-x} samples with *x* varying from zero to 72.

The 65 and 72 atomic percent Fe samples were also successfully modeled as a combination of amorphous FeGe and amorphous Fe_3Ge. A model of phase separation into a-Ge and amorphous Fe_3Ge failed for all compositions.

To further explore the issue of composition modulation in this system Lorentz used a XANES analysis procedure that was pioneered by Morrison, Paesler, Sayers, Tsu & Gonzalez-Hernandez (1985). XANES, as its name suggests, is the structure of the absorption coefficient near an absorption edge. Like EXAFS, XANES is extracted from absorption data. The normalized absorption coefficient, σ, multiplied by the incident photon energy, E, is related to, f'', the imaginary part of the scattering factor through the optical theorem

$$f'' = (mc/2e^2h)\, E\, \sigma. \qquad (1.2)$$

Here m is the electron mass, c is the speed of light, e is the electronic charge, and h is Plank's constant. XANES data are usually presented as f'' versus E.

The analysis technique used by Lorentz assumes that the XANES from a phase separated sample is a linear combination of the XANES from the two phases that make up the sample and that the XANES spectra from all samples that lie within a phase separated region are linearly related. This analysis is valid only if the individual phases have a well defined structure and composition and are so large that the interface between phases does not occupy an appreciable fraction of the sample volume. Therefore, this analysis technique is insensitive to extremely fine scale composition modulation, where the interfaces between phase separated regions may be comparable in size to the regions themselves. It is also insensitive to slowly varying composition modulations like those present in the early stages of spinodal decomposition.

In applying this analysis technique to his data, Lorentz found that the XANES from all the samples with compositions between 37 and 65 atomic percent Fe are linear combinations of each other. All of these spectra are linear combinations of the XANES from a-$Fe_{33}Ge_{67}$ and a-$Fe_{72}Ge_{28}$. Samples with compositions ranging from 0 to 33 atomic percent Fe do not have XANES patterns that are linearly related to each other nor to the XANES patterns from samples with concentrations exceeding 33 atomic percent Fe. Fits using the XANES from the *a*-Ge sample and *a*-$Fe_{33}Ge_{67}$ are poor for all samples in this composition range.

The XANES pattern for the 12 atomic percent Fe sample is shown in Figure I.6 along with the least squares fit from the *a*-Ge and the *a*-$Fe_{33}Ge_{67}$ XANES patterns. This figure shows f'', the imaginary part of the scattering factor, as a function of the incident photon energy, E. The fit is very poor compared to the fit, also shown in Figure I.6, to the 49 atomic percent Fe sample using the XANES patterns from *a*-$Fe_{33}Ge_{67}$ and *a*-$Fe_{72}Ge_{28}$. Samples with more than 33 atomic percent Fe are well fit with the phase separated XANES model and samples with less than 33 atomic percent Fe are not.

The phase separated concentration regime includes the ferromagnetic transition at approximately 43 atomic percent Fe. The appearance of ferromagnetic behavior at this concentration is easily explained by a phase separated model. The second phase clusters in a phase separated material are expected to become interconnected and form one "infinite cluster" when they occupy 15 percent of the total sample volume. Ferromagnetic *a*-$Fe_{72}Ge_{28}$ occupies 15 percent of the volume of a sample composed of *a*-$Fe_{33}Ge_{67}$ and *a*-$Fe_{72}Ge_{28}$ at an overall atomic Fe concentration of approximately 40 percent. Similar behavior is seen in the *a*-Fe_xSn_{100-x} system. Janot (1983) explains the onset of ferromagnetism in this system at 39 atomic percent Fe as the result of ferromagnetic *a*-Fe_2Sn occupying 15 percent of the sample volume and forming an interconnected cluster in an *a*-$Fe_{25}Sn_{75}$ matrix.

The main conclusion of Lorentz's combined SAXS and XANES analyses is that the *a*-Fe_xGe_{100-x} system is phase separated into *a*-$Fe_{33}Ge_{67}$ and *a*-$Fe_{72}Ge_{28}$ for all concentrations between 33 and 72 atomic percent Fe. For samples with less than 33 atomic percent Fe, the SAXS and XANES techniques used by Lorentz indicate homogeneity. The

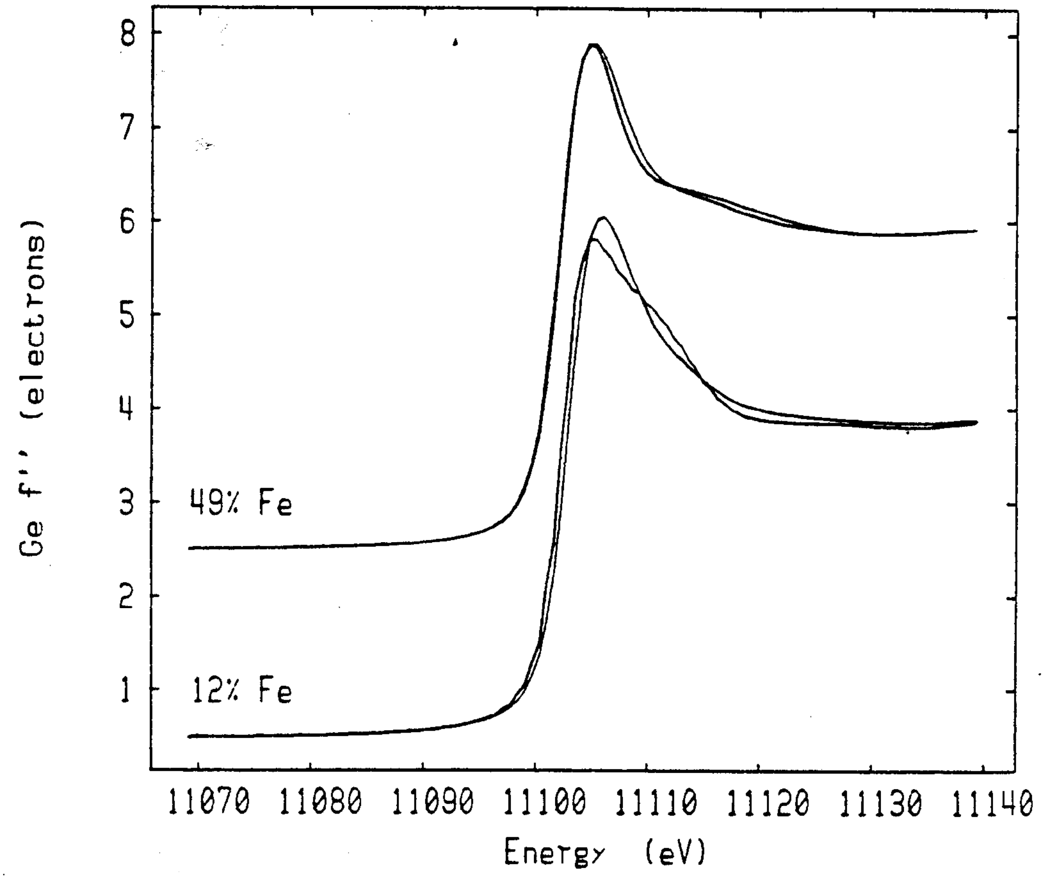

FIGURE I.6 Lorentz's (1986) plot of Ge edge XANES from the 49 atomic percent Fe sample and the 12 atomic percent Fe sample expressed as f'' versus incident photon energy. The XANES from the 49 percent sample is compared to the least squares fit of the XANES from the a-$Fe_{33}Ge_{67}$ and a-$Fe_{72}Ge_{28}$ samples while the XANES from the 12 percent sample is compared to the least squares fit of the XANES from the a-Ge and a-$Fe_{33}Ge_{67}$ samples.

techniques, however, as employed by Lorentz are insensitive to fine scale composition modulations.

1.6 QUESTIONS RAISED BY THE a-MO$_x$GE$_{100-x}$ AND a-FE$_x$GE$_{100-x}$ RESULTS

By the mid-1980's it was apparent that neither Mo nor Fe enters the a-Ge network substitutionally. Just how these metals enter the a-Ge network was, however, still unclear. The work of Lorentz pointed to a homogeneous picture for the a-Fe$_x$Ge$_{100-x}$ system with x less than 33, while the work of Kortright and of Ding & Andersen indicated fine scale composition modulation in the a-Mo$_x$Ge$_{100-x}$ system for all x less than approximately 23. Furthermore, Kortright's "Mo-modified" material seemed to resemble the crystalline Mo-Ge intermetallics, particularly c-MoGe$_2$, while Ding & Andersen saw Mo clusters in the same composition regime.

An obvious question is why does Fe enter the a-Ge network homogeneously while Mo clearly does not? Or even more importantly, does Fe really enter the a-Ge network homogeneously, or only appear to because the tools used by Lorentz and earlier workers were incapable of detecting fine scale composition modulation in this system?

Since there are at least two different models for how Mo modifies the a-Ge structure, which is correct? Is it possible to learn more about the structure of the "Mo-modified" material? Is the "Mo-modified" material a true phase? If it is, then as the Mo concentration increases does this phase simply occupy a larger fraction of the sample volume? If this is the case, there should be a composition at which the sample consists entirely of the single phase "Mo-modified" material. What is this composition? Both Kortright and Ding & Andersen think that the a-Mo$_x$Ge$_{100-x}$ samples become homogeneous somewhere between 20 and 25 atomic percent Mo. Is this reasonable especially since the first compound in the analogous equilibrium system, c-MoGe$_2$, occurs at 33 atomic percent

Mo? If the "Mo-modified" material is not a distinct phase, what is it? Is it, for example, a product of early stage spinodal decomposition?

Similarly, since Lorentz's work offered no evidence for composition modulation in a-Fe$_x$Ge$_{100-x}$ for x less than 33, how exactly does Fe enter the a-Ge network? Does it bond with Ge? If it does, why isn't there a detectable "Fe-modified" material?

The low metal concentration regime in these two systems is confusing and so is the metal rich regime. Again, the a-Mo$_x$Ge$_{100-x}$ and the a-Fe$_x$Ge$_{100-x}$ sputtered thin films exhibit opposite behavior. The a-Fe$_x$Ge$_{100-x}$ system appears to be phase separated for all x between 33 and 72, a composition range that appears to be homogeneous in the a-Mo$_x$Ge$_{100-x}$ system. Is this really so? and if so, why? Both systems are phase separated in the equilibrium state across the entire composition range except at those compositions corresponding to the stoichiometric compounds. The a-Fe$_x$Ge$_{100-x}$ system seems to have amorphous compounds that are analogous to c-FeGe$_2$ and c-Fe$_3$Ge, though an analog of c-FeGe is notably absent. Conversely, the a-Mo$_x$Ge$_{100-x}$ system appears to have no analogs with the crystalline Mo-Ge compounds.

A desire to further explore these questions and answer at least some of them, was the motivation for undertaking the work presented in this dissertation. Clearly, the tools used prior to the investigation described herein were not going to reveal much new information. A new investigative tool was sought. At the out set of this work the technique of anomalous small angle X-ray scattering (ASAXS) was being developed for application to inorganic solids.

1.7 THE ANOMALOUS SMALL ANGLE X-RAY SCATTERING TECHNIQUE

The anomalous small angle X-ray scattering technique combines the sensitivity of SAXS to long range electron density fluctuations (on the scale of tens to thousands of Ångströms) with the anomalous dispersion effect to yield species specific information about these fluctuations.

At incident X-ray energies much greater than any absorption edge in the probed atom, the scattering factor, f_0, is proportional, at very low scattering vectors, to the atomic number, Z, and is independent of energy. Near an absorption edge this simple relationship no longer holds and the scattering factor experiences energy dependent changes, as discussed in great detail by James (1982). The total scattering factor is now expressed as

$$f(k, E)=f_0(k)+f'(E)+if''(E) \qquad (1.3)$$

where f' and f'' are the real and imaginary changes from the high energy limit, f_0, of the scattering factor, f. Here E is the energy and k is the scattering vector and is equal to $4\pi\sin\theta/\lambda$.

The anomalous dispersion effect is very strong only within a small energy range, usually about 100 eV, near an absorption edge. Full utilization of the anomalous effect, therefore, only became feasible with the advent of intense, continuously tunable, X-ray sources such as synchrotrons. Early efforts demonstrating the viability of anomalous scattering experiments include the wide angle anomalous X-ray scattering studies of chalcogenide glasses by Fuoss, Eisenberger, Warburton & Bienenstock (1981) and the anomalous small angle X-ray scattering studies of organic macromolecules in solution by Stuhrmann (1980).

It should be mentioned here that small angle neutron scattering can produce species specific contrast variation through isotopic and isomorphic substitution. This method, however, requires the production of several samples at the same effective overall composition to achieve the contrast. In ASAXS the contrast variation is achieved by varying the X-ray wavelength rather than altering the sample. This eliminates the enormously difficult task of creating structurally identical samples of differing scattering efficiencies, as discussed by Simon, Lyon & de Fontaine (1985).

Early successes with ASAXS came from biophysics applications involving large molecules in solution. The value of applying ASAXS to inorganic solids was demonstrated by Goudeau, Naudon, Fontaine & Williams (1985 & 1986) in their work on the already well characterized Guinier-Preston zones in polycrystalline Al-Zn alloys. They made several intensity measurements at different energies below the Zn *K* absorption edge. By using equations known to be valid for this system that relate the ASAXS intensity to the scattering factor for zinc, they were able to extract values of f' for the Zn *K* edge. These values agree well with f' values for Zn obtained by Simon, Hoyt, Lyon, Pro, Davis, de Fontaine & Warburton (1985) from more conventional absorption experiments.

Once the utility of ASAXS for studying inorganic alloys was established on a known system, it was applied to complex unsolved problems. Lyon & Simon (1987) used ASAXS to determine partial structure factors in polycrystalline Cu-Ni-Fe alloys and show that phase separation in this system can not be modeled by segregation into two phases. Similarly, Simon & Lyon (1989) used ASAXS to extract the partial structure factors of polycrystalline Fe-Cr-Co alloys and discovered that this particular system does separate into two well-formed phases. Jemian, Weertman, Long & Spal (1991) were able to characterize $Cr_{23}C_6$ precipitates in Fe9Cr1Mo steel, as distinct from other precipitates, by performing ASAXS experiments near the Cr *K* absorption edge.

In amorphous alloys, ASAXS was used to advantage by Goudeau, Naudon, Rodmacq, Mangin & Chamberod (1985) and Goudeau, Naudon, Chamberod, Rodmacq & Williams (1987) in the study of hydrogenated *a*-Cu-Ti. These workers were able to establish, by working near both the Ti *K* edge and the Cu *K* edge, that the introduction of hydrogen into *a*-Cu-Ti alloys causes the precipitation of titanium hydride clusters. In ASAXS experiments on $(Fe_xMn_{1-x})_{35}Y_{65}$ glasses, Maret, Simon & Lyon (1989) determined that the segregation is best described as fine scale concentration fluctuations rather than phase separation into two phases. From the anomalous effect, they were able to extract the ratio of the partial atomic volumes. These values are very close to the values for the pure metals indicating clustering of like atoms.

Clearly, the ASAXS technique holds great promise for unraveling the intermediate range morphology of complex systems that reveal little structural information with more conventional techniques. ASAXS is applied here to answer some difficult questions about the structure of sputtered amorphous metal-germanium thin films of varying metal content.

REFERENCES FOR CHAPTER I

Audier, M., Guyot, P., Simon, J. P. & Valignat, N., *J. Phys. Coll.* **C8** (1985) C8-433.

Bennett, C. H., *J. Appl. Phys.* **43** (1972) 2727.

Bernal, J. D., *Nature (London)* **183** (1959) 141.

Bernal, J. D., *Nature (London)* **185** (1960) 68.

Bernal, J. D., *Proc. Roy. Soc., Ser. A* **280** (1964) 299.

Cargill III, G. S., *J. Appl. Phys.* **41** (1970) 12 & 2248.

Cargill III, G. S. & Cochrane, R. W., *J. Phys. (Paris)* **35** (1974) C4-269.

Cargill III, G. S., *Solid State Phys.* **30** (1975) 227.

Chopra, K. L., Nath, P. & Rastogi, A. C., *Phys. Stat. Sol. (a)* **27** (1975) 645.

Daver, H. & Massenet, O., *Solid State Comm.* **23** (1977) 393.

Ding, K. & Andersen, H. C., *Phys. Rev. B* **36** (1987) 2675.

Finney, J. L., *Proc. Roy. Soc., Ser. A* **319** (1970) 479.

Fuoss, P. H., Eisenberger, P., Warburton, W. K. & Bienenstock, A., *Phys. Rev. Lett.* **46** (1981) 1537.

Gaskell, P. H., In *Rapidly Quenched Metals III, Vol. 2,* edited by B. Cantor, Met. Soc. London (1978) 277.

Gaskell, P. H., *J. Non-Cryst. Sol.* **32** (1979) 207.

Geny, J. F., Marchal, G., Mangin, P., Janot, C. & Piecuch, M., *Phys. Rev. B* **25** (1982) 7449.

Goudeau, P., Naudon, A., Fontaine, A. & Williams, C. E., *J. Phys. Lett. (Paris)* **46** (1985) 255.

Goudeau, P., Naudon, A., Rodmacq, B., Mangin, P. & Chamberod, A., *J. Phys. Coll.* **C8** (1985) C8-479.

Goudeau, P., Naudon, A., Chamberod, A., Rodmacq, B. & Williams, C. E., *Europhys. Lett.* **3** (1987) 269.

Goudeau, P., Fontaine, A., Naudon, A. & Williams, C. E., *J. Appl. Cryst.* **19** (1986) 19.

James, R. W., *The Optical Principles of the Diffraction of X-rays*, Ox Bow Press, Woodbridge, CT (1982).

Janot, C., *J. Non-Cryst. Sol.* **56** (1983) 267.

Jemian, P. R., Weertman, J. R., Long, G. G. & Spal, R. D., *Acta Metall.* **39** (1991) 2477.

Kortright, J. B., Ph.D. thesis, Stanford University (1984).

Kortright, J. B. & Bienenstock, A., *Phys. Rev. B* **37** (1988) 2979.

Leung, P. K. & Wright, J. G., *Phil. Mag.* **30** (1974) 185 & 995.

Lorentz, R. D., Ph.D. thesis, Stanford University (1986).

Lorentz, R. D., Bienenstock, A. & Morrison, T. I., to appear in *Phys. Rev. B* (1994).

Lyon, O. & Simon, P., *Phys. Rev. B* **35** (1987) 5164.

Mangin, P., Marchal, G., Rodmacq, B. & Janot, C., *Phil. Mag.* **36** (1977) 643.

Mangin, P. & Marchal, G., *J. Appl. Phys.* **49** (1978) 1709.

Mangin, P., Marchal, G., Mourey, C. & Janot, C., *Phys. Rev. B* **21** (1980) 3047.

Maret, M., Simon, J. P. & Lyon, O., *J. Phys.: Cond. Matt.* **1** (1989) 10249.

Massenet, O., Daver, H. & Geneste, J., *J. Phys. Coll.* **C4** (1974) C4-279.

Morrison, T. I., Paesler, M. A., Sayers, D. E., Tsu, R. & Gonzalez-Hernandez, J., *Phys. Rev. B* **31** (1985) 5474.

Polk, D. E., *Scripta Met.* **4** (1970) 117.

Polk, D. E., *J. Non-Cryst. Sol.* **5** (1971) 365.

Polk, D. E., *J. Acta Met.* **20** (1972) 485.

Popescu, M. A., *J. Non-Cryst. Sol.* **35 & 36** (1980) 549.

Popescu, M. A., *J. Non-Cryst. Sol.* **56** (1983) 273.

Randhawa, H. S., Nath, P., Malhotra, L. K. & Chopra, K. L., *Solid State Comm.* **20** (1976) 73.

Sadoc, J. F., Dixmier, J. & Guinier, A., *J. Non-Cryst. Sol.* **12** (1973) 46.

Sawicki, J. A. & Sawicka, B. D., *Phys. Stat. Sol. (b)* **80** (1977) K41.

Simon, J. P., Hoyt, J. J., Lyon, O., Pro, R., Davis, B. E. C., de Fontaine, D. & Warburton, W. K., *J. Appl. Cryst.* **18** (1985) 181.

Simon, J. P. & Lyon, O., *Acta Metall.* **37** (1989) 1727.

Simon, J. P., Lyon, O. & de Fontaine, D., *J. Appl. Cryst.* **18** (1985) 230.

Spaepen, F., In *Rapidly Quenched Metals III, Vol. 2,* edited by B. Cantor, Met. Soc. London (1978) 253.

Stuhrmann, H. B., *Acta Cryst.* **A36** (1980) 996.

Turnbull, D. & Polk, D. E., *J. Non-Cryst. Sol.* **8-10** (1972) 19.

Uemura, O., Suzuki, Y. & Satow, T., *Phys. Stat. Sol. (a)* **41** (1977) 417.

Zachariasen, W. H., *J. Am. Chem. Soc.* **54** (1932) 3841.

CHAPTER II

SAMPLES

2.1 SAMPLES STUDIED IN THIS WORK

Sputtered amorphous metal-germanium thin films of twenty-five distinct compositions are examined in this work along with pure *a*-Ge. These films include twelve *a*-Fe_xGe_{100-x} samples with x varying from 5 to 71, seven *a*-Mo_xGe_{100-x} samples with x varying from 3 to 72, and six *a*-W_xGe_{100-x} samples with x varying from 7 to 78. The ASAXS technique was applied in this work to the *a*-Fe_xGe_{100-x} films of Lorentz and the *a*-Mo_xGe_{100-x} films of Kortright to answer some of the questions raised by their investigations. The *a*-W_xGe_{100-x} system was included in this study because the equilibrium W-Ge system, unlike the equilibrium Fe-Ge and Mo-Ge systems, contains no intermetallic phases. This apparent lack of chemical affinity between W and Ge atoms suggests that the *a*-W_xGe_{100-x} system may be a good candidate for phase separation.

2.2 THE EQUILIBRIUM SYSTEMS: FE-GE, MO-GE, AND W-GE

As hinted at in the above paragraph, the three systems, Fe-Ge, Mo-Ge, and W-Ge, have very different equilibrium phase diagrams. The equilibrium phase diagrams for the Fe-Ge and Mo-Ge systems, shown in Figures II.1 and II.2 (Moffatt, 1984), contain several compounds, some of which occur in different allotropes. Many compounds occur at the same metal concentration in both systems. The compounds with identical metal content, like $MoGe_2$ and $FeGe_2$, are not, however, isomorphous. Structural data for the crystalline components of the Fe-Ge and Mo-Ge phase diagrams, where available (Villars & Calvert, 1991), are given in Tables II.1, II.2, and II.3.

The Fe-Ge system has a eutectic at approximately 70 atomic percent Fe– not quite the position of the deep eutectic in typical melt-quenched metal-metalloid glasses– and another eutectic at approximately 25 atomic percent Fe. The Mo-Ge system has no

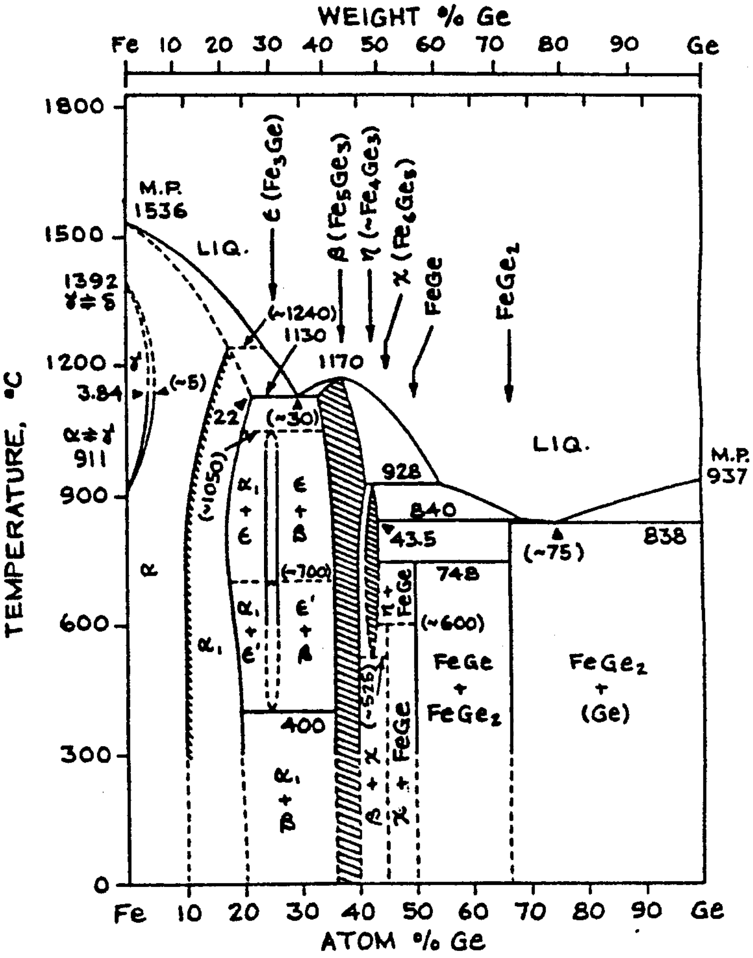

FIGURE II.1 The equilibrium phase diagram for the *c*-Fe-Ge system. Taken from Moffatt (1984). [Redrawn from Kubaschewski (1982).]

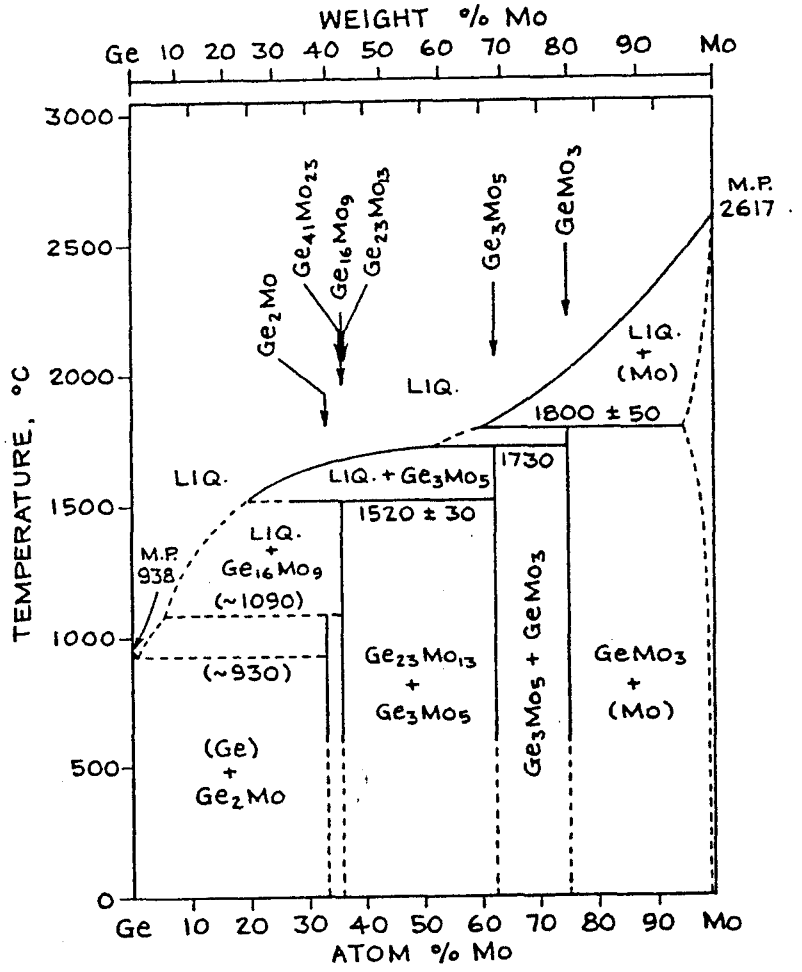

FIGURE II.2 The equilibrium phase diagram for the *c*-Mo-Ge system. Taken from Moffatt (1984). [Redrawn from Brewer & Lamoreaux (1980).]

TABLE II.1

Structural data for crystalline components of the equilibrium Fe-Ge system containing less than 60 atomic percent Fe.

Crystalline Compound/ Crystalline Structure	Unit Cell Dimensions (Å)			Number of Atoms per Unit Cell	Volume of Unit Cell (Å^3)
Ge diamond cubic	$a = 5.658$ $\alpha = 90^\circ$	$b = a$ $\beta = 90^\circ$	$c = a$ $\gamma = 90^\circ$	8	181.13
$FeGe_2$ tetragonal ($CuAl_2$)	$a = 5.908$ $\alpha = 90^\circ$	$b = a$ $\beta = 90^\circ$	$c = 4.957$ $\gamma = 90^\circ$	12	173.02
FeGe monoclinic (CoGe)	$a = 11.841$ $\alpha = 90^\circ$	$b = 3.9376$ $\beta = 103.51^\circ$	$c = 4.9354$ $\gamma = 90^\circ$	16	223.75
FeGe hexagonal (CoSn)	$a = 4.965$ $\alpha = 90^\circ$	$b = a$ $\beta = 90^\circ$	$c = 4.054$ $\gamma = 120^\circ$	6	86.55
FeGe cubic (FeSi)	$a = 4.689$ $\alpha = 90^\circ$	$b = a$ $\beta = 90^\circ$	$c = a$ $\gamma = 90^\circ$	8	103.10
Fe_6Ge_5 monoclinic (Fe_6Ge_5)	$a = 9.965$ $\alpha = 90^\circ$	$b = 7.826$ $\beta = 109.67^\circ$	$c = 7.801$ $\gamma = 90^\circ$	44	572.87

TABLE II.2

Structural data for crystalline components of the equilibrium Fe-Ge system containing more than 60 atomic percent Fe.

Crystalline Compound/ Crystalline Structure	Unit Cell Dimensions (Å)			Number of Atoms per Unit Cell	Volume of Unit Cell (Å^3)
Fe_5Ge_3 hexagonal ($InNi_2$)	$a = 4.020$ $\alpha = 90^\circ$	$b = a$ $\beta = 90^\circ$	$c = 5.024$ $\gamma = 120^\circ$	6	70.31
Fe_3Ge cubic (Cu_3Au)	$a = 3.665$ $\alpha = 90^\circ$	$b = a$ $\beta = 90^\circ$	$c = a$ $\gamma = 90^\circ$	4	49.23
Fe_3Ge cubic (F_3Bi)	$a = 5.75$ $\alpha = 90^\circ$	$b = a$ $\beta = 90^\circ$	$c = a$ $\gamma = 90^\circ$	16	190.11
Fe_3Ge hexagonal (Ni_3Sn)	$a = 5.169$ $\alpha = 90^\circ$	$b = a$ $\beta = 90^\circ$	$c = 4.222$ $\gamma = 120^\circ$	8	97.69
Fe bcc	$a = 2.8664$ $\alpha = 90^\circ$	$b = a$ $\beta = 90^\circ$	$c = a$ $\gamma = 90^\circ$	2	23.55

TABLE II.3

Structural data for crystalline components of the equilibrium Mo-Ge system.

Crystalline Compound/ Crystalline Structure	Unit Cell Dimensions (Å)			Number of Atoms per Unit Cell	Volume of Unit Cell (Å^3)
Ge diamond cubic	$a = 5.658$ $\alpha = 90^\circ$	$b = a$ $\beta = 90^\circ$	$c = a$ $\gamma = 90^\circ$	8	181.13
MoGe$_2$ orthorhomb. (SiCo$_2$)	$a = 6.343$ $\alpha = 90^\circ$	$b = 3.451$ $\beta = 90^\circ$	$c = 8.582$ $\gamma = 90^\circ$	12	187.86
MoGe$_2$ tetragonal (MoSi$_2$)	$a = 3.322$ $\alpha = 90^\circ$	$b = a$ $\beta = 90^\circ$	$c = 8.219$ $\gamma = 90^\circ$	6	90.70
Mo$_{13}$Ge$_{23}$ tetragonal (Mo$_{13}$Ge$_{23}$)	$a = 5.99$ $\alpha = 90^\circ$	$b = a$ $\beta = 90^\circ$	$c = 63.54$ $\gamma = 90^\circ$	144	2279.82
Mo$_5$Ge$_3$ tetragonal (Sn$_5$Si$_3$)	$a = 9.837$ $\alpha = 90^\circ$	$b = a$ $\beta = 90^\circ$	$c = 4.973$ $\gamma = 90^\circ$	32	481.22
Mo$_3$Ge cubic (Cr$_3$Si)	$a = 4.932$ $\alpha = 90^\circ$	$b = a$ $\beta = 90^\circ$	$c = a$ $\gamma = 90^\circ$	8	119.97
Mo bcc	$a = 3.147$ $\alpha = 90^\circ$	$b = a$ $\beta = 90^\circ$	$c = a$ $\gamma = 90^\circ$	2	31.17

eutectic near that of typical melt-quenched metal-metalloid glasses. The only eutectic in the Mo-Ge system is near 2 atomic percent Mo.

Another difference between the Mo-Ge and Fe-Ge systems is the relative sizes of the metal and metalloid atoms. In the Mo-Ge system the Mo atom is slightly bigger than the Ge atom. The Mo and Ge Goldschmidt atomic radii are 1.40 Å and 1.39 Å, respectively. In *c*-Mo, the distance of closest approach between atoms is 2.725 Å. In *c*-Ge it is 2.450 Å, since it is governed by the covalent radius. In the Fe-Ge system, however, the Ge atom is larger than the Fe atom. The Goldschmidt radius for Fe is 1.27 Å compared to 1.39 Å in Ge. The covalent radius for Fe is 1.165Å while for Ge it is 1.223 Å and for Mo it is 1.296 Å (Pauling, 1960). The distance of closest approach between Fe atoms in crystalline bcc Fe is 2.482 Å.

In sharp contrast to the Fe-Ge and Mo-Ge systems, the equilibrium phase diagram of the W-Ge system, according to most authors (Hansen, 1958; Elliott, 1965; Shunk, 1969) is a simple eutectic with no intermetallic compounds. One group, Povarova & Savitskii (1971), claims the existence of a compound, W_2Ge_3, in this system at atmospheric pressure. Their phase diagram is reproduced in Figure II.3. They claim that W_2Ge_3 is isomorphous with Mo_2Ge_3, but Mo_2Ge_3 is actually $Mo_{13}Ge_{23}$. Subsequent authors (Popova & Fomicheva, 1978; and Agoshkov, Gorbatenkov, Popova, & Fomicheva, 1981) returned to the claim that there are no compounds in the W-Ge system at atmospheric pressure. These authors were able to obtain W-Ge compounds at high pressures (77 kbars), but none of these phases was W_2Ge_3. Popova & Fomicheva obtained two forms of W_5Ge_3 and one form of WGe_2. Agoshkov et al., obtained these three phases plus a second form of WGe_2. Structural data for these compounds are presented in Table II.4 (Villars & Calvert, 1991). The two high pressure WGe_2 compounds are isomorphous with the two $MoGe_2$ compounds that form at atmospheric pressure.

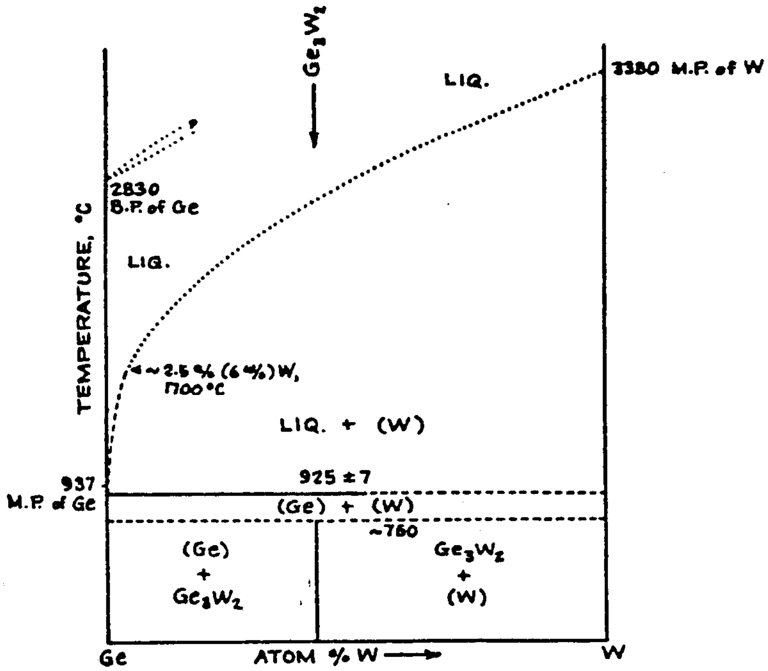

(Schematic only; not to scale)

FIGURE II.3 The equilibrium phase diagram for the *c*-W-Ge system according to Povarova & Savitskii. Taken from Moffatt (1984). [Redrawn from Povarova & Savitskii (1971).]

TABLE II.4

Structural data for crystalline compounds in the W-Ge system.

Crystalline Compound/ Crystalline Structure	Unit Cell Dimensions (Å)			Number of Atoms per Unit Cell	Volume of Unit Cell ($Å^3$)
Ge diamond cubic	$a = 5.658$ $\alpha = 90^\circ$	$b = a$ $\beta = 90^\circ$	$c = a$ $\gamma = 90^\circ$	8	181.13
WGe_2 orthorhomb. ($SiCo_2$)	$a = 6.399$ $\alpha = 90^\circ$	$b = 3.445$ $\beta = 90^\circ$	$c = 8.544$ $\gamma = 90^\circ$	12	188.35
WGe_2 tetragonal ($MoSi_2$)	$a = 3.320$ $\alpha = 90^\circ$	$b = a$ $\beta = 90^\circ$	$c = 8.192$ $\gamma = 90^\circ$	6	90.30
W_5Ge_3 tetragonal (Cr_5B_3)	$a = 6.25$ $\alpha = 90^\circ$	$b = a$ $\beta = 90^\circ$	$c = 11.72$ $\gamma = 90^\circ$	32	457.81
W_5Ge_3 tetragonal (W_5Si_3)	$a = 9.81$ $\alpha = 90^\circ$	$b = a$ $\beta = 90^\circ$	$c = 4.91$ $\gamma = 90^\circ$	32	472.52
W bcc	$a = 3.165$ $\alpha = 90^\circ$	$b = a$ $\beta = 90^\circ$	$c = a$ $\gamma = 90^\circ$	2	31.70

One factor contributing to the difficulty of phase formation in the W-Ge system is the huge difference in melting points between W and Ge (Nowotny, Benesovsky, & Brukl, 1961). Ge melts at 937° C while W melts at 3380° C, more than 500° above the boiling point of Ge at 2830° C. In contrast, Mo melts at 2617° C and Fe melts at 1536° C. Aside from the difference in melting point between Mo and W, one would expect the W-Ge and Mo-Ge systems to be quite similar. W, with atomic number 74, lies beneath Mo, with atomic number 42, in column VIB of the periodic table of the elements. Both Mo and W have six electrons in their outer shell. The electron configuration of Mo is $[Kr]4d^5 5s^1$ and that of W is $[Xe]4f^{14}5d^4 6s^2$. Similarly, the Pauling (1960) electron negativities of Mo and W are 1.8 and 1.7, respectively. Based on this information alone, one would expect Mo and W to interact similarly (probably by intermetallic or covalent bonding) with Ge whose electron negativity is 1.8 and whose electron configuration is $[Ar]3d^{10}s^2p^2$.

Additionally, the two metal atoms are almost the same size in spite of the 32 electron difference between them. The Goldschmidt atomic radius for Mo is 1.40 Å while for W it is 1.41 Å. The covalent radii of Mo and W are 1.296 and 1.304, respectively (Pauling, 1960). Similarly, the distance of closest approach for atoms is 2.725 Å in *c*-Mo and 2.739 Å in *c*-W. The facts that W has 32 more protons and electrons than Mo but with an interatomic distance in the bcc metal that is less than one percent greater than that in Mo, and a melting point that is 736° higher than that for Mo, indicate a very strong W-W interaction that exceeds the Mo-Mo interaction. The Mo-Ge and W-Ge systems are therefore very good systems to compare with the hope of separating chemical effects from purely geometrical effects.

The powerful W-W interaction makes the W-Ge system a likely candidate for phase separation, particularly into pure W and pure Ge as is seen in most versions of the equilibrium phase diagram. This may not hold for the sputtered amorphous system though. The vaporization of Ge at a temperature well below the W melting point and the sluggish reactivity of W at low temperatures probably preclude the formation of intermetallic compounds in any process involving the bulk components at atmospheric pressure. In sputtering, though, both W and Ge are in the vapor state and are rapidly quenched to a metastable solid. Under these conditions, W and Ge atoms may actually bond or may not have enough time to move into segregated regions.

2.3 THE SPUTTERING PROCESS

In the sputtering process, a low pressure gas, inside a vacuum chamber, is partially ionized and the ions are accelerated toward a cathode made of the target material. The ions impact the cathode with sufficient kinetic energy to dislodge individual atoms from the target. These atoms suffer collisions with the plasma and come to rest after their final collision with the substrate. In this process a gas of sputtered target atoms is formed and is very rapidly quenched upon impact with the substrate. This extremely rapid quench rate is often great enough to bypass crystallization, making the fabrication of amorphous materials possible.

The conceptual basis for the sputtering techniques used in this work is diode sputtering. In diode sputtering a high purity, low pressure gas is partially ionized by a large potential applied across two electrodes. The electrodes can be dc or rf powered. In the cases discussed here, the cathode with its target is one electrode. The rest of the chamber, which is at ground potential, forms the other electrode or counter-electrode. With this asymmetry in the electrode sizes, the small electrode is bombarded at high energy while the large electrode is bombarded at low energy. Thus, atoms are sputtered off the target and deposited on the rest of the chamber. In diode sputtering, secondary electrons emitted from the cathode upon ion bombardment have a long mean free path and bombard the counter-electrode with high energy. This can cause damage to the growing film and heat the substrate (Rossnagel, 1991). Triode sputtering is essentially just diode sputtering with a heated filament added to provide electrons to sustain the plasma independent of ion bombardment of the target (Parsons, 1991).

Most of the samples in this work were fabricated by magnetron sputtering. Magnetron sputtering is a further improvement on diode sputtering. It is accomplished by the addition of a radial magnetic field to the target. Typically, two cylindrical magnets of opposite polarity are arranged concentrically behind the planar circular cathode target such that the center of the target forms one pole and an annular ring on the edge of the target forms the second pole. Magnetic field lines emanate from the center of the target, run radially outward from the target center and reenter the target out its outer edge. In diode sputtering the electric field is necessarily perpendicular to the target surface and, therefore, also perpendicular to this radial magnetic field. Electrons in a crossed electric and magnetic field will drift perpendicular to both. Thus, in magnetron sputtering, the electrons are confined to drift in a closed loop close to the cathode surface. This serves to create a dense plasma close to the target which increases sputtering rates appreciably. Secondarily, the electrons are constrained near the cathode and bombard the growing film much less than in triode or conventional diode sputtering (Rossnagel, 1991). A schematic diagram of a sputtering chamber is shown in Figure II.4.

The microstructure of sputtered films is largely a function of the adatom mobility and the adatom mobility is strongly influenced by the substrate temperature and by particle bombardment (Parsons, 1991). Varying the sputtering parameters can change the film microstructure. A study of the effects of sputtering parameters on film morphology is not a part of this work but it is noted here that the use of triode sputtering for the Fe target and the use of magnetron sputtering for the other targets may be an important influence on the structures of the films studied here and the structural differences between them.

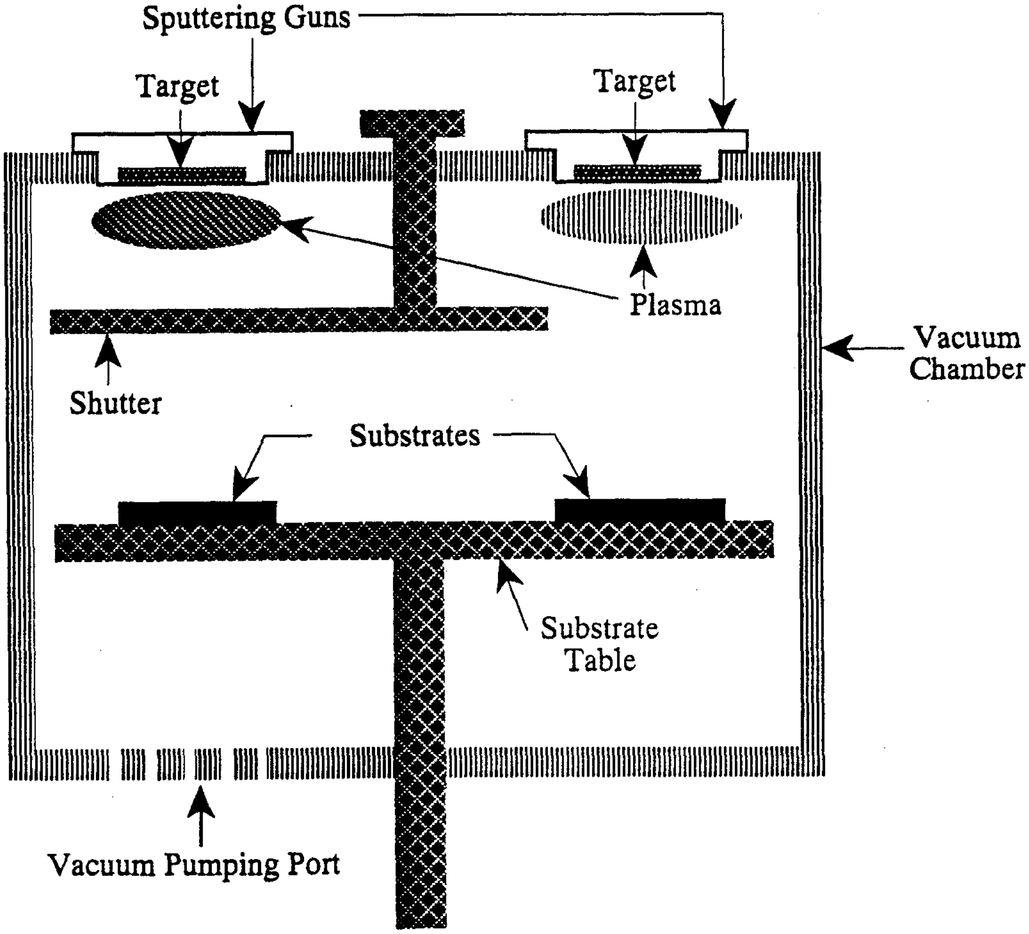

Figure II.4 Schematic diagram of a sputtering chamber.

2.4 SAMPLE PREPARATION

All the sputtered a-M_xGe_{100-x} samples examined in this dissertation were fabricated in the Vapor Phase Synthesis Laboratory of the Center for Materials Research at Stanford University. The a-Mo_xGe_{100-x} films and the a-Fe_xGe_{100-x} films used in this study are the same samples studied by and fabricated by Kortright and Lorentz, respectively. Their fabrication techniques have already been described in detail elsewhere (Kortright, 1984 & 1988; Lorentz, 1986 & 1994) but are summarized here along with the fabrication methods for the a-W_xGe_{100-x} samples.

(a) Substrates:

All of the a-Mo_xGe_{100-x} samples, all of the a-Fe_xGe_{100-x} samples, and some of the a-W_xGe_{100-x} samples were deposited on substrates of 0.001 inch thick Kapton. Kapton is an amorphous polyimide film produced by DuPont. Kortright erroneously identified his substrates (1984, 1988) as being 0.003 inch thick Kapton. They are, in fact, 0.001 inch thick Kapton. The remainder of the a-W_xGe_{100-x} samples were deposited on Si wafers for later removal as free-standing films. These were high purity, boron doped, p-type Si (100) wafers of 0.015 inch thickness and 3 inch diameter, with 20 to 30 ohm-cm resistance.

All the substrates were cleaned prior to deposition. The Kapton substrates for the a-Mo_xGe_{100-x} samples were rinsed in isopropyl alcohol, cleaned in trichloroethyne vapor, and dried with a hot air gun. The Kapton substrates for the a-Fe_xGe_{100-x} and a-W_xGe_{100-x} samples were cleaned in an RBS 35 wash, rinsed in deionized water, and dried with N_2 gas.

The Si wafers were cleaned in Stanford University's Center for Integrated Systems Laboratory following the standard cleaning procedure for integrated circuits. This entailed soaking the wafers for 20 minutes in 9:1 H_2SO_4:H_2O_2 held at 120° C, soaking for 10 minutes in 4:1 H_2SO_4:H_2O_2 at 90° C, soaking for 10 minutes in 5:1:1

$HCl:H_2O_2:H_2O$ at 70° C, soaking for 10 minutes in 5:1:1 $NH_4OH:H_2O_2:H_2O$ at 70° C, and soaking for 30 seconds in 50:1 $H_2O:HF$. The wafers were rinsed for 6 minutes in deionized water after each soak and were spun dry at the end of the entire cleaning procedure.

(b) Targets:

All the samples were made by cosputtering from individual targets of high purity Ge (99.999 % pure) and a high purity metal (typically 99.9% to 99.99% pure) in an argon atmosphere. For the free-standing a-W_xGe_{100-x} films, a 1 μm thick carbon layer was deposited between the substrate and the film and also on top of the film to shield it from the etching procedure that rendered the films free-standing.

All the targets were 1/8 inch thick. For the a-Mo_xGe_{100-x} and the a-Fe_xGe_{100-x} samples the targets were 2 inches in diameter. For the a-W_xGe_{100-x} samples some of the targets were 2 inches in diameter while others were 3 inches in diameter. The carbon target was 1/8 inch thick and 6 inches in diameter. The targets were attached to the sputtering guns with a conducting paste of silver flake in vacuum grease. The sputtering guns were electrically powered and water cooled.

(c) Sputtering:

In all cases the base pressure in the sputtering chamber was less than 2×10^{-6} Torr. The pressure of the argon sputtering gas was held between 2×10^{-3} and 4.5×10^{-3} Torr. The substrates were affixed to a rotating table. A shutter between the samples and the targets could be opened or closed to expose the substrates to or shield them from the targets. The targets were sputter cleaned for more than ten minutes, in all cases, with the shutter closed so that the substrates were not contaminated. The compositions of the films were controlled by varying the electrical power to the guns. The Mo, W, and Ge targets were magnetron sputtered with a magnet behind the target to confine the argon plasma to the vicinity of the target. The Fe target was triode sputtered because the Fe atoms are ferromagnetic.

In all cases, the metal target was run with dc power while the Ge target was rf powered with the rest of the chamber at ground. The source-to-substrate distance was between 3 inches and 4 1/2 inches in all runs. The substrates were not heat-sunk in any of the sputtering runs. In each run the table was warm to the touch after deposition.

The a-Mo_xGe_{100-x} samples were made in a sputter-down geometry with the Mo and Ge targets on the ceiling of the sputtering chamber and the substrates on the table below the targets. For these samples the targets were tilted in toward the central axis of the chamber by 12.5 degrees. A substrate of 0.001 inch thick Kapton was affixed to the center of the table with a 4 1/2 inch diameter copper gasket. The Mo target was run at less than 0.55 Amps while the Ge target was run at less than 350 Watts. The table rotation speed for the a-Mo_xGe_{100-x} samples was constant at 10 revolutions per second. With a growth rate of 4-8 Å/sec, it took about 1/2 sec to deposit a monolayer. Therefore, it took 5 revolutions of the table to deposit one monolayer and compositional layering was avoided.

The a-Fe_xGe_{100-x} samples were prepared in a sputter-up geometry with the targets at the bottom of the chamber and the substrates on the ceiling. The targets were not angled in towards the center of the table but were held parallel to the table. The substrates were placed directly over the center of the targets. The Kapton substrates were held to the table with 4 inch diameter copper gaskets. The Ge target was run at powers between 150 and 350 Watts while the Fe target was run at currents between 0.15 and 0.50 Amps. The table rotation speed was held constant at 5 revolutions per second. The average deposition rate of 1.2 Å/sec insured 10 revolutions per monolayer and, therefore, no compositional layering.

The a-W_xGe_{100-x} samples were made in a sputter-down geometry with the targets on the ceiling of the chamber and the substrates on the table below. The targets were not angled in toward the center of the table but were parallel to the table. The substrates were placed directly under the center of the targets. Kapton substrates were held to the table with 4 inch diameter copper gaskets while the silicon substrates were held with double sticky tape. The Ge target was run at powers between 175 and 450 Watts. The W target was run at currents between 0.11 and 0.55 Amps. For the free-standing films the 6 inch diameter carbon target was run at 1.6 Amps. Since W peels away from most surfaces, a 100 Å layer of Ge was deposited on the carbon covered Si substrates as an adhesive layer between the sample and the substrate.

(d) Etching:

The a-W_xGe_{100-x} films that were deposited on Si were rendered free-standing by etching the Si in potassium hydroxide (KOH) (Wilson, 1990). A solution of 1.4:1.0 KOH:H_2O, using 45% IC grade KOH, was held at 80° C in a constant temperature water bath. Immersion of the samples in this solution for approximately four hours dissolved the Si leaving the a-W_xGe_{100-x} films intact. The free floating films were removed from the KOH solution and rinsed in deionized water.

2.5 PRELIMINARY CHARACTERIZATION

(a) Crystallinity:

Since the purpose of this work is to learn more about the structure of amorphous materials it is essential that all the samples studied here be truly amorphous and not crystallized or partially crystallized. Lorentz used continuous X-ray diffraction scans to checked all of his a-Fe_xGe_{100-x} samples for crystallinity (Lorentz, 1986). Those samples used here were clearly amorphous. The a-Mo_xGe_{100-x} samples used in this work were all studied by Kortright with anomalous wide angle X-ray scattering. His structure factors for these samples show that they are clearly amorphous (Kortright, 1984).

Since the a-Fe_xGe_{100-x} and the a-Mo_xGe_{100-x} samples were fabricated several years ago they were rechecked for evidence of crystallization. Not all twenty samples of Kortright and Lorentz were rechecked. Only a handful of samples from representative regions of the a-Fe_xGe_{100-x} and a-Mo_xGe_{100-x} systems were re-examined with wide angle X-ray scattering and Laue diffraction. None of these samples showed any evidence of crystallization and it was assumed that none of the other samples had degraded either. The a-W_xGe_{100-x} samples were all tested with wide angle X-ray scattering for evidence of crystallinity and all proved to be amorphous.

(b) Impurity concentrations:

In vapor deposited films, incorporation of small amounts of reactive residual gases, particularly oxygen and carbon, is inevitable. Sputtering in a an argon atmosphere will also, necessarily, incorporate argon atoms into the growing film. These noble gas atoms, however, will not react with the atoms of the growing film and their worst possible influence on the structure of the film will be the formation of argon bubbles.

Kortright (1984) extensively investigated the level of gas contamination in his a-Mo_xGe_{100-x} films. He was unable to detect any argon in his films with electron microprobe analysis. This indicates that argon contamination, if any, is present on the order of an atomic percent or less. To separate surface oxidation from oxidation of the bulk, Kortright continuously monitored the oxygen and carbon Auger lines while sputtering the film away (depth profiling). The intensities of the carbon and oxygen lines dropped by two orders of magnitude upon removal of several hundred Ångströms of film. From these weak Auger lines, Kortright placed an upper bound of about an atomic percent on the bulk oxygen and carbon contamination. The surface oxide layer was only several hundred Ångströms thick, which is small compared to the several micron thicknesses of the films.

Kortright's analysis showed that no significant gas contamination of growing films occurs in the sputtering process when the base pressure is less than 2 x 10^{-6} Torr and the argon pressure is 2 x 10^{-3} Torr. Grundy (1980) noted that the structure of evaporated, amorphous, single metal films was not influenced by varying the background pressure from 10^{-8} to 10^{-6} Torr. Grundy also noted that at these pressures occluded gases were present in the films at concentrations of approximately 0.04 to 1 atomic percent. This is consistent with Kortright's observations. In light of this information no extensive analysis of residual gas contamination was performed on the a-Fe_xGe_{100-x} or a-W_xGe_{100-x} samples since these films were fabricated under the same conditions as the a-Mo_xGe_{100-x} films.

Of greater concern than bulk contamination during film growth is the issue of oxidation over time since these same films have been used for structural investigations over a period of several years. One important data point in this regard is the visual appearance of the films. The films have remained shiny, silvery, and metallic looking over the course of their lifetimes. Wide angle X-ray scans on films from all three systems show no structural changes with time. Scans taken recently look no different than scans taken several years ago. That these films do not degrade with time is to be expected. Amorphous films, particularly metal-semiconductor films, are used as passivation layers because of their corrosion resistant properties (Brusic, MacInnes & Aboaf, 1978; Fehlner, 1978; Hashimoto, Naka, Noguchi, Asami & Masumoto, 1978).

(c) Sample metal concentration:

Any valid description of the structure of these films as a function of concentration requires an accurate knowledge of the sample composition. Kortright and Lorentz used electron microprobing techniques to determine the compositions of their films. Electron microprobing uses electrons to excite low energy fluorescence lines in a material. The spot size of the electron beam is small, typically 30 μm wide. Also the excited photons that are emitted from the sample come necessarily from atoms that are close to the surface, usually within a thousand Ångströms of the surface. Therefore, the electron microprobe technique samples a much smaller volume of the film than is actually illuminated by X-rays in any X-ray absorption or scattering measurement. Electron microprobe results also require a complex normalization program that accounts for both the fluorescence efficiency of individual atomic species and the subsequent absorption of the fluorescent photons in the material as a function of photon energy and sample composition as well as secondary fluorescences (Colby, 1971).

A more thorough evaluation of the sample composition is accomplished with X-ray absorption measurements that determine the absorption edge jump of each atomic species present in the sample (Wilson, 1990). This technique averages over the entire film as opposed to sampling a microscopic volume near the surface.

Sample absorption due to a particular atomic species is determined by comparing the intensity of the X-ray beam incident upon the sample to that transmitted through the sample as a function of energy across an absorption edge of that particular species. The transmitted intensity is related to the incident intensity through the equation

$$I_t = I_0 R(E) \exp\left\{-\left[\sum_{\alpha} \mu_\alpha(E) t\right]\right\} \tag{2.1}$$

where I_t is the transmitted intensity, I_0 is the incident intensity, $R(E)$ is the detector response function, μ_α is the absorption coefficient of the atomic species α, and is summed over all species in the path of the X-ray beam, E is the incident photon energy, and t is the thickness of the film. The detector response is a slowly varying function of energy as are the absorption coefficients of all atoms that do not have an absorption edge near the edge being scanned. The natural logarithm of the ratio of the incident intensity to the transmitted intensity then gives the absorption coefficient times the sample thickness, $\mu_a t$, for the atom of interest, plus a background function, $B(E)$, that includes the logarithm of the detector response function and the absorption coefficients of the other atoms. In equation form:

$$\ln(I_0/I_t) = \mu_a t + B(E) \tag{2.2}$$

where

$$B(E) = \ln[R(E)] + \sum_{\alpha \neq a} \mu_\alpha t \tag{2.3}$$

The subscript a refers to the atomic species whose absorption edge is scanned in the data set. The subscript α refers to any atomic species.

The absorption coefficient, μ, can be expressed as the absorption cross-section, σ, times the atomic density, ρ:

$$\mu_a = \rho_a \sigma_a. \tag{2.4}$$

The atomic density, ρ_a, divided by the atomic weight, w_a, and multiplied by Avagadro's number, A, gives the number density, N_a, or number of a atoms per unit volume. So,

$$\mu_a = (w_a/A) N_a \sigma_a. \tag{2.5}$$

The absorption cross-section is related to the imaginary part of the scattering factor, f'', through the optical theorem:

$$\sigma_a = (2e^2 h / mcE) f'' \tag{2.6}$$

where e is the electron charge, h is Plank's constant, m is the electron mass, and c is the speed of light.

Now,

$$\ln(I_0/I_t) = [(w_a/A)(2e^2 h / mcE) f'']N_a t + B(E). \tag{2.7}$$

Cromer & Liberman's (1970) theoretical calculations for the free atom values of f'' can be used to extract $N_a t$, the number density of a atoms times the film thickness, from the data. This is accomplished by fitting the sum of the theoretical f'' values and a polynomial in $(1/E)$, representing the background function, to the data. The fit excludes the data right near the absorption edge that is influenced by interatomic interactions. The scaling factor that relates the theoretical values of f'' to the data is the number density times the thickness, $N_a t$. (Wilson, 1990).

The same procedure applied to the absorption edge of the other atomic species, b, in the film yields $N_b t$, the value of the number density of b atoms times the film thickness. Simple arithmetic now gives the atomic concentration, χ, of either species:

$$\chi_a = [N_a t/(N_a t + N_b t)]. \qquad (2.8)$$

This technique of identifying sample composition was applied to all twenty-six samples used in the ASAXS experiments. Absorption data were collected on beam line 4-1 at the Stanford Synchrotron Radiation Laboratory. Each sample was held normal to the beam and the X-ray intensity both before and after the sample was measured with an ionization chamber while the incident X-ray beam was scanned in energy with a silicon double crystal monochromator. The incident X-ray energy was scanned through an accessible absorption edge of each material in each film. This means that the Ge *K* absorption edge was scanned in each sample as was either the Fe K absorption edge, the Mo *K* absorption edge, or the W *L* absorption edges, depending on the film. Si (111) crystals were used to monochromatize the beam for scans through the Fe, Ge, and W absorption edges. Si (220) crystals were used to monochromatize the beam to scan the Mo absorption edge.

The sample concentrations, in atomic percent metal, for the a-Fe_xGe_{100-x}, a-Mo_xGe_{100-x}, and the a-W_xGe_{100-x} samples are given in Tables II.5, II.6, and II.7, respectively. Lorentz's and Kortright's values for the metal atomic percents as determined by electron microprobe are also given in the tables. Lorentz's values coincide well with the values obtained from the absorption method. There is a greater spread between the microprobe results of Kortright and the absorption results. This is a function of sample preparation and available sample.

Lorentz's samples were fabricated with the targets parallel to the substrates so that the samples passed first over one target and then over the next. Lorentz's samples were

TABLE II.5

Iron content of a-Fe_xGe_{100-x} samples as determined by electron microprobe and X-ray absorption measurements.

Sputtering Run Number (from Lorentz)	Atomic % Metal Electron Microprobe Results (from Lorentz)	Atomic % Metal X-ray Absorption Results
82-143	0	0
83-591	5	4.75
83-501	12	11.62
82-729	18	18.16
83-602	20	18.69
83-502	27	24.43
83-505	30	27.54
83-503	33	34.11
83-601	37	36.54
83-593	44	44.11
83-599	49	49.43
83-600	65	65.06
83-598	72	71.06

TABLE II.6

Molybdenum content of a-Mo_xGe_{100-x} samples as determined by electron microprobe and X-ray absorption measurements.

Sputtering Run Number (from Kortright)	Atomic % Metal Electron Microprobe Results (from Kortright)	Atomic % Metal X-ray Absorption Results
82-640	2	2.51
82-639	4	5.56
82-533	8	14.03
82-539	14	13.31
82-011	25	31.67
81-583	42	38.51
82-643	65	72.41

TABLE II.7

Tungsten content of a-W_xGe_{100-x} samples as determined by sputtering rates, electron microprobe, and X-ray absorption measurements.

Sputtering Run Number	Atomic % Metal Sputtering Rate /Electron Microprobe Results	Atomic % Metal X-ray Absorption Results
86-013	8 / 7	7.44
86-014	10 / 8	8.39
87-045	20/17	17.37
87-055	40 / 38	44.66
89-008	41 / 51	50.20
87-056	55 / 58	77.87

lined up along one circle that passed directly over each target. All samples from one sputtering run were thus identical. In Kortright's setup the sputtering targets were angled in towards the center of the substrate table. Kortright had a large substrate at the center of the table surrounded by smaller substrates. The samples from one sputtering run were therefore not all identical. Many of the a-Mo_xGe_{100-x} samples studied here were taken from Kortright's smaller substrates, whereas Kortright studied samples taken from the larger substrates. Thus, the absorption results obtained here are valid for exactly the samples studied here and in no way invalidate Kortright's results.

The compositions of the a-W_xGe_{100-x}samples as determined by microprobing and as predicted from sputtering rates are also given in Table II.7. The microprobe results and the absorption results are very close with the exception of two samples, 87-055 and 87-056. These samples and sample 87-045 were prepared as free-standing filmsso, as stated above, there was a 100 Å a-Ge layer between the film and the substrate. Apparently, the microprobe measurements for samples 87-055 and 87-056 were performed on the side of the free-standing film with the a-Ge layer. This illustrates the difficulties inherent in the small sampling volume accessible to microprobing.

Since the absorption results are the most appropriate for the samples studied here, the compositions quoted will be those determined from X-ray absorption measurements, rounded to the nearest atomic percent.

(d) Sample thickness:

Knowledge of the sample thicknesses is essential for normalizing the ASAXS data. The X-ray absorption method used above to determine the samples' compositions yields $N_\alpha t$, the product of the number density and the thickness. Values for the thicknesses of the films have been extracted from the $N_\alpha t$ product by assuming a value for N_α, and dividing. The choice of values for the number densities is somewhat arbitrary. The N_α for the amorphous films were takento be 95 percent of the N_α values for the crystalline material of identical composition taking into account the phase separation in the crystalline material and the volume fractions occupied by the different phases. N_α values for the crystalline components of the Fe-Ge, Mo-Ge, and W-Ge systems are displayed in Tables II.8 and II.9.

The most stable phase of the polymorphic compounds was chosen in calculating the N_α for the amorphous samples. For example, the cubic Cu_3Au-like phase of Fe_3Ge was chosen over the other Fe_3Ge phases. The most stable end products of phase separation that appear in the Mo-Ge equilibrium phase diagram were used in calculating the number densities of the a-Mo_xGe_{100-x} samples. These are Ge, the orthorhombic form of $MoGe_2$, $Mo_{13}Ge_{23}$, Mo_5Ge_3, Mo_3Ge, and Mo. In calculating the number densities for the a-Fe_xGe_{100-x} samples, only Ge, $FeGe_2$, and Fe_3Ge were used as end products of phase separation. This choice is based on the implications of Lorentz's XANES and SAXS results. For the a-W_xGe_{100-x} system the metastable compounds, WGe_2 and W_5Ge_3, as well as Ge and W were used as end products of phase separation. Inclusion of the metastable W-Ge compounds as end products of phase separation was prompted by implications of the ASAXS data which will be discussed in later chapters.

As an example, the a-$Fe_{12}Ge_{88}$ sample has a 12 atomic percent Fe analog in the crystalline system that is phase separated into Ge and $FeGe_2$. In this crystalline sample, $FeGe_2$ occupies 26 percent of the sample volume and Ge occupies the other 74 percent of the volume. The average number density of Ge atoms in this sample is 0.74 times the number density of Ge atoms in pure Ge plus 0.26 times the number density of Ge atoms in $FeGe_2$. Ninety-five percent of the resultant average Ge number density for c-$Fe_{12}Ge_{88}$ was taken as the Ge number density for the a-$Fe_{12}Ge_{88}$ sample. The $N_{Ge}t$ value obtained from the Ge edge X-ray absorption measurement of a-$Fe_{12}Ge_{88}$ was then divided by this theoretical value of N_{Ge} to get t, the thickness of the film. A similar calculation was performed at the Fe edge.

TABLE II.8

Total number densities, Ge number densities, and metal (M) number densities of crystalline compounds in the Fe-Ge system. *N* is the number of atoms and *V* is the volume in Å^3.

Crystalline Compound	Crystalline Structure	N_{total}/V (Å^{-3})	N_{Ge}/V (Å^{-3})	N_M/V (Å^{-3})
Ge	diamond cubic	0.04417	0.04417	0
$FeGe_2$	tetrag. ($CuAl_2$)	0.06936	0.04624	0.02312
FeGe	monocl. (CoGe)	0.07151	0.03575	0.03575
FeGe	hex. (CoSn)	0.06932	0.03466	0.03466
FeGe	cubic (FeSi)	0.7759	0.03880	0.03880
Fe_6Ge_5	monocl. (Fe_6Ge_5)	0.07681	0.03491	0.04189
Fe_5Ge_3	hex. ($InNi_2$)	0.08534	0.03200	0.05334
Fe_3Ge	cubic (Cu_3Au)	0.08125	0.02031	0.06094
Fe_3Ge	cubic (F_3Bi)	0.08416	0.02104	0.06312
Fe_3Ge	hex. (Ni_3Sn)	0.08189	0.02047	0.06142
Fe	bbc	0.08493	0	0.08492

TABLE II.9

Total number densities, Ge number densities, and metal (M) number densities of crystalline compounds in the Mo-Ge, and W-Ge systems. N is the number of atoms and V is the volume in Å^3.

Crystalline Compound	Crystalline Structure	N_{total}/V (Å^{-3})	N_{Ge}/V (Å^{-3})	N_M/V (Å^{-3})
Ge	diamond cubic	0.04417	0.04417	0
$MoGe_2$	orthorh. ($SiCo_2$)	0.06388	0.04258	0.02129
$MoGe_2$	tetrag. ($MoSi_2$)	0.06615	0.04410	0.02205
$Mo_{13}Ge_{23}$	tetr. ($Mo_{13}Ge_{23}$)	0.06316	0.04035	0.02281
Mo_5Ge_3	tetrag. (Sn_5Si_3)	0.06650	0.02494	0.04156
Mo_3Ge	cubic (Cr_3Si)	0.06668	0.01667	0.05001
Mo	bcc	0.06416	0	0.06416
WGe_2	orthorh. ($SiCo_2$)	0.06371	0.04247	0.02124
WGe_2	tetrag. ($MoSi_2$)	0.06645	0.04430	0.02215
W_5Ge_3	tetrag. (Cr_5B_3)	0.06990	0.02621	0.04369
W_5Ge_3	tetrag. (W_5Si_3)	0.06772	0.02540	0.04233
W	bcc	0.06309	0	0.06309

Results of such calculations performed at both the metal edge and the Ge edge for each sample are listed in Tables II.10, II.11, and II.12. In most cases, the thicknesses obtained from the metal edge absorption data and those obtained from the Ge edge absorption data differ by less than three percent. Exceptions to this are the two lowest metal concentration samples from each system: a-Fe_5Ge_{95}, a-$Fe_{12}Ge_{88}$, a-Mo_3Ge_{97}, a-Mo_6Ge_{94}, a-W_7Ge_{93}, and a-W_8Ge_{92}, with thickness discrepancies ranging from 4 to 17 percent. These discrepancies are due less to the poorer quality of the absorption data for the dilute element than to magnification of errors for the dilute element by division of the experimentally determined $N_\alpha t$ value by a very small theoretical N_α. To compensate for this, the two values of the thickness for each sample were weighted by the respective atomic percents and added to yield the thickness value used for normalization of the ASAXS data.

Lorentz's values for the thicknesses of the a-Fe_xGe_{100-x} films are included in Table II.9 for reference. He obtained his values by a combination of 1) direct measurement with a mechanical profilimeter (Alpha-step 100 model, Tencor Inst., Mountain View, CA) of the thicknesses of films deposited on glass slides and 2) thickness calculations based on the absorption edge jump, McMaster's values for absorption (McMaster, Kerr DelGrande, Mallett & Hubbell, 1969), and least squares fitting to crystalline densities. In most cases Lorentz's values are close to the values determined by the absorption method used here. The exception to this is the pure a-Ge sample. Lorentz's value for the thickness of this sample is, for unknown reasons, almost twice as large as the value obtained here. The thickness values used here are presumed to be more relevant to this study than Lorentz's values because they were determined by measurements of the exact slices of sample that were used in the ASAXS experiments.

TABLE II.10

Thicknesses of *a*-Fe_xGe_{100-x} films as determined from Ge edge and Fe edge absorption data and the thicknesses used in this dissertation. Lorentz's values are included for reference.

Sample Atomic % Fe	Thickness (μm) from Lorentz	Thickness (μm) Ge Absorption	Thickness (μm) Fe Absorption	Thickness (μm) Used
0	1.19	0.67		0.67
5	2.14	1.58	1.51	1.58
12	0.87	1.00	0.96	1.00
18	0.34	0.38	0.38	0.38
19	0.83	0.90	0.89	0.90
24	0.91	1.14	1.17	1.15
28	0.14	0.17	0.17	0.17
34	1.25	1.10	1.11	1.10
37	0.95	0.96	0.95	0.96
44	1.41	1.38	1.38	1.38
49	0.94	0.74	0.75	0.74
65	1.02	1.02	1.02	1.02
71	2.67	2.74	2.74	2.74

TABLE II.11

Thicknesses of a-Mo_xGe_{100-x} films as determined from Ge edge and Mo edge absorption measurements and the thicknesses used in this dissertation.

Sample Atomic % Mo	Thickness (μm) Ge Absorption	Thickness (μm) Mo Absorption	Thickness (μm) Used
3	2.10	1.75	2.09
6	2.14	1.97	2.13
13	4.81	4.94	4.83
14	1.99	1.99	1.99
32	8.16	8.04	8.12
39	6.61	6.48	6.56
72	5.28	5.38	5.35

TABLE II.12

Thicknesses of a-W_xGe_{100-x} films as determined from Ge edge and W edge absorption measurements and the thicknesses used in this dissertation.

Sample Atomic % W	Thickness (μm) Ge Absorption	Thickness (μm) W Absorption	Thickness (μm) Used
7	2.89	3.08	2.90
8	3.31	3.47	3.32
17	6.33	6.47	6.35
45	5.52	5.43	5.48
50	1.03	1.04	1.04
78	4.12	4.07	4.08

REFERENCES FOR CHAPTER II

Agoshkov, V. M., Gorbatenkov, V. D., Popova, S. V. & Fomicheva, L. N., *Neorganicheskie Materialy* **17**, Izvestiya Academii Nauk SSSR (1981) 2044.

Brewer, L. & Lamoreaux, R. H., *Atomic Energy Rev., Special Issue No.* **7**, Internat. Atomic Energy Agency, Vienna (1980) 253.

Brusic, V., MacInnes, R. D. & Aboaf, J., In *Passivity of Metals, Proc. 4th Int. Symp. on Passivity, 1977,* edited by R. P. Frankenthal & J. Kruger, The Electrochemical Society, Inc., Princeton, NJ (1978) 170.

Colby, J. W., In *Proc. 6th Nat. Conf. on Electron Microprobe Analysis*, Electron Probe Analysis Society of America, Pittsburgh, PA (1971) 17A.

Cromer, D. T. & Liberman, D., *J. Chem. Phys.* **53** (1970) 1891.

Elliott, R. P., *Constitution of Binary Alloys, 1st Supplement*, McGraw-Hill Book Co., New York (1965).

Fehlner, F. P., In *Passivity of Metals, Proc. 4th Int. Symp. on Passivity, 1977,* edited by R. P. Frankenthal & J. Kruger, The Electrochemical Society, Inc., Princeton, NJ (1978) 181.

Grundy, P. J., *J. Magn. & Magn. Mat.* **21** (1980) 1.

Hansen, M., *Constitution of Binary Alloys, 2nd Edition*, McGraw-Hill Book Co., New York (1958).

Hashimoto, K., Naka, M., Noguchi, J., Asami, K. & Masumoto, T., In *Passivity of Metals, Proc. 4th Int. Symp. on Passivity, 1977,* edited by R. P. Frankenthal & J. Kruger, The Electrochemical Society, Inc., Princeton, NJ (1978) 156.

Kortright, J. B., Ph.D. thesis, Stanford University (1984).

Kortright, J. B. & Bienenstock, A., *Phys. Rev. B* **37** (1988) 2979.

Kubaschewski, O., *Iron– Binary Phase Diagrams*, Springer-Verlag, Berlin (1982) 43.

Lorentz, R. D., Ph.D. thesis, Stanford University (1986).

Lorentz, R. D., Bienenstock, A. & Morrison, T. I., to appear in *Phys. Rev. B* (1994).

McMaster, W. H., Kerr DelGrande, N., Mallett, J. H. & Hubbell, J. H., National Bureau of Standards, *Compilation of X-Ray Cross Sections,* Lawrence Livermore Laboratory, CA and US Dept. of Commerce, NTIS, Springfield, VA (1969).

Moffatt, W. G., *The Handbook of Binary Phase Diagrams*, Genium Publishing Corp., Schenectady (1984).

Nowotny, H., Benesovsky, F. & Brukl, C., *Monatsh. Chem.* **92** [In German] (1961) 365.

Parsons, R., In *Thin Film Processes II*, edited by J. L. Vossen & W. Kern, Academic Press, Inc., San Diego (1991) 177.

Pauling, L., *The Nature of the Chemical Bond and the Structure of Molecules and Crystals: An Introduction to Modern Structural Chemistry,* 3rd Edition, Cornell University Press, Ithaca (1960).

Popova, S. V. & Fomicheva, L. N., *Neorganicheskie Materialy* **14,** Izvestiya Academii Nauk SSSR (1978) 684.

Povarova, K. B. & Savitskii, E. M., In *Phase Diagrams of Metallic Systems* [in Russian], Nauka, Moscow (1971) 95.

Rossnagel, S. M., In *Thin Film Processes II*, edited by J. L. Vossen & W. Kern, Academic Press, Inc., San Diego (1991) 11.

Shunk, E. A., *Constitution of Binary Alloys, 2nd Supplement*, McGraw-Hill Book Co., New York (1969).

Villars, P. & Calvert, L. D., *Pearson's Handbook of Crystallographic Data for Intermetallic Phases*, 2nd Edition, ASM International Materials Park, OH (1991).

Wilson, L. C., Ph.D. thesis, Stanford University (1990).

CHAPTER III

ACQUISITION OF ANOMALOUS SMALL ANGLE X-RAY SCATTERING DATA

3.1 ASAXS EXPERIMENTS PERFORMED FOR THIS WORK

Three sets of ASAXS experiments were performed for this dissertation. The first set was a series of feasibility experiments performed on beam line 4-2 at the Stanford Synchrotron Radiation Laboratory (SSRL) in February of 1989. In the feasibility experiments, ASAXS data were collected at three energies beneath the germanium absorption edge of *a*-$Fe_{12}Ge_{88}$, *a*-W_8Ge_{92}, and *a*-$Mo_{14}Ge_{86}$ and at three energies beneath the metal absorption edges of *a*-$Fe_{12}Ge_{88}$, and *a*-W_8Ge_{92} to see if any new information could be obtained from the application of this technique to these samples. Positive results from these experiments spurred two subsequent data collection efforts. These consisted of an experimental run on the Oak Ridge National Laboratory beam line X14A at the National Synchrotron Light Source (NSLS) at Brookhaven in December of 1989 and another experimental run on beam line 4-2 at SSRL in August of 1991.

All of these experiments were performed using the SSRL Biotechnology Resource's SAXS camera equipped with a position sensitive detector (Rice & Wakatsuki, 1991; Wakatsuki et al., 1992). A linear position sensitive proportional counter was used for all the experiments performed at SSRL while a position sensitive quadrant detector was used for the experiments performed at NSLS. SAXS patterns were collected on all twenty-six samples described in Chapter II. These include twelve *a*-Fe_xGe_{100-x} samples with x equal to 5, 12, 18, 19, 24, 28, 34, 37, 44, 49, 65, and 71, seven *a*-Mo_xGe_{100-x} samples with x equal to 3, 6, 13, 14, 32, 39, and 72, six *a*-W_xGe_{100-x} samples with x equal to 7, 8, 17, 45, 50 , and 78, and pure *a*-Ge.

Data were collected at 200, 100, 30, 20, and 10 eV below the Ge K absorption edge (11103 eV) of every sample. Data were also collected at 200, 100, 30, 20, and 10 eV below the Fe K absorption edge (7112 eV) of each a-Fe_xGe_{100-x} sample and at 200, 100, 30, 20, and 10 eV below the W L_{III} absorption edge (10204 eV) of each a-W_xGe_{100-x} sample. Attempts to collect data near the Mo K absorption edge (19999 eV) were unsuccessful because the argon gas in the position sensitive proportional counters was more efficiently ionized by fluorescent X-rays from the Ge in the a-Mo_xGe_{100-x} samples than by the elastically scattered X-rays.

3.2 BEAM LINE OPTICS

Beam line X14A at NSLS is a bending magnet beam line with a constant offset monochromator that both monochromatizes and horizontally focuses the X-ray beam (Habenschuss, Ice, Sparks & Neiser, 1988). Focusing of the vertical divergence is accomplished with a variable magnification, platinum coated, cylindrical mirror (Ice & Sparks, 1988). The vertical focal point can be placed anywhere from in front of the sample to infinity. The double crystal monochromator is composed of two Si (111) crystals. The first crystal is flat. The second is conically bent with the apex of the cone pointing toward the synchrotron source. This second crystal focuses the horizontal divergence of the beam without altering the vertical divergence. The second crystal provides the monochromator with variable magnification and sets the location of the horizontal beam focus.

In these experiments the beam was focused on the sample. Ideally, with a perfect focus, the best angular resolution is obtained with the beam focused at the detector. In practice, the best angular resolution is often obtained with the focal point located upstream of the detector (Stephenson, 1982). No systematic study of angular resolution versus focal point was undertaken as part of this work. Since the beam at NSLS was already well focused at the sample position and moving the focal point to the location of the detector would have consumed many hours, with possibly only a marginal increase in angular resolution, no refocusing was attempted.

The size of the beam on X14A is 1 mm vertical by 1.5 mm horizontal. The energy resolution of this beam line is 3.5 eV at 10 keV (Ice & Sparks, 1989). During these experiments, NSLS was run at an energy of 2.5 GeV with a current ranging from 50 to 200 mA.

Beam line 4-2 at SSRL is an 8-pole wiggler beam line. A platinum coated toroidal focusing mirror with unit magnification controls both the vertical and the horizontal divergence of the beam. For these experiments the location of the X-ray focus was at the SAXS detector for energies below 10.5 keV. Since platinum has an absorption edge at 10.5 keV, the flux from the mirror is greatly reduced for energies at and above 10.5 keV. Flux from the mirror was increased at the Ge edge by defocusing the mirror. Mirror cut-off was not a problem at NSLS, and for all of the data collected there the beam was focused at the sample.

On beam line 4-2, the double crystal monochromator holds two flat crystals parallel to each other. The exit height of the beam is, therefore, a function of the energy selected by the crystals. Si (111) crystals were chosen as the monochromatizing elements. The beam size is 2 mm vertical by 20 mm horizontal. The energy resolution of this beam line is approximately 5 x 10^{-4}. During these experiments, SSRL was run at an energy of 3.0 GeV with a current ranging from 30 to 100 mA.

3.3 OVERVIEW OF THE SAXS CAMERA

(a) Basic scattering geometry:

All the ASAXS experiments described here were performed with the SSRL Biotechnology Resource's SAXS camera configured in the geometry shown in Figure III.1. In this geometry, a finely collimated, monochromatic, X-ray beam, traveling in the horizontal plane, strikes a thin film sample held normal to the beam. Upon impact with the sample, the X-ray beam is scattered in all directions. The scattered beam is intercepted by a position sensitive detector held normal to the transmitted (and incident) beam. The detector

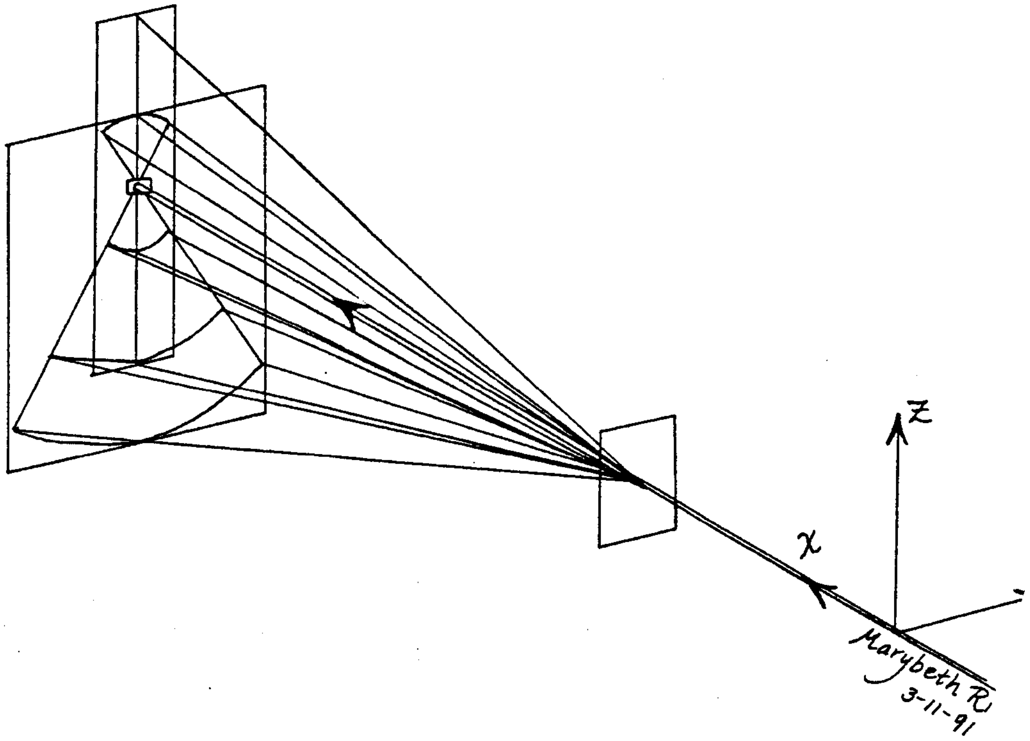

FIGURE III.1 The basic scattering geometry for the ASAXS experiments. beam, traveling in the *x* direction, strikes a thin film sample held perpendic sample scatters the X-ray beam in all directions. The scattered beam is linear or a quadrant detector positioned parallel to the sample and normal beam. The transmitted beam, marked by the arrow, impinges on the beam is positioned such that its longest axis coincides with the vertical. Thus, the linear detector collects data along a line perpendicular to the horizontal plane while the quadrant detector collects data within a sector of a circle that is normal to the transmitted beam. The solid angle of radiation that is subtended by the detector is determined by the sample to detector distance. The greater the distance, the smaller the solid angle. The transmitted beam is prevented from hitting the detector by a beam stop. The detector is held stationary during data collection and the entire scattering pattern is collected by counting in time.

(b) Basic components of the SAXS camera:

The essential components of the SAXS camera are: 1) a set of defining slits for determining the beam size, 2) a detector for measuring the incident beam intensity, 3) a set of guard slits for cutting the parasitic scattering from the defining slits, 4) a holder for the sample, 5) a detector for measuring the intensity of the transmitted beam, 6) a variable length scattering path, 7) a beam stop to prevent the transmitted beam from striking the SAXS detector, and 8) a position sensitive detector for collecting the SAXS pattern.

Since this SAXS camera was in various stages of development during these experiments, the details of the data collection scheme varied from experiment to experiment. The eight components mentioned above, however, were always present in some form. A drawing of the SAXS camera in a configuration similar to the one used for the experiments at NSLS is shown in Figure III.2. The optical path for both the NSLS and the SSRL experiments is displayed in Figure III.3.

3.4 DETECTORS

(a) Measurement of the incident beam intensity:

The intensity of the X-ray beam incident on the sample was continuously measured in all the ASAXS experiments described here. During the feasibility experiments, the

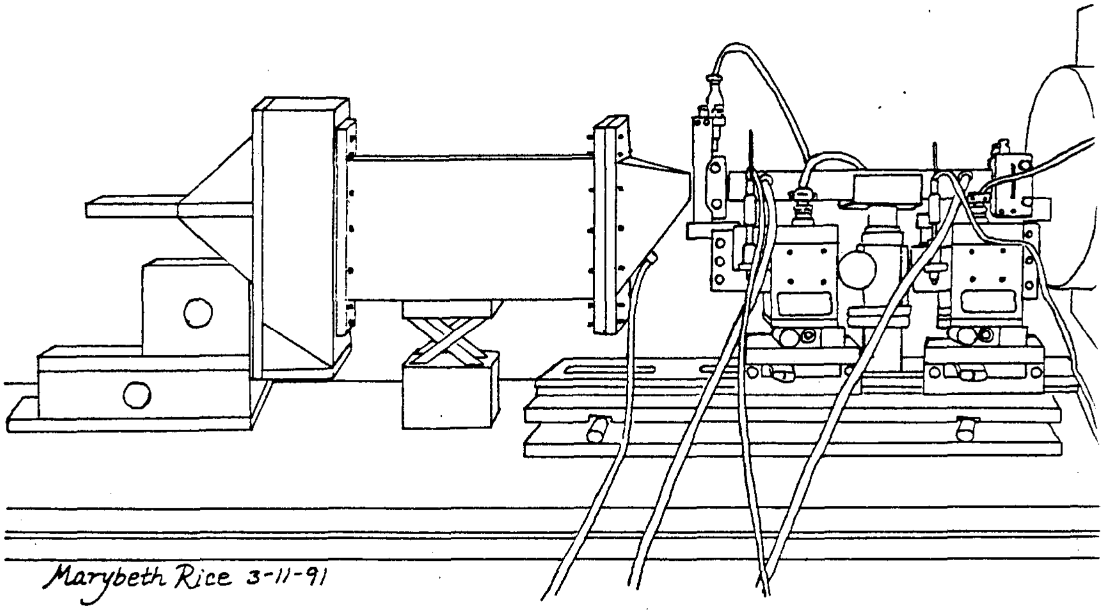

Marybeth Rice 3-11-91

FIGURE III.2 A drawing of the SAXS camera in a configuration similar to the one used at NSLS. Mounted on an optical rail are, from right to left, the defining slits on a y-z translation stage, the ionization chamber on its holder, and the guard slits on another y-z translation stage (y, z directions as defined in Figure III.1). To the left of the optical rail are the helium pathway and the quadrant detector on its holder. In this configuration, the sample was taped to the downstream side of the guard slits.

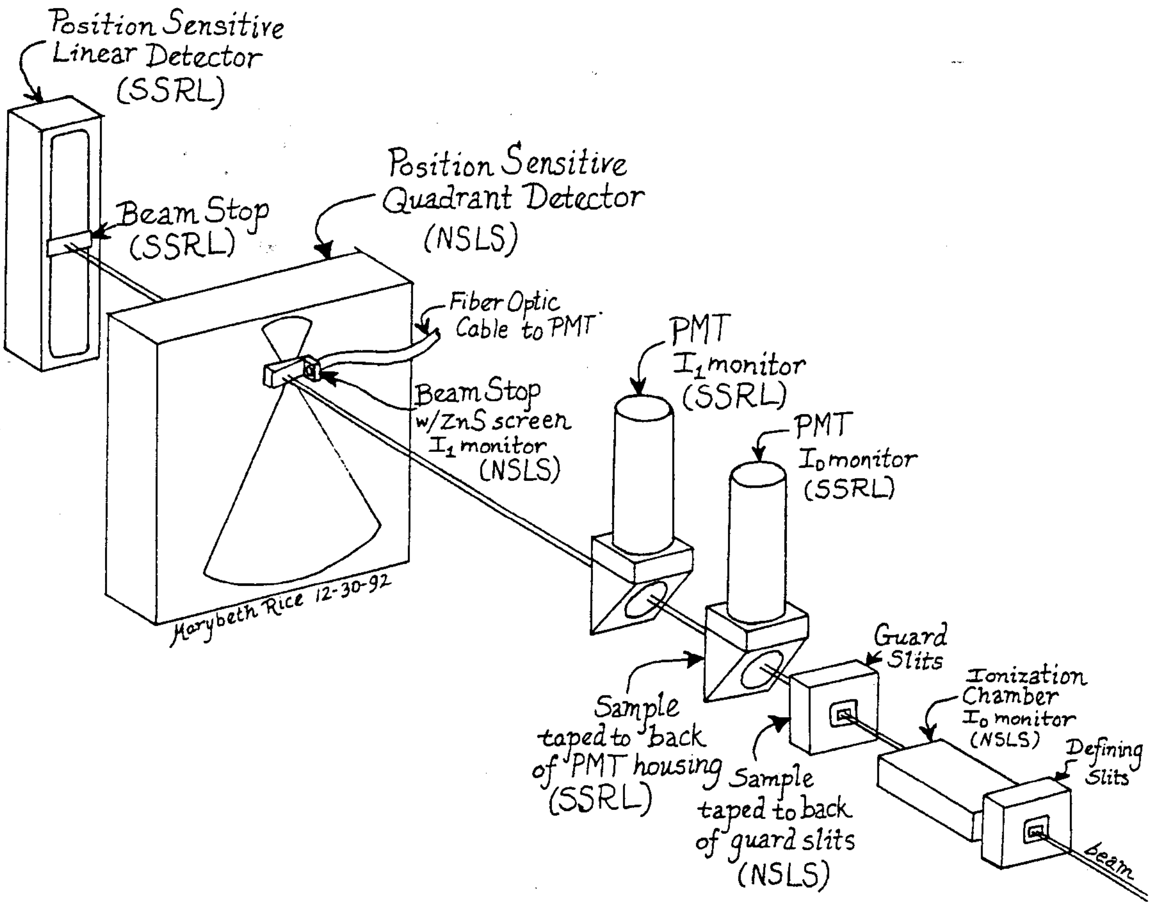

FIGURE III.3 The relative placement of the essential components of the SAXS camera for the ASAXS experiments at NSLS and at SSRL. Shown here are the incident beam, the defining slits, the guard slits, the incident intensity (I_0) monitor, the location of the sample, the transmitted intensity (I_1) monitor, the beam stop, and the position sensitve detector for both sets of experiments. This figure minus the linear detector and the PMT's (photomultiplier tubes) shows the experimental setup at NSLS. This figure minus the ionization chamber and the quadrant detector with its ZnS beamstop shows the experimental setup at SSRL.

incident intensity monitor was a 30 cm long ionization chamber filled with 80 % helium-20 % nitrogen gas. During the experiments at NSLS, the incident intensity was monitored with a 13.6 cm long nitrogen filled ionization chamber. The incident intensity monitor for the second set of experiments performed at SSRL was a photomultiplier tube held perpendicular to the incident beam. A sheet of polypropylene film placed in the beam at a 45° angle deflected a fraction of the incident photons into the photomultiplier tube.

(b) Measurement of the transmitted beam intensity:

Several schemes were employed in the measurement of the transmitted beam intensity. For the feasibility experiments and the experiments at NSLS, the beam stop was used to probe the transmitted beam intensity. The beam stop, shown in Figure III.4, is an aluminum wedge with its surface oriented at 45° to the transmitted beam. To detect photons, the surface of the beam stop was covered with a ZnS fluorescent screen. The ZnS screen emits optical photons when excited by X-rays. During the feasibility experiments these optical photons were detected with an unbiased photo-diode with an active area of 5.1 mm^2. During the NSLS experiments, the optical photons from the ZnS screen were transmitted to a photomultiplier tube via fiber optic cables made of fused silica. So, for the feasibility experiments and the NSLS experiments, the method for detecting the transmitted beam was twofold. First the X-rays in the transmitted beam were converted to optical photons with a fluorescent ZnS screen. Then the optical photons were counted by an optical photon detector.

For the second set of experiments at SSRL, the transmitted beam was monitored with a X-ray photomultiplier tube oriented perpendicular to the transmitted beam. A polypropylene film, located just after the sample, and oriented at 45° to the transmitted beam, deflected part of the transmitted beam into the photomultiplier tube. This method eliminates the down-conversion of the X-ray photons to optical photons, but samples only a fraction of the beam rather than the entire beam.

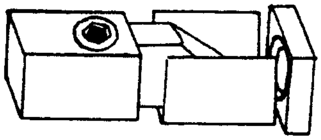

Marybeth Rice
3-11-91

FIGURE III.4 The beam stop.

(c) Detection of the SAXS pattern:

In all the ASAXS experiments discussed here, the SAXS pattern was collected with a position sensitive proportional counter. For the feasibility experiments and the second set of experiments at SSRL, the proportional counter was a linear detector. The experiments at NSLS employed a quadrant detector. Both types of detector are position sensitive proportional counters and both work on the same basic principle (Gabriel, 1977; Towns-Andrews et al., 1989).

The linear detector is a gas filled chamber with an anode wire that is held at a high positive potential. Perpendicular to the anode wire is an array of cathode wires. Each cathode wire feeds into a tap on a delay line. When a photon enters the detector it ionizes the gas. The liberated electron is accelerated toward the wire and ionizes more gas atoms in its path. The effect cascades so that a burst of charge is induced on the cathode, which is capacitively coupled to the anode, at the position where the photon entered the detector. This signal runs in opposite directions down both sides of the delay line. The time it takes for the signal to reach one end of the line as opposed to the time it takes to reach the other end depends on where on the cathode wires the signal originated. Hence, the time difference for the arrival of the signal at the ends of the delay line determines the location of the event. This gives the detector its position sensitive capability. An exploded diagram of the linear detector is shown in Figure III.5.

The quadrant detector works on the same principal except that now the single anode wire is replaced by a grid of anode wires and the cathode consists of an array of concentric arcs that form the sector of a circle. The signals from these arcs feed into a delay line. The difference between the arrival times of the signal at the ends of the delay line determines which arc collected the event. An exploded diagram of the quadrant detector is shown in Figure III.6.

The linear detector and the quadrant detector were both developed by Dr. Andre Gabriel of EMBL, Grenoble (Gabriel, 1977; Towns-Andrews et al., 1989). The linear detector used for the feasibility experiments had a gold plated tungsten anode wire that was 7.2 mm long and 20 μm thick. The spatial resolution of this detector is 100-200 μm. The linear detector is shown in Figure III.7. The quadrant detector was used for the NSLS experiments. Its cathode plane is specially plated so that the scattering patterns are integrated along the arcs. The length of the active area is 185 mm and the arcs form 60° sectors which are concentric with the center of the pattern. The spatial resolution of the quadrant detector is about 500 μm. The quadrant detector is shown in Figure III.8. The linear detector used for the second set of experiments at SSRL has an active length of 200 mm and a spatial resolution of 100-200 μm.

In all cases, the detectors must be filled with high purity gas to operate. The smaller linear detector used a gas of 10% carbon dioxide-90% argon that was continuously flowed at a pressure of 35 psi during data collection. The larger linear detector and the quadrant detector used a gas of 30% carbon dioxide-70% argon. Gas was flowed continuously through the larger linear detector. The quadrant detector was filled with gas and sealed before data acquisition.

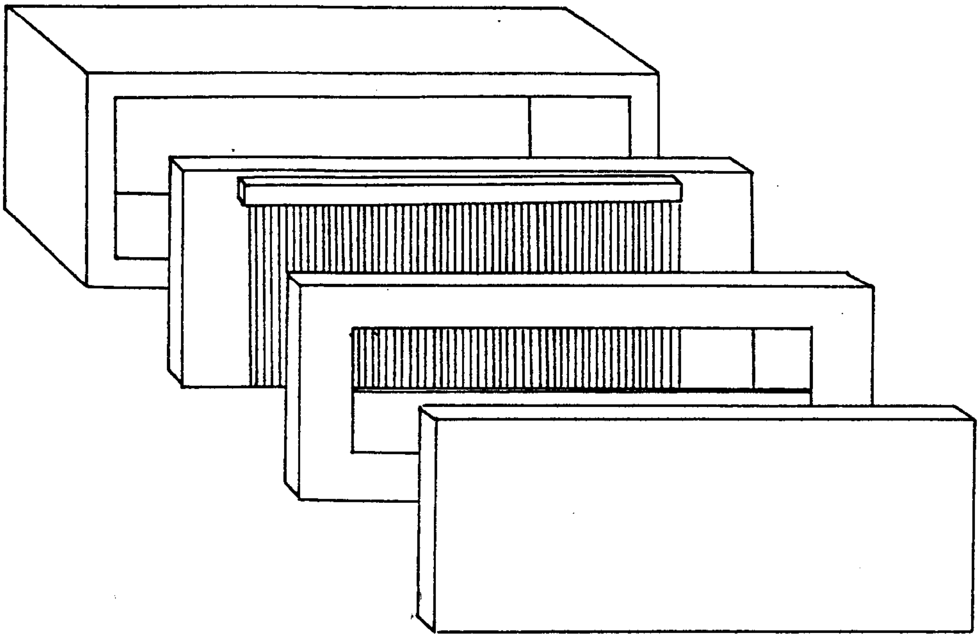

Marybeth Rice
3-11-91

FIGURE III.5 An exploded diagram of the linear detector. From top to bottom are: the gas chamber, the cathode board, the anode wire, and the beryllium window.

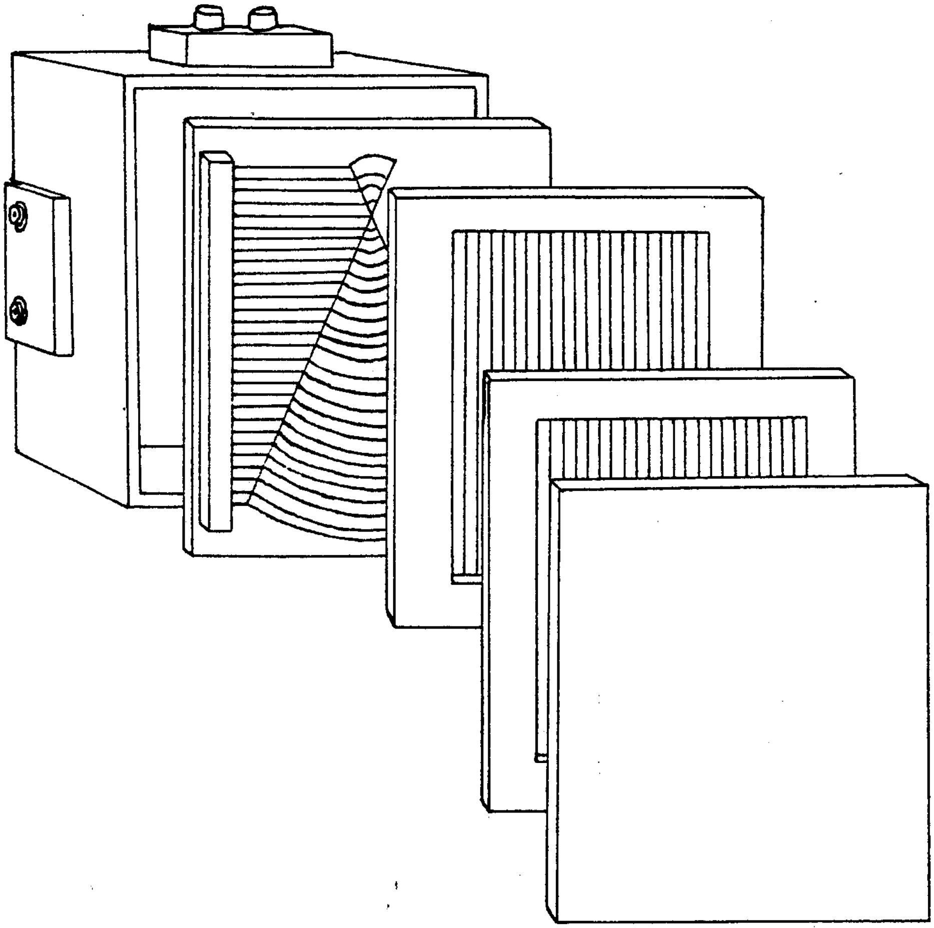

Marybeth Rice
3-11-91

FIGURE III.6 An exploded view of the quadrant detector. From top to bottom are: the gas chamber, the cathode board, the anode wires, the cathode wires for the drift chamber, and the beryllium window.

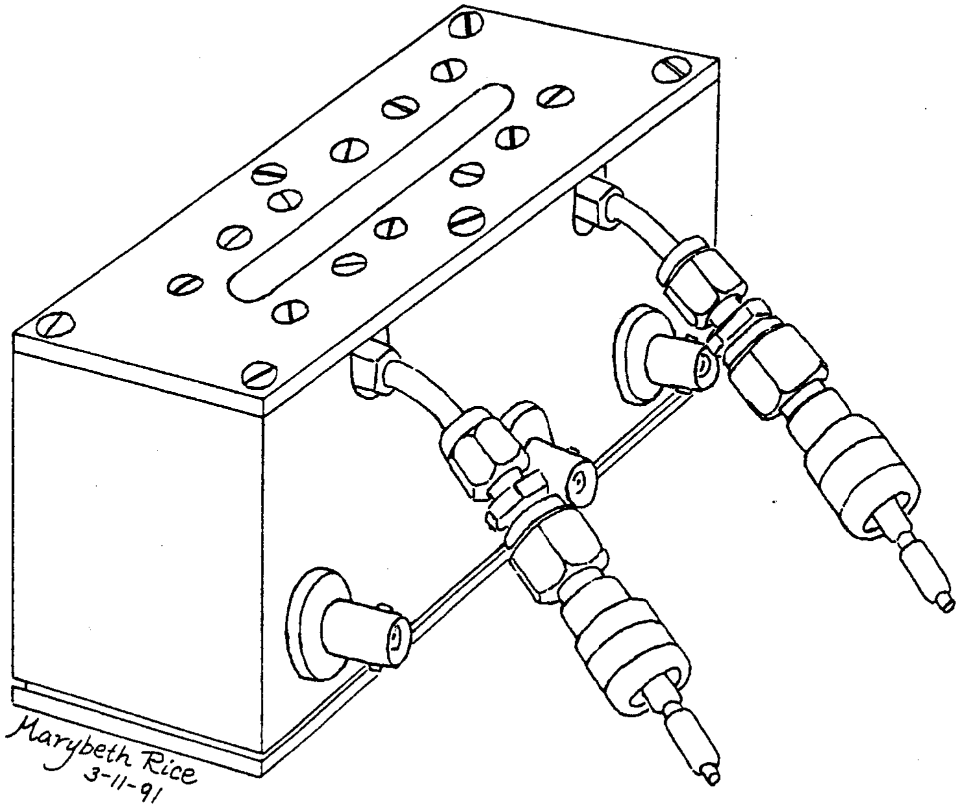

FIGURE III.7 The linear detector.

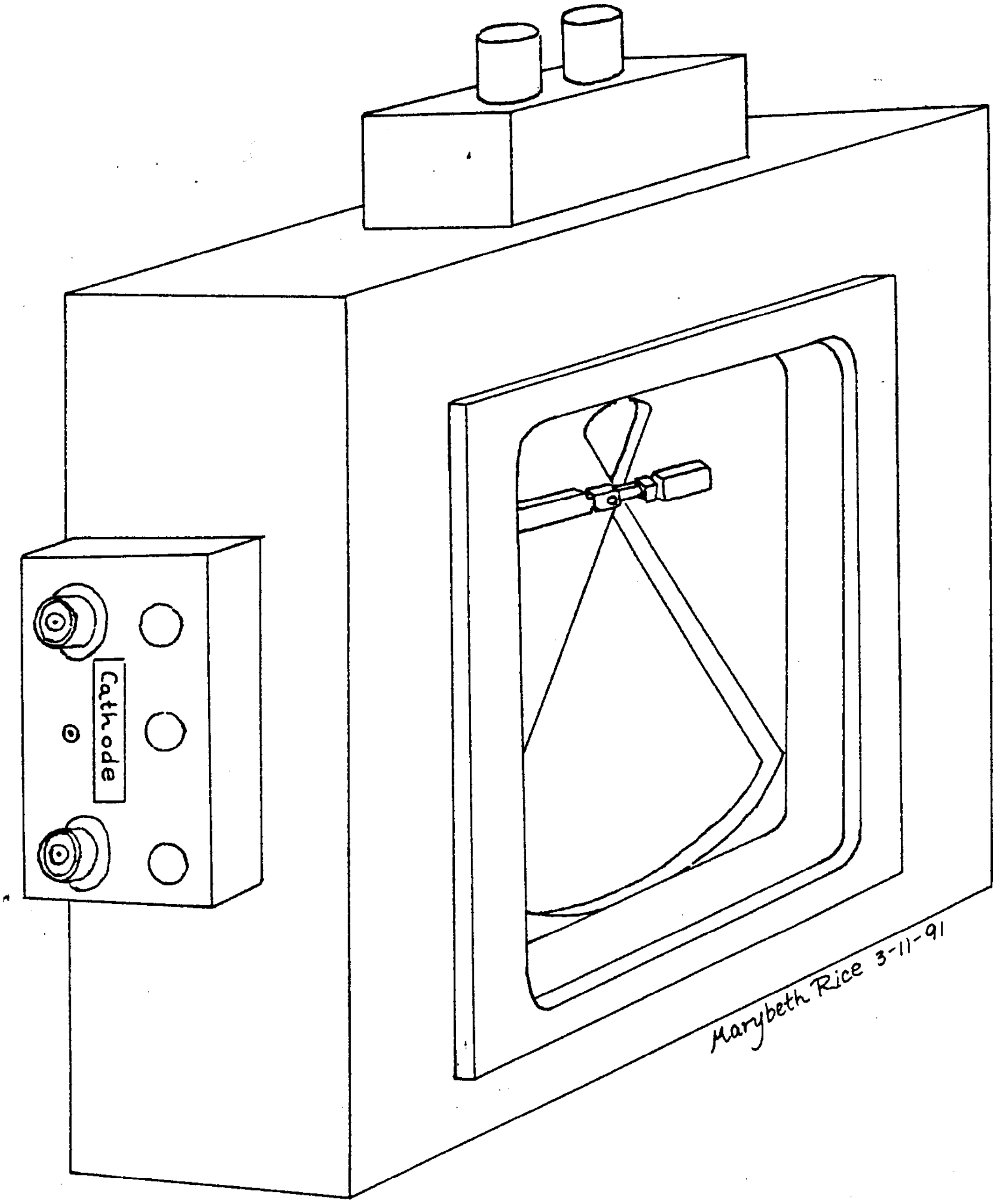

FIGURE III.8 The quadrant detector.

3.5 NON-DETECTING COMPONENTS OF THE SAXS CAMERA

(a) Scattering paths:

The X-rays scattered by the sample follow a flight path that extends from the sample to the detector. Background scattering is greatly reduced by removing air from this scattering path. The flight path for the linear detectors was evacuated, while the flight path of the quadrant detector was filled with helium. Both flight paths are made of flanged tubes that bolt together: aluminum tubes for the linear detector and Plexiglas tubes for the quadrant detector. In each case the total length of the scattering path is adjustable. The vacuum path had a mica window on the end next to the sample and a Kapton window on the end next to the detector. The helium path had a mica window on the end next to the sample and bolted directly onto the detector, obviating the need for a rear window.

(b) Slits:

Two sets of slits are used to control the beam that reaches the sample, the defining slits and the guard slits. Both are Huber tantalum slits with adjustable vertical and transverse slits. The defining slits determine the size and shape of the incident beam. At SSRL the defining slits were 400 μm wide by 500 μm high. At NSLS the defining slits were set to 500 μm high and were wide open horizontally because of the tightly focused horizontal divergence of beam line X14A. The guard slits are placed just before the sample and are used to cut parasitic scattering from the defining slits. The guard slits also improve the collimation of the beam especially when their distance from the defining slits is large. In all experiments the guard slits were 500 μm wide. The vertical slits of the guard slits are motorized so that the aperture can be adjusted remotely with X-rays in the hutch. The vertical aperture of the guard slits was adjusted so that the parasitic scattering was cut as much as possible without cutting the direct beam.

3.6 EQUIPMENT SETUP AT NSLS

The first component of the SAXS camera that the beam encounters, in any experiment, is the pair of defining slits. At NSLS the beam was very tightly focused in the horizontal dimension (1.5 mm) so the horizontal aperture of the defining slits was wide open. The vertical aperture of the defining slits was set to 500 μm, half the vertical dimension of the beam. The defining slits were immediately followed by a 13.6 cm long, nitrogen filled, ionization chamber which monitored the incident beam intensity. The ionization chamber was followed by a six foot long helium path. The guard slits followed the long helium path. They were set to 500 μm wide by approximately 500 μm high. As discussed earlier, the vertical aperture of the guard slits is set remotely to a size that cuts the parasitic scattering from the defining slits without cutting the main beam. The samples were mounted in cardboard frames that were taped to the downstream side of the guard slits. The helium filled scattering path was about 80 cm long. It had a mica window next to the sample and was bolted to the quadrant detector at the other end. The quadrant detector was filled with a gas that was 30 % carbon dioxide and 70 % argon. The beam stop was mounted on the detector. Its surface was covered with a ZnS film oriented at 45° to the transmitted beam. Optical photons from the ZnS film, excited by X-rays in the transmitted beam, were carried to a photomultiplier tube by fiber optical cables.

3.7 EQUIPMENT SETUP AT SSRL

The size of the beam entering the hutch on beam line 4-2 at SSRL is 1 mm high by 10 mm wide. This beam was cut down to 500 μm high by 400 μm wide by the defining slits. These slits were followed by a seven foot long vacuum pipe that was pumped to a rough vacuum. The vacuum path was followed by the guard slits whose aperture was set to 500 μm wide by approximately 500 μm high. The intensity of the incident beam was monitored by a photomultiplier tube placed just after the guard slits. A piece of polypropylene film was oriented at 45° to the beam so that a fraction of the incident photons were scattered into the photomultiplier tube which was placed perpendicular to the beam. The samples, in cardboard frames, were taped to the downstream side of the polypropylene housing. Following the sample was a second photomultiplier tube in the same configuration as the first with a piece of polypropylene film oriented at 45° to the beam. This detector was used to monitor the transmitted beam intensity. The polypropylene film and its housing were located inside an evacuated scattering path. This path was 123 cm long. Like the first vacuum path, it was pumped to a rough vacuum– a thousandth of an atmosphere. The window of the scattering path near the sample was made of mica. The window near the SAXS detector was made of Kapton. The SAXS detector for these experiments was the linear position sensitive detector with a 20 cm active length. Gas with a composition of 30 % carbon dioxide and 70 % argon was flowed in the detector during data acquisition. The beam stop was mounted on the down stream end of the scattering path. It was a small rectangular slab of lead.

3.8 ELECTRONICS

The three detectors: the incident intensity monitor, the transmitted intensity monitor, and the SAXS detector receive their power from high voltage power supplies. Signals from the detectors are ultimately collected by a computer after processing by electronics modules (Boulin et al., 1988; Rice & Wakatsuki, 1991; Wakatsuki et al., 1992). The SAXS detector produces two signals for each event. These signals, called start and stop signals, run down the two sides of the delay line, are amplified, discriminated and fed to a time-to-digital converter. Signals from the time-to-digital converter are collected in a histogramming memory and are transferred to the computer, a VAXstation, via the CAMAC dataway. Signals from the ionization chamber, the photodiode, and the photomultiplier tubes are amplified, converted into frequency, and collected in an up/down counter. The computer reads the information in the up/down counter.

REFERENCES FOR CHAPTER III

Boulin, C. J., Kempf, R., Gabriel, A., Koch, M. H. J., *Nucl. Instrum. & Meth. in Phys. Res.* **A269** (1988) 312.

Gabriel, A., *Rev. Sci. Instrum.* **48** (1977) 1303.

Habenschuss, A., Ice, G. E., Sparks, C. J. & Neiser, R. A., *Nucl. Instrum. & Meth. in Phys. Res.* **A266** (1988) 215.

Ice, G. E. & Sparks, C. J., *Nucl. Instrum. & Meth. in Phys. Res.* **A266** (1988) 394.

Ice, G. E. & Sparks, C. J., Sixth National Conference on Synchrotron Radiation Instrumentation, Berkeley, CA, USA, 7-10 Aug. 1989, *Nucl. Instrum. & Meth. in Phys. Res.* **A291** (1990) 110.

Rice, M. & Wakatsuki, S., A User's Guide to the Small-Angle X-ray Scattering/Diffraction Data Acquisition System at SSRL, SSRL Publication PROD-UG-SAS 09/91-R01 (1991).

Stephenson, G. B., Ph.D. thesis, Stanford University, 1982.

Towns-Andrews, E., Berry, A., Bordas, J., Mant, G. R., Murray, P. K., Roberts, K., Sumner, I., Worgan, J. S., Lewis, R. & Gabriel, A., *Rev. Sci. Instrum.* **60** (1989) 2346.

Wakatsuki, S., Hodgson, K. O., Eliezer, D., Rice, M., Hubbard, S., Gillis, N,. Doniach, S. & Spann, U., *Rev. Sci. Instrum.* **63** (1992) 1736.

CHAPTER IV

REDUCTION OF ANOMALOUS SMALL ANGLE X-RAY SCATTERING DATA

4.1 NECESSARY CORRECTIONS TO RAW ASAXS DATA

The raw ASAXS data were collected as counts per channel of the position sensitive detector. The quantity of interest is the absolute differential scattering cross section per unit volume, $d\Sigma/d\Omega$, measured as a function of the magnitude of the scattering vector, k. Here k is equal to $4\pi\sin\theta/\lambda$, where 2θ is the scattering angle and λ is the wavelength of the incident light. The absolute differential scattering cross section per unit volume, $d\Sigma/d\Omega$, is the ratio of the number of photons scattered per second divided by the incident flux (photons per second per cm^2) per unit solid angle per unit sample volume (Russell, Lin, Spooner & Wignall, 1988). In terms of the measured count rate, $I(k)$,

$$\left[\frac{d\Sigma}{d\Omega}(k)\right]=\frac{I(k)}{tI_0e^{-\mu t}}\frac{r^2}{\varepsilon\Delta a}, \qquad (4.1)$$

where t is the sample thickness, I_0 is the flux incident on an area, A, of the sample, the illuminated volume, V, is equal to A times t, $e^{-\mu t}$ is the attenuation factor with μ equal to the linear absorption coefficient, r is the sample-to-detector distance, Δa is the area of a detecting element so that $\Delta a/r^2$ is the solid angle subtended by the detecting element, and ε is the counting efficiency of the detector. For SAXS, the attenuation factor is free of angular dependence since the scattering angles are all so close to zero.

The absolute differential scattering cross section is ideally free of all background scattering including substrate scattering, air scattering, parasitic scattering, background fluorescence, and resonant Raman scattering, and is free of experimental artifacts such as smearing and detector response functions.

All the procedures followed to liberate the absolute differential scattering cross section from the raw data are described sequentially in the next section.

4.2 PROCEDURES FOLLOWED IN ASAXS DATA REDUCTION

(a) Correcting for the spatial response of the position sensitive SAXS detector:

Ideally, a position sensitive detector should have a uniform response across its entire active area. In reality, the response of the detector varies from place to place largely due to contamination of the anode wire (or wires), as well as imperfections in the cathode wires and other circuitry. Artifacts in the data caused by detector non-uniformity can be eliminated by dividing each data set by the detector response.

At SSRL, the spatial response of the linear position sensitive detector was measured by illuminating the entire active area of the detector with X-rays from an Fe^{55} source. Fe^{55} is a good source for measuring detector response since it emits characteristic manganese K_α and K_β radiation which is uniform and isotropic. The detector response was necessarily measured with the same electronics configuration as that used for the ASAXS data collection. The detector response data were collected after all the ASAXS data had been collected. Hence, the detector degradation was not measured as a function of time. The spatial response of the linear detector varied by about 20 percent across the length of the detector except at two points near the center where the anode wire was damaged. Here the counting rate was reduced from the average by 67 percent.

Unfortunately, time constraints prohibited collection of an Fe^{55} pattern at NSLS, so the NSLS data sets are not corrected for spatial variations in the detector response. The interior components of the detector used at NSLS were replaced immediately before data collection, so damage to the anode wires should have been minimal.

(b) Centering the SAXS pattern:

Since the SAXS patterns are symmetric with respect to the center of the transmitted beam, the zero of the SAXS pattern was found by folding the scattering above the beamstop onto the scattering below the beamstop so that the two patterns coincided. The choice of the zero of the SAXS pattern determines the position of the SAXS peaks.

(c) Scaling by the transmitted intensity (absorption correction):

All of the SAXS patterns should be divided by the incident intensity, I_0, to account for fluctuations of the incident beam. Since the samples all have different compositions and thicknesses, each absorbs a different fraction of the incident beam as a function of energy, and each has a unique attenuation factor, $e^{-\mu t}$. Corrections for variations in incident flux and sample absorption as a function of energy can be performed simultaneously by dividing the data by the transmitted intensity, I_t, since

$$I_t = I_0 e^{-\mu t}. \tag{4.2}$$

For the SSRL data, the performance of the I_t monitor was inconsistent, so the data were normalized by I_0. The attenuation factors, $e^{-\mu t}$, were extracted from the absorption data and applied to the I_0 normalized data. The attenuation factor for a Kapton supported film actually is the product of the attenuation factor for the metal-germanium film and the attenuation factor for the Kapton substrate, so

$$e^{-\mu t} = \exp[-\mu_{\mathrm{sample}}\, t_{\mathrm{sample}} - \mu_{\mathrm{Kapton}}\, t_{\mathrm{Kapton}}]. \tag{4.3}$$

(d) Dead time correction:

The dead time correction accounts for the non-linearity of the SAXS detector as a function of count rate. The count rates of the position sensitive detectors were so low during these experiments that the dead time correction was negligible.

(e) Averaging data sets together:

The SAXS data were collected in multiple cycles. In this work each cycle consists of one SAXS pattern collected at each of the five specified energies beneath the relevant absorption edge. The data were collected in multiple short cycles rather than one long cycle to spot trouble arising from changes in the beam, the sample, or the detector performance. Multiple data sets for a given sample at a given energy were averaged together.

(f) Calculating the number of channels per millimeter:

The SAXS data are collected as counts versus channel number. To convert the channel numbers into a meaningful variable it is essential to know how many channels there are per millimeter detecting length of the linear or quadrant detector. For the linear detector this was accomplished experimentally by collecting an air scattering profile with a slotted mask placed over the detector. This is a very accurate method of determining the number of channels per millimeter. Since the slots are identical in size and spacing, examination of the intensity pattern through the slotted mask shows clearly how many channels, on average, are collecting photons per unit length of the detector (Rice & Wakatsuki, 1990).

At the time of the NSLS experiments, no mask had been fabricated for the quadrant detector. The number of channels per millimeter for the quadrant detector was computed by dividing the number of channels in the SAXS profile by the active length of the quadrant detector. This is a less accurate method than that of the slotted mask. Use of this quantity, however, in the calculation of the sample-to-detector distance yielded a very reasonable result. The sample-to-detector distance (of approximately 94 cm) was already known to within 2 centimeters by measurement with a tape measure. Uncertainty in the sample-to-detector distance arises from the unknown distance of the cathode plane of the detector from the beryllium window.

More important than the exact value of the number of channels per millimeter or the exact value of the sample-to-detector distance is correct determination of the scattering angle which is a function of the ratio of the number channels per millimeter to the sample-to-detector distance. The scattering angle was accurately determined by observation of the position of the peaks of a polycrystalline cholesterol myristate sample, as discussed in the next section.

(g) Determining the sample to detector distance:

For all the experiments the sample-to-detector distance was determined by observing the position of the (100) reflection of polycrystalline cholesterol myristate. This reflection corresponds to a Bragg spacing of 51.5 Å (Hubbard, 1987). Since the wavelength of the incident radiation is known, the scattering angle can be calculated from Bragg's law. The scattering angle, the position of the 51.5 Å peak and knowledge of the number of channels per millimeter, are sufficient to determine the sample-to-detector distance from simple geometry.

(h) Converting from channel number to scattering vector:

The distance between each channel and the center of the transmitted beam and the sample-to-detector distance determine the scattering angle. The number of channels per millimeter, the wavelength of the incident light, and the sample-to-detector distance were used to convert the data from counts versus channel number to counts versus the magnitude of the scattering vector. The magnitude of the scattering vector, k, is equal to $4\pi\sin\theta/\lambda$, where 2θ is the scattering angle and λ is the wavelength of the incident intensity.

(i) Correcting for quadrant detector aperture:

The quadrant detector collects data along arcs that form a sector of a circle. The intensity of the collected radiation thus increases as the size of the arcs increases. A scattering pattern that would look flat if collect with a linear detector will look like a ramp when collect with the quadrant detector. To correct for this aspect of the spatial response of the quadrant detector, the data were divided at each point by the length of the arc at that point.

(j) Correcting for energy responses of the detectors:

The response of each detector used in the ASAXS experiments varies as a function of energy. The position sensitive SAXS detectors have an ionization efficiency that decreases with increasing photon energy for all energies between 4 and 20 keV. The I_t monitor at NSLS was a ZnS fluorescent screen attached to a photomultiplier tube, both of which respond differently to photons of different energy. The SSRL data were normalized by the counts in the I_0 monitor multiplied by the experimentally determined attenuation factor, $e^{-\mu t}$, as described above. The I_0 monitor for the SSRL data was a photomultiplier tube whose counting efficiency increases with increasing photon energy in the energy ranges of interest. The data were corrected for the energy response of the SAXS detector and the I_t or I_0 monitor simultaneously by comparison to a standard.

Kapton was used as a standard to correct the NSLS data, while lupolen was used to correct the SSRL data. Both of these substances are organic polymers that do not scatter anomalously in the vicinity of the Ge, Fe, Mo, or W absorption edges. Changes in scattering due to the anomalous effect were thus separated from the apparent changes in scattering due to the energy responses of the detectors.

The SSRL data were corrected for the energy responses of the detectors by dividing the SAXS data at each energy by the normalized intensity of the lupolen peak at that energy. This step is included in the process of putting the scattering cross sections on an absolute scale (see section (*o*) below for more detail). The NSLS data were corrected by multiplying the data at each energy by a scaling factor such that the intensities of the Kapton peak at all energies coincided.

(k) Background subtraction including background absorption correction:

The intensity of a beam scattered by a film in transmission, I, is equal to the fraction of incident radiation scattered by a unit volume of the sample, E, times the incident intensity, I_0, times the thickness of the film, t, times the attenuation factor $e^{-\mu t}$:

$$I = EtI_0e^{-\mu t}. \qquad (4.4)$$

For a Kapton supported film, radiation is scattered by both the film and the Kapton. The radiation scattered by each experiences absorption due to the film plus the Kapton. So,

$$I = E_f t_f I_0 e^{-(\mu_f t_f + \mu_K t_K)} + E_K t_K I_0 e^{-(\mu_f t_f + \mu_K t_K)} \qquad (4.5)$$

where the subscript f refers to the film and the subscript K refers to the Kapton. Normalization of the SAXS intensity by the transmitted intensity leaves

$$[I/I_t] = E_f t_f + E_K t_K. \qquad (4.6)$$

Proper removal of the Kapton (or other background) signal is thus accomplished by subtracting the Kapton (or other background) scattering normalized by its transmitted intensity.

ASAXS data were collected at each energy for each substrate- either air for free-standing films or the appropriate number of Kapton layers for Kapton supported films. All background data were divided by $I_t{=}I_0e^{-\mu t}$. The NSLS data were divided directly by I_t, while the SSRL data were divided by I_0 times the experimentally determined $e^{-\mu t}$. Unfortunately, Kapton scatters strongly at small angles, and scatters anisotropically. The Kapton subtraction was often imperfect, so for some data sets the background was scaled by a factor between 0.7 and 1.2 to improve the subtraction.

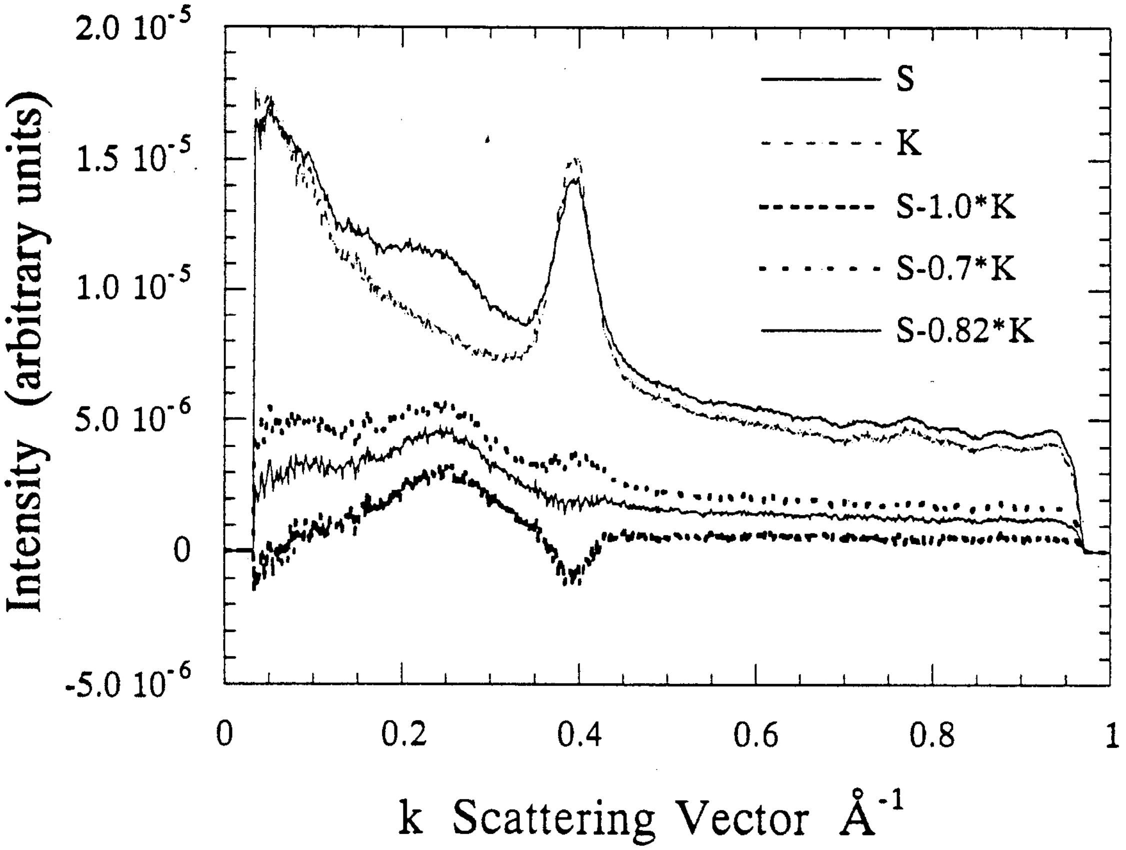

Figure IV.1 Kapton subtraction for the a-$Fe_{18}Ge_{82}$ sample. The curve S is the scattering from the sample on Kapton. K is the scattering from Kapton alone. Note that the Kapton peak near 0.4 $Å^{-1}$ is larger for the Kapton alone. The three lower curves are attempts to subtract the Kapton from the sample on Kapton. The lowest curve is a straight subtraction- too much Kapton has been subtracted. In the middle curve the Kapton intensity was scaled by 0.7 before subtraction- too little Kapton has been subtracted. The second curve from the bottom shows the result of scaling the Kapton intensity by 0.82 before subtraction. This is the best background subtraction for this sample.

(l) Desmearing and the lack of such a need:

Smearing of SAXS patterns arises from the finite dimensions of the beam and of the detector aperture. The intensity profile that the detector sees, $I_{sm}(k)$, is related to the desmeared intensity profile, $I_{dsm}(k)$, by the equation

$$I_{sm}(k) = \int_{-\infty}^{+\infty} \int_{-\infty}^{+\infty} P(t)Q(u)I_{dsm}\left(\left[t^2 + (k-u)^2\right]^{1/2}\right)dtdu \qquad (4.7)$$

where *P(t)* is the convolution, in the vertical direction, of the intensity distribution of the beam with the detector aperture and *Q*(*u*) is the convolution, in the horizontal direction, of the intensity distribution of the beam with the detector aperture. The variables of integration are *t,* the coordinate in the direction of the slit length, and *u,* the coordinate in the direction of the slit width (Glatter, 1982; Feigin & Svergun, 1987).

As described in the previous chapter, the beam size for all the ASAXS experiments was very close to 0.5 mm by 0.5 mm. This is essentially a pin hole. Desmearing of representative ASAXS data sets by the method of Lake (1967) produced a negligible change in the SAXS profile. Smearing effects were not considered further and the data presented here are not desmeared.

(m) Correcting for solid angle:

The data sets were all corrected for solid angle variations due to variable camera lengths and variable detector apertures. The data collected in each detecting element were divided by the solid angle subtended by that detecting element. The solid angle, $d\Omega$, is defined as

$$d\Omega = \Delta a / r^2, \qquad (4.8)$$

where Δa is the area of the detecting element, and *r* is the sample-to-detector distance. The area of a detecting element of the quadrant detector was taken to be the length of the detecting channel times the length of the arc associated with that channel. Since the quadrant detector data were already corrected in a previous step for the arc length at each channel, the solid angle correction consisted of dividing the data by the channel length and multiplying the data by the square of the sample-to-detector distance. The area of a detecting element of the linear detector was taken to be the length of the detecting channel times the width of the detector aperture.

(n) Correcting for sample thickness:

Scattering patterns from samples of different thicknesses can only be compared if the varying thicknesses are taken into account. Hence, the SAXS pattern from each film was divided by the film thickness. The thickness of each film was determined as described in the previous chapter.

(o) Putting scattering cross sections on an absolute scale:

The differential scattering cross section is put on an absolute scale by division by the detector counting efficiency, ε. The detector counting efficiency is determined by a calibration standard, in this case lupolen (polyethylene) from T. Russell. The differential scattering cross section for this lupolen standard at its maximum is

$$\left[\frac{d\Sigma}{d\Omega}(k_m)\right]_l = \frac{I(k_m)_l}{t_l I_0 e^{-\mu_l t_l}} \frac{r^2}{\varepsilon \Delta a} = 4.25\,\mathrm{cm}^{-1}, \tag{4.9}$$

where the subscript l refers to lupolen and k_m is the is the position of the maximum. The detector efficiency is then

$$\frac{1}{\varepsilon} = \left[\frac{d\Sigma}{d\Omega}(k_m)\right]_l \frac{t_l I_0 e^{-\mu_l t_l}}{I(k_m)_l} \frac{\Delta a}{r^2}. \tag{4.10}$$

The absolute differential scattering cross section for the sample of interest can now be determined:

$$\left[\frac{d\Sigma}{d\Omega}(k)\right]_s = \frac{I(k)_s}{t_s I_0 e^{-\mu_s t_s}} \frac{r^2}{\varepsilon \Delta a} = \frac{I(k)_s}{t_s I_0 e^{-\mu_s t_s}} \frac{r^2}{\Delta a} \left[\frac{d\Sigma}{d\Omega}(k_m)\right]_l \frac{t_l I_0 e^{-\mu_l t_l}}{I(k_m)_l} \frac{\Delta a}{r^2} \tag{4.11}$$

$$\left[\frac{d\Sigma}{d\Omega}(k)\right]_s = \frac{I(k)_s}{t_s I_0 e^{-\mu_s t_s}} \frac{t_l I_0 e^{-\mu_l t_l}}{I(k_m)_l} 4.25\ \mathrm{cm}^{-1}.$$

The lupolen scattering pattern was normalized by I_0 multiplied by the theoretical attenuation factor. The theoretical attenuation factor for lupolen was determined at each energy by solution of the Victoreen equation with tabulated values from the *International Tables for X-Ray Crystallography* (Lonsdale,1968). The value of the attenuation factor for lupolen at the wavelength of Cu K_α radiation was provided by T. Russell and was used to match the theoretical attenuation factors to the true attenuation factors.

The lupolen sample only became available during the SSRL experimental run. The NSLS data were put on an absolute scale by comparison with the SSRL data, since data were collected on some of the same samples for both experimental runs.

(p) Removal of fluorescence from lower shells:

Data collected near at the Ge edge for a-Fe_xGe_{100-x} and a-W_xGe_{100-x} samples contain fluorescence from Fe or W. This fluorescence is just a constant background. It was removed by subtraction such that the absolute differential cross section at large k converged with the value observed at the lower edge.

(q) Removal of resonant Raman scattering:

Some samples exhibit resonant Raman scattering at 10 or 20 eV below the absorption edge. Similar to fluorescence, resonant Raman appears as a constant background. The appropriate constant to subtract was determined by making the data sets for the same sample converge at large k.

(r) Interpolation of data:

The data were interpolated to standardize the abscissa scale. This facilitates subtraction of data sets collected at different energies.

REFERENCES FOR CHAPTER IV

Feigin, L. A. & Svergun, D. I., *Structure Analysis by Small Angle X-Ray and Neutron Scattering*, Plenum Press, New York (1987).

Glatter, O., In *Small Angle X-Ray Scattering*, edited by O. Glatter & O. Kratky, Academic Press, London (1982).

Hubbard, S. R., Ph.D. thesis, Stanford University (1987).

Lake, J. A., *Acta. Cryst.* **23** (1967) 191.

Lonsdale, K. General Editor, *International Tables for X-Ray Crystallography*, Vol. III, Kynoch Press, Birmingham, England (1968).

Rice, M. & Wakatsuki, S., *A User's Guide to the Small-Angle X-Ray Scattering/Diffraction Data Acquisition System at SSRL*, SSRL Publication PROD-UG-SAS 09/91-R01 (1991).

Russell, T. P., Lin, J. S., Spooner, S. & Wignall, G. D., *J. Appl. Cryst.* **21** (1988) 629.

CHAPTER V

ASAXS RESULTS: SAMPLES WITH x<25

In this chapter and the next, the results of the ASAXS experiments are presented and discussed. First, a brief review of SAXS theory is offered to establish notation and set the stage for discussion of the experimental results.

Classical treatments of small angle X-ray scattering theory (Guinier & Fournet, 1955; Porod, 1982; Feigin & Svergun, 1987; Russell, 1991) deal only with elastic, coherent, single scattering processes. These simplifications are valid, in light of the small contribution of inelastic, incoherent and multiple scattering processes to SAXS data, and are retained here.

5.1 REVIEW OF SAXS THEORY

(a) Scattering from a collection of atoms- the concept of an effective electron density:

The intensity of radiation scattered from a collection of atoms is the absolute square of the sum of the scattered amplitudes. The scattered amplitudes have magnitudes proportional to the atomic scattering factors, f_n, and phases given by $2\pi/\lambda$ times the difference in the optical path lengths. With the notation A_e is the amplitude of radiation scattered by one electron, $\mathbf{s}_0$ is the unit vector defining the direction of the incident radiation, $\mathbf{s}$ is the unit vector defining the direction of the scattered radiation, $\mathbf{r}_n$ is the vector that defines the location of the nth atom relative to an arbitrary origin, and the vector $\mathbf{k}=(2\pi/\lambda)(\mathbf{s}\text{-}\mathbf{s}_0)$, the amplitude of radiation scattered by a collection of atoms can be expressed as

$$A(\mathbf{k}) = A_e(\mathbf{k})\sum_n f_n(\mathbf{k})e^{-i\frac{2\pi}{\lambda}(\mathbf{s}-\mathbf{s}_0)\cdot\mathbf{r}_n} = A_e(\mathbf{k})\sum_n f_n(\mathbf{k})e^{-i\mathbf{k}\cdot\mathbf{r}_n} \qquad (5.1)$$

where f_n is the atomic scattering factor for the nth atom and the sum is taken over all atoms.

The scattering angle formed by the vectors $\mathbf{s}_0$ and $\mathbf{s}$ is defined as 2θ so that the magnitude of $\mathbf{k}$ is $k=(4\pi\sin\theta)/\lambda$. Over the range of small $\mathbf{k}$ values probed in SAXS experiments, the atomic scattering factor for each atom is essentially constant (not a function of $\mathbf{k}$). At incident photon energies far from any absorption edges, f is equal to Z, the number of electrons in the atom.

The sample under study (collection of atoms) is often treated as a continuous medium with electron density $\rho(\mathbf{r}_n)$ such that a volume element dV at a point $\mathbf{r}_n$ will contain $\rho(\mathbf{r}_n)dV$ electrons. This is valid when the incident photon energy is much greater than any absorption edge in the material. The sum in equation (5.1) is replaced by an integral and the scattered amplitude is given by

$$A(\mathbf{k}) = A_e(\mathbf{k})\int_V \rho(\mathbf{r}_n)\ e^{-i\mathbf{k}\bullet\mathbf{r}_n}dV \qquad (5.2)$$

where V is the illuminated volume of the sample. The scattered amplitude is proportional to the Fourier transformation of the electron density distribution.

In the case of anomalous scattering, the scattered amplitude is altered due to the modification of the atomic scattering factor near an absorption edge. The scattered amplitude is proportional to the Fourier transformation of an effective electron density $\rho_{eff}(\mathbf{r}_n, E)$.

This is more obvious when the electron density is expressed in terms of the number density, $N_\alpha(\mathbf{r}_n)$, of each atomic species α times the effective number of electrons per atom

$$\rho(\mathbf{r}_n) = \sum_{\alpha} \left|Z_\alpha + f_\alpha^{'}(E) + if_\alpha^{''}(E)\right| N_\alpha(\mathbf{r}_n). \qquad (5.3)$$

The dependence of the scattered amplitude on the atomic scattering factors is now clear:

$$A(\mathbf{k}) = A_e(\mathbf{k})\sum_{\alpha} \int_V \left|Z_\alpha + f_\alpha^{'}(E) + if_\alpha^{''}(E)\right| N_\alpha(\mathbf{r}_n)\ e^{-i\mathbf{k}\bullet\mathbf{r}_n}dV\ . \qquad (5.4)$$

When anomalous scattering data are considered, the full expression for the atomic scattering factor is used and the scattered amplitude is proportional to the Fourier transformation, not of the actual electron density, but of an apparent or effective electron density. In this way, species specific information is obtained from the sample.

(b) Anomalous dispersion:

As already stated in Chapter I, the atomic scattering factor behaves anomalously near an absorption edge of the probed atom (James, 1982). Here, the total scattering factor is augmented by f' and f'', the real and imaginary changes from the high energy limit, f_0. In SAXS experiments, f_0 is just Z, the atomic number and

$$f(E)=Z+f'(E)+if''(E). \qquad (5.5)$$

As the absorption edge of an atom is approached from lower energies, f'' remains essentially constant while f' rapidly becomes increasingly negative. This behavior is readily apparent in Figures V.1 and V.2 which show f'' and f' for *a*-Ge.

Measuring the intensity of radiation scattered by a composite sample at different energies below a constituent atom's absorption edge gives species specific information about the sample. As will be described in detail later, the anomalous effect was used here to extract information about which atoms in the metal-germanium alloys contribute to the small angle X-ray scattering pattern.

For each sample discussed here, experimental values of f' and f'' were extracted from the absorption data. As shown in section 2.5, part *(c)* of Chapter II, f'' is related to the absorption cross-section through the optical theorem. As stated there

$$\ln\left(\frac{I_0}{I_t}\right)=\left[\left(\frac{w_a}{A}\right)\left(\frac{2e^2h}{mcE}\right)f''\right]N_a t+B(E), \qquad (5.6)$$

where I_0 is the incident beam intensity, I_t is the transmitted beam intensity, w_a is the atomic weight of atom a, A is Avogadro's number, e is the electron charge, h is Planck's constant, m is the electron mass, c is the speed of light, E is the photon energy, N_a is the number density of a atoms, t is the sample thickness, and $B(E)$ represents the background absorption. $N_a t$ and $B(E)$ were determined from equation (5.6) by fitting to the data as described in Chapter II, section 2.5 *(c)*. Once these values were known, the experimental values of f'' could be extracted from the data. Experimental values of f' were calculated

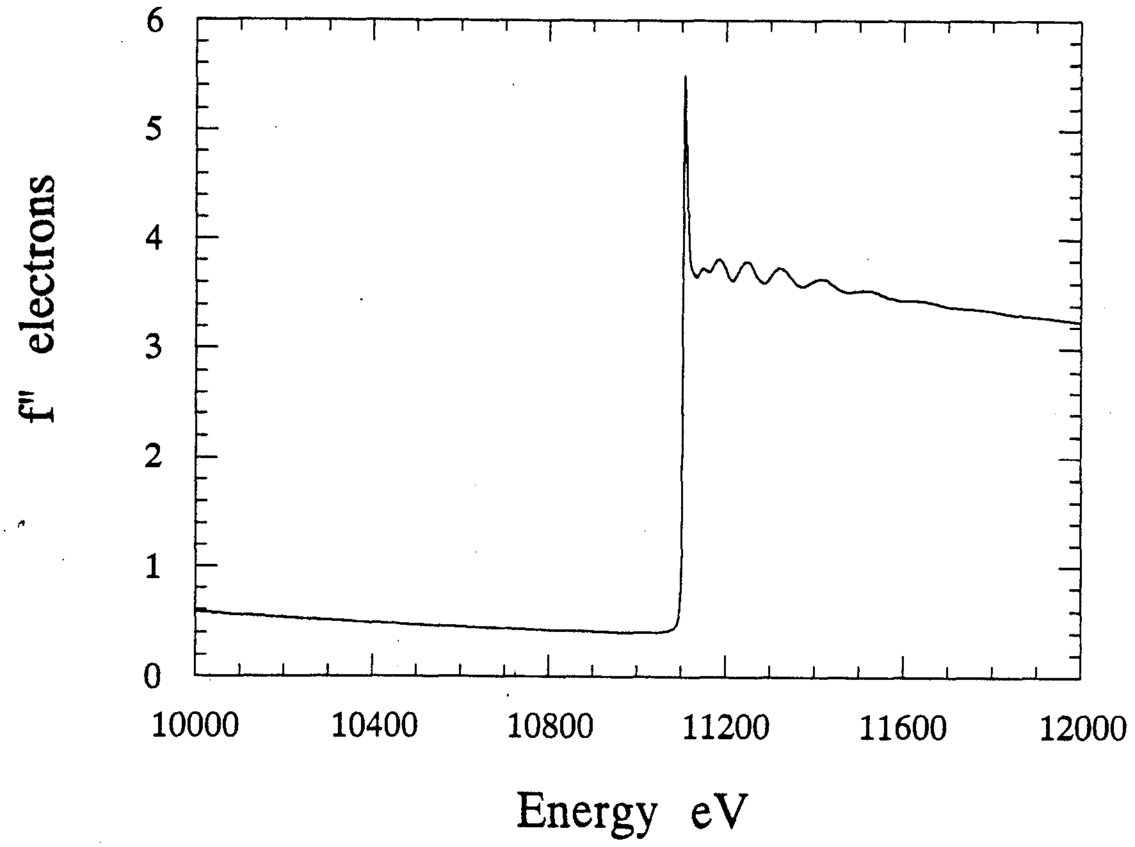

FIGURE V.1 Experimentally determined values of f'' for *a*-Ge plotted as a function of incident photon energy.

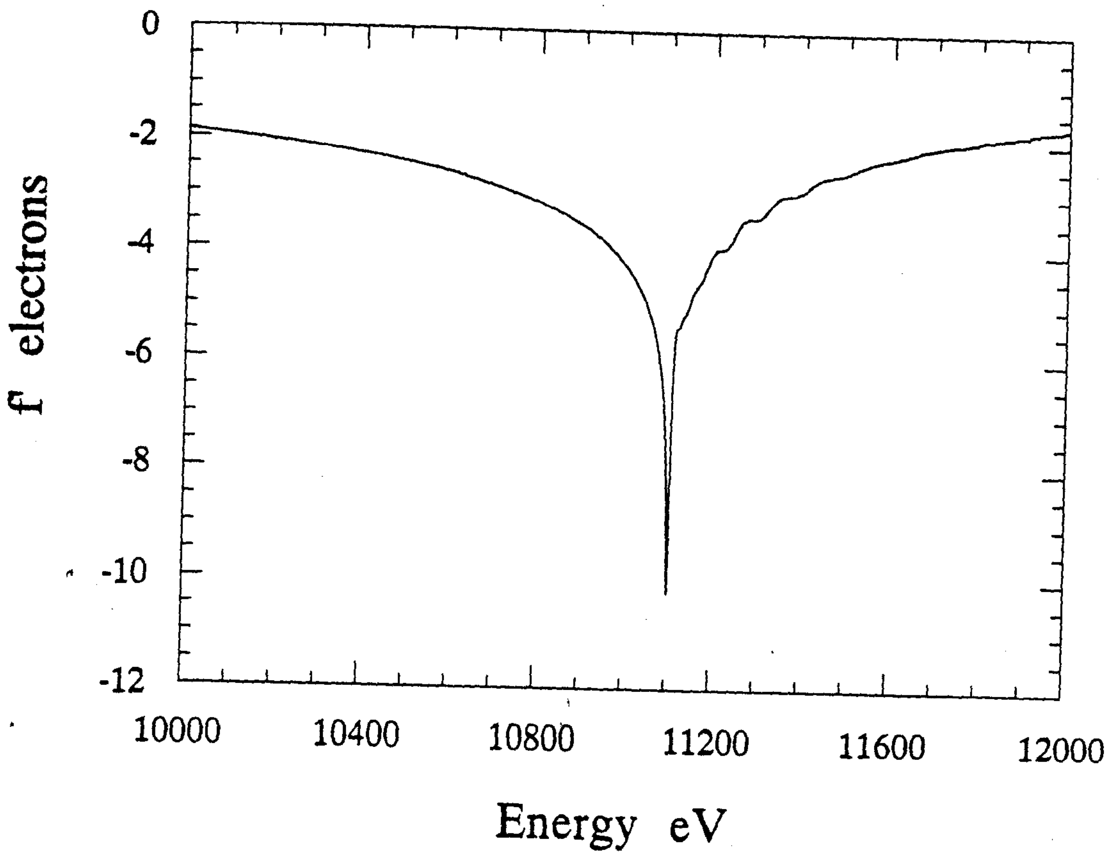

FIGURE V.2 Experimentally determined values of f' for *a*-Ge plotted as a function of incident photon energy.

from the experimental values of f'' through application of the Kramers-Kronig relationship (Hoyt et al., 1984; Ludwig, 1986):

$$f'(\omega_0) = \frac{2}{\pi} ⨍_0^{\infty} \frac{\omega f''(\omega)}{\omega_0^2 - \omega^2}\, d\omega \tag{5.7}$$

where $\omega = 2\pi E/h$, and $⨍$ denotes the Cauchy principal value of the integral.

(c) The effective electron density fluctuation:

The observable quantity in X-ray scattering is not the amplitude but rather the intensity, the absolute square of the amplitude

$$I(\mathbf{k},E) = I_e(\mathbf{k}) \int_{V_1} \int_{V_2} \rho_{eff}(\mathbf{r}_n,E) \rho_{eff}^*(\mathbf{r}_m,E)\; e^{-i\mathbf{k}\bullet(\mathbf{r}_n-\mathbf{r}_m)} dV_1 dV_2. \tag{5.8}$$

In equation (5.8), I_e is the intensity of radiation scattered by a single free electron. It is the scattered amplitude of a free electron multiplied by its complex conjugate

$$I_e(\mathbf{k}) = A_e(\mathbf{k}) A_e{}^*(\mathbf{k}) = I_0 \left(\frac{e^2}{mc^2} \right) \frac{1}{r^2} \sin^2 \psi \tag{5.9}$$

where I_0 is the incident beam intensity, e is the electronic charge, m is the mass of the electron, c is the speed of light, r is the distance between the electron and the point of observation and ψ is the angle between the scattered beam and the direction of acceleration of the electron. The quantity e^2/mc^2 is the classical electron radius, r_e, and is equal to 2.82×10^{-13} cm. For the small angle X-ray scattering experiments described here, ψ is approximately equal to 90°, therefore $\sin^2\psi$ is taken as equal to 1.

The average effective electron density of the sample, $\rho_0(E)$, is a constant at any particular photon energy and its Fourier transformation is a delta function at $\mathbf{k}=0$. What one observes in a scattering experiment is the absolute square of the Fourier transformation of the variation of the effective electron density about the mean

$$I(\mathbf{k},E) = I_e(\mathbf{k}) \left| \int_V \left[\rho_{eff}(\mathbf{r}_n,E) - \rho_0(E) \right] e^{-i\mathbf{k}\cdot\mathbf{r}_n} dV \right|^2. \tag{5.10}$$

The effective electron density fluctuation $[\rho_{eff}(\mathbf{r}_n,E)-\rho_0(E)]$, is often given its own symbol, $\eta(\mathbf{r}_n,E)$, so that

$$I(\mathbf{k},E) = I_e(\mathbf{k}) \left| \int_V \eta(\mathbf{r}_n, E) e^{-i\mathbf{k}\cdot\mathbf{r}_n} dV \right|^2 . \tag{5.11}$$

(d) The correlation function and the invariant:

By a simple change of variables, equation (5.11) can be rewritten as the Fourier transformation of the effective electron density fluctuation pair correlation function

$$I(\mathbf{k},E) = I_e(\mathbf{k}) \int_V e^{-i\mathbf{k}\cdot\mathbf{r}_n} d^3\mathbf{r}_n \int_V \eta(\mathbf{r}', E)\eta^*(\mathbf{r}_n + \mathbf{r}', E) d^3\mathbf{r}' . \tag{5.12}$$

The correlation function, $\gamma(\mathbf{r}_n)$, introduced by Debye & Bueche (1949), is defined as the average over all two-point correlations of the effective electron density fluctuation

$$\gamma(\mathbf{r}_n, E) = \left\langle \eta(\mathbf{r}', E)\eta^*(\mathbf{r}_n + \mathbf{r}', E) \right\rangle = \frac{1}{V} \int_V \eta(\mathbf{r}', E)\eta^*(\mathbf{r}_n + \mathbf{r}', E) d^3\mathbf{r}' . \tag{5.13}$$

In terms of the correlation function the intensity can be expressed as

$$I(\mathbf{k},E) = I_e(\mathbf{k}) V \int_V \gamma(\mathbf{r}_n, E) e^{-i\mathbf{k}\cdot\mathbf{r}_n} d^3\mathbf{r}_n \tag{5.14}$$

and vice versa

$$V\gamma(\mathbf{r}_n, E) = \frac{1}{(2\pi)^3 I_e(\mathbf{k})} \int_V I(\mathbf{k},E) e^{i\mathbf{k}\cdot\mathbf{r}_n} d^3\mathbf{k}. \tag{5.15}$$

For $\mathbf{r}_n$=0, equation (5.15) takes a particularly simple form

$$V\gamma(0, E) = \frac{1}{(2\pi)^3 I_e(\mathbf{k})} \int_V I(\mathbf{k},E) d^3\mathbf{k} = V\left\langle |\eta(E)|^2 \right\rangle . \tag{5.16}$$

This equation shows that the integral of the intensity over reciprocal space depends only on the mean square fluctuation of the effective electron density. For this reason this integral is called the invariant, Q,

$$Q = \int_V I(\mathbf{k},E) d^3\mathbf{k}. \tag{5.17}$$

(e) SAXS- a probe of intermediate range structure:

Due to the reciprocal relationship between **r** and **k**, the larger an object is in spatial extent, the narrower its first scattering maximum (and are subsidiary maxima) will be in **k** space. Small angle X-ray scattering, SAXS, is, therefore, a probe of electron density fluctuations of larger than atomic scale dimensions. Typical dimensions of objects accessible to SAXS are in the range of 10-1000 Å. SAXS is thus a probe of the intermediate range structure of materials.

(f) Particulate systems:

The central use of small angle X-ray scattering (SAXS) is as a tool to determine the large scale (relative to an atom) electron density distribution within a sample. This means identifying the types, sizes, and distribution of chemical species and physical defects (such as cracks and voids) in the sample. This information is often difficult to recover unambiguously from the SAXS intensity. The equation relating the effective electron density fluctuations to the scattered intensity can be of limited value in solving the structure of a system unless *a priori* knowledge is available or simplifying assumptions can be made.

One of the most common simplifying assumptions in SAXS theory is that the object under investigation is phase separated into two types of regions, each with its own distinct electron density. Furthermore, one phase is assumed to take the form of particles of a well defined shape immersed in the second phase and the particles are assumed to be so widely spaced as to behave as a collection of isolated particles. While these assumptions may seem unrealistic, they are valid for many systems, e.g., large molecules in dilute solutions.

The easiest particle shape to consider (and the only shape considered here) is a sphere. The form factor (the amplitude of scattered radiation, in electron units, divided by the number of electrons in the particle) for a uniform sphere of radius R is given by

$$\Phi(kR) = 3\frac{\sin(kR) - (kR)\cos(kR)}{(kR)^3}. \qquad (5.18)$$

The intensity of radiation scattered by a dilute array of N identical spheres of volume V_p and effective electron density $\rho_p(E)$, immersed in a medium of effective electron density $\rho_m(E)$, is given by

$$I(k) = I_e(k)NV_p{}^2\left(\rho_p(E) - \rho_m(E)\right)^2 \Phi^2(kR). \qquad (5.19)$$

The vector **k** has been replaced by a scalar k in equation (5.19) due to the orientational symmetry of spheres.

(g) Reciprocity:

An aspect of SAXS, apparent in equation (5.19), that adds to the complexity of structure determination is that the intensity is a function of the square of the effective electron density fluctuations. This means, for example, that the SAXS from a collection of N spherical cavities of radius R embedded in a material of constant electron density ρ_0, and the SAXS from a collection of N spheres of radius R and electron density ρ_0 will be indistinguishable. This is the Babinet principle of reciprocity which is valid even when the electron density is a complex quantity.

(h) Non-dilute systems:

For many systems, the assumption of a dilute distribution of particles is not valid and interparticle interference must be taken into account. The main manifestation of interparticle interference is the appearance of a shoulder or a peak in the SAXS pattern at a non-zero value of k. In mathematical descriptions of the intensity of radiation scattered by a system of densely packed particles, the total intensity scattered by N particles is set equal to the intensity scattered by N isolated particles plus a second term that accounts for the interparticle interference. The interparticle interference term is designed so that it will go to zero for dilute systems. The interparticle interference term is usually described as a function of a probability distribution, $P(r)$, that gives the probability of finding two particles separated by a distance r. The equation for the total intensity scattered from a densely packed system of identical spheres is expressed as

$$I(k) = NI_p(k)\left[1 - \frac{N}{V}\int_0^\infty \left(1 - P(r)\right) \frac{\sin kr}{kr} 4\pi\, r^2 dr\right] \qquad (5.20)$$

where $I_p(k)$ is the intensity of radiation scattered by one sphere and the phase factor has been replaced by its average over all orientations (Debye, 1915). This is the well known formula of Zernicke and Prins (1927).

A solution to the Zernicke-Prins equation for describing the intensity of scattering from a collection of densely packed, identical spheres is the Born-Green (Born & Green, 1946) approximation given by

$$I(k) = I_e(k) N V_p^2 \left(\rho_p(E) - \rho_m(E)\right)^2 \Phi^2(kR) \left[\frac{1}{1 + \frac{8V_p}{v_1}\Phi(2kR)}\right] \qquad (5.21)$$

where v_1 is the sample volume divided by the number of particles in the sample. The Born-Green approximation was derived for liquids where the particles are atoms that can not come any closer than the sum of their radii, $2R$. The quantity V_p/v_1 is actually c, the fraction of the total sample volume occupied by the spherical particles.

(i) Inhomogeneous particles:

Another cause of a peak in the SAXS pattern at non-zero k values is a dilute (or dense) collection of identical inhomogeneous particles. The inhomogeneous particle considered here is a sphere with a spherical core of effective electron density $\rho_c(E)$ and an outer spherical shell of effective electron density $\rho_s(E)$ immersed in a background matrix of effective electron density $\rho_m(E)$. The intensity of radiation scattered from a dilute collection of such identical, inhomogeneous spheres is given by

$$I(k) = I_e(k) N_p \left[V_c \, (\rho_c(E) - \rho_s(E))\Phi(kR_c) + V_s \, (\rho_s(E) - \rho_m(E))\Phi(kR_s)\right]^2 \qquad (5.22)$$

where R_c is the radius of the core, V_c is the volume of the core, R_s is the radius of the entire sphere, V_s is the volume of the entire sphere, and N_p is the number of spheres in the illuminated volume.

(j) A note on notation:

The equations of SAXS theory have been presented in terms of the intensity, $I(k)$, the square of the scattered amplitude, $A(k)$. This notation is consistent with all the classical texts on X-ray diffraction and SAXS. In the discussions of the data that follow, the quantity of interest is the absolute differential scattering cross section per unit volume, $d\Sigma/d\Omega\ (k)$. The differential scattering cross section per unit volume has already been defined in Chapter IV as the number of photons scattered per second divided by the incident flux (photons per second per cm^2) per unit solid angle per unit sample volume (Russell, Lin, Spooner & Wignall, 1988). In terms of the measured count rate, $I_m(k)$,

$$\left[\frac{d\Sigma}{d\Omega}(k)\right]=\frac{I_m(k)}{tI_0e^{-\mu t}}\frac{r^2}{\varepsilon\Delta a}, \qquad (5.23)$$

where t is the sample thickness, I_0 is the flux incident on an area, A, of the sample, the illuminated volume, V, is equal to A times t, $e^{-\mu t}$ is the attenuation factor with μ equal to the linear absorption coefficient, r is the sample-to-detector distance, Δa is the area of a detecting element so that $\Delta a/r^2$ is the solid angle subtended by the detecting element, and ε is the counting efficiency of the detector. The relationship between the classical intensity, $I(k)$, and the differential scattering cross section per unit volume, $d\Sigma/d\Omega\ (k)$, is

$$\frac{I(k)}{VI_e}=\frac{1}{r_e^2}\frac{d\Sigma}{d\Omega}(k) \qquad (5.24)$$

where V is the illuminated volume, and r_e is the classical electron radius.

5.2 THE PURE *a*-GE SAMPLE

ASAXS data from the pure *a*-Ge film are displayed in Figures V.3 and V.4. Figure V.3 shows the absolute differential scattering cross section per unit volume, $d\Sigma/d\Omega(k)$, (hereafter referred to as the "differential scattering cross section" or just "scattering cross section") at five different photon energies beneath the K absorption edge of Ge. As the incident photon energy is increased beneath the Ge edge, the scattering cross section decreases in magnitude. This is what one would expect for a single element system.

Figure V.4 shows the behavior of the differential scattering cross section as the incident photon energy is increased beneath the Fe *K* absorption edge. Across most of the *k* range shown in Figure V.4, the scattering cross section remains constant as the incident photon energy is increased beneath the Fe edge. This is also the expected result for photon energies far from any absorption edge in the material. At extremely low *k*, ($k<0.02$ Å^{-1}), there appears to be a decrease in $d\Sigma/d\Omega(k)$ with increasing photon energy. The data at low *k*, however, are contaminated by parasitic scattering. The *k* range that suffers from parasitic contamination (typically $k<0.01$ or 0.02, depending on the camera length and the incident photon energy) is excluded from further consideration.

As is apparent in Figures V.3 and V.4, the pure *a*-Ge sample exhibits small angle X-ray scattering. Since this scattering obviously does not arise from chemical inhomogeneities, it must arise from simple density fluctuations such as cracks and voids. A simple fit to equation (5.19), assuming identical spherical voids, yields a void radius of 120 Å and a volume fraction of .001. This is consistent with figures in the literature for the volume fraction of voids in sputtered *a*-Ge (Shevchik & Paul, 1974). The SAXS may be better described by cracks.

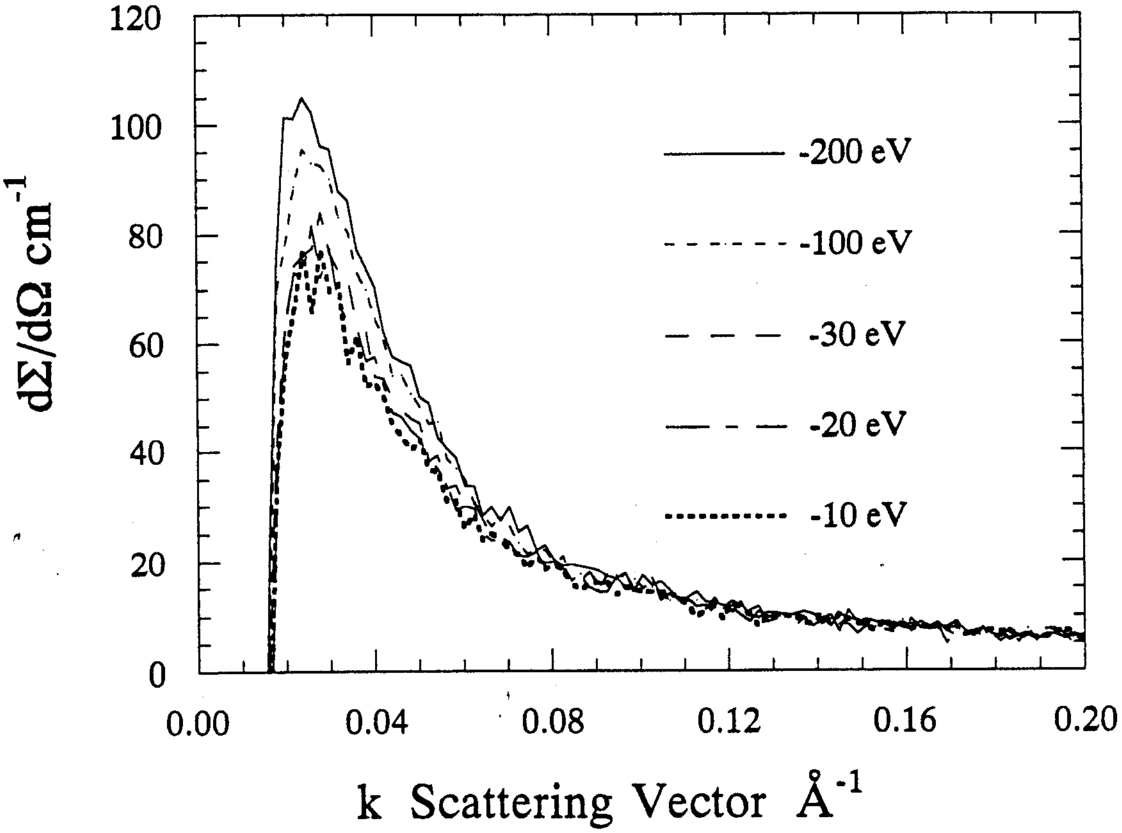

FIGURE V.3 The differential scattering cross section, $d\Sigma/d\Omega(k)$, for the *a*-Ge sample at incident photon energies of 200, 100, 30, 20, and 10 eV below the Ge *K* absorption edge.

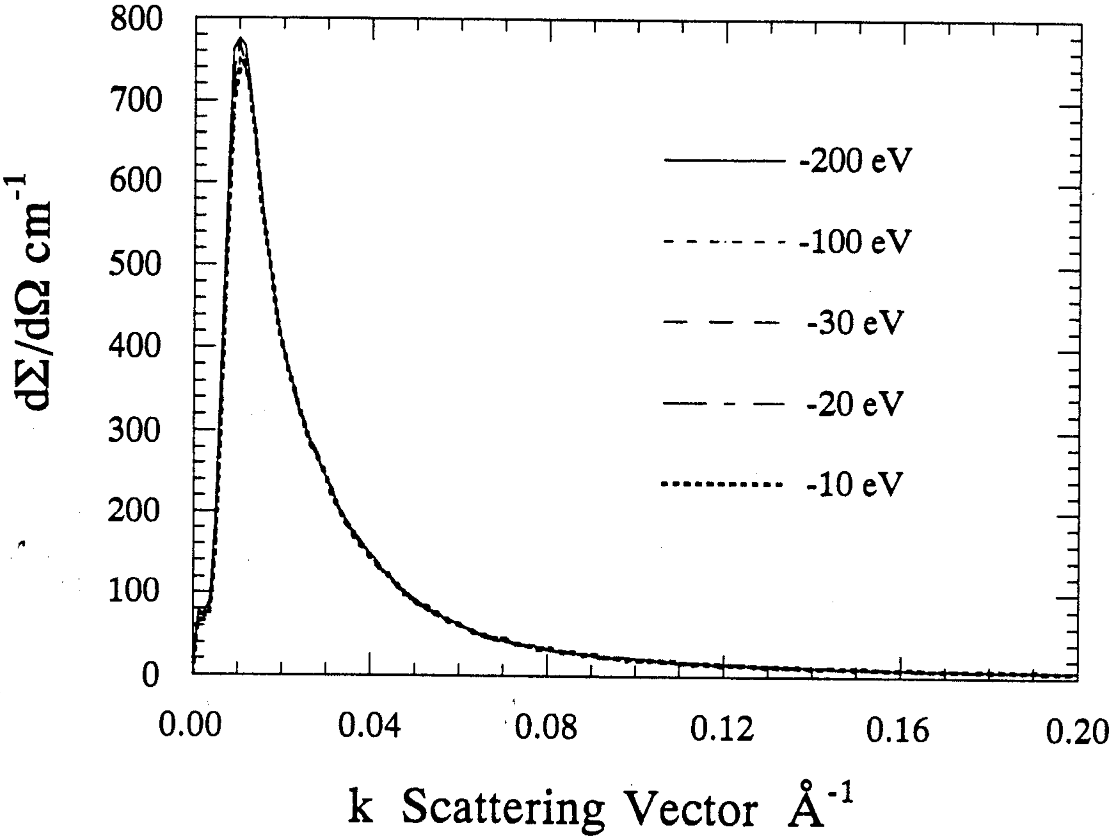

FIGURE V.4 The differential scattering cross section, $d\Sigma/d\Omega(k)$, for the *a*-Ge sample at incident photon energies of 200, 100, 30, 20, and 10 eV below the Fe *K* absorption edge.

5.3 THE ASAXS DATA AND UNIFORM GE DISTRIBUTION

(a) Appearance of the ASAXS data for samples with homogeneous Ge distribution:

The most striking result of the ASAXS experiments is the behavior of the differential scattering cross section, $d\Sigma/d\Omega(k)$, for all the metal-germanium samples with less than 25 atomic percent metal. All three systems, a-Fe$_x$Ge$_{100-x}$, a-W$_x$Ge$_{100-x}$, and a-Mo$_x$Ge$_{100-x}$, have a peak in $d\Sigma/d\Omega(k)$ at a k value between approximately 0.15 and 0.30 Å^{-1} for these low metal concentration samples. Additionally, for the a-Fe$_x$Ge$_{100-x}$ and the a-W$_x$Ge$_{100-x}$ samples, the differential scattering cross section decreases as the photon energy is increased below the metal absorption edge. Below the Ge absorption edge, the differential scattering cross section remains unchanged as the photon energy is increased from lower energies for all the a-Fe$_x$Ge$_{100-x}$, a-W$_x$Ge$_{100-x}$, and a-Mo$_x$Ge$_{100-x}$ samples in this concentration range. As previously mentioned, experimental difficulties prevented data collection for the a-Mo$_x$Ge$_{100-x}$ samples at the Mo K absorption edge.

The ASAXS results for the a-Fe$_x$Ge$_{100-x}$, a-W$_x$Ge$_{100-x}$, and a-Mo$_x$Ge$_{100-x}$ samples with $0<x<25$ are presented in Figures V.5-V.14. Each figure shows the differential scattering cross section, $d\Sigma/d\Omega(k)$, for five different incident photon energies beneath an absorption edge of a particular sample. Some of the plots show a small sharp peak near k=0.4 Å^{-1}. This is the remainder of the Kapton peak after imperfect background subtraction.

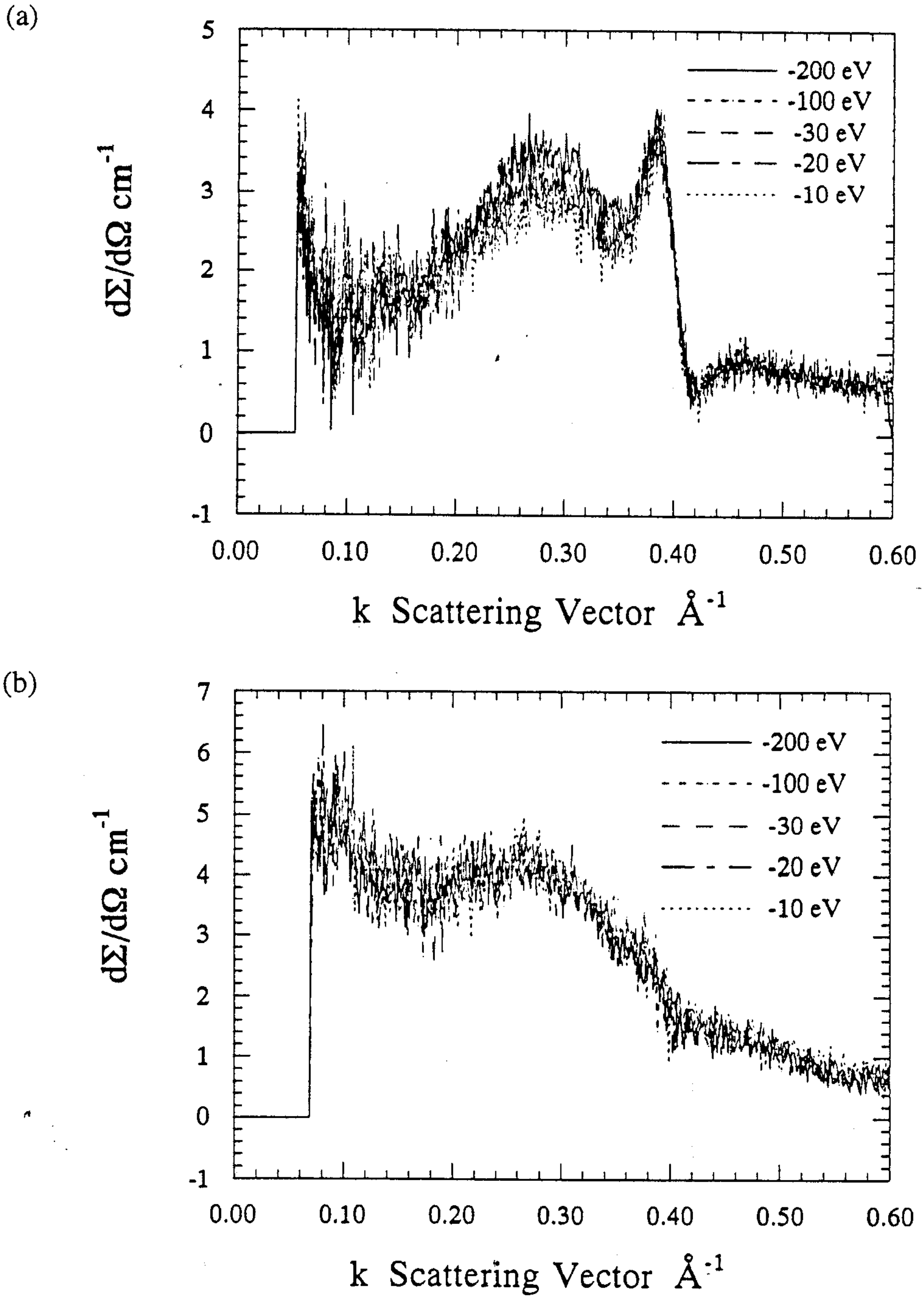

FIGURE V.5 The *a*-Fe_5Ge_{95} sample. (a) The differential scattering cross section at incident photon energies of 200, 100, 30, 20, and 10 eV below the Fe *K* absorption edge. Residual Kapton peak seen at k=0.4 Å^{-1}. (b) The differential scattering cross section at incident photon energies of 200, 100, 30, 20, and 10 eV below the Ge *K* absorption edge.

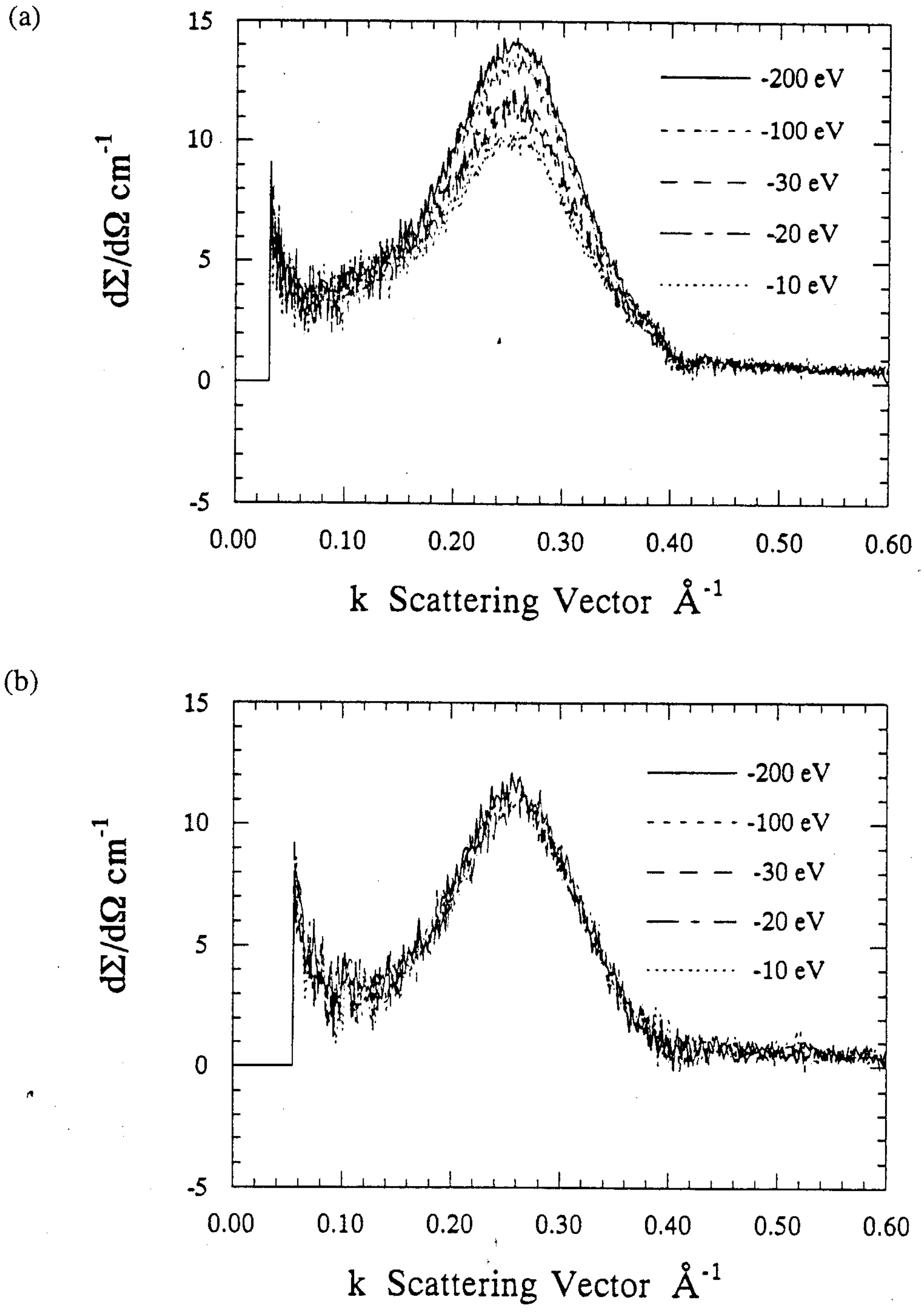

FIGURE V.6 The a-$Fe_{12}Ge_{88}$ sample. (a) The differential scattering cross section at incident photon energies of 200, 100, 30, 20, and 10 eV below the Fe *K* absorption edge. (b) The differential scattering cross section at incident photon energies of 200, 100, 30, 20, and 10 eV below the Ge *K* absorption edge.

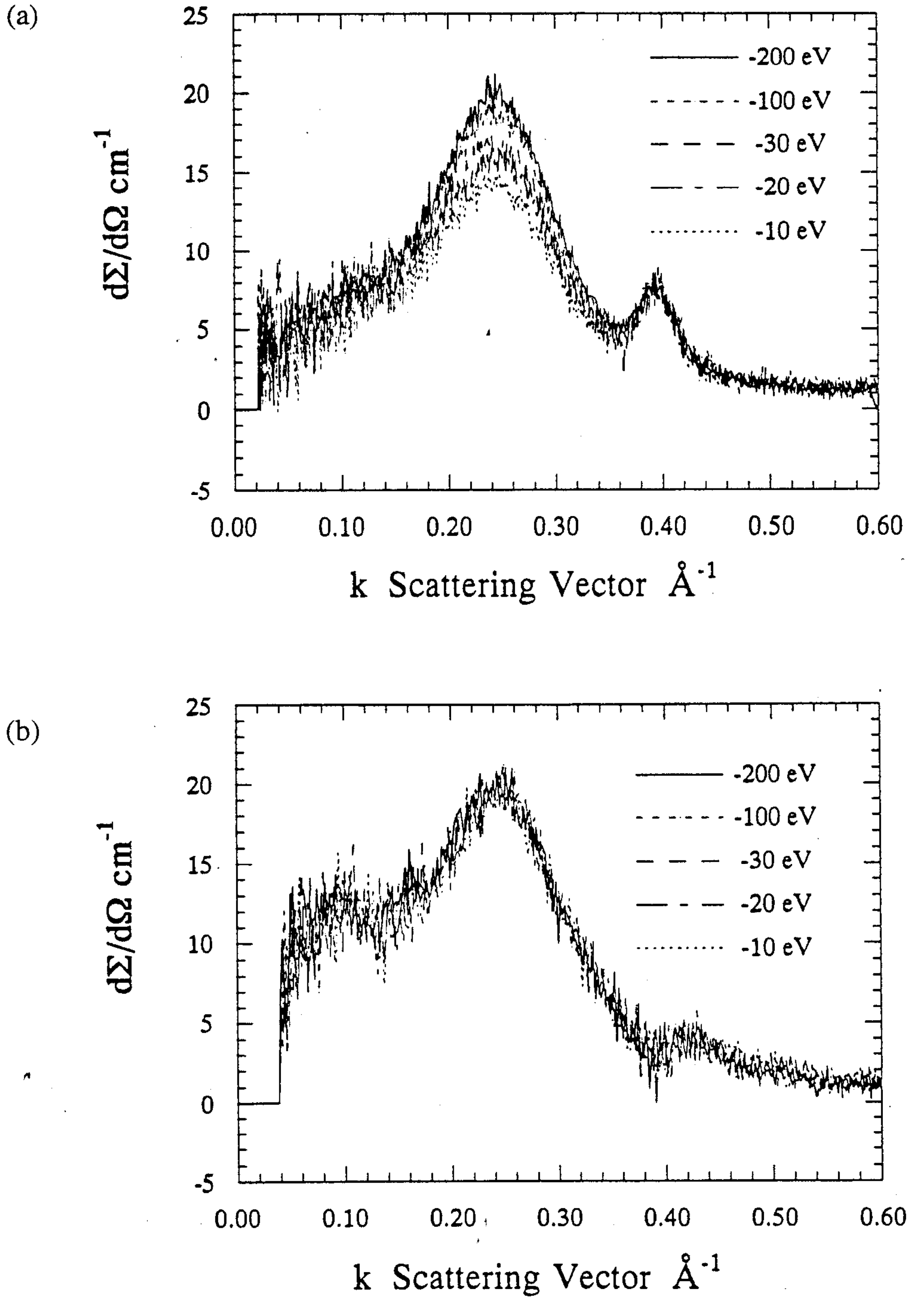

FIGURE V.7 The *a*-$Fe_{18}Ge_{82}$ sample. (a) The differential scattering cross section at incident photon energies of 200, 100, 30, 20, and 10 eV below the Fe *K* absorption edge. Residual Kapton peak near *k*=0.4 Å^{-1}. (b) The differential scattering cross section at incident photon energies of 200, 100, 30, 20, and 10 eV below the Ge *K* absorption edge.

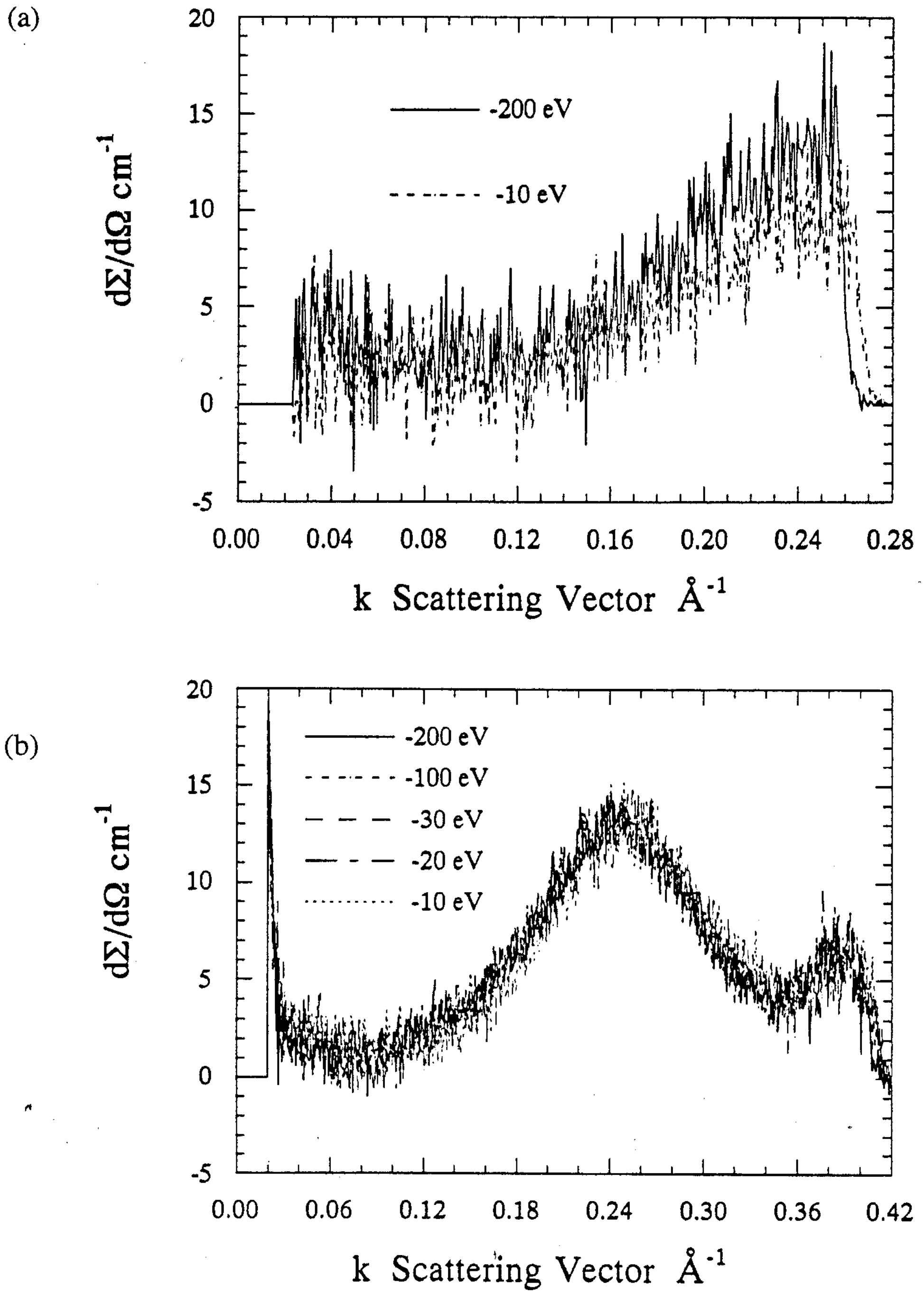

FIGURE V.8 The a-$Fe_{19}Ge_{81}$ sample. (a) The differential scattering cross section at incident photon energies of 200 and 10 eV below the Fe K absorption edge (only two energies are shown for clarity). (b) The differential scattering cross section at incident photon energies of 200, 100, 30, 20, and 10 eV below the Ge K absorption edge. Residual Kapton peak near k=0.4 Å^{-1}.

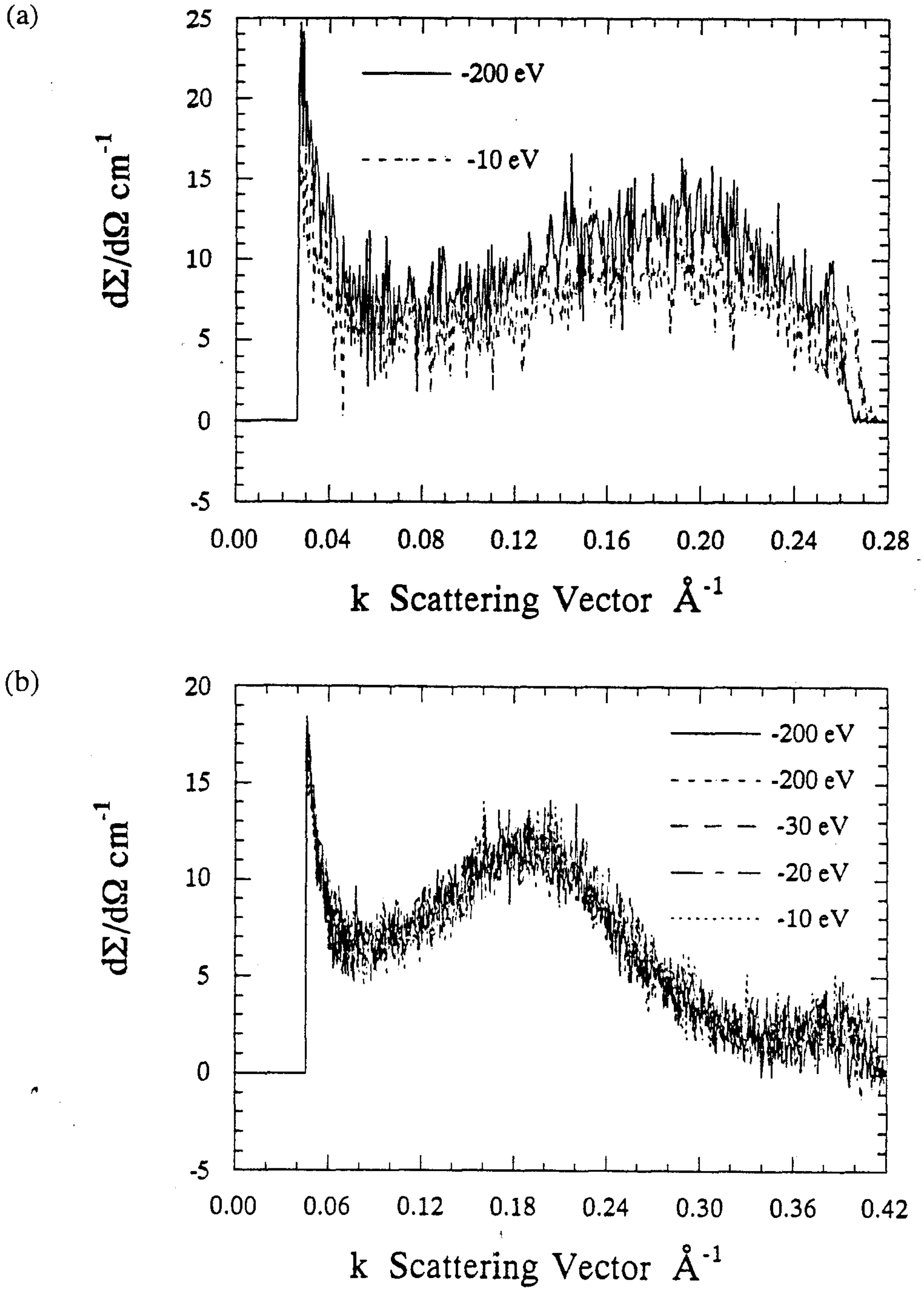

FIGURE V.9 The a-$Fe_{24}Ge_{76}$ sample. (a) The differential scattering cross section at incident photon energies of 200 and 10 eV below the Fe K absorption edge (only two energies are shown for clarity). (b) The differential scattering cross section at incident photon energies of 200, 100, 30, 20, and 10 eV below the Ge K absorption edge. Residual Kapton peak near k=0.4 $Å^{-1}$.

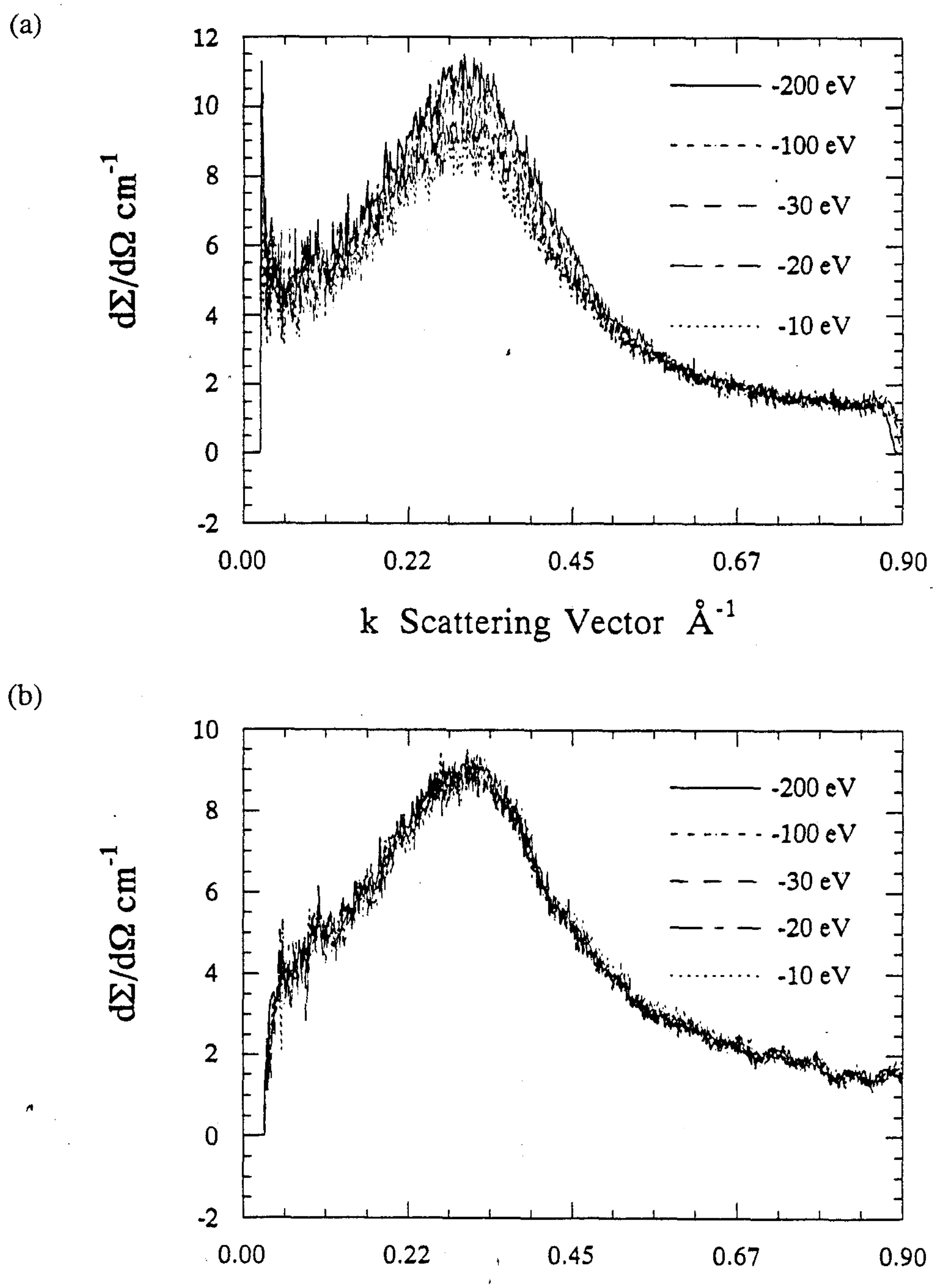

FIGURE V.10 The a-W_7Ge_{93} sample. (a) The differential scattering cross section at incident photon energies of 200, 100, 30, 20, and 10 eV below the W L_{III} absorption edge. (b) The differential scattering cross section at incident photon energies of 200, 100, 30, 20, and 10 eV below the Ge K absorption edge.

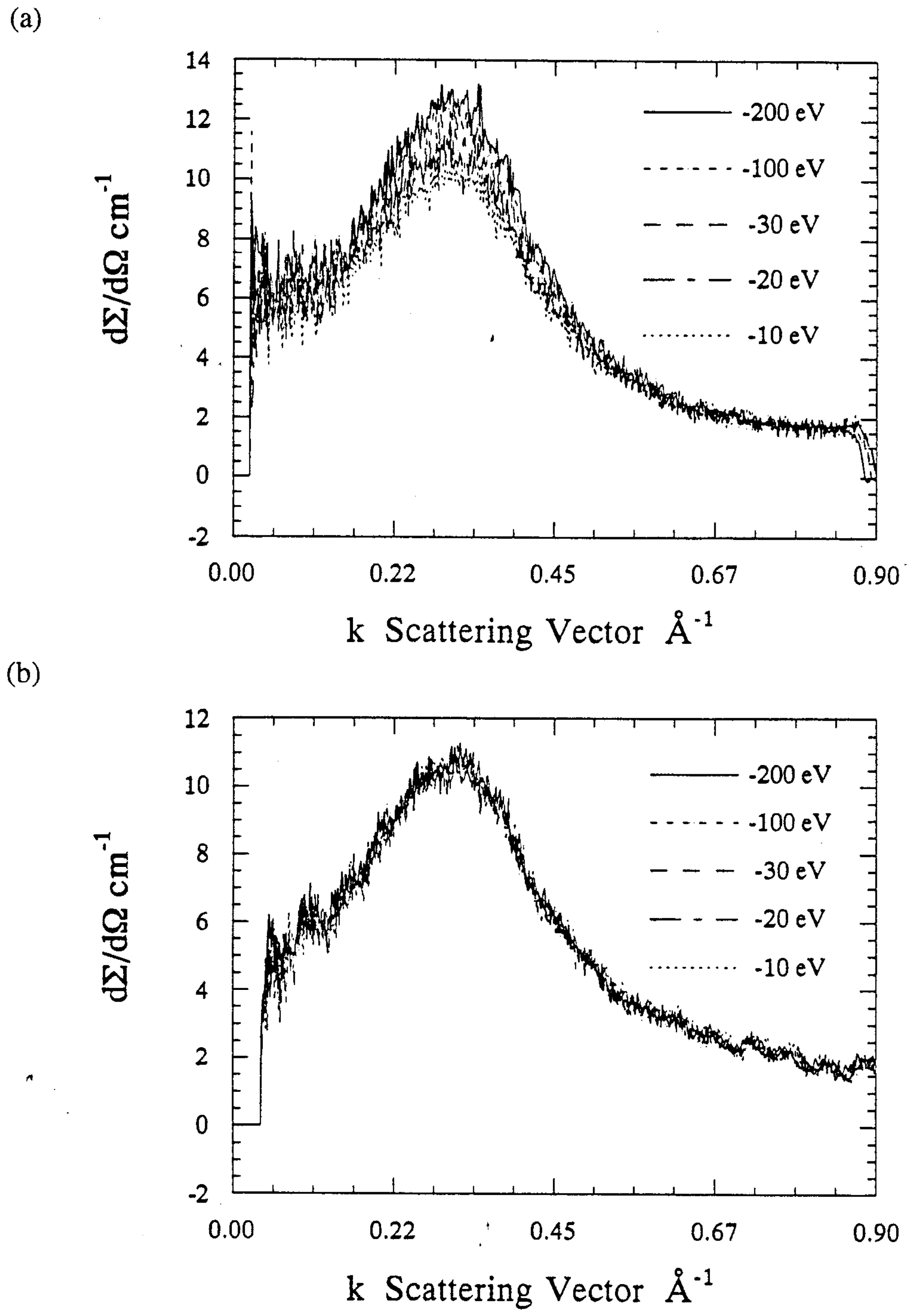

FIGURE V.11 The *a*-W_8Ge_{92} sample. (a) The differential scattering cross section at incident photon energies of 200, 100, 30, 20, and 10 eV below the W L_{III} absorption edge. (b) The differential scattering cross section at incident photon energies of 200, 100, 30, 20, and 10 eV below the Ge *K* absorption edge.

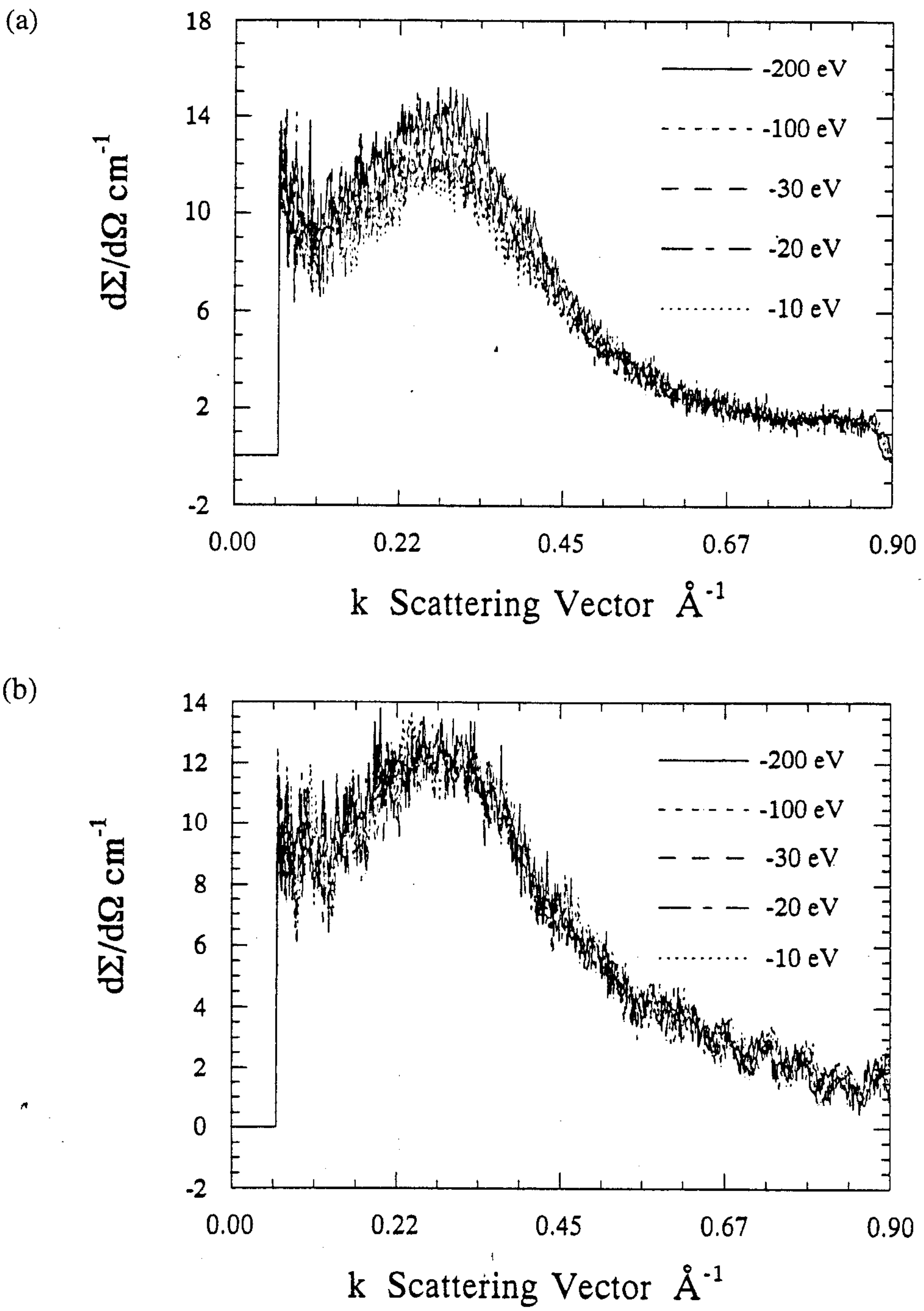

FIGURE V.12 The a-$W_{17}Ge_{83}$ sample. (a) The differential scattering cross section at incident photon energies of 200, 100, 30, 20, and 10 eV below the W L_{III} absorption edge. (b) The differential scattering cross section at incident photon energies of 200, 100, 30, 20, and 10 eV below the Ge K absorption edge.

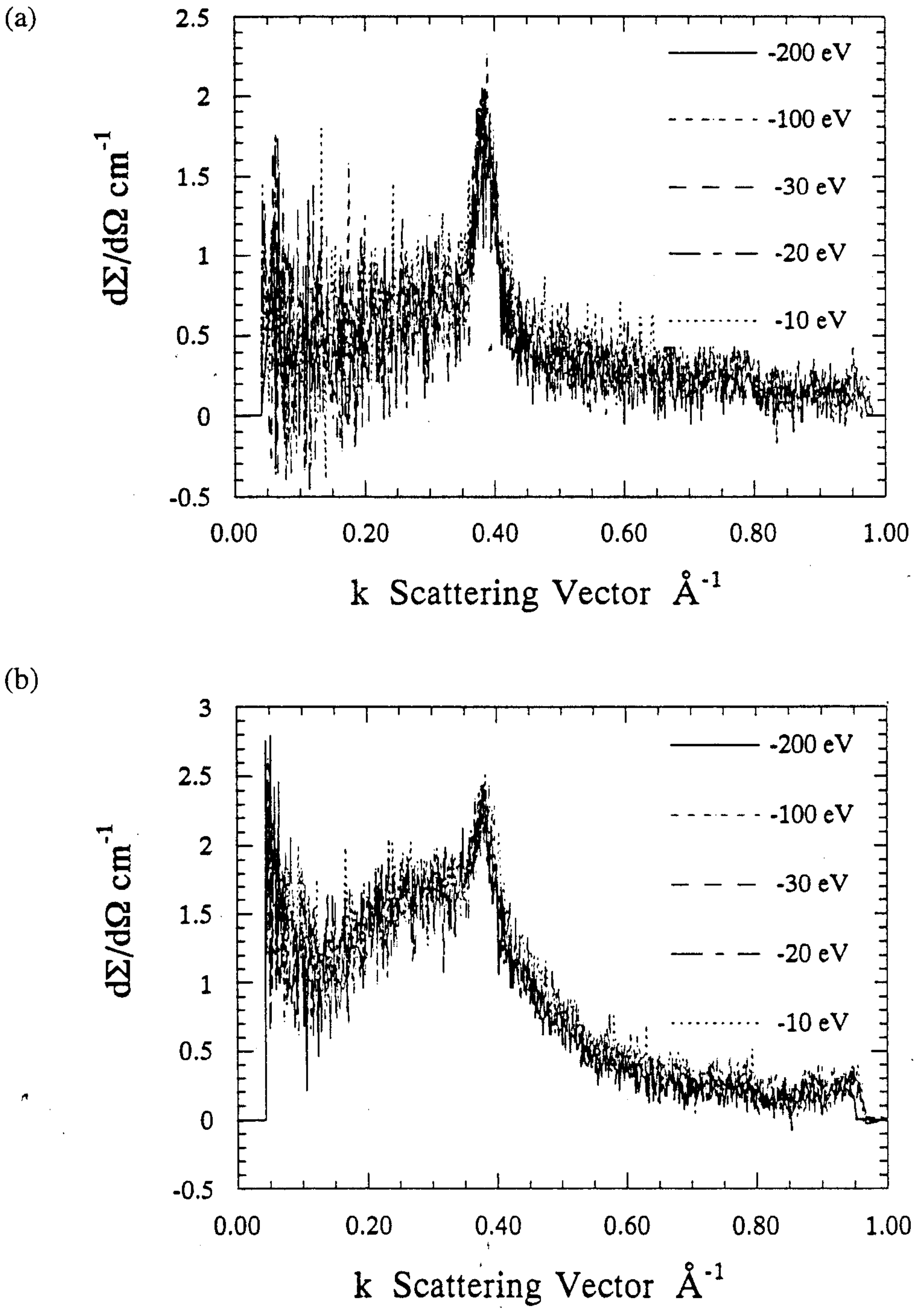

FIGURE V.13 The differential scattering cross section at incident photon energies of 200, 100, 30, 20, and 10 eV below the Ge *K* absorption edge in (a) *a*-Mo_3Ge_{97} and (b) *a*-Mo_6Ge_{94}. Residual Kapton peak near k=0.4 $Å^{-1}$.

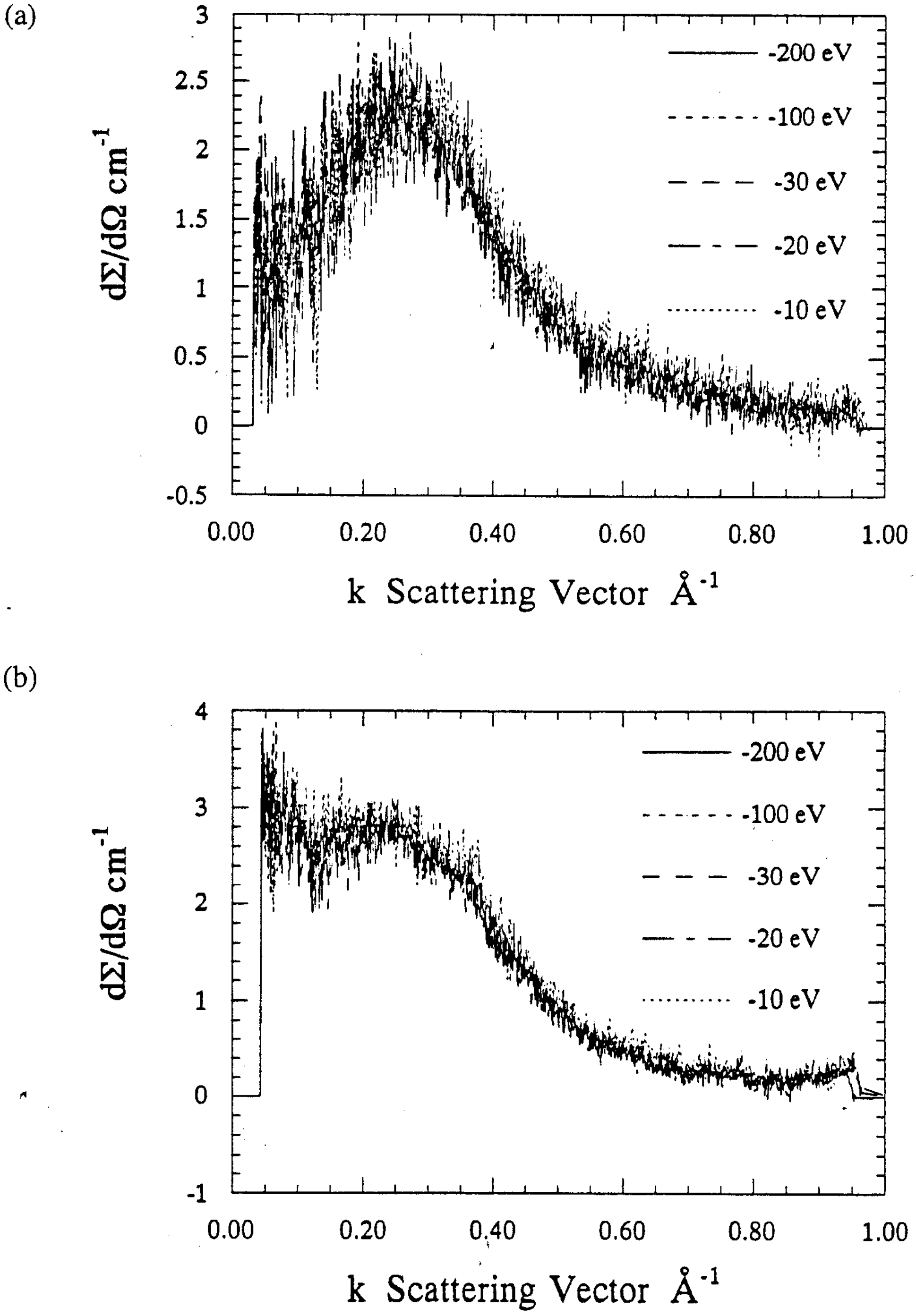

FIGURE V.14 The differential scattering cross section at incident photon energies of 200, 100, 30, 20, and 10 eV below the Ge *K* absorption edge in (a) *a*-$Mo_{13}Ge_{87}$ and (b) *a*-$Mo_{14}Ge_{86}$.

The presence of a well defined peak in the scattering cross section for each of these samples at a value of k near 0.25 $Å^{-1}$ broadcasts immediately two important pieces of information. First, all of these samples have electron density fluctuations on a scale of tens of Ångströms. Second, the entities that give rise to the peaks can not be described as a dilute concentration of homogeneous particles.

Further information is also immediately available from the behavior of the ASAXS patterns beneath the Ge absorption edge. As the photon energy is increased beneath the Ge K absorption edge, f' for Ge rapidly becomes increasingly negative. The radiation scattered by each Ge atom should, therefore, be reduced as the photon energy is increased. The peak in $d\Sigma/d\Omega(k)$ for each of these samples, however, does not change as the photon energy approaches the Ge K absorption edge. This means that Ge atoms do not contribute to these peaks. These peaks are not caused by fluctuations in the density of Ge atoms-- the density of Ge atoms is *uniform* through out each of these samples.

A uniform Ge density implies three other things. One, the peaks do not arise from voids and/or cracks. If the density fluctuations were the result of voids and/or cracks, the density of Ge atoms would not be uniform throughout the samples. Two, the electron density fluctuations must, therefore, arise from fluctuations in the density of metal atoms. Three, the metal atoms can not be clumped together because, again, the distribution of Ge atoms would not be uniform.

The picture that emerges just from looking at the data is one in which the a-Fe_xGe_{100-x}, a-W_xGe_{100-x}, and the a-Mo_xGe_{100-x} samples with less than 25 atomic percent metal are all compositionally modulated on a scale of approximately 25 Å. The distribution of Ge atoms is uniform across each of these samples. The electron density fluctuations must arise from fluctuations in the density of metal atoms. The metal atoms, however, must be incorporated into a Ge containing substance that probably has a Ge number density similar to that of pure Ge. More rigorous proofs of these ideas follow.

(b) Theoretical treatment in terms of a two phase model:

The differential scattering cross section of small angle X-ray scattering, $d\Sigma/d\Omega(k)$, is related to the effective electron density fluctuation, $\rho(E)-\rho_0(E)$, through the expression

$$\frac{Q}{V}=\frac{1}{2\pi^2\ VI_e(k)}\int_0^\infty I(k)k^2dk=\frac{1}{2\pi^2 r_e^{\ 2}}\int_0^\infty \frac{d\Sigma}{d\Omega}(k)k^2dk=\frac{1}{NV}\int_V(\rho(E)-\rho_0(E))^2dV. \quad (5.25)$$

With the notation N is the number of atoms in the illuminated volume, V is the illuminated volume, f_A and f_B are the scattering factors for elements A and B, respectively, and m is the fraction of A atoms in the material, $\rho_0(E)$ is expressed as

$$\rho_0(E)=\frac{N}{V}[mf_A+(1-m)f_B]. \quad (5.26)$$

For a binary alloy that is phase separated into two phases, the effective electron density in phase 1 will be given by

$$\rho_1(E)=\frac{N_1}{V_1}[m_1f_A+(1-m_1)f_B], \quad (5.27)$$

while the effective electron density in phase 2 will be given by

$$\rho_2(E)=\frac{N_2}{V_2}[m_2f_A+(1-m_2)f_B] \quad (5.28)$$

where the subscripts 1 and 2 refer to the values of the variables in phases 1 and 2 respectively.

By denoting the volume fraction of the sample occupied by phase 1 as c, the integral in equation (5.25), which is really the sum of two integrals:

$$Q=\frac{1}{N}\int_V(\rho(E)-\rho_0(E))^2dV=\frac{1}{N}\left\{\int_{V_1}(\rho(E)-\rho_0(E))^2dV_1+\int_{V_2}(\rho(E)-\rho_0(E))^2dV_2\right\} \quad (5.29)$$

can be evaluated as

$$Q=\left(\frac{1}{N}\right)\left\{cV(\rho_1(E)-\rho_0(E))^2+(1-c)\ \ V(\rho_2(E)-\rho_0(E))^2\right\}. \quad (5.30)$$

Since ρ_0 is obviously equal to $[c\rho_1(E)+(1-c)\rho_2(E)]$, equation (5.30) can now be expressed as

$$Q=\frac{V}{N}\left[c(1-c)(\rho_1(E)-\rho_2(E))^2\right]. \quad (5.31)$$

This equation can be expressed in terms of f_A and f_B by use of equations (5.27) and (5.28), giving

$$Q=\frac{V}{N}[c(1-c)]\left\{\left[\frac{N_1}{V_1}m_1-\frac{N_2}{V_2}m_2\right]f_A+\left[\frac{N_1}{V_1}(1-m_1)-\frac{N_2}{V_2}(1-m_2)\right]f_B\right\}^2. \quad (5.32)$$

If the second phase of the material merely consists of voids, equation (5.32) reduces to

$$Q=\frac{V}{N}[c(1-c)]\left\{\frac{N_1}{V_1}[m_1f_A+(1-m_1)f_B]\right\}^2 \quad (5.33)$$

which will decrease as the scattering factor decreases beneath the absorption edge of either element in the sample. If Q remains unchanged as the scattering factor is varied beneath the absorption edge of one of the elements in the material, the coefficient in equation (5.32) for that scattering factor must be zero. Whether the scattering factor in question belongs to element A or element B, the result is the same:

$$\frac{N_1}{V_1}m_1=\frac{N_2}{V_2}m_2 \qquad \text{for } A \text{ atoms} \qquad (5.34)$$

or

$$\frac{N_1}{V_1}(1-m_1)=\frac{N_2}{V_2}(1-m_2) \qquad \text{for } B \text{ atoms.} \qquad (5.35)$$

When the differential scattering cross section remains constant as the scattering factor of one of the elements changes, the number density of that element is the same in phase 1 as it is in phase 2.

When the total number density of atoms in phases 1 and 2 is the same and is also equal to the number density of atoms in the bulk material, $N_1/V_1=N_2/V_2=N/V$, and equation (5.32) reduces to the Gerold equation (Gerold, 1961)

$$Q=\frac{N}{V}c(1-c)(m_1-m_2)^2(f_A-f_B)^2. \quad (5.36)$$

An investigation of the density of Ge atoms in *c*-Ge, *c*-Fe-Ge compounds, *c*-W-Ge compounds and *c*-Mo-Ge compounds provides a check on whether it is possible for Ge to be present in two phases in *a*-M_xGe_{100-x} samples and have the same density within each phase. The results of this investigation are displayed in Table V.1 and confirm this

TABLE V.1

Number density of Ge in various crystals.

Crystalline Compound/ Crystalline Structure	Volume of Unit Cell (Å^3)	Number of Atoms per Unit Cell	Total Number Density (Å^{-3})	Ge Number Density (Å^{-3})	Metal Number Density (Å^{-3})
Ge diamond cubic	181.13	8	0.0442	0.0442	0
$FeGe_2$ tetragonal ($CuAl_2$)	173.02	12	0.0694	0.0462	0.0231
$MoGe_2$ orthorhombic ($SiCo_2$)	187.86	12	0.0639	0.0426	0.0213
$MoGe_2$ tetragonal ($MoSi_2$)	90.70	6	0.0662	0.0441	0.0221
WGe_2 orthorhombic ($SiCo_2$)	188.35	12	0.0637	0.0425	0.0212
WGe_2 tetragonal ($MoSi_2$)	90.30	6	0.0664	0.0443	0.0221

hypothesis. Phase separation of a-M$_x$Ge$_{100-x}$ samples with $0<x<25$ into a-Ge and an amorphous MGe$_2$-like substance is consistent with the data.

(c) Theoretical treatment for the general case:

The above treatment is based on the assumption of classical phase separation in which the material separates into two distinct phases, each with a well defined electron density. This type of formulation excludes composition fluctuations that vary continuously rather than abruptly. A completely general description of the SAXS starts with the general equation for the total amplitude of radiation scattered by a sample (equation (5.4))

$$A(\mathbf{k}) = A_e(\mathbf{k}) \sum_{\alpha} \int_V f_\alpha N_\alpha(\mathbf{r}_n)\, e^{-i\mathbf{k}\bullet\mathbf{r}_n} dV. \tag{5.4}$$

With the notation

$$\tilde{N}_\alpha(\mathbf{k}) = \int_V N_\alpha(\mathbf{r}_n)\, e^{-i\mathbf{k}\bullet\mathbf{r}_n} dV, \tag{5.37}$$

the intensity of scattered radiation can be expressed as

$$I(\mathbf{k}) = A(\mathbf{k})A^*(\mathbf{k}) = I_e(\mathbf{k}) \sum_{\alpha} \sum_{\beta} f_\alpha f_\beta^* \tilde{N}_\alpha(\mathbf{k}) \tilde{N}_\beta^*(\mathbf{k}). \tag{5.38}$$

In term of the differential scattering cross section

$$\frac{d\Sigma}{d\Omega}(\mathbf{k}) = \frac{r_e^2}{V} \sum_{\alpha} \sum_{\beta} f_\alpha f_\beta^* \tilde{N}_\alpha(\mathbf{k}) \tilde{N}_\beta^*(\mathbf{k}). \tag{5.39}$$

When combining SAXS with the anomalous dispersion effect, the full expression for f_α must be used

$$f_\alpha(k,E) = f_{\alpha 0}(k) + f_\alpha'(k,E) + i f_\alpha''(k,E). \tag{5.40}$$

Recalling that f_α'' remains small and nearly invariant while f_α' rapidly becomes increasingly negative as the α absorption edge is approached from lower energy, the scattering cross section below the absorption edge of atom A will change as a function of photon energy as

$$\frac{\partial}{\partial f_A'}\left[\frac{d\Sigma}{d\Omega}(\mathbf{k})\right] = 2\frac{r_e^2}{V} \mathrm{Re}\left[\tilde{N}_A(\mathbf{k}) \sum_{\alpha} f_\alpha^* \tilde{N}_\alpha^*(\mathbf{k})\right]. \tag{5.41}$$

That is, the derivative of the scattering cross section at **k** with respect to the real part of the atomic scattering factor of atom A is proportional to the Fourier transformation of $N_A(\mathbf{r}_n)$ evaluated at **k**.

Now, if A is distributed homogeneously,

$$\tilde{N}_A(\mathbf{k}) = \tilde{N}_A(0)\delta(\mathbf{k}) \tag{5.42}$$

and

$$\frac{\partial}{\partial f'_A}\left[\frac{d\Sigma}{d\Omega}(\mathbf{k})\right] = 0 \tag{5.43}$$

for all **k** not equal to zero.

So, even in the most general case, a scattering cross section that does not change as the photon energy is changed beneath an absorption edge of a constituent atomic species indicates homogeneous distribution of that species.

5.4 TRENDS WITH COMPOSITION FOR SAMPLES WITH $0<x<25$

The differential scattering cross sections, $d\Sigma/d\Omega(k)$, for the a-Fe$_x$Ge$_{100-x}$, a-W$_x$Ge$_{100-x}$ and a-Mo$_x$Ge$_{100-x}$ samples with $0<x<25$ exhibit similar behavior as a function of incident photon energy. Other similarities between these three systems emerge when the scattering cross sections are considered as a function of metal concentration. Figure V.15 displays a plot of $d\Sigma/d\Omega(k)$ for the five a-Fe$_x$Ge$_{100-x}$ samples with $0<x<25$ at an incident photon energy of 10903 eV (200 eV below the Ge K absorption edge). The magnitude of the peak in the scattering cross section increases as x increases from 5 to 12 to 18. As the Fe concentration changes from 18 to 19 atomic percent the magnitude of the peak in $d\Sigma/d\Omega(k)$ decreases. A further decrease is seen as x goes from 19 to 24. Across this concentration regime, the position of the peak moves steadily toward smaller values of k with increasing x.

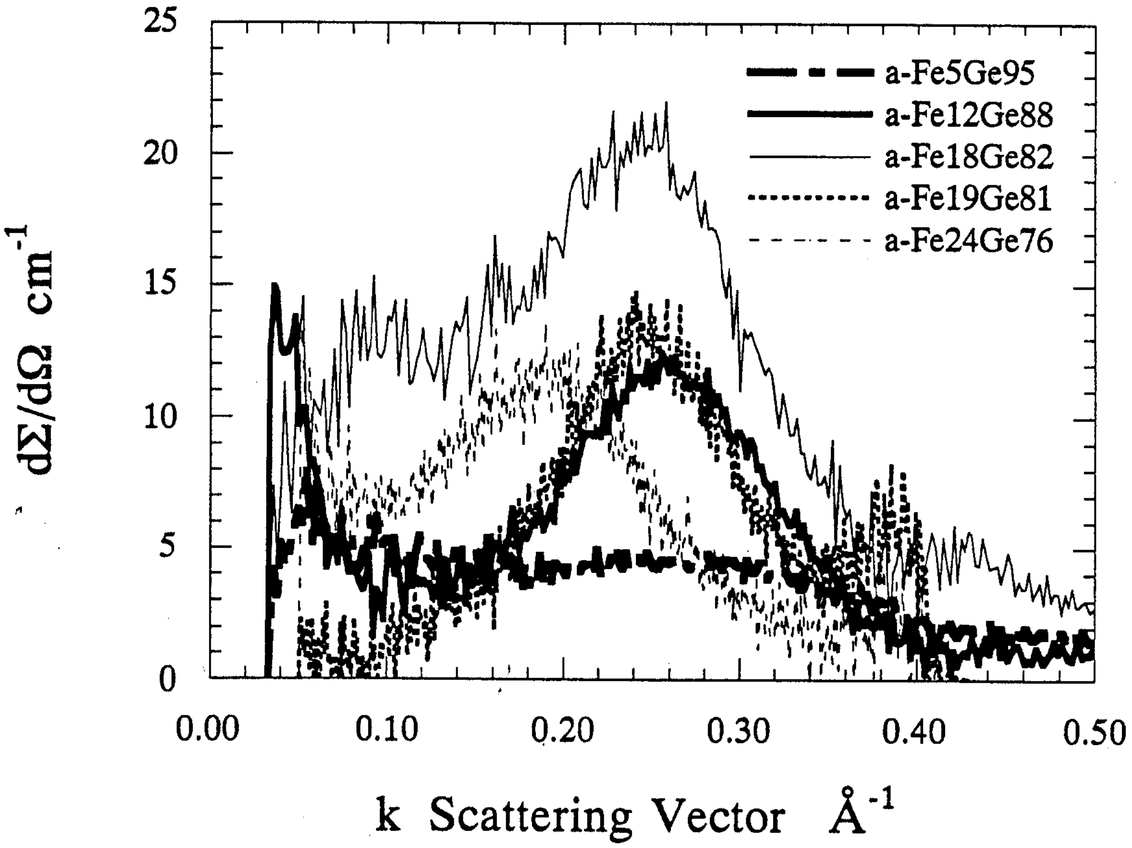

FIGURE V.15 The scattering cross sections for the a-Fe$_x$Ge$_{100-x}$ samples with $0<x<25$ at an incident photon energy of 10903 eV.

It must be mentioned here that the data from the samples with x equal to 5, 12, and 18 were collected at NSLS while the data from the samples with x equal to 19 and 24 were collected at SSRL. This means that all five data sets displayed in Figure V.25 are not necessarily on exactly the same scale. The SSRL data were put on an absolute scale by comparison with a lupolen standard. The NSLS data were matched to the SSRL data by comparing data taken on the a-$Fe_{28}Ge_{72}$ sample with both experimental set ups. Data were collected both at SSRL and at NSLS on several other samples as well. The scaling factor that was used to match the NSLS data sets to the SSRL data sets worked perfectly for some samples but not for others. In some cases the magnitude of the scattering cross sections collected at NSLS and SSRL for a particular sample differed by as much as twenty percent.

A twenty percent error in the peak heights of the NSLS data sets would not alter the trend displayed in Figure V.25. The magnitude of the peak in the scattering cross section increases with composition, up to some particular metal concentration, and then decreases with the further addition of metal atoms. This trend is consistent with the principle of reciprocity: the SAXS pattern from a sample with a volume fraction c of phase A dispersed in phase B is indistinguishable from the SAXS pattern from a sample with a volume fraction c of phase B dispersed in phase A.

Similar trends with composition are seen in the a-W_xGe_{100-x} and a-Mo_xGe_{100-x} samples. A plot of the scattering cross sections for the three a-W_xGe_{100-x} samples with $0<x<25$ is shown in Figure V.16. The scattering cross sections for the a-Mo_xGe_{100-x} samples with $0<x<25$ are shown in Figure V.17. Like the a-Fe_xGe_{100-x} samples, the a-W_xGe_{100-x} and a-Mo_xGe_{100-x} samples display a peak in the scattering cross section that initially increases with the addition of metal atoms and moves toward smaller values of k. The principle of reciprocity and the behavior of the a-Fe_xGe_{100-x} samples suggest that the a-W_xGe_{100-x} and a-Mo_xGe_{100-x} samples may display a decrease in the magnitude of the peak in the scattering cross section with increasing metal concentration above some value of x.

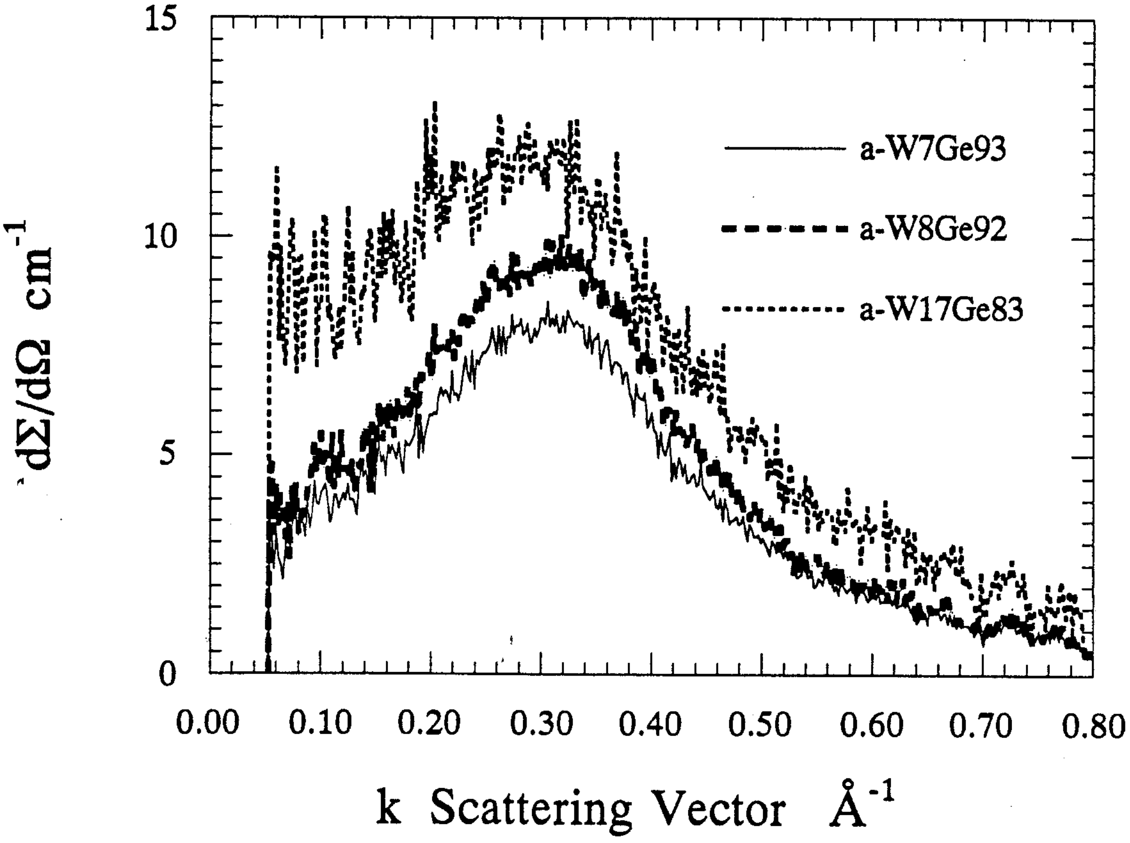

FIGURE V.16 The scattering cross sections for the a-W$_x$Ge$_{100-x}$ samples with $0<x<25$ at an incident photon energy of 10903 eV.

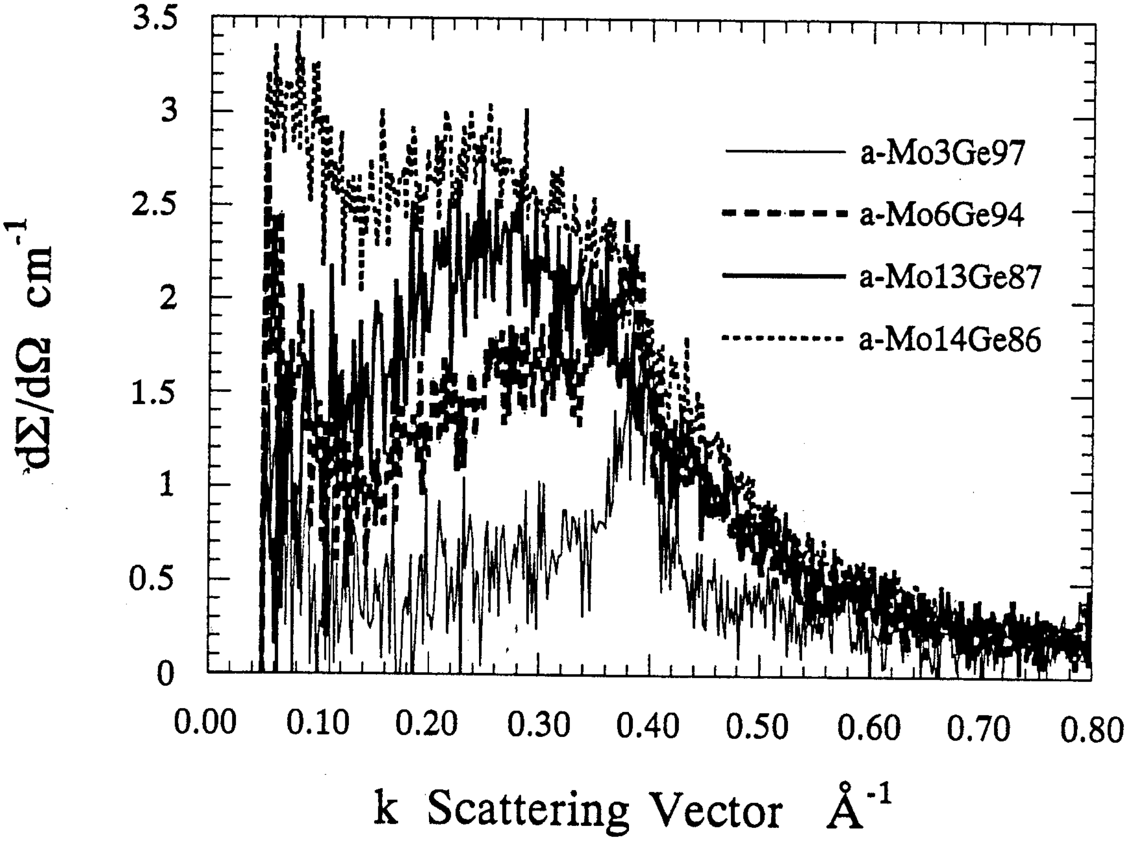

FIGURE V.17 The scattering cross sections for the a-Mo$_x$Ge$_{100-x}$ samples with $0<x<25$ at an incident photon energy of 10903 eV.

Not enough samples in this concentration regime were studied to characterize the trends in $d\Sigma/d\Omega(k)$ as a function of metal content.

The maxima of the scattering cross sections for all three systems are displayed as a function of concentration in Figure V.18. As already mentioned, there are not enough data points in this graph to draw detailed conclusions about the behavior of the peak in the scattering cross section as a function of concentration for the a-W_xGe_{100-x} and the a-Mo_xGe_{100-x} system. For the a-Fe_xGe_{100-x} system a model of phase separation into a-Ge and a-$FeGe_2$ is considered. The integral of the scattering cross section over reciprocal space is proportional to the product of the volume fractions, c and $(1-c)$, of the two phases

$$Q = \frac{V}{N}\left[c(1-c)(\rho_1(E) - \rho_2(E))^2\right]. \qquad (5.31)$$

For phase separation into a-Ge and a-$FeGe_2$, the magnitude of the peak in the scattering cross section (as a function of x) would reach its maximum between 19 and 20 atomic percent Fe. Given the difficulties in matching the SSRL and NSLS data sets, the a-Fe_xGe_{100-x} data presented in Figure V.16 may be consistent with such a picture.

Nonetheless, one obvious aspect of Figure V.18 is that the maxima in the scattering cross sections of the a-Mo_xGe_{100-x} samples are significantly smaller than those of the other two systems. This is seen more clearly in Figure V.19 where the scattering cross sections for a-$Mo_{13}Ge_{67}$, a-W_8Ge_{92} and a-$Fe_{12}Ge_{88}$ are plotted on the same set of axes. The maxima in $d\Sigma/d\Omega(k)$ for the a-$Fe_{12}Ge_{88}$ and the a-W_8Ge_{92} samples are about five times greater in magnitude than that for a-$Mo_{13}Ge_{67}$. While the peaks in $d\Sigma/d\Omega(k)$ for a-$Mo_{13}Ge_{67}$ and a-W_8Ge_{92} differ in height by a factor of five they are similar in breadth. The peak in $d\Sigma/d\Omega(k)$ for a-$Fe_{12}Ge_{88}$, however, is much sharper. These results indicate that the morphologies of the three systems are different.

Polynomial fits to all of the data sets collected at 10903 eV on samples in the $0<x<25$ concentration regime were used to extract the magnitudes and the positions of the maxima in $d\Sigma/d\Omega(k)$. Where possible the breadths (full width half maximum- FWHM) of

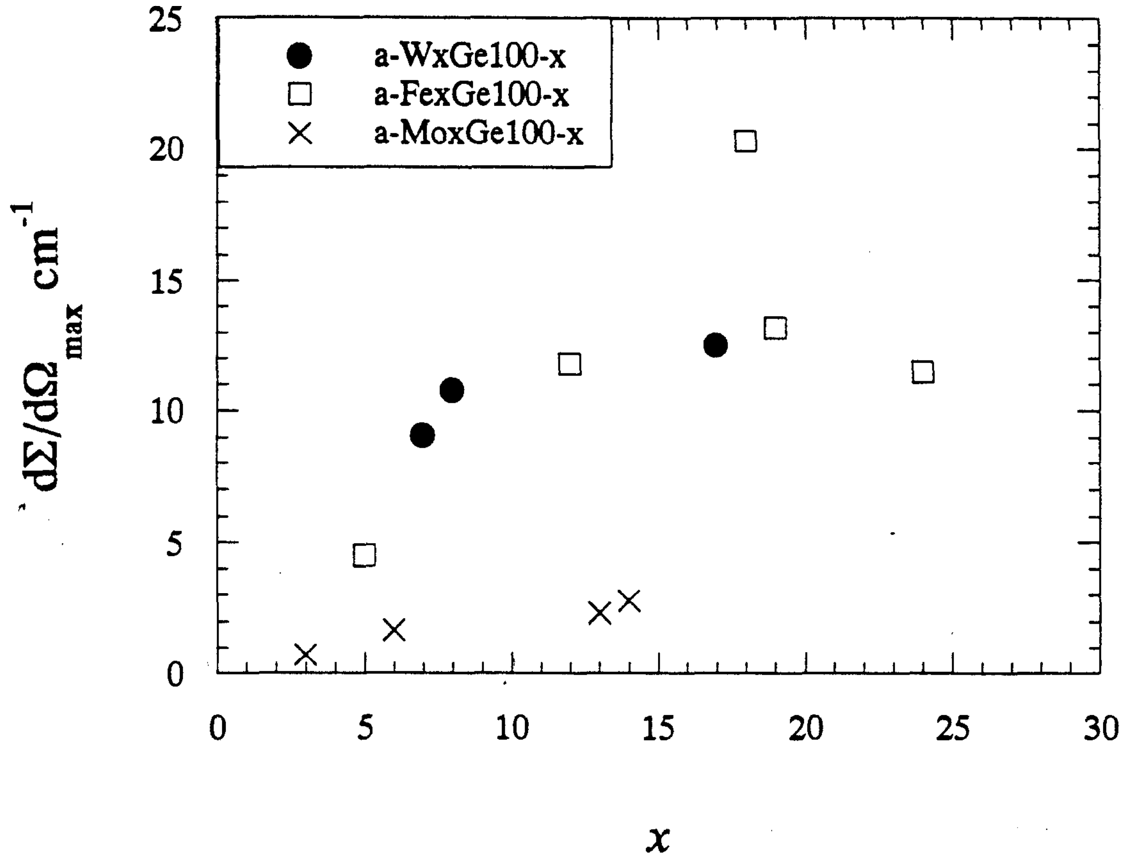

FIGURE V.18 The magnitudes of the maxima in $d\Sigma/d\Omega(k)$ for the a-Mo$_x$Ge$_{100-x}$, a-Fe$_x$Ge$_{100-x}$ and a-W$_x$Ge$_{100-x}$ systems plotted as a function of x.

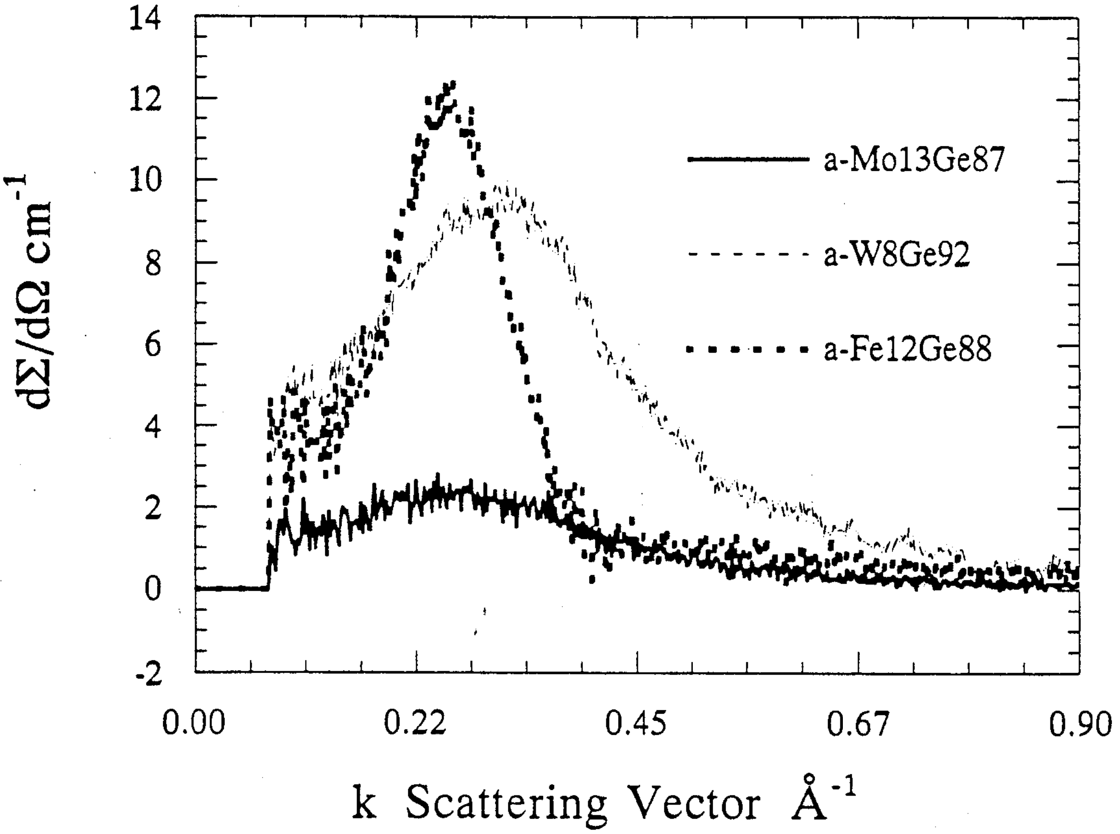

FIGURE V.19 The scattering cross sections for a-$Mo_{13}Ge_{87}$, a-W_8Ge_{92}, and a-$Fe_{12}Ge_{88}$ at an incident photon energy of 10903 eV.

TABLE V.2

Peak heights, positions, and widths for $d\Sigma/d\Omega(k)$ of a-$\mathrm{Fe}_x\mathrm{Ge}_{100\text{-}x}$, a-$\mathrm{W}_x\mathrm{Ge}_{100\text{-}x}$, and a-$\mathrm{Mo}_x\mathrm{Ge}_{100\text{-}x}$.

System	x	peak height $d\Sigma/d\Omega_{\mathrm{max}}$ (cm^{-1})	peak position $k_{d\Sigma/d\Omega\mathrm{max}}$ (Å^{-1})	FWHM (Å^{-1})
a-$\mathrm{Fe}_x\mathrm{Ge}_{100\text{-}x}$	5	4.49	0.264	
	12	11.79	0.258	0.137
	18	20.33	0.244	
	19	13.17	0.248	0.120
	24	11.47	0.189	
a-$\mathrm{W}_x\mathrm{Ge}_{100\text{-}x}$	7	8.06	0.308	0.304
	8	9.47	0.314	0.306
	17	11.80	0.294	
a-$\mathrm{Mo}_x\mathrm{Ge}_{100\text{-}x}$	3	0.71	0.295	
	6	1.65	0.291	
	13	2.31	0.250	0.318
	14	2.77	0.230	

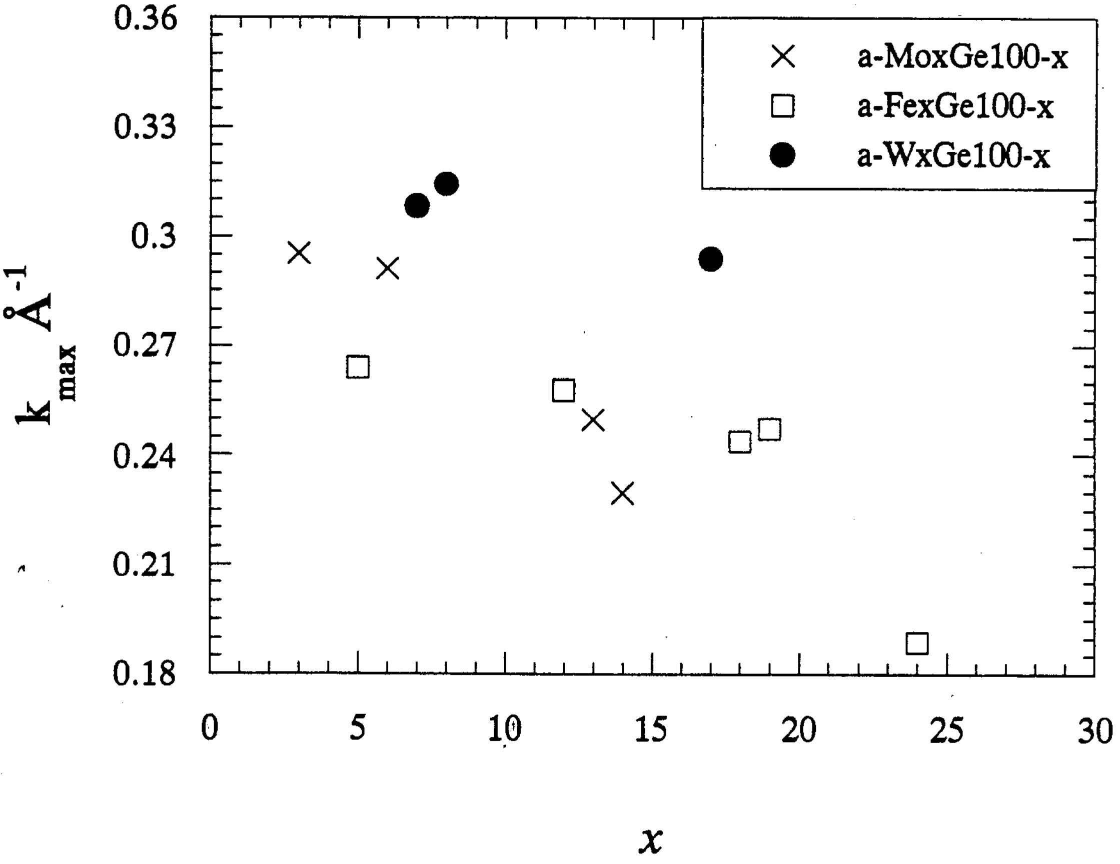

FIGURE V.20 The positions of the maxima in $d\Sigma/d\Omega(k)$ for the a-Mo$_x$Ge$_{100-x}$, a-Fe$_x$Ge$_{100-x}$ and a-W$_x$Ge$_{100-x}$ systems plotted as a function of x.

the peaks were also calculated. These results are summarized in Table V.2. The positions of the maxima are plotted as a function of concentration in Figure V.20.

Since the Ge is distributed homogeneously throughout each sample with $x<25$, the SAXS peak must arise from fluctuations in the density of metal atoms. If the metal atoms were distributed in the same way (identical morphologies) in each of the three systems, the SAXS patterns for samples with identical x would have the same shape and would scale as Z^2 for photon energies far from the metal absorption edges. Figure V.19 and Table V.2 show that this is not the case. The SAXS peak is much sharper for the a-Fe_xGe_{100-x} samples than for the other samples indicating less dispersion in particle sizes and interparticle distances for the a-Fe_xGe_{100-x} system.

The SAXS peaks for the a-Mo_xGe_{100-x} samples and the a-W_xGe_{100-x} samples display similar breadth but do not scale as Z^2. This is apparent in Figure V.21 which shows a superposition of the SAXS pattern for the a-W_8Ge_{92} sample and 4.66 times the SAXS pattern for the a-$Mo_{13}Ge_{87}$ sample. Since there are 0.6 times as many metal atoms in the a-W_8Ge_{92} sample as in the a-$Mo_{13}Ge_{87}$ sample and $(Z_W/Z_{Mo})^2$ is equal to about 3.1, the SAXS pattern for a-$Mo_{13}Ge_{87}$ (assuming similar morphologies) should coincide with that of a-W_8Ge_{92} when the former is multiplied by 1.9.

Of the three systems the a-Fe-Ge system has metal atoms with the lowest Z (Z=26), but the SAXS patterns for the a-Fe_xGe_{100-x} samples have the greatest intensity and the narrowest peaks. A distribution of particle sizes, shapes and interparticle distances broadens and flattens the SAXS peak. One can see, in a qualitative way, that the a-Fe_xGe_{100-x} system has the most well defined structure. It is interesting to remember, at this point, that unlike the a-Mo_xGe_{100-x} and the a-W_xGe_{100-x} samples, the a-Fe_xGe_{100-x} samples were triode sputtered (constant electron bombardment of the growing film).

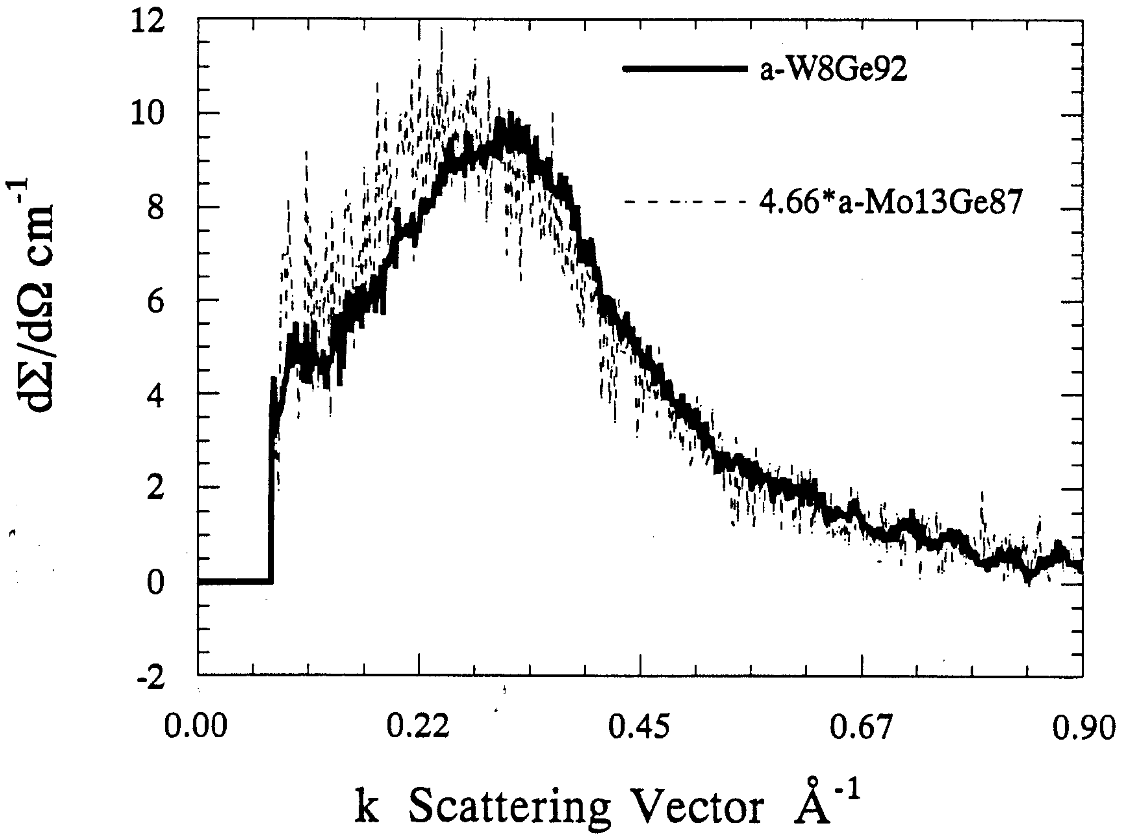

FIGURE V.21 Superposition of the SAXS pattern for the a-W_8Ge_{92} sample and 4.66 times the SAXS pattern for a-$Mo_{13}Ge_{87}$ sample. Both patterns were collected at an incident photon energy of 10903 eV.

5.5 MODEL CALCULATIONS

To further investigate the concept of phase separation of a-M$_x$Ge$_{100-x}$ alloys into a-Ge and a-MGe$_2$ simple model calculations were performed. Only the most simple models were considered: (a) identical homogeneous spheres of a-MGe$_2$ (a-Ge) immersed in a-Ge (a-MGe$_2$), and (b) identical inhomogeneous spheres with an inner core of a-MGe$_2$ (a-Ge) and an outer shell of a-Ge (a-MGe$_2$) immersed in a matrix of a-M$_x$Ge$_{100-x}$. For the homogeneous sphere model, interparticle interference effects were included. For the inhomogeneous particle model, interparticle interference effects were not treated.

(a) Models of homogeneous particles:

Using the Born-Green approximation for the interparticle interference function, the intensity of radiation scattered by a dense collection of identical homogeneous spheres is given by

$$I(k) = I_e(k)NV_p^2\left(\rho_p(E)-\rho_m(E)\right)^2\Phi^2(kR)\left[\frac{1}{1+\frac{8V_p}{v_1}\Phi(2kR)}\right]. \qquad (5.21)$$

When expressed in terms of the differential scattering cross section per unit volume, equation (5.21) becomes

$$\frac{d\Sigma}{d\Omega}(k) = r_e^2\frac{N}{V}V_p^2\left(\rho_p(E)-\rho_m(E)\right)^2\Phi^2(kR)\left[\frac{1}{1+\frac{8NV_p}{V}\Phi(2kR)}\right]. \qquad (5.44)$$

Recalling that NV_p/V is just the volume fraction, c, occupied by the spheres gives

$$\frac{d\Sigma}{d\Omega}(k) = r_e^2cV_p\left(\rho_p(E)-\rho_m(E)\right)^2\Phi^2(kR)\left[\frac{1}{1+8c\Phi(2kR)}\right]. \qquad (5.45)$$

As noted in section 5.1 (h), the Born-Green approximation was derived for liquids in which the closest approach of particles (in this case atoms) can be as small as the sum of their radii, $2R$. This is not a reasonable model for precipitates in an alloy. Precipitates leave behind a surrounding depletion region (Pederson, 1993) so that the particles come no closer than 2σ, where σ is the radius of the particle-plus-depletion region, as shown in Figure V.22. Equation (5.45) is now expressed as

$$\frac{d\Sigma}{d\Omega}(k) = r_e^2 c V_p \left(\rho_p(E) - \rho_m(E)\right)^2 \Phi^2(kR)\left[\frac{1}{1+8\eta\Phi(2k\sigma)}\right]. \quad (5.46)$$

The volume fraction of particles, c, has been replaced in the interparticle interference function with the volume fraction, η, of the particles-plus-depletion region.

The volume fraction, η, occupied by the spherical particles-plus-depletion region is related quite simply to the atomic fraction, x, of metal atoms in the sample. With the notation n_1 is the number density of atoms in phase 1, n_2 is the number density of atoms in phase 2, m_1 is the atomic fraction of metal atoms in phase 1, m_2 is the atomic fraction of metal atoms in phase 2, V_R is the volume of one spherical particle and V_σ is the volume of the particle-plus-depletion region

$$\eta = \frac{V_\sigma}{V_R}\left[\frac{\left(n_2 m_2 - x n_2\right)}{x\left(n_1 - n_2\right) - \left(n_1 m_1 - n_2 m_2\right)}\right]. \quad (5.47)$$

Equation (5.46) was used to calculate the differential scattering cross section for models of identical, homogeneous, spherical particles of a-MGe$_2$ (a-Ge) immersed in a-Ge (a-MGe$_2$). The number densities were taken to be 0.95 times those of the analogous crystalline phases. Representative results of the calculations are shown in Figures V.23-V.26. As can be seen in Figures V.23 and V.24, the model comes close to reproducing the data for the a-Fe$_x$Ge$_{100-x}$ and a-W$_x$Ge$_{100-x}$ samples. The fit is less satisfactory for the a-Mo$_x$Ge$_{100-x}$ system. It must be emphasized that the model is extremely simple and does not account for variations in particle shapes, sizes, or interparticle distances. Nor does it consider the composition of the interface between particle and matrix. The inclusion of polydispersity in the model would tend to broaden the peaks and diminish the maxima.

Figure V.26 shows the data and the model calculation for all five incident photon energies below the Fe K absorption edge at which data were collected. The model has been multiplied by 1.25 to improve the fit. The trend in the magnitude of the scattering cross section as a function of incident photon energy is well reproduced by the model.

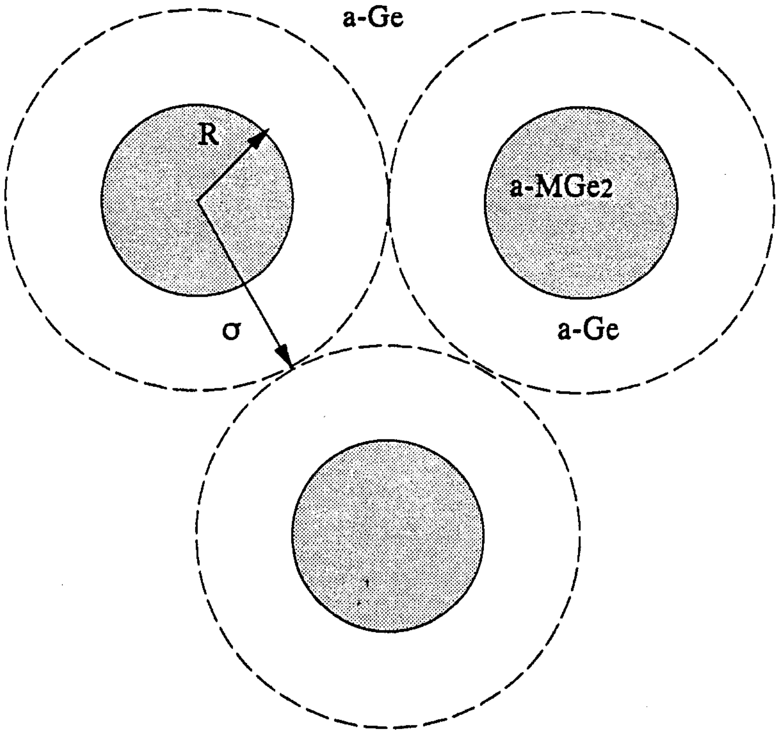

FIGURE V.22 The homogeneous sphere model showing the particles with radius *R* and the particle-plus-depletion region with radius σ.

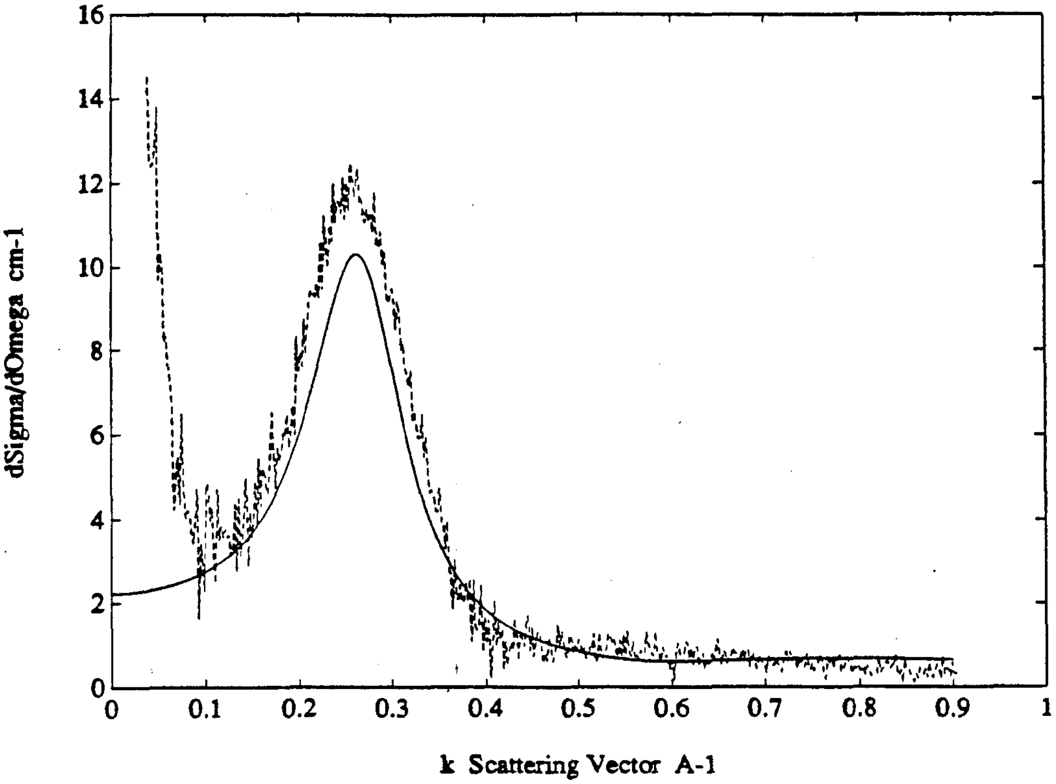

FIGURE V.23 Homogeneous particle model for the a-$Fe_{12}Ge_{88}$ sample at an incident photon energy of 10903 eV. Smooth line: spheres of a-$FeGe_2$ in an a-Ge matrix with R=7.4 Å and σ=10.45 Å. Noisy line: data.

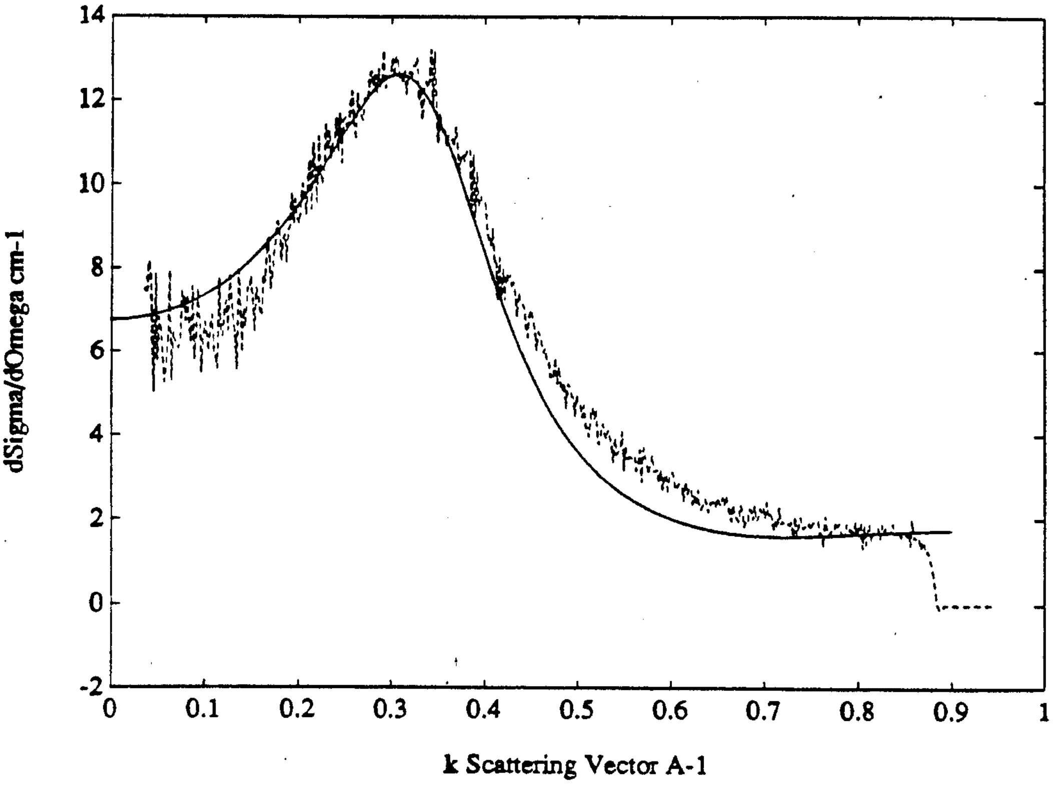

FIGURE V.24 Homogeneous particle model for the a-W_8Ge_{92} sample at an incident photon energy of 10004 eV. Smooth line: spheres of a-WGe_2 in an a-Ge matrix with R=6.2 Å and σ=7.9 Å. Noisy line: data.

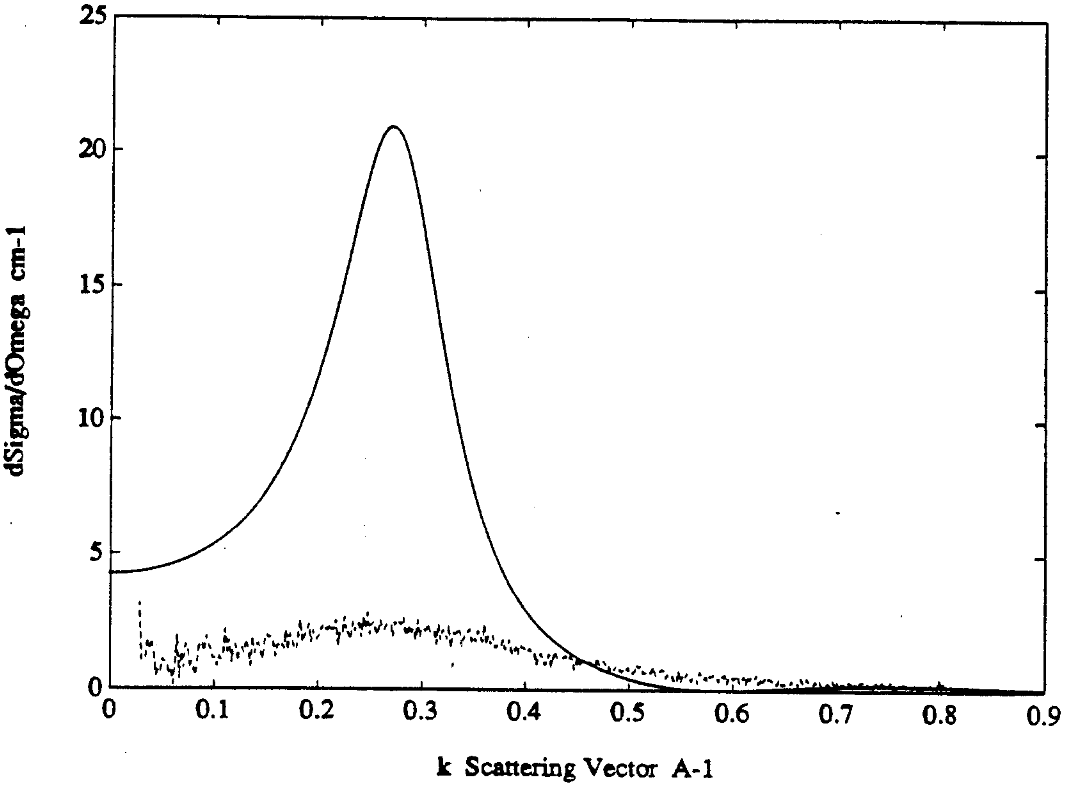

FIGURE V.25 Homogeneous particle model for the *a*-$Mo_{13}Ge_{87}$ sample at an incident photon energy of 10903 eV. Smooth line: spheres of *a*-$MoGe_2$ in an *a*-Ge matrix with R=7.6 Å and σ=10.0 Å. Noisy line: data.

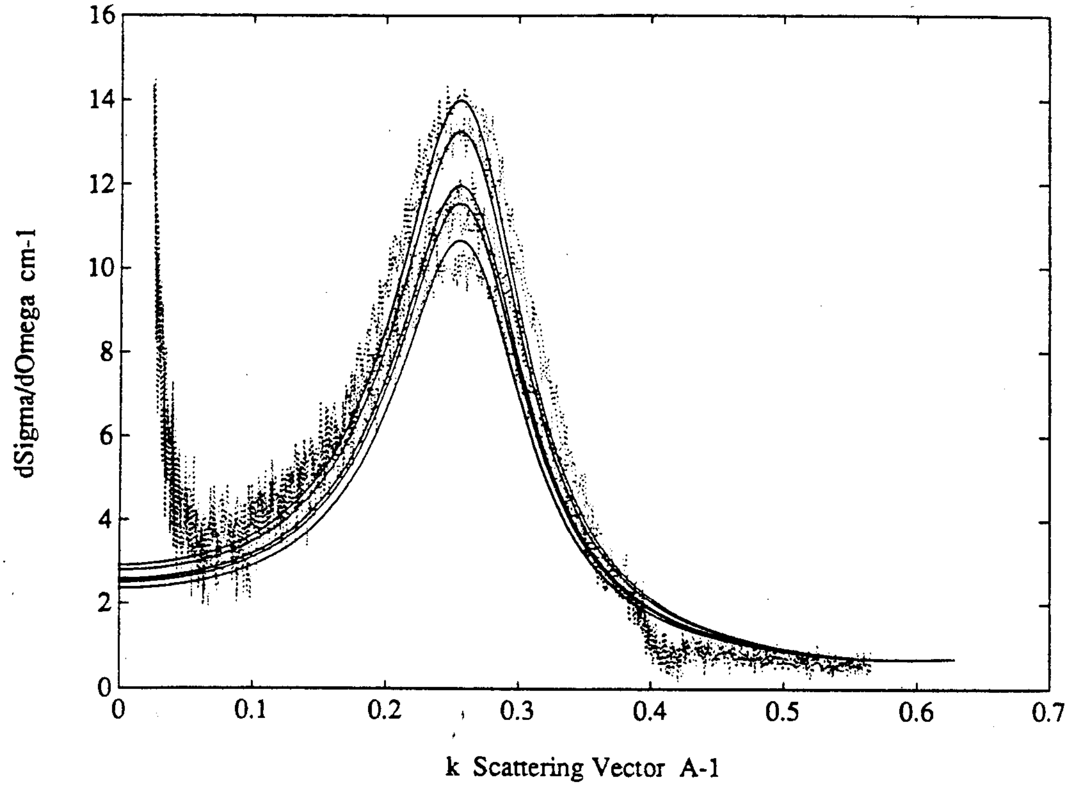

FIGURE V.26 Homogeneous particle model for the a-Fe$_{12}$Ge$_{88}$ sample at incident photon energies of 200, 100, 30, 20, and 10 eV below the Fe K absorption edge. Smooth lines: spheres of a-FeGe$_2$ in an a-Ge matrix with R=7.6 Å and σ=10.7 Å. (Model has been scaled by 1.25 to match the data). Noisy lines: data.

(b) Models of inhomogeneous particles:

An inhomogeneous particle model of identical spheres, each with a spherical core of *a*-MGe_2 (*a*-Ge) and a concentric spherical shell of *a*-Ge (*a*-MGe_2), immersed in a matrix of *a*-M_xGe_{100-x} was considered next (Guinier & Fournet, 1955). A schematic of the model is shown in Figure V.27. Since the matrix is unreacted and the phase separation takes place only within the spheres, the core of a sphere must occupy a volume fraction, c, of the total sphere that is consistent with the overall composition. If the radius of the outer sphere is R, the radius of the inner sphere will be $c^{1/3}R$. Expressing equation (5.22) in terms of the differential scattering cross section per unit volume gives

$$\frac{d\Sigma}{d\Omega}(k) = r_e^2 \frac{N_p}{V}\left[V_c\,(\rho_c(E)-\rho_s(E))\Phi(kR_c)+V_s\,(\rho_s(E)-\rho_m(E))\Phi(kR_s)\right]^2. \quad (5.48)$$

Representative results of calculations using equation (5.48) and 95% of the number densities of the analogous crystalline phases are displayed in Figures V.28-V.30. Like the homogeneous particle model, the inhomogeneous particle model comes close to reproducing the data. While the inhomogeneous particle model fits the data from the *a*-Mo_xGe_{100-x} samples better than the homogeneous model, it fits the *a*-Fe_xGe_{100-x} and the *a*-W_xGe_{100-x} data less well.

The homogeneous particle model provides a better description of the *a*-Fe_xGe_{100-x} and *a*-W_xGe_{100-x} systems than does the inhomogeneous particle model. The *a*-Mo_xGe_{100-x} system, as seen in section 5.4, has very diffuse scattering compared to the other two systems and is better described by the inhomogeneous particle model. For the *a*-$Mo_{13}Ge_{87}$ sample displayed in Figure V.30, the composite spheres occupy only 22 % of the sample volume. This means that 78 % of the sample is homogeneous. There are 1.3 x 10^{-19} inhomogeneous particles per cm^3, so, on average each particle has 77,000 Å^3 (42.5 Å)^3 allotted to it. The average sphere separation is 42.5 Å while the sphere diameter is 32 Å.

The qualitative arguments of section 5.4 indicate a more advanced degree of phase separation for the *a*-Fe_xGe_{100-x} and *a*-W_xGe_{100-x} systems. The simple homogeneous and inhomogeneous particle models show this explicitly.

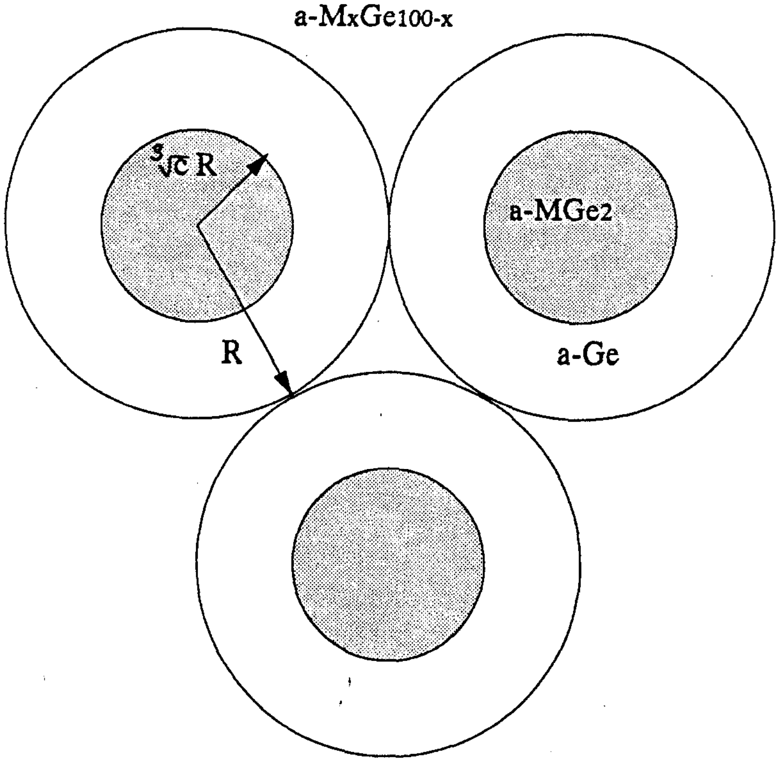

FIGURE V.27 The inhomogeneous sphere model showing particles with total radius (core plus shell) *R* and core regions with radius $c^{1/3}R$.

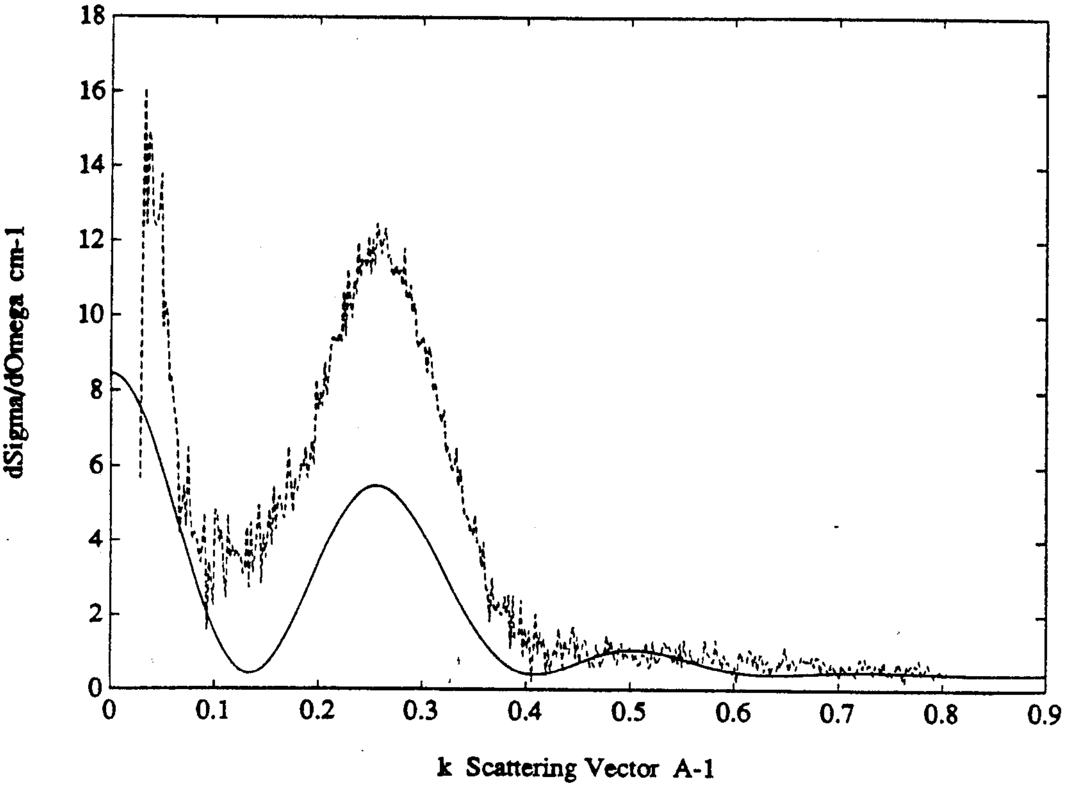

FIGURE V.28 Inhomogeneous particle model for the a-$Fe_{12}Ge_{88}$ sample at an incident photon energy of 10903 eV. Smooth line: sphere cores of a-$FeGe_2$, shells of a-Ge, matrix of a-$Fe_{12}Ge_{88}$ with R=18 Å and $c^{1/3}R$=11.5 Å. Noisy line: data.

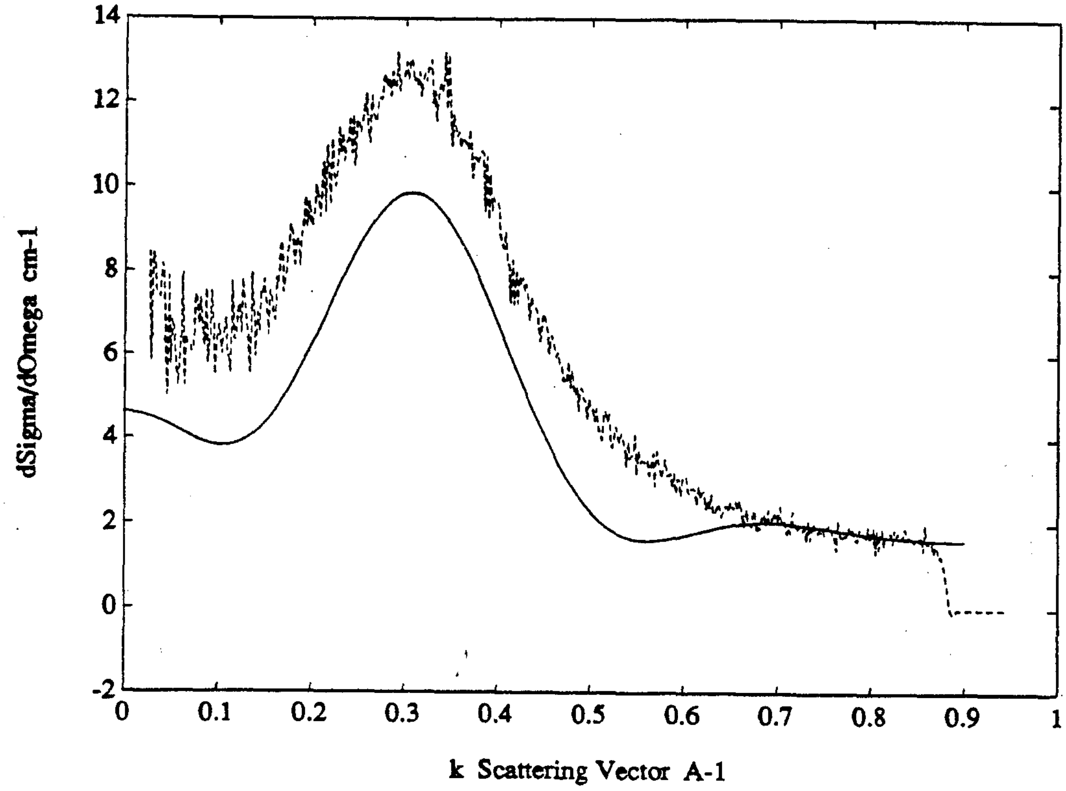

FIGURE V.29 Inhomogeneous particle model for the *a*-W_8Ge_{92} sample at an incident photon energy of 10004 eV. Smooth line: sphere cores of *a*-WGe_2, shells of *a*-Ge, matrix of *a*-W_8Ge_{92} with R=14 Å and $c^{1/3}R$=7.9 Å. Noisy line: data.

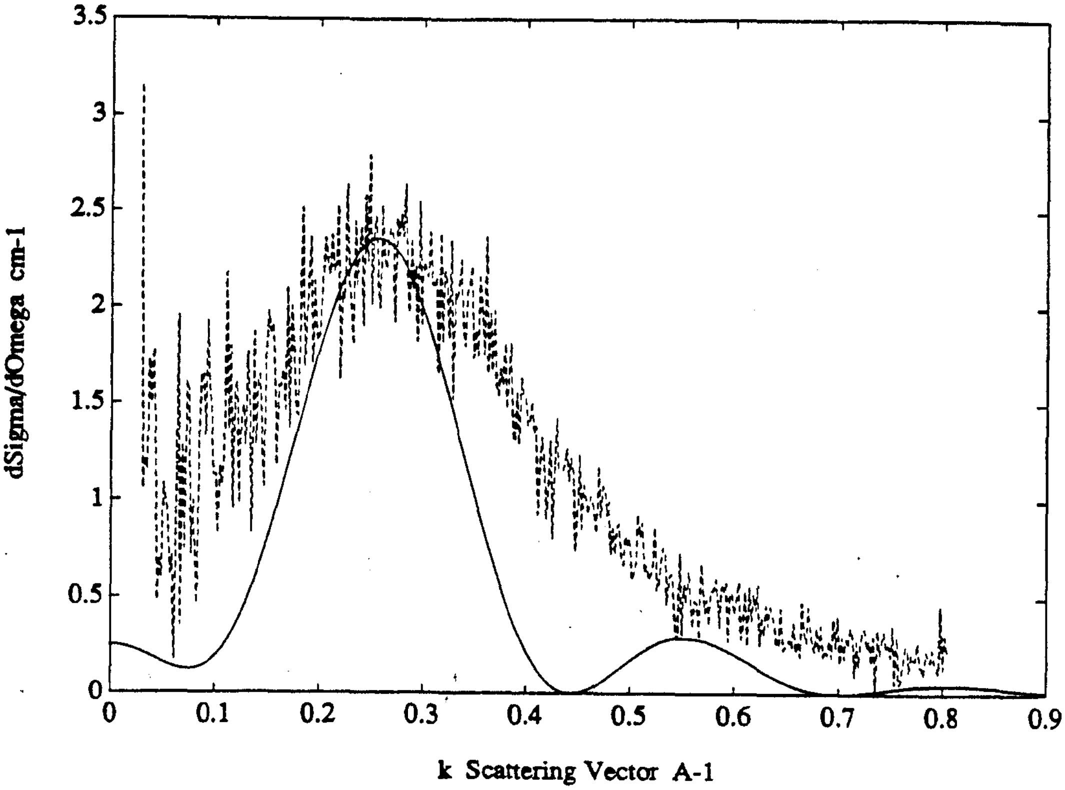

FIGURE V.30 Inhomogeneous particle model for the a-$Mo_{13}Ge_{87}$ sample at an incident photon energy of 10903 eV. Smooth line: sphere cores of a-$MoGe_2$, shells of a-Ge, matrix of a-$Mo_{13}Ge_{87}$ with R=16 Å and $c^{1/3}R$=10.8 Å. Noisy line: data.

REFERENCES FOR CHAPTER V

Born, M. & Green, H. S., *Proc. Roy. Soc. (London)* **A-188** (1946) 10.

Debye, P., *Ann. Physik* **46** (1915) 809.

Debye, P. & Bueche, A. M. J., *Appl. Phys.* **20** (1949) 518.

Feigin, L. A. & Svergun, D. I., *Structure Analysis by Small-Angle X-Ray and Neutron Scattering*, Plenum Press, New York (1987).

Gerold, V., *Phys. stat. sol.* **1** (1961) 37.

Guinier, A. & Fournet, G., *Small-Angle Scattering of X-Rays*, John Wiley & Sons, Inc., New York, (1955).

Hoyt, J. J., de Fontaine, D. & Warburton, W. K., *J. Appl. Cryst.* **17** (1984) 344.

James, R. W., *The Optical Principles of the Diffraction of X-Rays*, Ox Bow Press, Woodbridge, CT (1982).

Ludwig, Jr., K. F., Ph.D. thesis, Stanford University (1986).

Pederson, J. S., *Phys. Rev. B* **47** (1993) 657.

Porod, G., In *Small Angle X-Ray Scattering*, edited by O. Glatter & O. Kratky, Academic Press, London (1982) 20.

Russell, T. P., In *Handbook on Synchrotron Radiation*, Vol. 3, edited by G. S. Brown & D. E. Moncton, Elsevier Science Publishers, North Holland (1991) 379.

Russell, T. P., Lin, J. S., Spooner, S. & Wignall, G. D., *J. Appl. Cryst.* **21** (1988) 629.

Shevchik, N. J., & Paul, W., *J. Non-Cryst. Solids* **16** (1974) 55.

Zernicke, F. & Prins, J. A., *Z. Phys.*, **41** (1927) 184.

CHAPTER VI

ASAXS RESULTS: SAMPLES WITH $x>25$

In contrast to the similar ASAXS patterns obtained from the a-Fe_xGe_{100-x}, a-Mo_xGe_{100-x}, and a-W_xGe_{100-x} systems in the concentration range $0<x<25$, the ASAXS patterns from these systems in the concentration range $x>25$ are very dissimilar. ASAXS data from representative samples of the more metal rich concentration regime of each system are presented and discussed in this chapter.

6.1 THE a-FE_xGE_{100-x} SAMPLES WITH $33<x<75$

The six a-Fe_xGe_{100-x} samples with $x>33$ exhibit strong scattering at k values between 0.02 and 0.04 Å^{-1}. The ASAXS data for each of these samples are presented in Figures VI.1-VI.12. At the Fe edge, where the low k resolution is better, a shoulder or a peak can be discerned in the SAXS pattern of many of the samples. This indicates a non-dilute distribution of the electron density fluctuations or the presence of composite particles.

For each of these six samples, the magnitude of the scattering cross section, $d\Sigma/d\Omega(k)$, displays a large decrease as the incident photon energy is increased beneath the Fe K absorption edge. Beneath the Ge K absorption edge, the magnitude of $d\Sigma/d\Omega(k)$ increases slightly as the incident photon energy is increased. The ASAXS data for each sample at 200 eV and at 10 eV below the Ge edge are shown together on an expanded scale so this effect is more readily obvious. To further characterize the anomalous effect at the Ge edge, the difference between $d\Sigma/d\Omega(k)$ at 10 eV below the Ge edge and $d\Sigma/d\Omega(k)$ at 200 eV below the Ge edge is shown for each sample in Figures VI.13-VI.15.

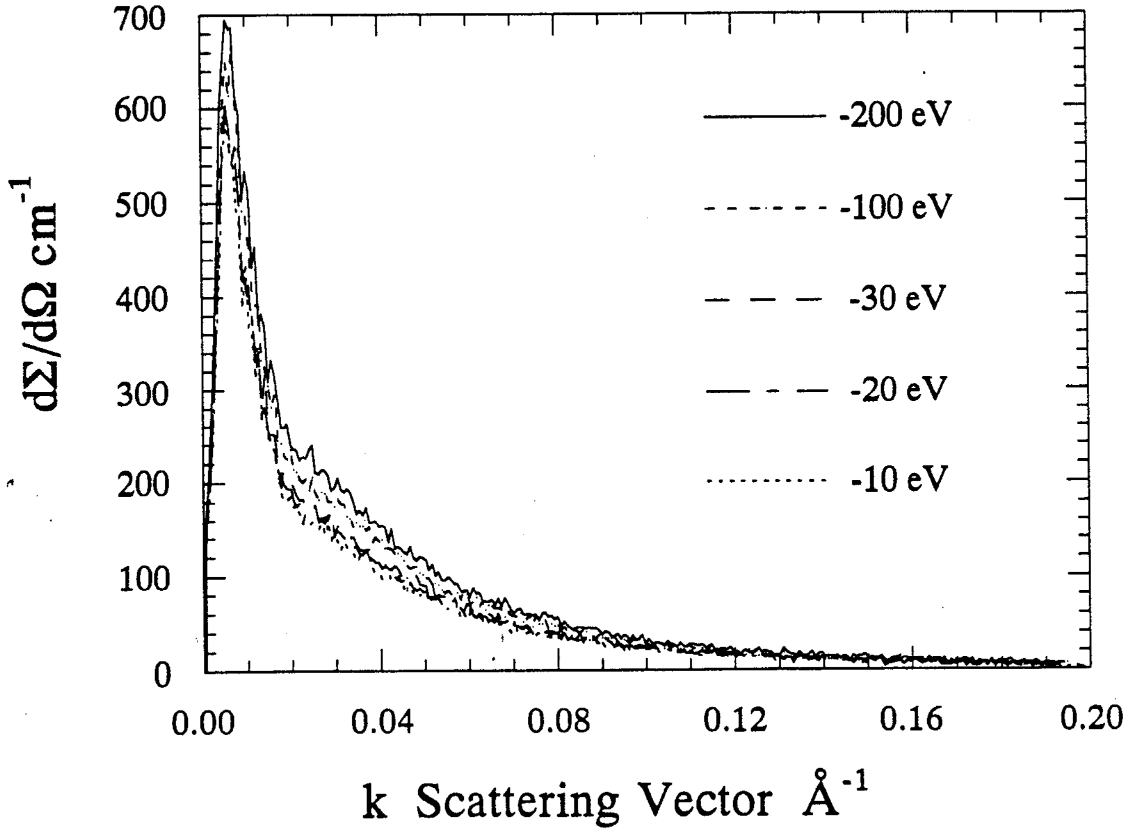

FIGURE VI.1 The differential scattering cross section for the *a*-$Fe_{34}Ge_{66}$ sample at incident photon energies of 200, 100, 30, 20, and 10 eV below the Fe *K* absorption edge.

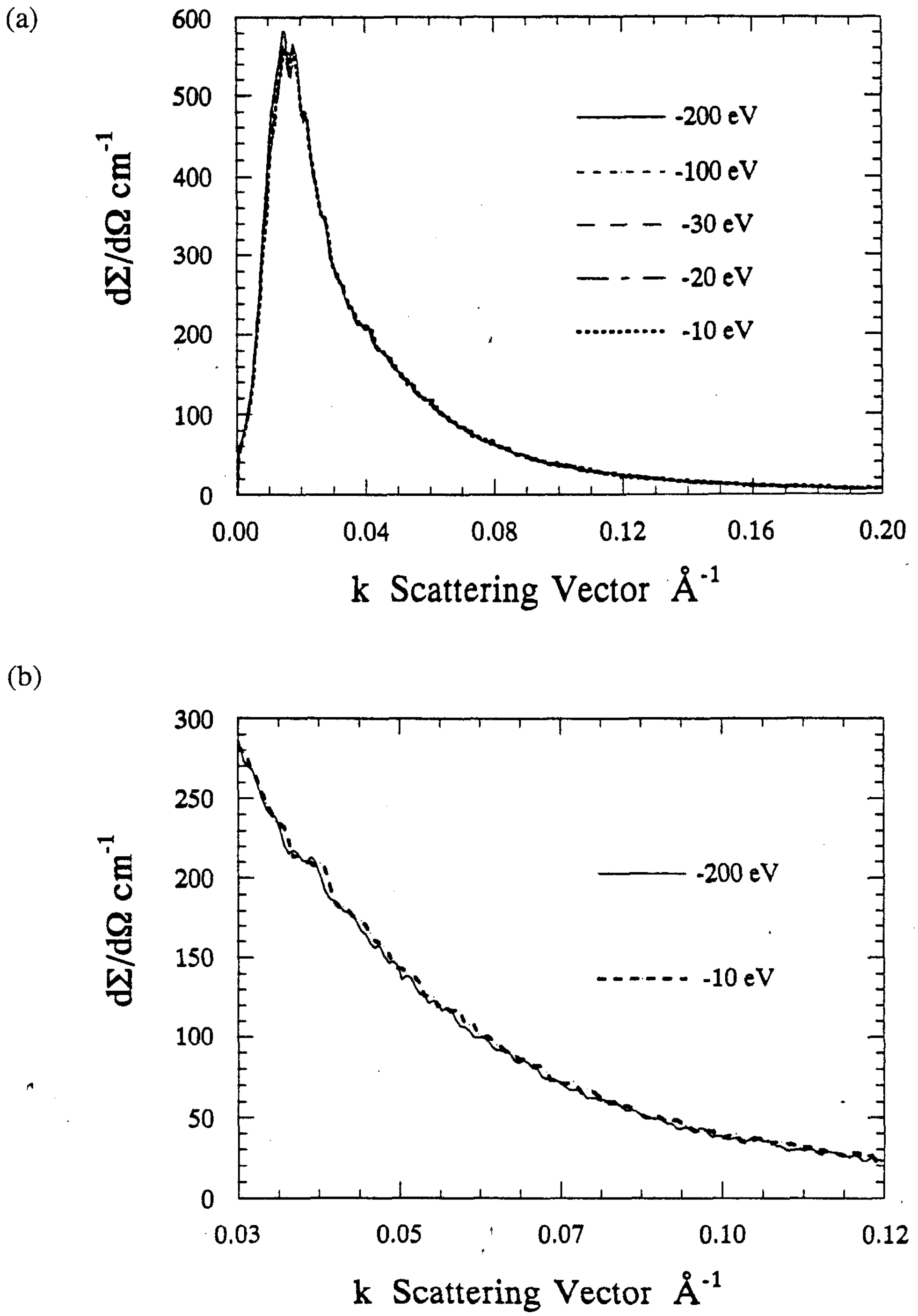

FIGURE VI.2 The differential scattering cross section for the a-$Fe_{34}Ge_{66}$ sample (a) at incident photon energies of 200, 100, 30, 20, and 10 eV below the Ge K absorption edge and (b) on an expanded scale at incident photon energies of 200 and 10 eV below the Ge K absorption edge.

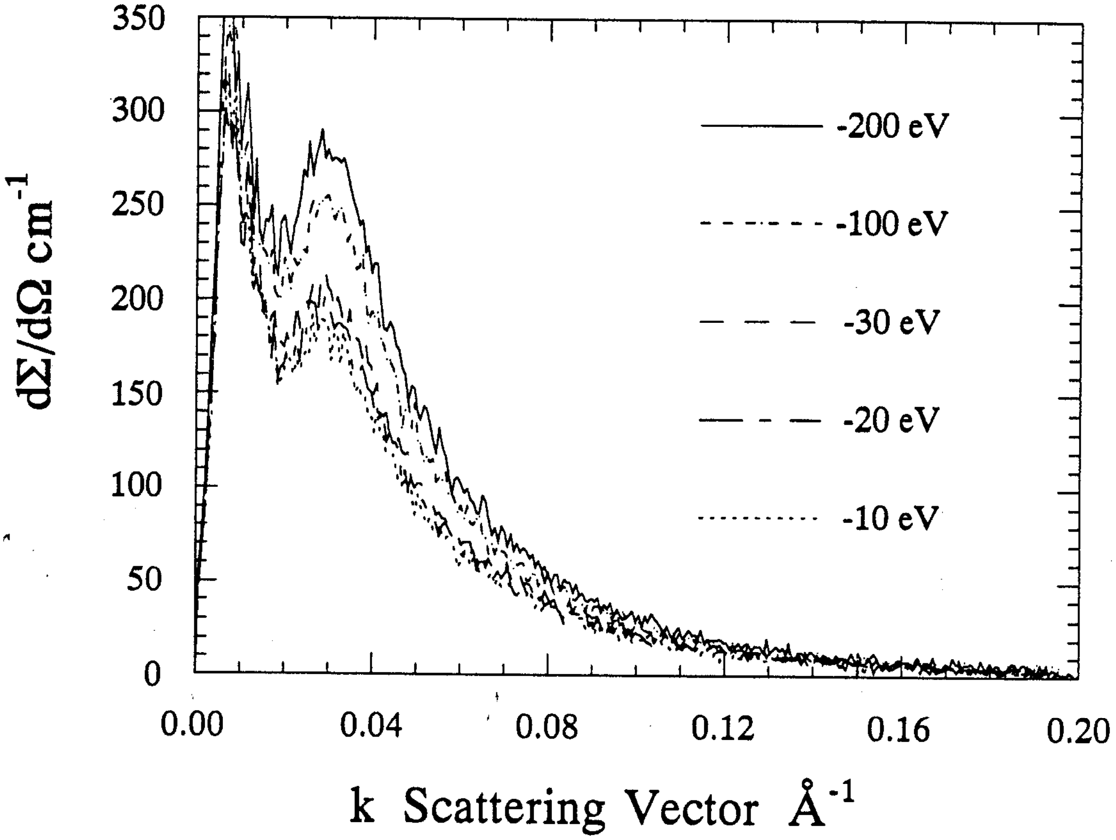

FIGURE VI.3 The differential scattering cross section for the *a*-$Fe_{37}Ge_{63}$ sample at incident photon energies of 200, 100, 30, 20, and 10 eV below the Fe *K* absorption edge.

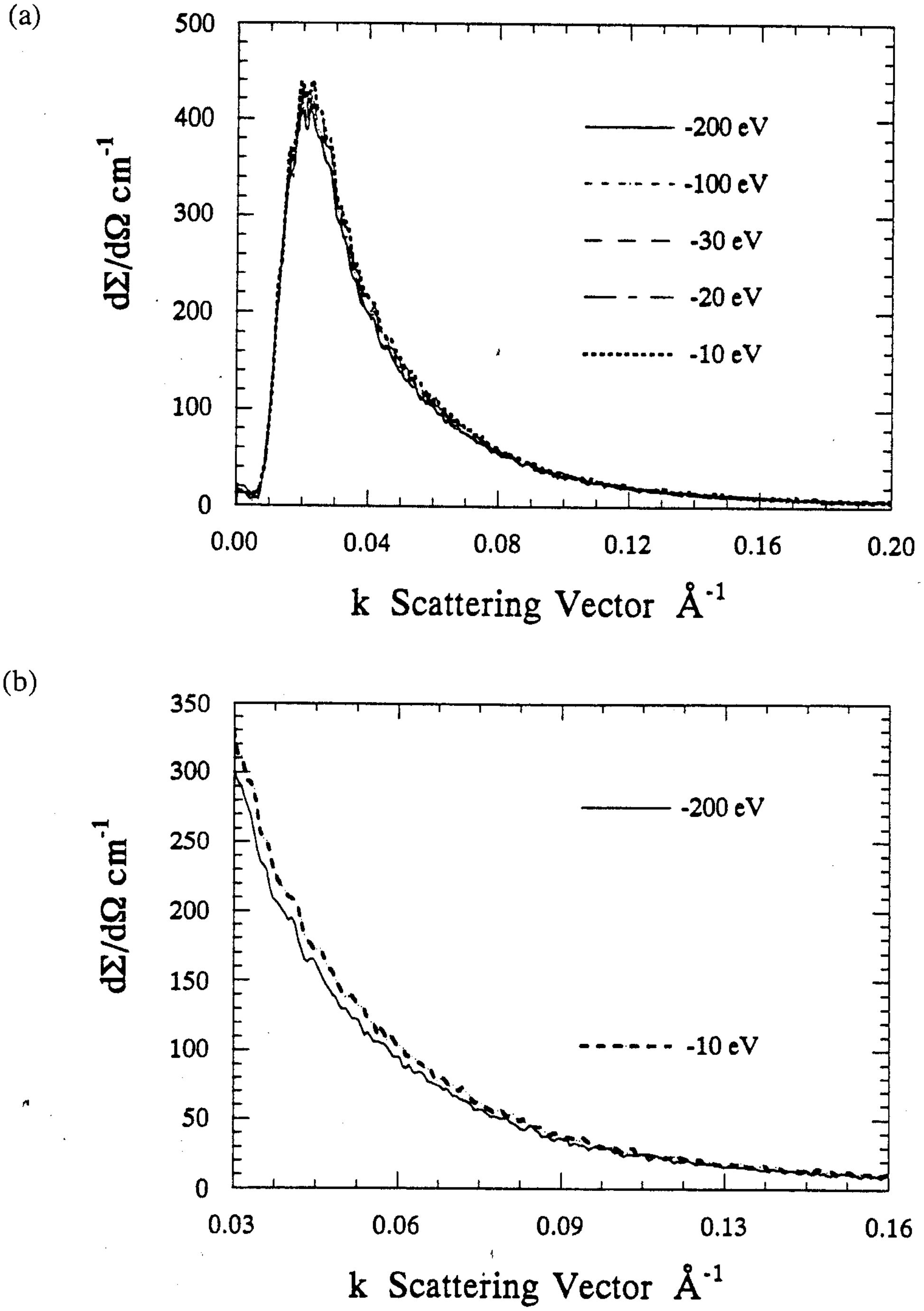

FIGURE VI.4 The differential scattering cross section for the *a*-$Fe_{37}Ge_{63}$ sample (a) at incident photon energies of 200, 100, 30, 20, and 10 eV below the Ge *K* absorption edge and (b) on an expanded scale at incident photon energies of 200 and 10 eV below the Ge *K* absorption edge.

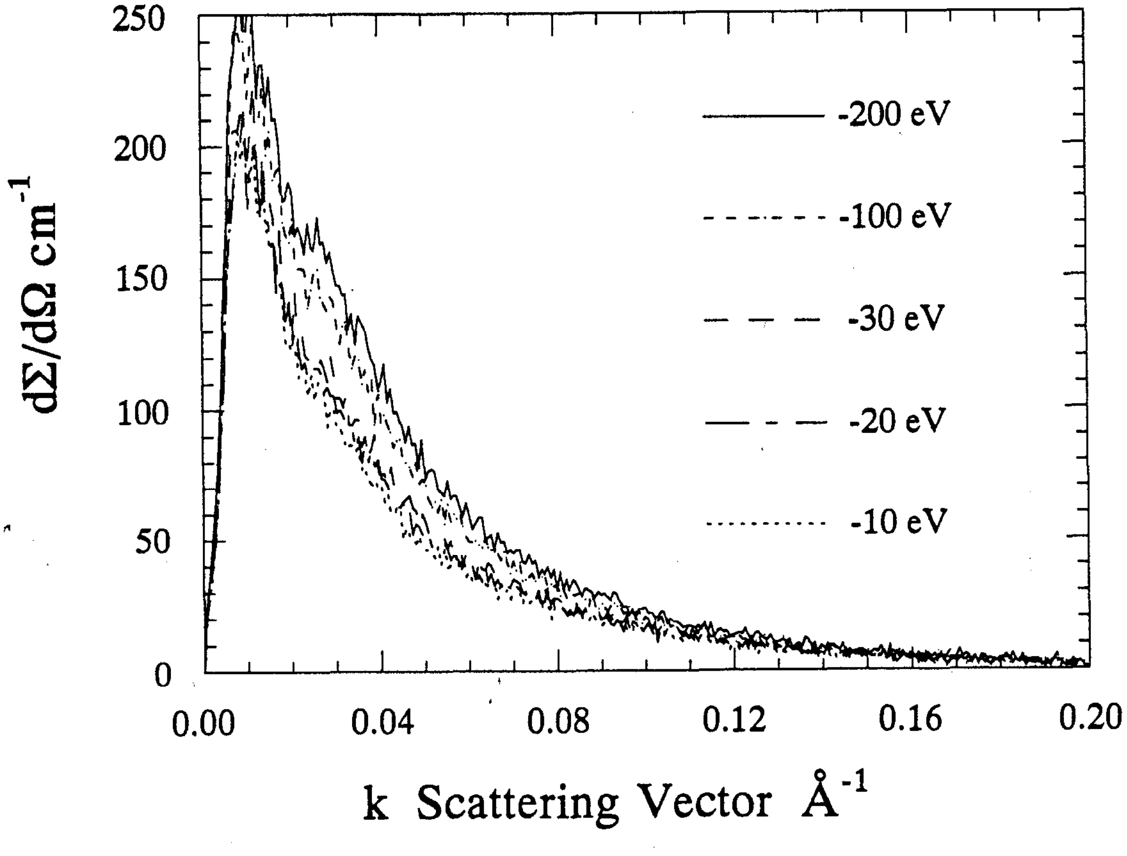

FIGURE VI.5 The differential scattering cross section for the a-$Fe_{44}Ge_{56}$ sample at incident photon energies of 200, 100, 30, 20, and 10 eV below the Fe *K* absorption edge.

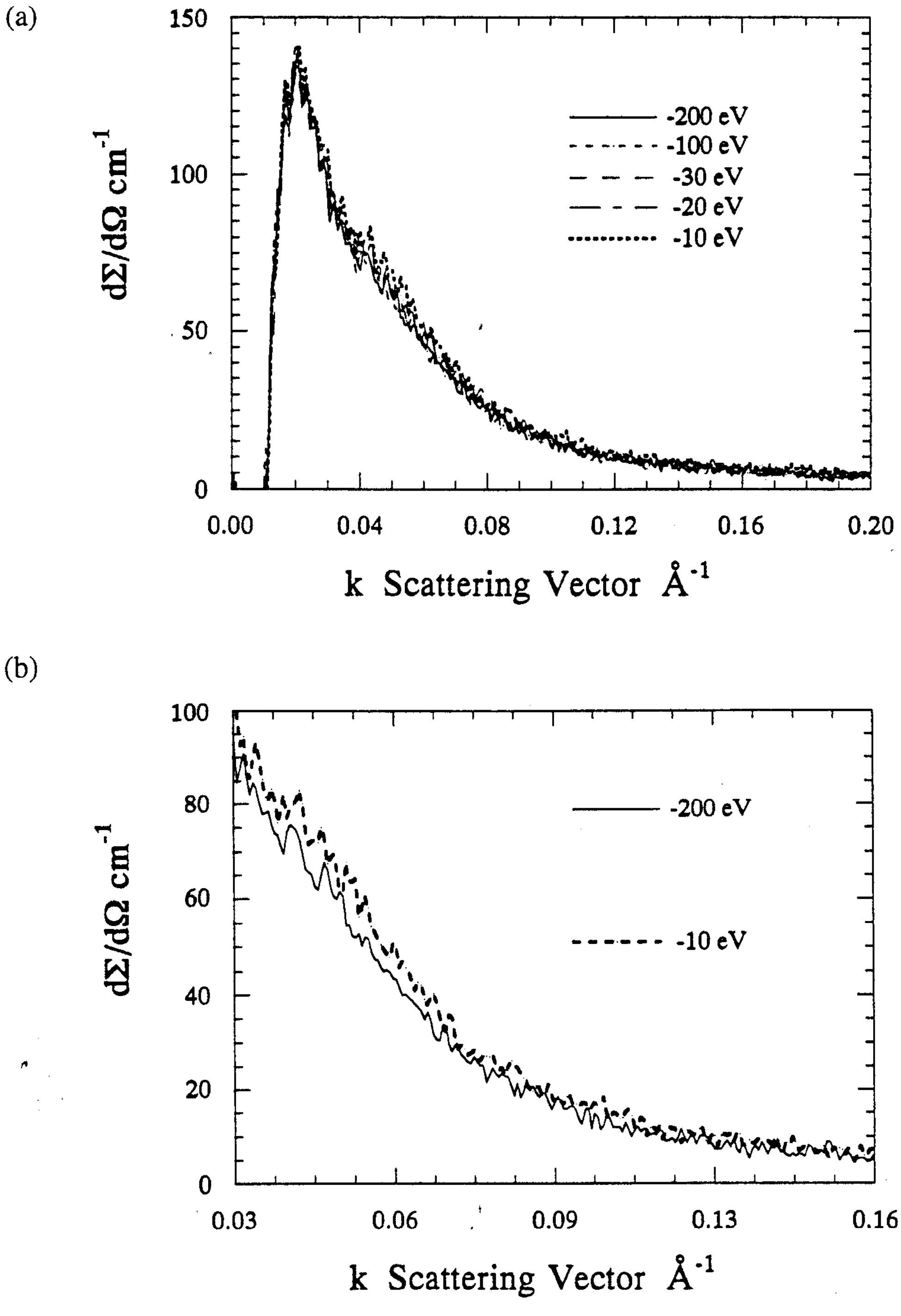

FIGURE VI.6 The differential scattering cross section for the *a*-$Fe_{44}Ge_{56}$ sample (a) at incident photon energies of 200, 100, 30, 20, and 10 eV below the Ge *K* absorption edge and (b) on an expanded scale at incident photon energies of 200 and 10 eV below the Ge *K* absorption edge.

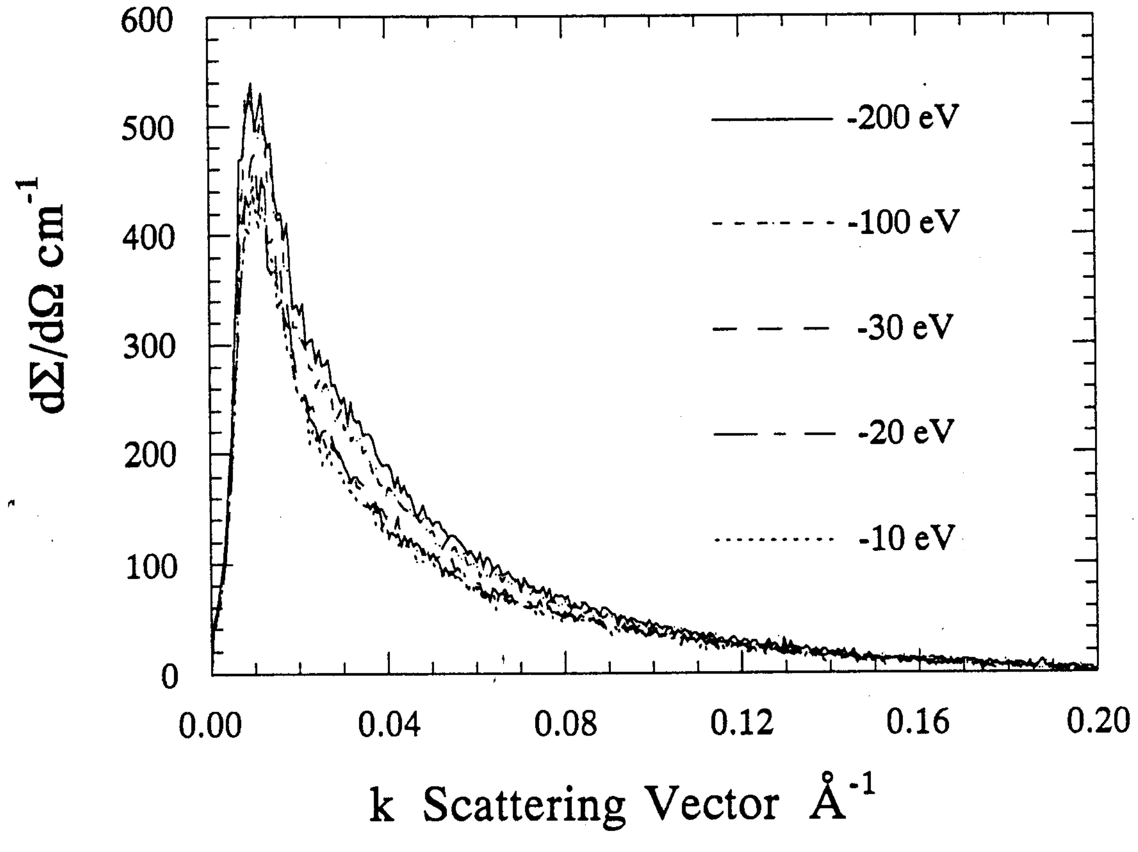

FIGURE VI.7 The differential scattering cross section for the *a*-$Fe_{49}Ge_{51}$ sample at incident photon energies of 200, 100, 30, 20, and 10 eV below the Fe *K* absorption edge.

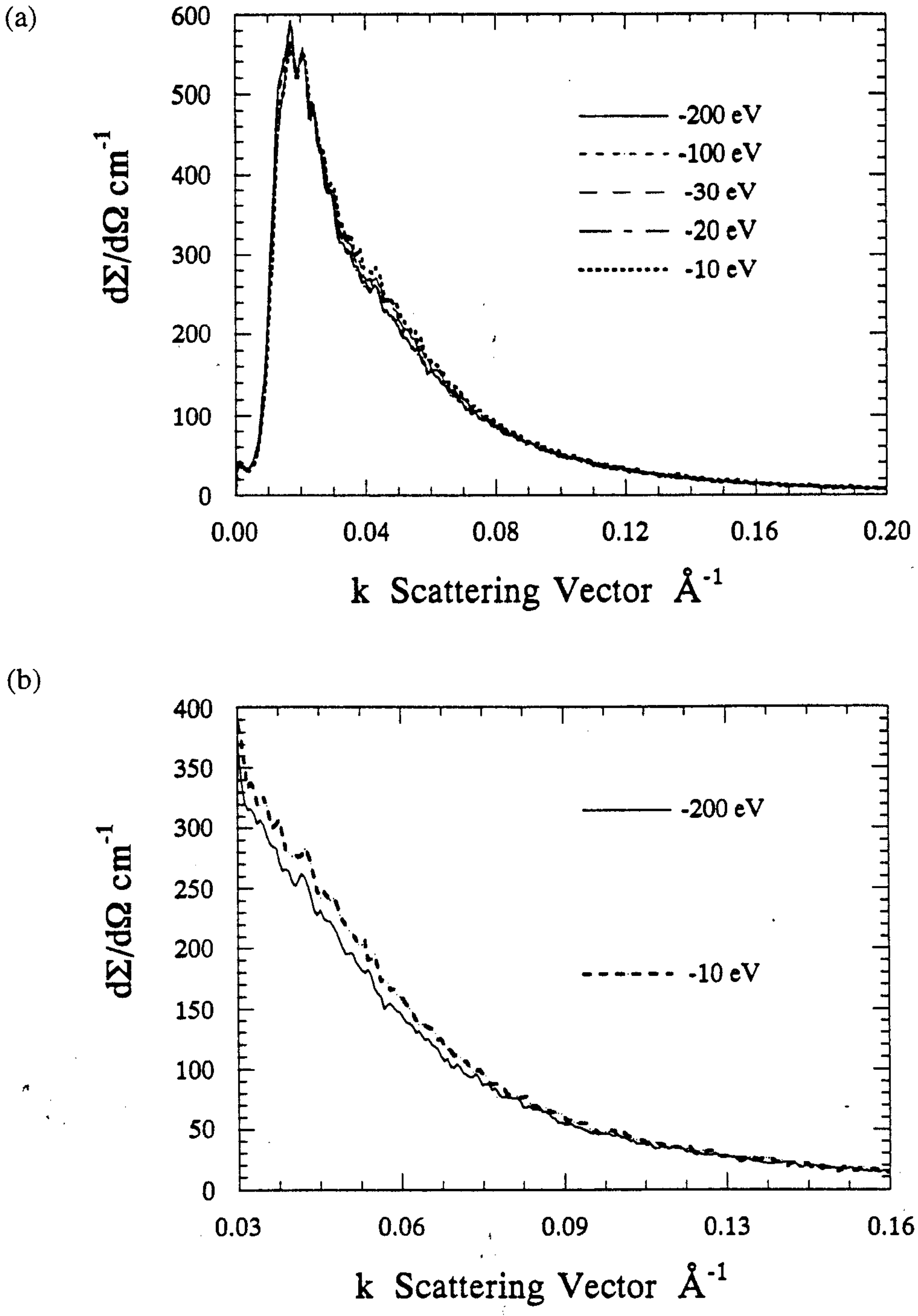

FIGURE VI.8 The differential scattering cross section for the *a*-$Fe_{49}Ge_{51}$ sample (a) at incident photon energies of 200, 100, 30, 20, and 10 eV below the Ge *K* absorption edge and (b) on an expanded scale at incident photon energies of 200 and 10 eV below the Ge *K* absorption edge.

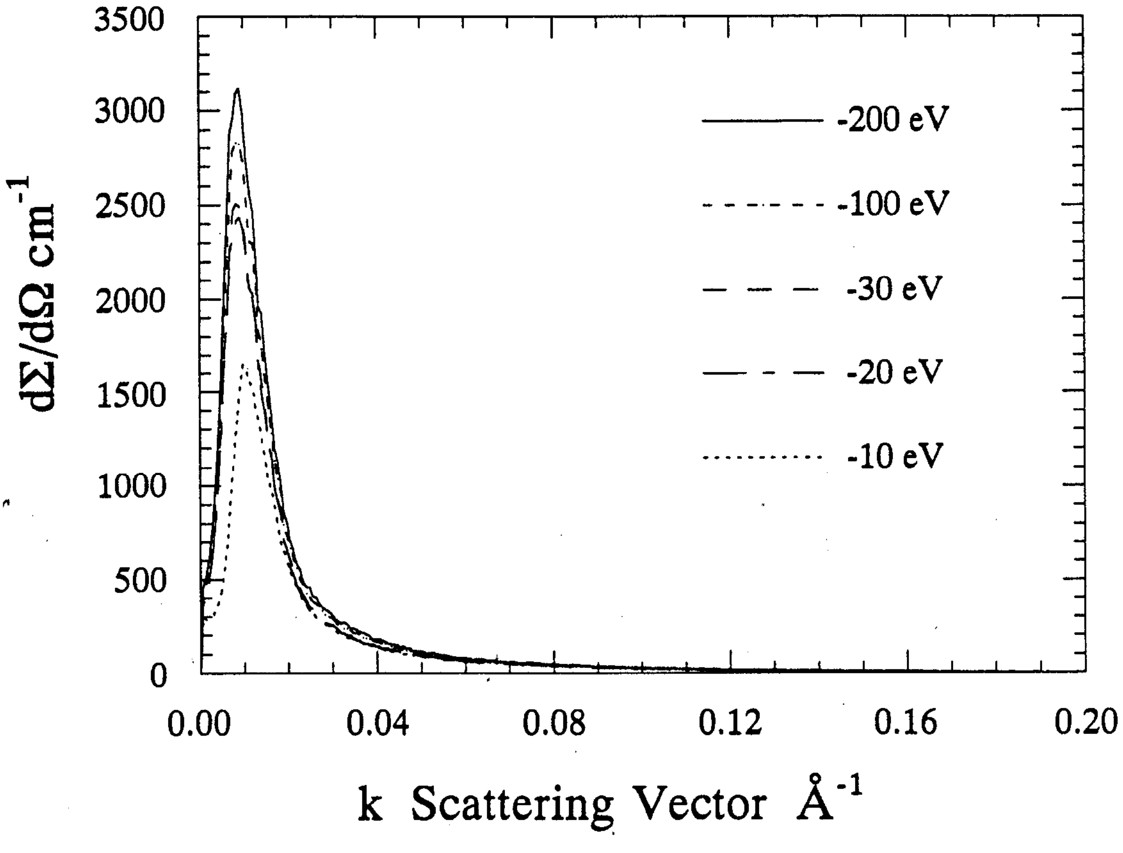

FIGURE VI.9 The differential scattering cross section for the *a*-$Fe_{65}Ge_{35}$ sample at incident photon energies of 200, 100, 30, 20, and 10 eV below the Fe *K* absorption edge.

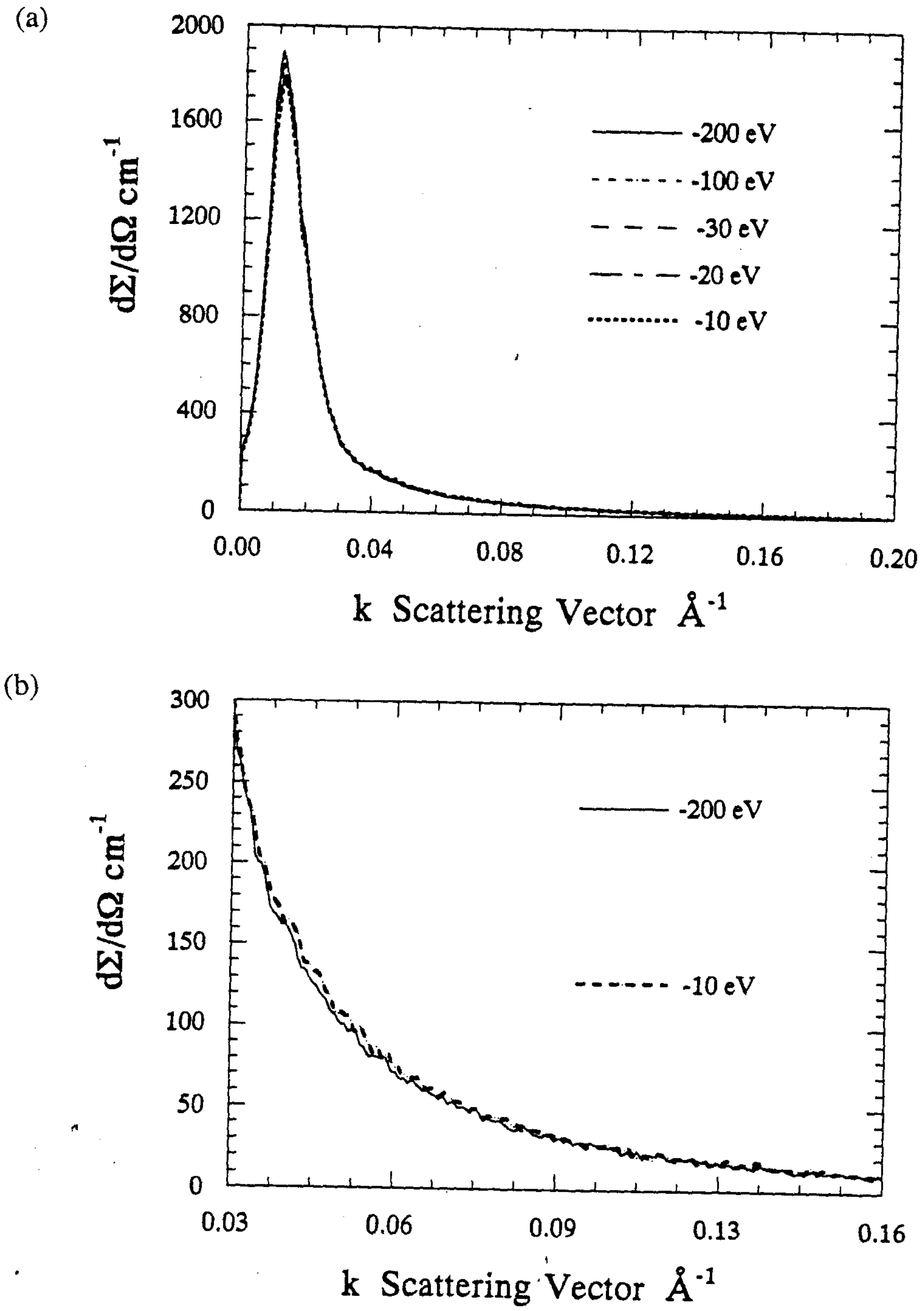

FIGURE VI.10 The differential scattering cross section for the a-$\mathrm{Fe}_{65}\mathrm{Ge}_{35}$ sample (a) at incident photon energies of 200, 100, 30, 20, and 10 eV below the Ge *K* absorption edge and (b) on an expanded scale at incident photon energies of 200 and 10 eV below the Ge *K* absorption edge.

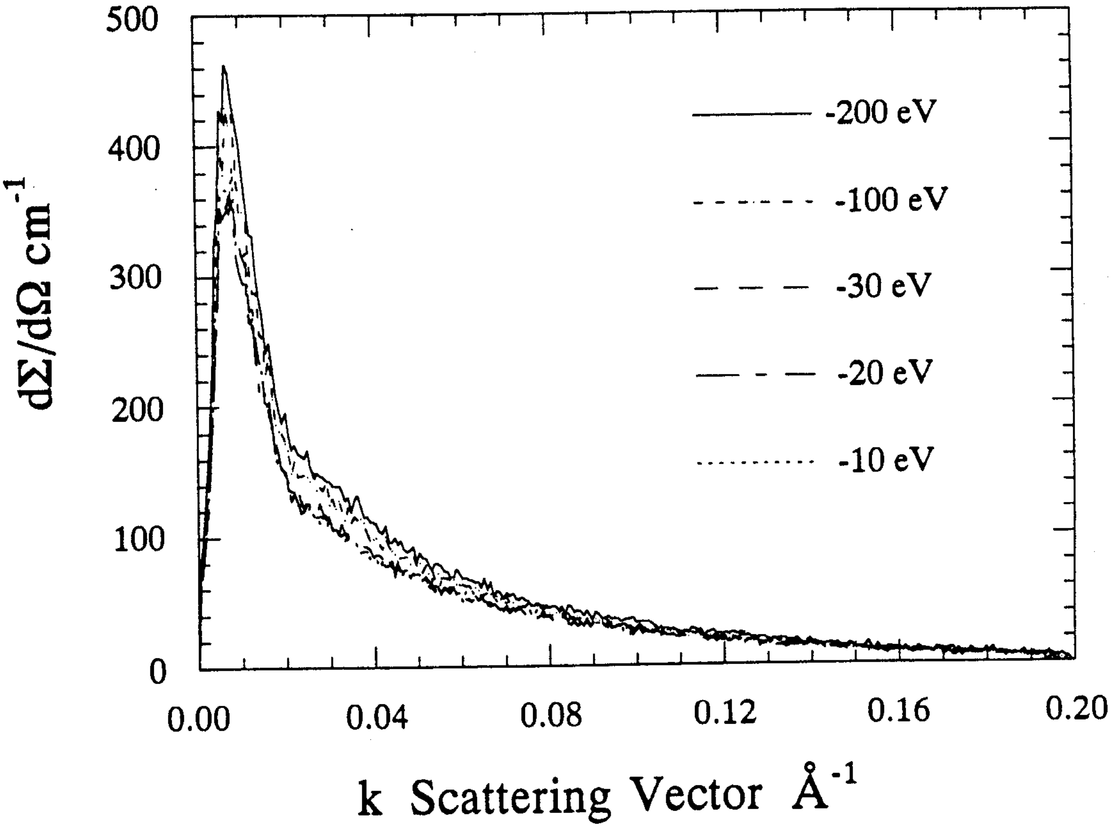

FIGURE VI.11 The differential scattering cross section for the a-$Fe_{71}Ge_{28}$ sample at incident photon energies of 200, 100, 30, 20, and 10 eV below the Fe K absorption edge.

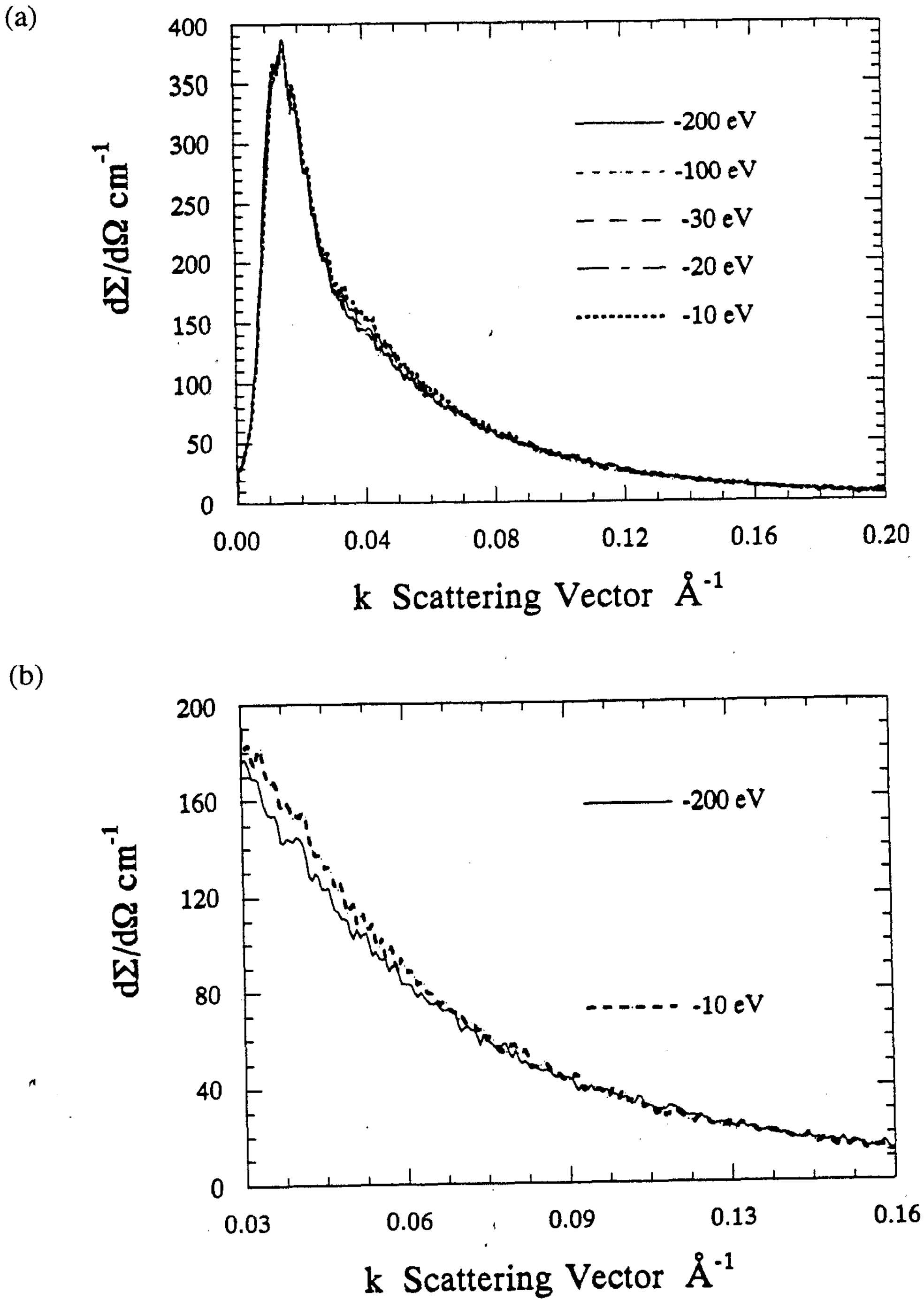

FIGURE VI.12 The differential scattering cross section for the *a*-$Fe_{71}Ge_{29}$ sample (a) at incident photon energies of 200, 100, 30, 20, and 10 eV below the Ge *K* absorption edge and (b) on an expanded scale at incident photon energies of 200 and 10 eV below the Ge *K* absorption edge.

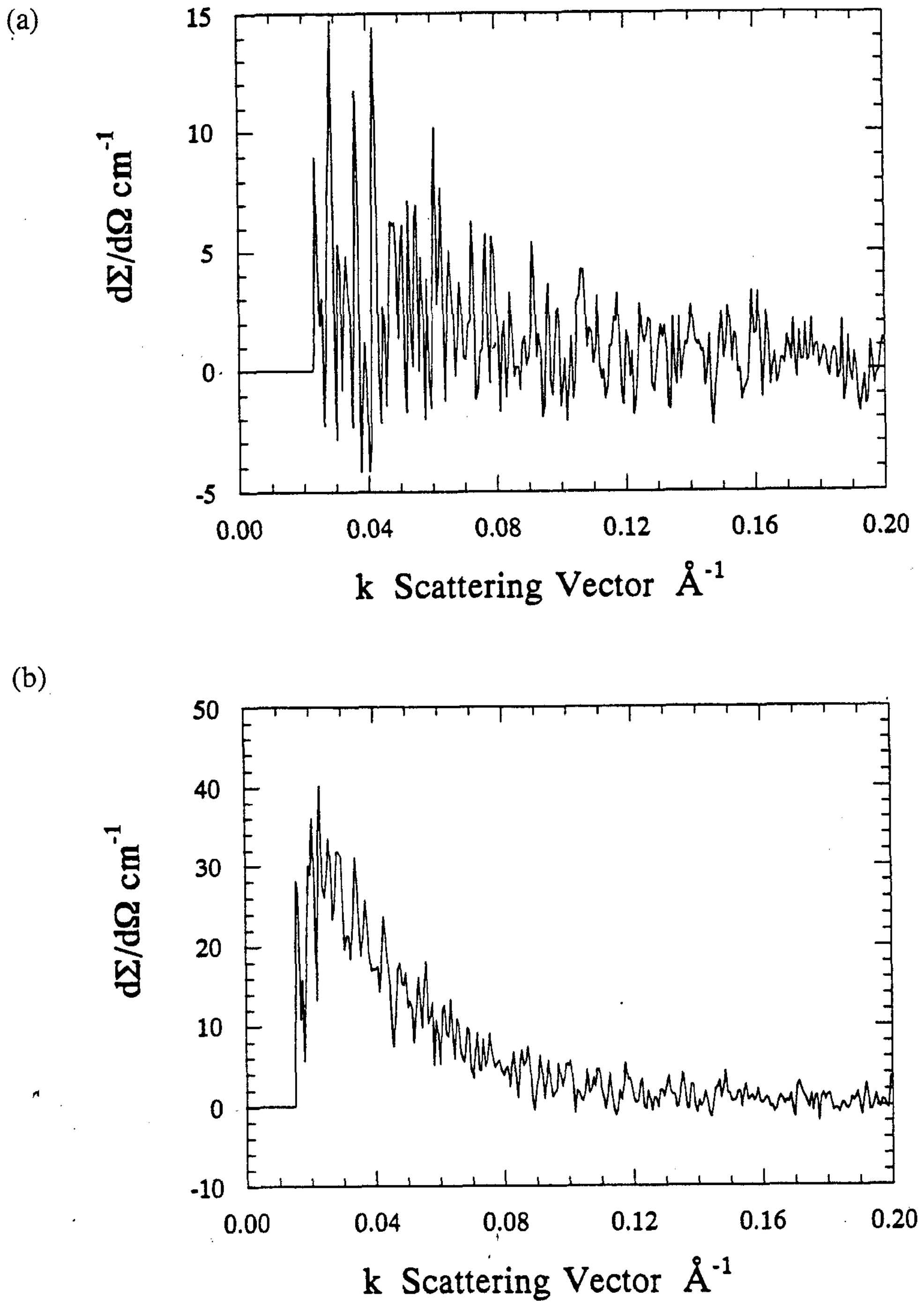

FIGURE VI.13 The result of $d\Sigma/d\Omega(k)$ at 11093 eV (10 eV below the Ge K absorption edge) minus $d\Sigma/d\Omega(k)$ at 10903 eV for (a) the a-$Fe_{34}Ge_{66}$ sample and (b) the a-$Fe_{37}Ge_{63}$ sample.

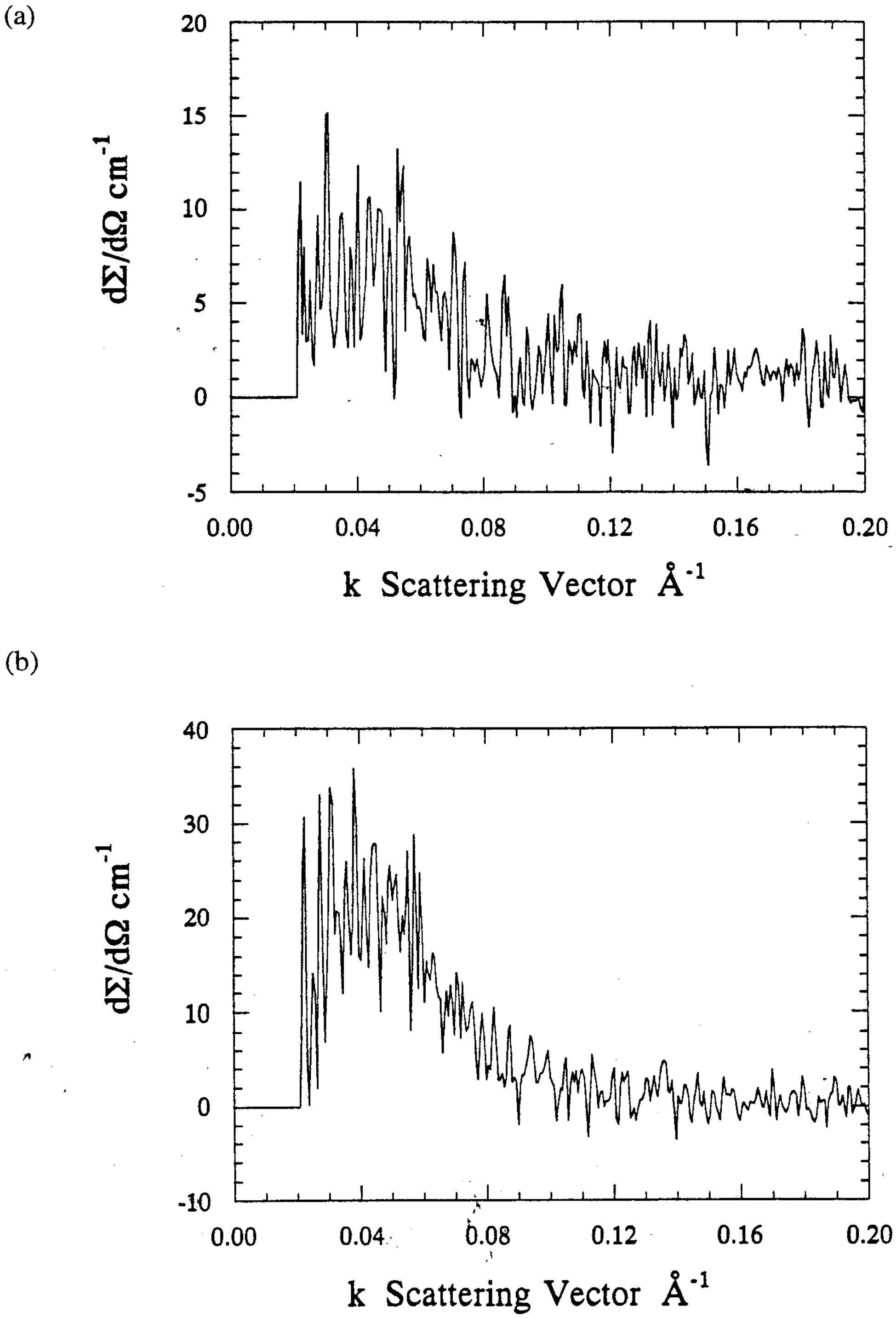

FIGURE VI.14 The result of $d\Sigma/d\Omega(k)$ at 11093 eV minus $d\Sigma/d\Omega(k)$ at 10903 eV for (a) the a-$Fe_{44}Ge_{56}$ sample and (b) the a-$Fe_{49}Ge_{51}$ sample.

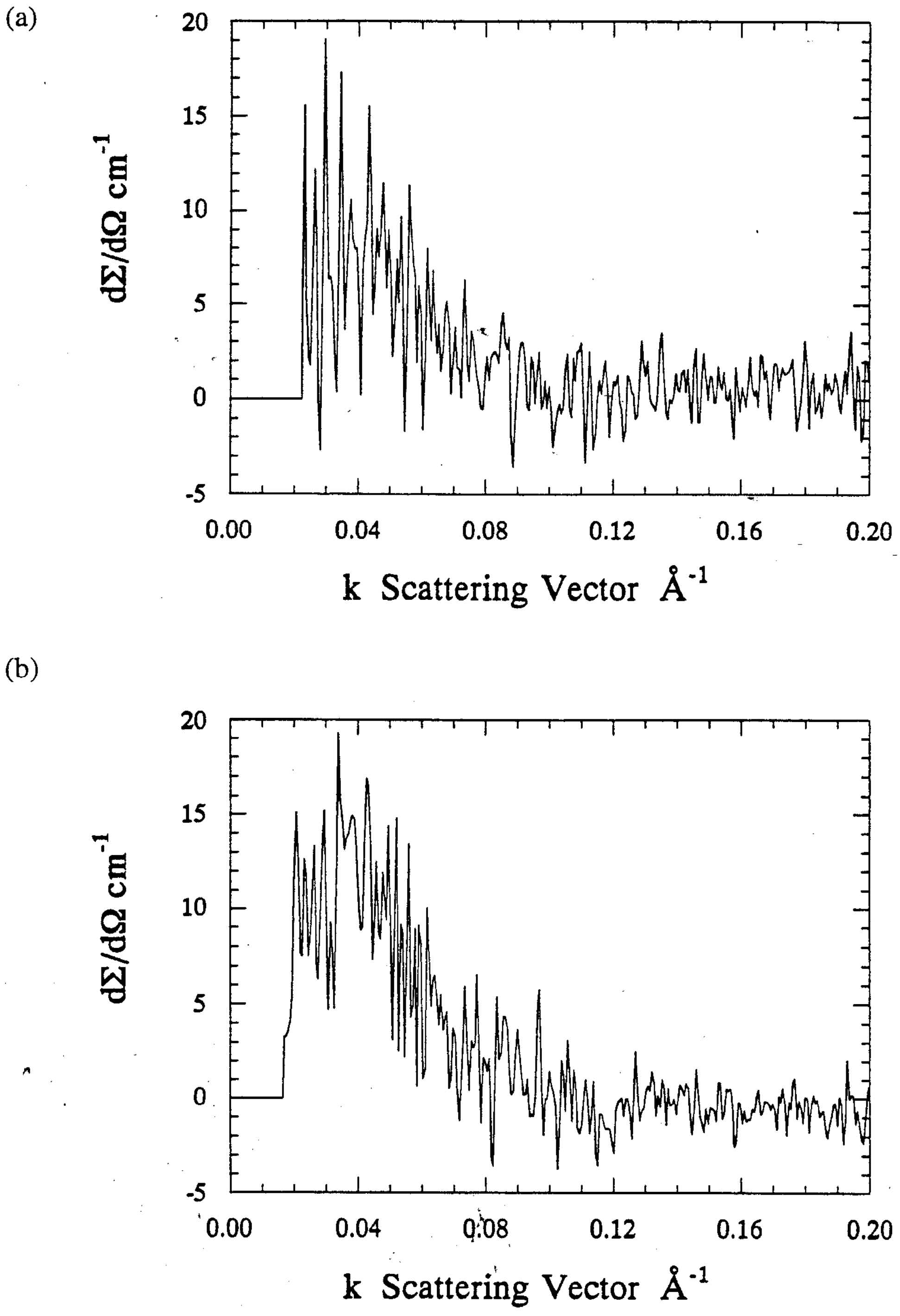

FIGURE VI.15 The result of $d\Sigma/d\Omega(k)$ at 11093 eV minus $d\Sigma/d\Omega(k)$ at 10903 eV for (a) the a-$Fe_{65}Ge_{35}$ sample and (b) the a-$Fe_{71}Ge_{28}$ sample.

The increase in the magnitude of $d\Sigma/d\Omega(k)$ with increasing photon energy below the Ge edge of each sample in the composition range $34\leq x\leq 71$ shows clearly that the electron density fluctuations that give rise to the SAXS patterns are not simply cracks or voids, but, rather, include some type of chemical inhomogeneity. As shown in Chapter V, equation (5.33), a scattering cross section due solely to simple density fluctuations such as cracks and/or voids would decrease as the photon energy was increased beneath the absorption edge of either element in a binary alloy. The data from these six samples, therefore, indicate phase separation across the composition range $34\leq x\leq 71$.

The similar behavior of the ASAXS for all of these samples suggests that the same phases are present in each and that the end points of phase separation lie outside the range $34\leq x\leq 71$. The assumption that there are analogs between the crystalline and amorphous phases of Fe-Ge points to a-FeGe$_2$ and a-Fe$_3$Ge (a-Fe$_{33}$Ge$_{67}$ and a-Fe$_{75}$Ge$_{25}$) as the likely products of phase separation in the $34\leq x\leq 71$ composition range. The very slight anomalous effect at the Ge edge for the a-Fe$_{34}$Ge$_{66}$ sample compared to the more metal rich samples also supports a-Fe$_{33}$Ge$_{67}$ as an end point of phase separation. Furthermore, the strong increase in the scattering cross section with increasing photon energy beneath the Ge edge for the a-Fe$_{49}$Ge$_{51}$ sample shows that a-FeGe is not a likely end product of phase separation. The XANES analysis of Lorentz (1986) and Lorentz et al. (1994) indicates phase separation into a-FeGe$_2$ and a-Fe$_3$Ge for these same samples. The ASAXS data are now considered in light of this evidence.

In a two phase system, the differential scattering cross section, $d\Sigma/d\Omega(k)$, is proportional to the absolute square of the effective electron density difference, $|\rho_1(E)-\rho_2(E)|^2$, (recall equation (5.46)) which can be expressed in terms of the atomic scattering factors, f_α, the atomic number density, N_n/V_n, of each phase n, and the fraction, m_n, of A atoms in each phase n:

$$\frac{d\Sigma}{d\Omega}(k)\alpha\left|\left[\frac{N_1}{V_1}m_1-\frac{N_2}{V_2}m_2\right]f_A+\left[\frac{N_1}{V_1}(1-m_1)-\frac{N_2}{V_2}(1-m_2)\right]f_B\right|^2. \qquad (6.1)$$

The anomalous corrections to the atomic scattering factors of Fe and Ge are listed in Table VI.1 for incident photon energies of 200, 100, 30, 20 and 10 eV below the K absorption edges of Fe and Ge. Cromer-Liberman (1970) values are used far from the edge (e.g., f'_{Ge} at 6912 eV), while the experimentally determined values for the six samples were averaged together to obtain the corrections close to the edge. For Ge, Z is equal to 32 while for Fe, Z is equal to 26. The real ($Z+f'$) and the imaginary (f'') parts of the total atomic scattering factors for Fe and Ge are listed in Table VI.2. As is clear from Table VI.2, the atomic scattering factors for Fe and Ge are nearly identical close to the Ge K absorption edge.

If the samples in the composition range $34 \leq x \leq 71$ were chemically homogeneous and the SAXS arose from simple density fluctuation such as cracks or voids, the absolute square of the effective electron density difference, $|\rho_1(E)-\rho_2(E)|^2$, would decrease with increasing photon energy beneath both the Fe and the Ge K absorption edges as shown in Table VI.3 for the a-$Fe_{37}Ge_{63}$ sample. In the calculation of $|\rho_1(E)-\rho_2(E)|^2$, the number density of atoms in the second phase (cracks or voids), N_2, is zero. The a-$Fe_{37}Ge_{63}$ sample was chosen as a representative of the $34 \leq x \leq 71$ composition range. The number of Fe atoms per unit volume, $(N_1/V_1)m_1$ and the number of Ge atoms per unit volume, $(N_1/V_1)(1-m_1)$, were taken to be 0.95 times the values determined by interpolating between the number densities of Fe and Ge in c-$FeGe_2$ and the hexagonal form c-FeGe. These trends are obviously not consistent with the data.

TABLE VI.1

f' and *f''* for Fe and Ge near the Fe and Ge absorption edges.

Energy (eV)	f'_{Ge}	f''_{Ge}	f'_{Fe}	f''_{Fe}
6912.	-0.853	1.16	-3.21	0.490
7012.	-0.879	1.13	-3.92	0.493
7082.	-0.898	1.11	-5.24	0.505
7092.	-0.900	1.11	-5.69	0.518
7102.	-0.903	1.11	-6.66	0.597
10903.	-3.59	0.508	0.0913	1.94
11003.	-4.32	0.501	0.105	1.91
11073.	-5.69	0.518	0.114	1.89
11083.	-6.17	0.537	0.115	1.88
11093.	-7.09	0.607	0.116	1.88

TABLE VI.2

The real and imaginary parts of the total atomic scattering factors for Fe and Ge near the Fe and Ge absorption edges.

Energy (eV)	Re[f_{Ge}]	Im[f_{Ge}]	Re[f_{Fe}]	Im[f_{Fe}]
6912.	31.15	1.16	22.79	0.490
7012.	31.12	1.13	22.09	0.493
7082.	31.10	1.11	20.77	0.505
7092.	31.10	1.11	20.31	0.518
7102.	31.10	1.11	19.34	0.597
10903.	28.41	0.508	26.09	1.94
11003.	27.68	0.501	26.11	1.91
11073.	26.32	0.518	26.11	1.89
11083.	25.83	0.537	26.12	1.88
11093.	24.92	0.607	26.12	1.88

TABLE VI.3

The values of $|\rho_1(E)-\rho_2(E)|^2$ for the a-$Fe_{37}Ge_{63}$ sample near the Fe and Ge absorption edges assuming homogeneous a-$Fe_{37}Ge_{63}$ as phase 1 and cracks or voids as phase 2.

Energy (eV)	$\lvert\rho_1(E)-\rho_2(E)\rvert^2$
6912.	3.64
7012.	3.56
7082.	3.44
7092.	3.39
7102.	3.31
10903.	3.51
11003.	3.39
11073.	3.18
11083.	3.11
11093.	2.97

If the samples in the $34 \leq x \leq 71$ composition range are phase separated into a-$FeGe_2$ and a-Fe_3Ge, the absolute square of the effective electron density difference, $|\rho_1(E)-\rho_2(E)|^2$, will behave as shown in Table VI.4. These calculations were performed using a-$FeGe_2$ as phase 1 with an atomic number density equal to 0.95 times that of c-$FeGe_2$ and a-Fe_3Ge as phase 2 with an atomic number density equal to 0.95 times that of the cubic form of c-Fe_3Ge:

$$\frac{N_1}{V_1} = 0.95\left(0.06936\ \frac{atoms}{\mathring{A}^3}\right) \tag{6.2}$$

and

$$\frac{N_2}{V_2} = 0.95\left(0.08125\ \frac{atoms}{\mathring{A}^3}\right). \tag{6.3}$$

Therefore,

$$m_1=0.33, \qquad (1-m_1)=0.67, \tag{6.4}$$
$$m_2=0.75, \qquad \text{and} \qquad (1-m_2)=0.25.$$

This then gives

$$\left[\frac{N_1}{V_1}m_1 - \frac{N_2}{V_2}m_2\right]f_A = (0.95)[-0.0378]f_{Fe} \tag{6.5}$$

and

$$\left[\frac{N_1}{V_1}(1-m_1) - \frac{N_2}{V_2}(1-m_2)\right]f_B = (0.95)[0.260]f_{Ge}. \tag{6.6}$$

So, the scattering cross section, $d\Sigma/d\Omega(k)$, is proportional to

$$(0.95)^2|[-0.0378]f_{Fe} + [0.0260]f_{Ge}|^2. \tag{6.7}$$

The scattering cross section for samples that are phase separated into a-$FeGe_2$ and a-Fe_3Ge will decrease as the incident photon energy changes from 200 to 100 to 30 eV below the Fe K absorption edge. The scattering cross section will then increase as the incident photon energy changes from 30 to 20 to 10 eV below the Fe K absorption edge. This trend is obviously not consistent with the ASAXS data from any of the samples in the $34 \leq x < 71$ composition range.

If the number densities of the amorphous phases are assumed to scale not as 0.95 times the number densities of the crystalline phases but, say, a-FeGe$_2$ has a number density equal to 0.93 times that of c-FeGe$_2$ and a-Fe$_3$Ge has a number density of 0.98 times that of c-Fe$_3$Ge, the trend in $|\rho_1(E)-\rho_2(E)|^2$ with energy, shown in Table VI.4, can be reproduced for energies near the Fe K absorption edge.

Table VI.4 shows an increase in $|\rho_1(E)-\rho_2(E)|^2$ with increasing energy beneath the Ge K absorption edge. While this trend is consistent with the data, the scattering cross sections of the individual samples are not an order of magnitude larger at the Ge edge than at the Fe edge as indicated in the table. This is seen more clearly in Figure VI.16 which shows the data for the a-Fe$_{37}$Ge$_{63}$ sample and a model calculation for homogeneous spheres of a-Fe$_3$Ge, with R=47 Å and σ=100 Å, immersed in a-FeGe$_2$ (recall equation (5.46) and the discussion in Chapter V, section 5.5 (a)). The peak in the scattering cross section for the Fe edge data is absent from the Ge edge data due to the poorer k space resolution at the shorter X-ray wavelength. The peak at the Ge edge (if there is one) blends into the parasitic scattering. The model produces a peak in the scattering cross section at the correct k value with the correct order of magnitude, for incident photon energies near the Ge edge. The minute value of the predicted scattering cross sections for incident photon energies near the Fe K absorption edge, however, is very obvious in this figure.

A composite particle model (described in Chapter V, section 5.5 (b)) was also tried, both with spheres with a-Fe$_3$Ge cores and a-FeGe$_2$ shells and vice versa. The better fit was with a model of spheres with cores of a-Fe$_3$Ge and shells of a-FeGe$_2$. The results are shown in Figure VI.17. This model is also unsatisfactory. For incident photon energies near the Fe K absorption edge, the model produces a peak in the scattering cross section at k=0, rather than at k=0.03.

Altering the scaling of the densities of the amorphous phases relative to the crystalline phases, as described above (such as .98 times the number density of a-Fe$_3$Ge and .93 times the number density of c-FeGe$_2$), does not increase the predicted scattering

TABLE VI.4

The values of $|\rho_1(E)-\rho_2(E)|^2$ for the $34 \leq x \leq 71$ samples near the Fe and Ge absorption edges assuming phase separation with a-FeGe$_2$ as phase 1 and a-Fe$_3$Ge as phase 2.

Energy (eV)	$\lvert\rho_1(E)-\rho_2(E)\rvert^2$
6912.	0.0028
7012.	0.00082
7082.	0.00049
7092.	0.0014
7102.	0.0051
10903.	0.0598
11003.	0.0688
11073.	0.0872
11083.	0.0943
11093.	0.108

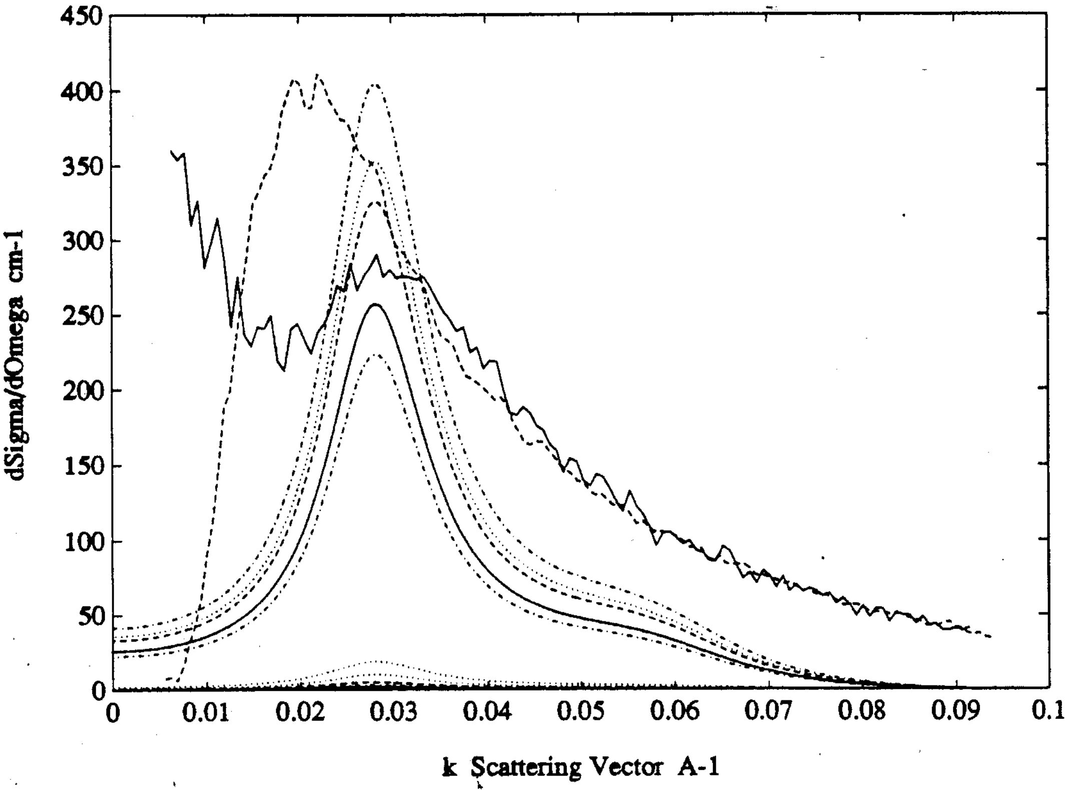

FIGURE VI.16 Homogeneous particle model for the *a*-$Fe_{37}Ge_{63}$ sample at five energies beneath the Ge K absorption edge and at five energies beneath the Fe K absorption edge. Smooth lines: spheres of *a*-Fe_3Ge, with R=47 Å and σ=100 Å, in a matrix of *a*-$FeGe_2$. Noisy lines: data at 200 eV below the Ge edge (-----) and at 200 eV below the Fe edge (——).

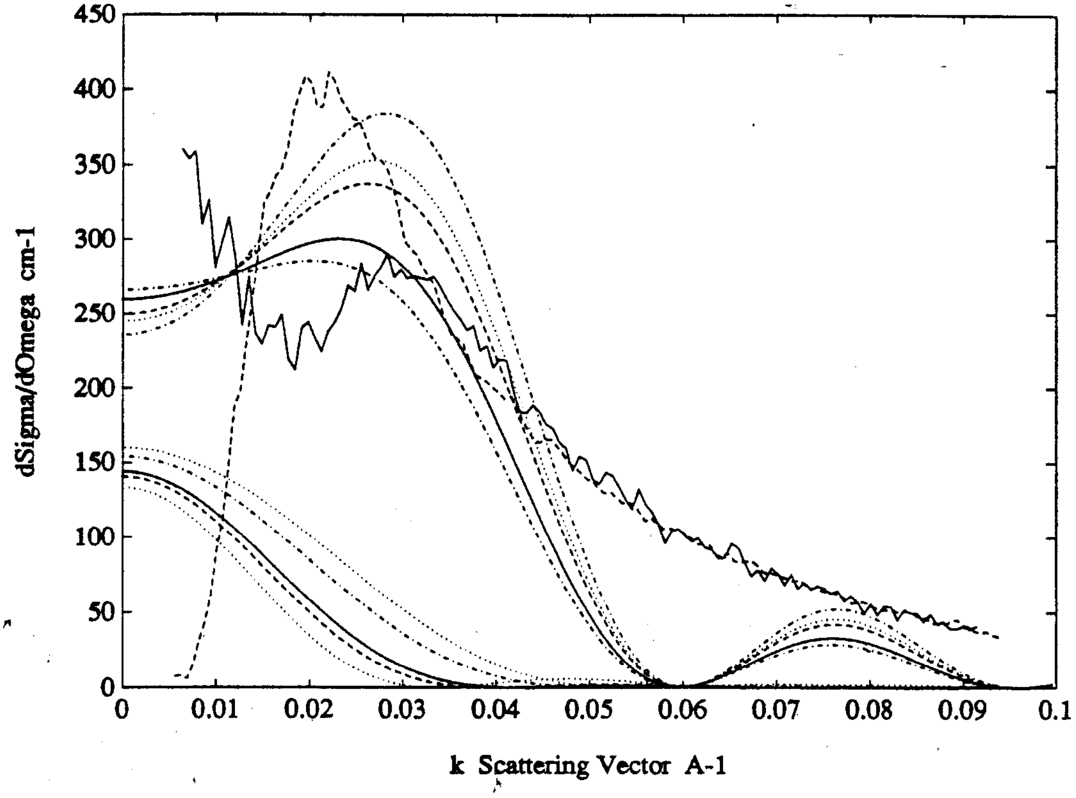

FIGURE VI.17 Inhomogeneous particle model for the *a*-$Fe_{37}Ge_{63}$ sample at five energies beneath the Ge *K* absorption edge and at five energies beneath the Fe *K* absorption edge. Smooth lines:: Spheres with cores of *a*-$FeGe_2$ ($c^{1/3}R$=93 Å) and shells of *a*-Fe_3Ge (R=95 Å) in a *a*-$Fe_{37}Ge_{63}$ matrix. Noisy lines: Ge edge data (------) and Fe edge data (———).

cross sections near the Fe edge by the necessary orders of magnitude. Resorting to other crystalline analogs, such as the hexagonal phase of c-Fe_3Ge, does not improve the model at the Fe edge either.

These data show that the a-Fe_xGe_{100-x} samples in the $34 \leq x \leq 71$ composition range are not phase separated solely into amorphous phases of Fe_3Ge and $FeGe_2$ that have number densities similar to the crystalline phases. Resorting to other phases, such as a-Fe and a-Ge, and all other two phase combinations of the crystalline analogs, did not reproduce the data either. As discussed above, the data also do not match a model of voids in a homogeneous amorphous matrix. The voids model, however, at least predicts scattering cross sections of the same order of magnitude at both edges. This led to a model of phase separation into a-Fe_3Ge and a-$FeGe_2$ in combination with voids.

The result of a model of homogeneous spheres of a-Fe_3Ge plus voids in an a-$FeGe_2$ matrix is shown in Figure VI.18. In this model the voids occupy 0.4 % of the total sample volume. While the model does not accurately reproduce the shape of the SAXS pattern (the peak at k=0.03 for the scattering cross section at the Fe edge is overwhelmed by the void scattering), it at least produces scattering cross sections at the Fe edge that are similar in magnitude to those at the Ge edge and to the data. The correct trend in the magnitude of the scattering cross section with changing f' at both edges is also observed with this model. This is the best of the models explored here. The analysis presented here strongly suggests that the samples with $34 \leq x \leq 71$ contain chemical fluctuations as well as simple density fluctuations like cracks or voids.

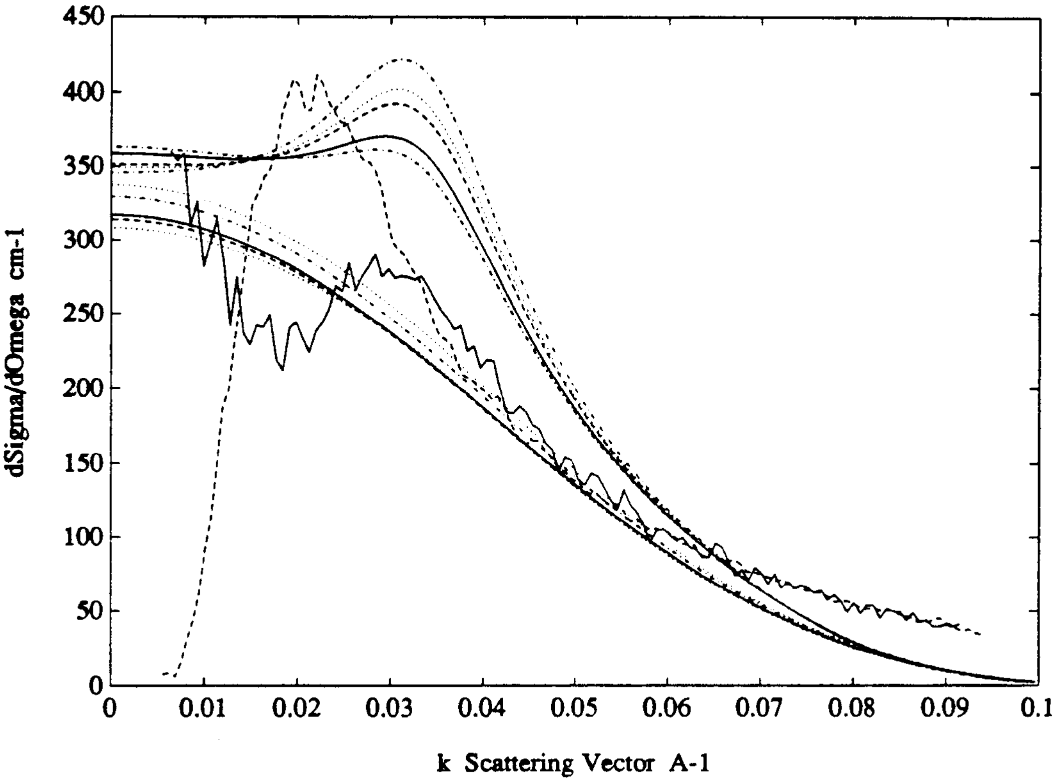

FIGURE VI.18 The homogeneous sphere model plus voids for the *a*-$Fe_{37}Ge_{63}$ sample at five energies below the Ge *K* absorption edge and at five energies below the Fe *K* absorption edge. Smooth lines: spheres of *a*-Fe_3Ge (R=47 Å, σ=100 Å) and 40 Å radius voids (occupying a volume fraction of .004) in a matrix of *a*-$FeGe_2$. Noisy lines: Ge edge data (------) and Fe edge data (——).

6.2 THE a-FE$_{28}$GE$_{72}$ SAMPLE

The scattering cross sections for the a-Fe$_{28}$Ge$_{72}$ sample are displayed in Figure VI.19. This sample has a SAXS pattern that resembles neither those of the $x<25$ samples nor those of the $x>33$ samples. The magnitude of the scattering cross section decreases with increasing energy beneath both the Fe K absorption edge and the Ge K absorption edge. The peak in the scattering cross section for this sample is 50 times greater than those of the samples with x just a few atomic percent smaller (x=18, 19, 24). This immediately suggests voids as the source of scattering. A model of voids in a homogeneous matrix of a-Fe$_{28}$Ge$_{72}$, however, produces scattering cross sections that are 30 times greater than the data. Furthermore, a peak at a non-zero k value requires a volume fraction of voids in excess of 0.20. This is an unreasonable model.

No model of phase separation into a-Ge and a-FeGe$_2$ (either homogeneous spheres or inhomogeneous spheres) can reproduce the decrease in the scattering cross section with increasing energy below the Ge K absorption edge. A model of spheres of a-Ge, with R=70 Å and σ=85 Å, in an a-FeGe$_2$ matrix produces a peak in the scattering cross section at the correct value of k but with a magnitude three times too large.

This leads again to a model of chemical phase separation plus voids. The addition of voids with a radius of 25 Å, filling 6 % of the sample volume, to the above model reproduces the trend in $d\Sigma/d\Omega(k)$ with energy at both edges. The model, however, has a peak in $d\Sigma/d\Omega(k)$ that is now six times larger than the data.

(a)

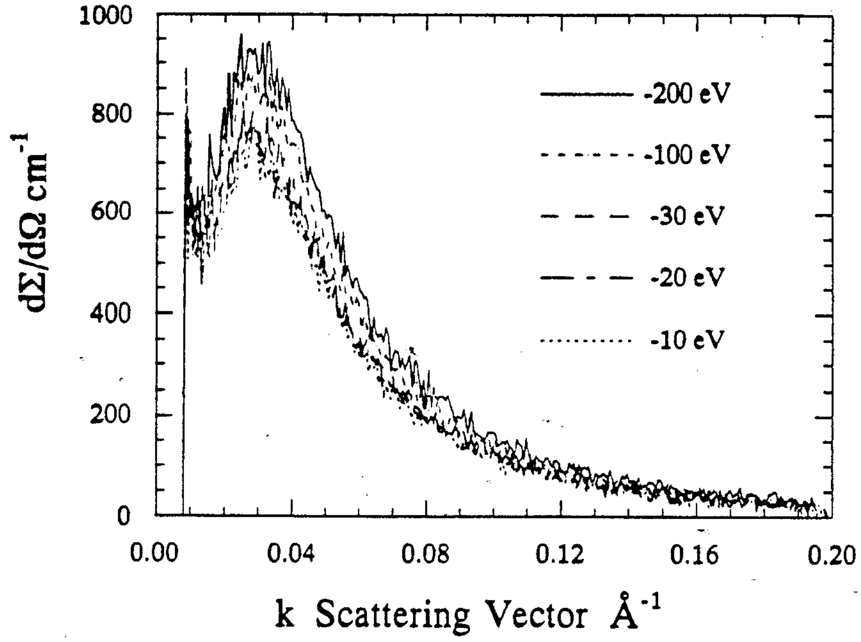

(b)

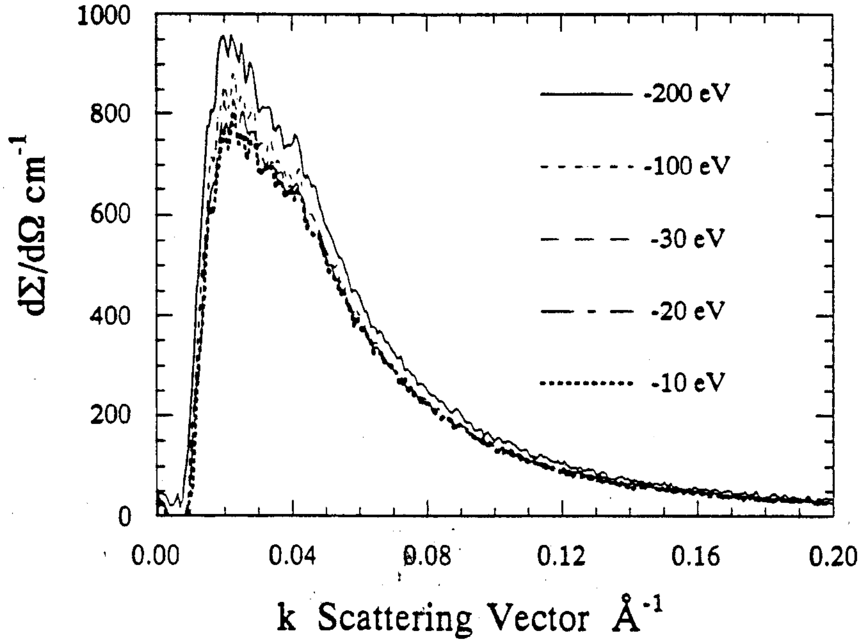

Figure VI.19 The *a*-$Fe_{28}Ge_{72}$ sample. (a) The scattering cross section for incident photon energies of 200, 100, 30, 20, and 10 eV below the Fe *K* absorption edge. (b) The scattering cross section for incident photon energies of 200, 100, 30, 20, and 10 eV below the Ge *K* absorption edge.

6.3 THE a-MO$_x$GE$_{100-x}$ SAMPLES WITH $x>25$

The scattering cross sections near the Ge *K* absorption edge for the a-Mo$_x$Ge$_{100-x}$ samples with x equal to 32, 39, and 72 are shown in Figures VI.20 & VI.21. As mentioned previously, no Mo edge data were collected. These SAXS patterns are essentially featureless, indicating no phase separation on the length scales explored here. This is consistent with the analysis of Kortright (1984) and Kortright et al. (1988) in which the samples in structural regions I & II ($x>25$) were described as apparently homogeneous.

The lack of features in the SAXS patterns of the a-Mo$_x$Ge$_{100-x}$ samples with $x>25$ contrasts sharply with the behavior of the a-Fe$_x$Ge$_{100-x}$ samples in this concentration regime. Phase separation in the a-Fe$_x$Ge$_{100-x}$ samples may well arise from the deposition conditions (triode sputtering as opposed to magnetron sputtering). Regan (1993) reports the absence of significant small angle scattering for magnetron sputtered a-Fe$_x$Ge$_{100-x}$ samples with $x>33$.

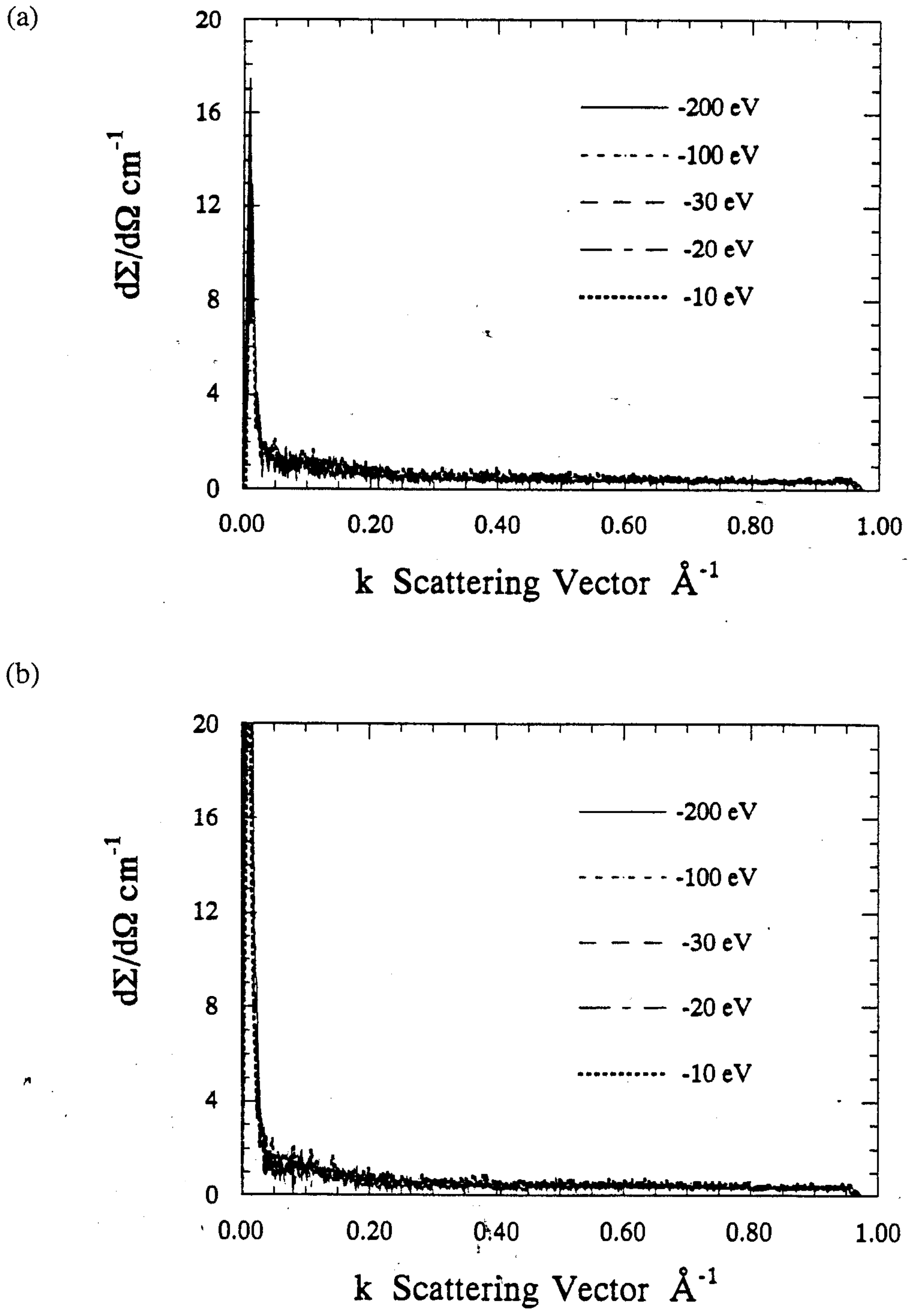

FIGURE VI.20 The scattering cross sections at 200, 100, 30, 20, and 10 eV below the Ge *K* absorption edge of (a) the *a*-$Mo_{32}Ge_{68}$ sample and (b) the *a*-$Mo_{39}Ge_{61}$ sample.

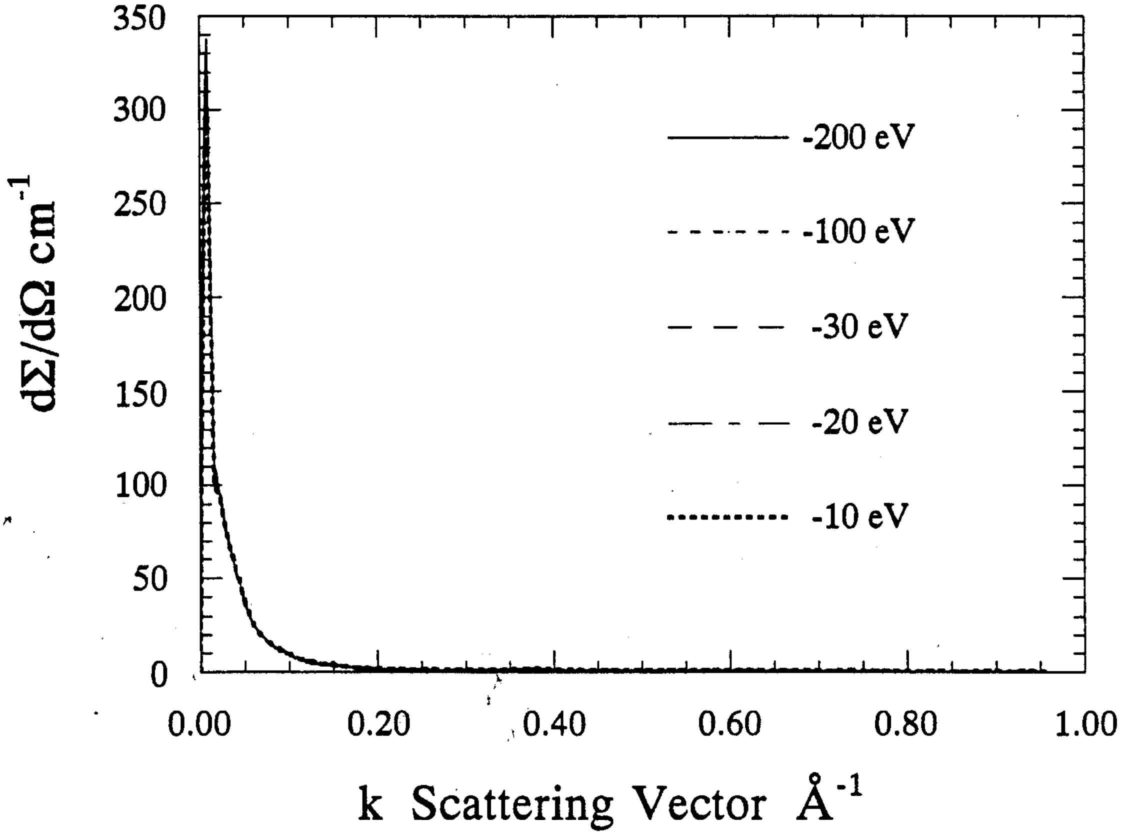

FIGURE VI.21 The scattering cross sections at 200, 100, 30, 20, and 10 eV below the Ge *K* absorption edge of the *a*-$Mo_{72}Ge_{28}$ sample.

6.4 THE a-W$_x$GE$_{100-x}$ SAMPLES WITH $x>25$

Three a-W$_x$Ge$_{100-x}$ samples in the $x>25$ concentration regime, a-W$_{45}$Ge$_{55}$, a-W$_{50}$Ge$_{50}$, and a-W$_{78}$Ge$_{22}$ were studied. Scattering cross sections for these samples at incident photon energies near the W L_{III} absorption edge and the Ge K absorption edge appear in Figures VI.22-VI.24. Like the a-Mo$_x$Ge$_{100-x}$ samples with $x>25$, the a-W$_{78}$Ge$_{22}$ sample is essentially featureless. Additionally, its wide angle X-ray scattering pattern is similar to those of melt-quench glasses, with a sharp first peak and a broadened split second peak. This sample seems to be homogeneous.

The a-W$_{45}$Ge$_{55}$ and the a-W$_{50}$Ge$_{50}$ samples have scattering cross sections that resemble neither those of the a-Mo$_x$Ge$_{100-x}$ nor of the a-Fe$_x$Ge$_{100-x}$ system in the $x>25$ concentration regime. Both samples display a very broad diffuse peak in the scattering cross section at large k that decreases slightly with increasing photon energy beneath the W L_{III} absorption edge and remains unchanged as the photon energy is increased beneath the Ge K absorption edge. A model of voids in a homogeneous matrix would show a decrease in the scattering cross section as the photon energy was increased beneath either absorption edge. Additionally, the model requires a volume fraction of voids in excess of 0.20 to produce a peak in the scattering cross section at a non-zero k value. This seems physically unreasonable.

Aside from the pure elements, there are only two crystalline compounds, each with two allotropes, in the W-Ge system. These are two high pressure forms of c-WGe$_2$ and two high pressure forms of c-W$_5$Ge$_3$ (see Chapter II, section 2.2). Homogeneous and inhomogeneous particle models were generated using 0.95 times the densities of the c-WGe$_2$ and c-W$_5$Ge$_3$ compounds. All four possible combinations of the allotropes were tried. The results of the homogeneous particle model for the a-W$_{45}$Ge$_{55}$ sample are shown in Figure VI.25. The model produces a peak at the correct k value with the correct magnitude for a photon energy of 200 eV below the W L_{III} absorption edge. It also predicts a much larger decrease in the scattering cross section with increasing photon

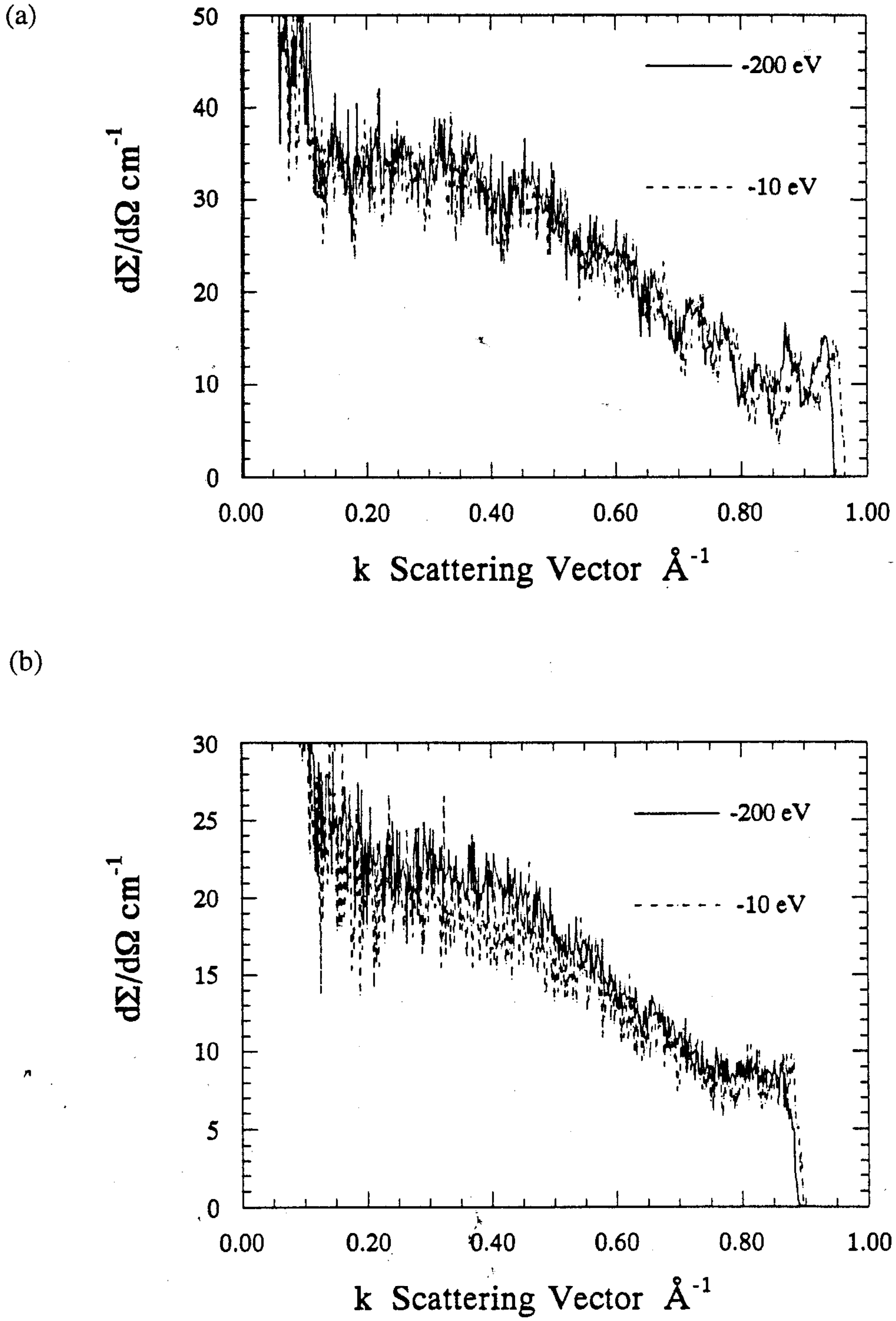

FIGURE VI.22 The a-$W_{45}Ge_{55}$ sample. (a) At 200 and 10 eV below the Ge K absorption edge. (b) At 200 and 10 eV below the W L_{III} absorption edge.

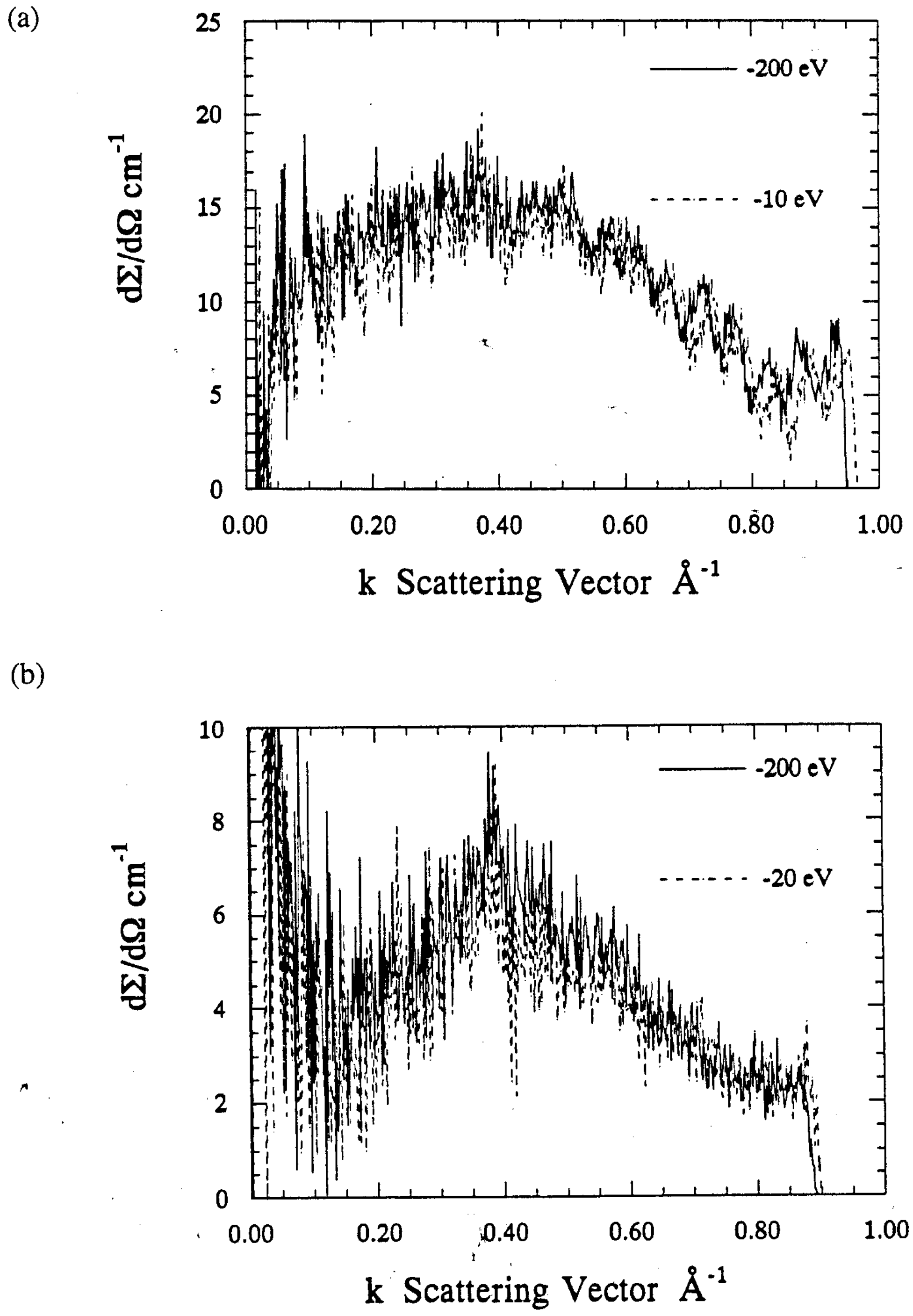

FIGURE VI.23 The a-$W_{50}Ge_{50}$ sample. (a) At 200 and 10 eV below the Ge K absorption edge. (b) At 200 and 20 eV below the W L_{III} absorption edge.

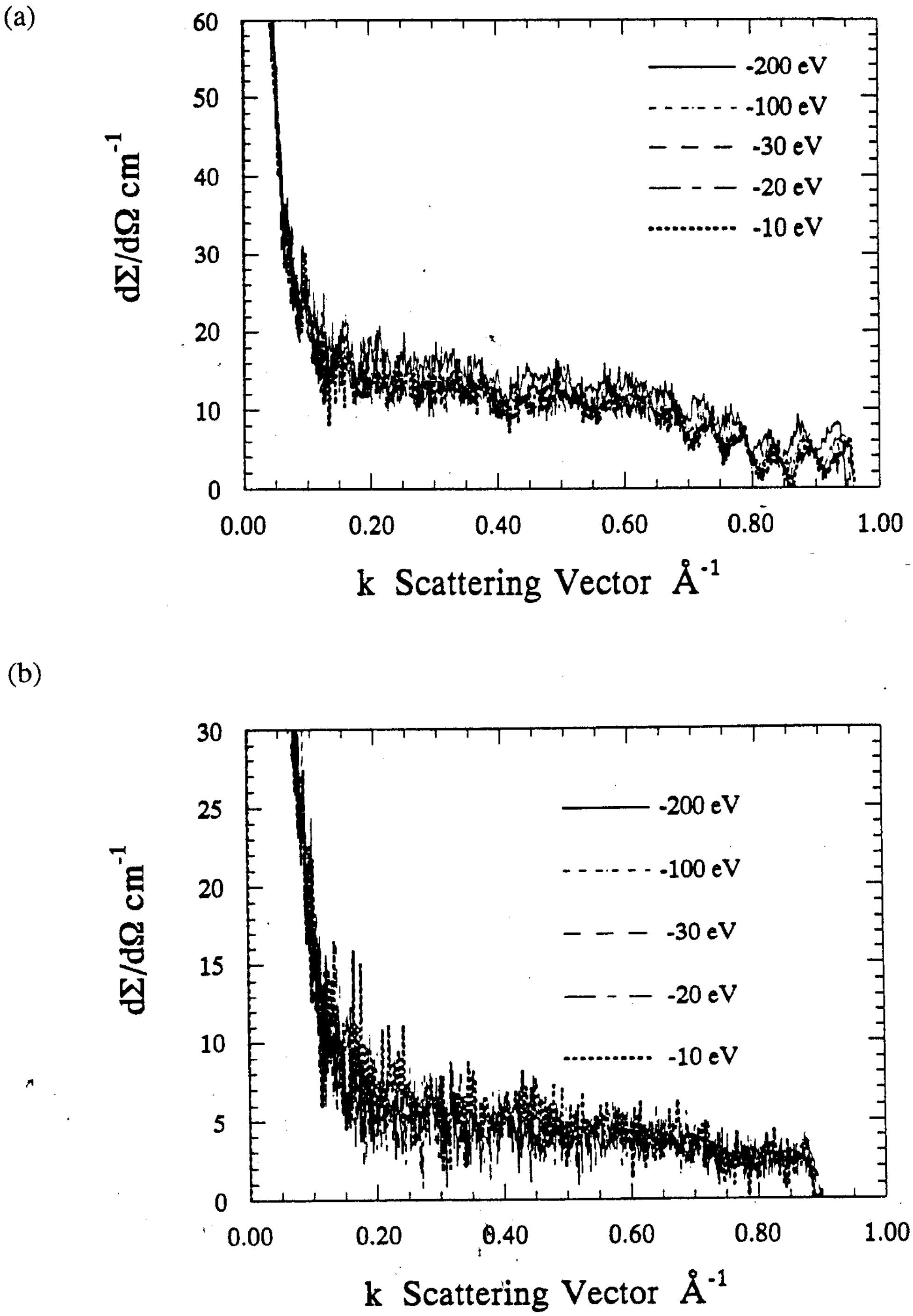

FIGURE VI.24 The a-$W_{78}Ge_{22}$ sample. (a) At 200, 100, 30, 20, and 10 eV below the Ge K absorption edge. (b) At 200, 100, 30, 20, and 10 eV below the W L_{III} absorption edge.

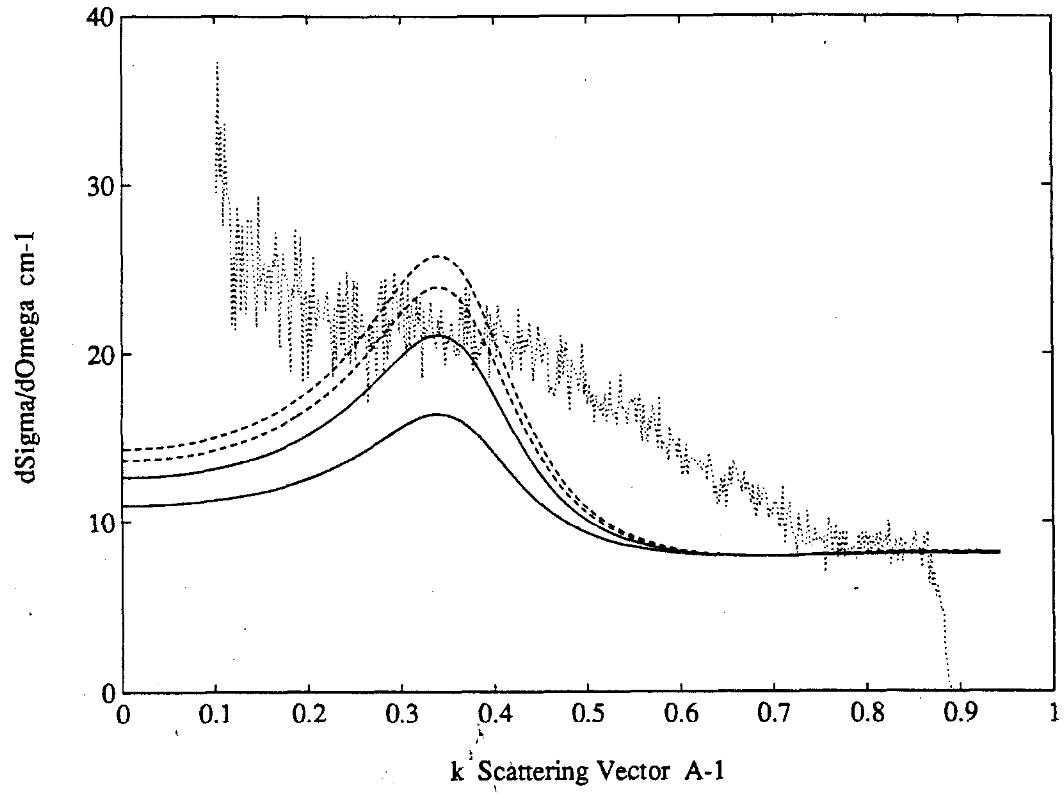

FIGURE VI.25 The homogeneous particle model for the a-$W_{45}Ge_{55}$ sample. Smooth lines: homogeneous spheres of a-W_5Ge_3 in a matrix of a-WGe_2 with R=6.5 Å and σ=7.5 Å. (------) 200 eV and 10 eV below the Ge edge, (——) 200 eV and 10 eV below the W edge. Noisy line: data at 200 eV below the W L_{III} edge.

energy below the W edge than is seen in the data. The model predicts a small increase in the scattering cross section with increasing photon energy beneath the Ge edge. These trends are not seen in the data, however, the larger effect at the W edge compared to the Ge edge is consistent with the data. The amorphous end products of phase separation may not have densities similar to the high pressure crystalline compounds.

The inhomogeneous particle model does a better job of reproducing the trends in $d\Sigma/d\Omega(k)$ with energy, but it must be multiplied by a factor of 7 to match the data. Similar results obtain for the a-$W_{50}Ge_{50}$ sample. The size of the spheres in these models is very small. The homogeneous particle models require radii 6.5 Å for the a-$W_{45}Ge_{55}$ sample and 5.5 Å for the a-$W_{50}Ge_{50}$ sample. Unlike the a-Fe_xGe_{100-x} system or the a-Mo_xGe_{100-x} system, the a-W_xGe_{100-x} system displays very fine scale phase separation into the metallic regime.

REFERENCES FOR CHAPTER VI

Cromer, D. T. & Liberman, D., *J. Chem. Phys.* **53** (1970) 1891.

Kortright, J. B., Ph.D. thesis, Stanford University (1984).

Kortright, J. B. & Bienenstock, A., *Phys. Rev. B* **37** (1988) 2979.

Lorentz, R. D., Ph.D. thesis, Stanford University (1986).

Lorentz, R. D., Bienenstock, A. & Morrison, T. I., to appear in *Phys. Rev. B* (1994).

Regan, M. J., Ph.D. thesis, Stanford University (1993).

CHAPTER VII

CONCLUSIONS

This work has addressed the following questions.

- For each of the a-M_xGe_{100-x} systems studied here, is the semiconductor-metal transition accomplished through homogeneous alloy formation or through phase separation?
- Are the apparent differences between Kortright's (1984) and Lorentz's (1986) studies of the respective a-Mo_xGe_{100-x} and the a-Fe_xGe_{100-x} systems in the semiconductor-metal transition region real or due to insufficiencies of experimental techniques? In particular, is the a-Mo_xGe_{100-x} system compositionally modulated and the a-Fe_xGe_{100-x} system homogeneous in this composition regime?
- Similarly, Kortright's (1984) and Lorentz's (1986) work point to homogeneous alloy formation in the a-Mo_xGe_{100-x} system for $25<x<72$ and phase separation in the a-Fe_xGe_{100-x} system for $33<x<72$. Can this be verified? and
- For the phase separated samples, can the end products of phase separation be identified?

7.1 SUMMARY OF THE RESULTS FOR SAMPLES WITH $x<25$

The ASAXS study presented here has shown that the three systems of sputtered amorphous thin films, a-Fe_xGe_{100-x}, a-Mo_xGe_{100-x}, and a-W_xGe_{100-x} are all compositionally modulated for $0<x<25$. The semiconductor-metal transition is accomplished through phase separation in all three systems. None of the samples in this composition regime is homogeneous. Furthermore, the distribution of Ge atoms is uniform through out each of these samples. The density fluctuations arise from fluctuations in the distribution of metal atoms. The metal atoms in this composition regime are incorporated into an amorphous metal-germanium phase that seems to be best described as a-MGe$_2$. The data are consistent with fine scale phase separation into a-Ge and a-MGe$_2$ with the size scale of the inhomogeneities ranging from about 10 to 25 Å.

Comparisons of representative samples from the three different systems in the semiconductor-metal transition regime show that the a-Fe$_x$Ge$_{100-x}$ system has scattering cross sections with the largest and narrowest peaks for a given x, the a-Mo$_x$Ge$_{100-x}$ system has the broadest and most diffuse peaks, and the a-W$_x$Ge$_{100-x}$ system is intermediate to the other two. This suggests a more well developed stage of phase separation in the a-Fe$_x$Ge$_{100-x}$ system and a less complete degree of phase separation in the a-Mo$_x$Ge$_{100-x}$ system.

Simple model calculations show that the a-Fe$_x$Ge$_{100-x}$ system and the a-W$_x$Ge$_{100-x}$ system are well described as collection of identical homogeneous spheres of a-MGe$_2$ (a-Ge) immersed in a matrix of a-Ge (a-MGe$_2$). The a-Mo$_x$Ge$_{100-x}$ system, however, is better described as a collection of identical inhomogeneous spheres with spherical cores of a-MoGe$_2$ and concentric spherical shells of a-Ge immersed in a homogeneous (unreacted) matrix of a-Mo$_x$Ge$_{100-x}$. Only a small portion (<25 %) of each sample in the a-Mo$_x$Ge$_{100-x}$ system is occupied by the phase separated composite spheres. Most of the sample is unreacted. Model calculations show that the data from the a-Mo$_x$Ge$_{100-x}$ system is, indeed, consistent with incomplete phase separation while the data from the a-Fe$_x$Ge$_{100-x}$ and a-W$_x$Ge$_{100-x}$ systems is consistent with complete phase separation.

7.2 SUMMARY OF THE RESULTS FOR SAMPLES WITH $x>25$

ASAXS data from the a-Fe$_x$Ge$_{100-x}$ samples with $34 \leq x \leq 71$ indicate the presence of chemical inhomogeneities across this entire composition regime. The most likely candidates for the end products of phase separation are a-FeGe$_2$ and a-Fe$_3$Ge. Model calculations of both homogeneous and inhomogeneous particle systems containing various combinations of a-Fe$_x$Ge$_{100-x}$, a-FeGe$_2$, a-Fe$_3$Ge fail utterly to reproduce the data. The consideration of other chemical constituents in these models does not improve the fit. The model only begins to approach the data when voids are included in the a-FeGe$_2$ (a-Fe$_3$Ge) matrix along with homogeneous spheres of a-Fe$_3$Ge (a-FeGe$_2$). For these metallic samples, the sphere radii are on the order of 100 Å. This is large compared to the sphere radii for the semiconductor-rich samples which are on the order of 10 Å.

In contrast to the a-Fe$_x$Ge$_{100-x}$ samples, the a-Mo$_x$Ge$_{100-x}$ samples have SAXS patterns that are essentially featureless. This shows, in agreement with Kortright's work, that the a-Mo$_x$Ge$_{100-x}$ samples with x>25 are homogeneous.

The metallic a-W$_x$Ge$_{100-x}$ samples, unlike the metallic a-Fe$_x$Ge$_{100-x}$ or the metallic a-Mo$_x$Ge$_{100-x}$ samples, show very fine scale phase separation. Model calculations indicate phase separation into a-W$_5$Ge$_3$ and a-WGe$_2$ with sphere radii of about 6 Å.

7.3 THE COMBINED PICTURE

Of the three systems studied here, the a-Fe$_x$Ge$_{100-x}$ system shows the greatest degree of phase separation across its entire composition range. Only the a-Fe$_x$Ge$_{100-x}$ system shows large scale phase separation in the metallic regime. The a-Fe$_x$Ge$_{100-x}$ system also shows the greatest degree of phase separation in the semiconducting regime with the narrowest and most intense SAXS peaks of the three systems.

The a-Mo$_x$Ge$_{100-x}$ system displays the smallest degree of phase separation. The semiconducting samples are only partially phase separated with the majority of the samples volume remaining unreacted (homogeneous) while the metallic samples are completely homogeneous.

The a-W$_x$Ge$_{100-x}$ system is intermediate to the other two systems. The semiconducting a-W$_x$Ge$_{100-x}$ samples have SAXS peaks that are more intense than the SAXS peaks for the a-Mo$_x$Ge$_{100-x}$ system while being broader and more diffuse than those of the a-Fe$_x$Ge$_{100-x}$ system. The metallic a-W$_x$Ge$_{100-x}$ samples exhibit very fine scale phase separation.

This forms a consistent picture. Across the entire composition range, $0<x<75$, the a-Fe_xGe_{100-x} samples display the greatest degree of phase separation, the a-Mo_xGe_{100-x} samples display the smallest tendency to phase separate, and the a-W_xGe_{100-x} samples are intermediate to the a-Fe_xGe_{100-x} and a-Mo_xGe_{100-x} samples. During sample fabrication, the Ge, W, and Mo targets were all magnetron sputtered, while the Fe target was triode sputtered. In magnetron sputtering, the plasma is magnetically confined to a region close to the target. The substrate is thus relatively free of charged particle bombardment. In triode sputtering the plasma is not confined and the growing film is continuously bombarded by free electrons. This rain of electrons on the growing film obviously adds energy to the evolving structure and probably drives the phase separation seen in the a-Fe_xGe_{100-x} films.

7.4 IMPLICATIONS FOR FURTHER INVESTIGATIONS

This work leaves its share of unanswered questions. Now that it is clear that the a-M_xGe_{100-x} samples in the semiconductor-metal transition region all phase separate into a-Ge and probably a-MGe_2, it will be interesting to figure out the structure of the a-MGe_2 phases. The semiconductor-metal transition in these alloys clearly proceeds structurally by phase separation but the details of the electrical transition are not understood, e.g., does the electrical conduction at a given composition proceed by variable range hopping, tunneling from one metallic cluster to the next, or through a continuous metallic path induced by percolation of the metallic phase?

Similar questions apply to the metallic samples. The a-Fe_xGe_{100-x} samples studied here show large scale phase separation probably into a-$FeGe_2$ and a-Fe_3Ge. The ferromagnetic transition at about 40 atomic percent in these samples is explained well by percolation of a-Fe_3Ge in a-$FeGe_2$ (Lorentz et al., 1994). The magnetron sputtered samples studied by Regan (1993) show no phase separation in the metallic regime. At what composition do those films become ferromagnetic and by what mechanism?

The metallic regime of the a-Fe_xGe_{100-x} system begs for better characterization as does that of the a-W_xGe_{100-x} system. Since the phase separation in the a-Fe_xGe_{100-x} system seems to be driven by the electron bombardment inherent in triode sputtering, a full characterization of the structure of these types of films as a function of various fabrication parameters may prove to be enlightening. Finally, annealing studies performed on these samples would provide a lot of information about the stability of the various phases.

REFERENCES FOR CHAPTER VII

Kortright, J. B., Ph.D. thesis, Stanford University (1984).

Lorentz, R. D., Ph.D. thesis, Stanford University (1986).

Lorentz, R. D., Bienenstock, A. & Morrison, T. I., to appear in *Phys. Rev. B* (1994).

Regan, M. J., Ph.D. thesis, Stanford University (1993).